Université de Montréal

Time-Dependent Density-Functional Study of Absorption Spectra of Open-Shell Molecules and Alkali Metal Clusters

par

Jingang Guan

Département de Chimie

Faculté des arts et des sciences

Thèse présentée à la Faculté des études supérieures

en vue de l'obtention du grade de

Philosophiæ Doctor (Ph.D.)

en Chimie

septembre, 1999

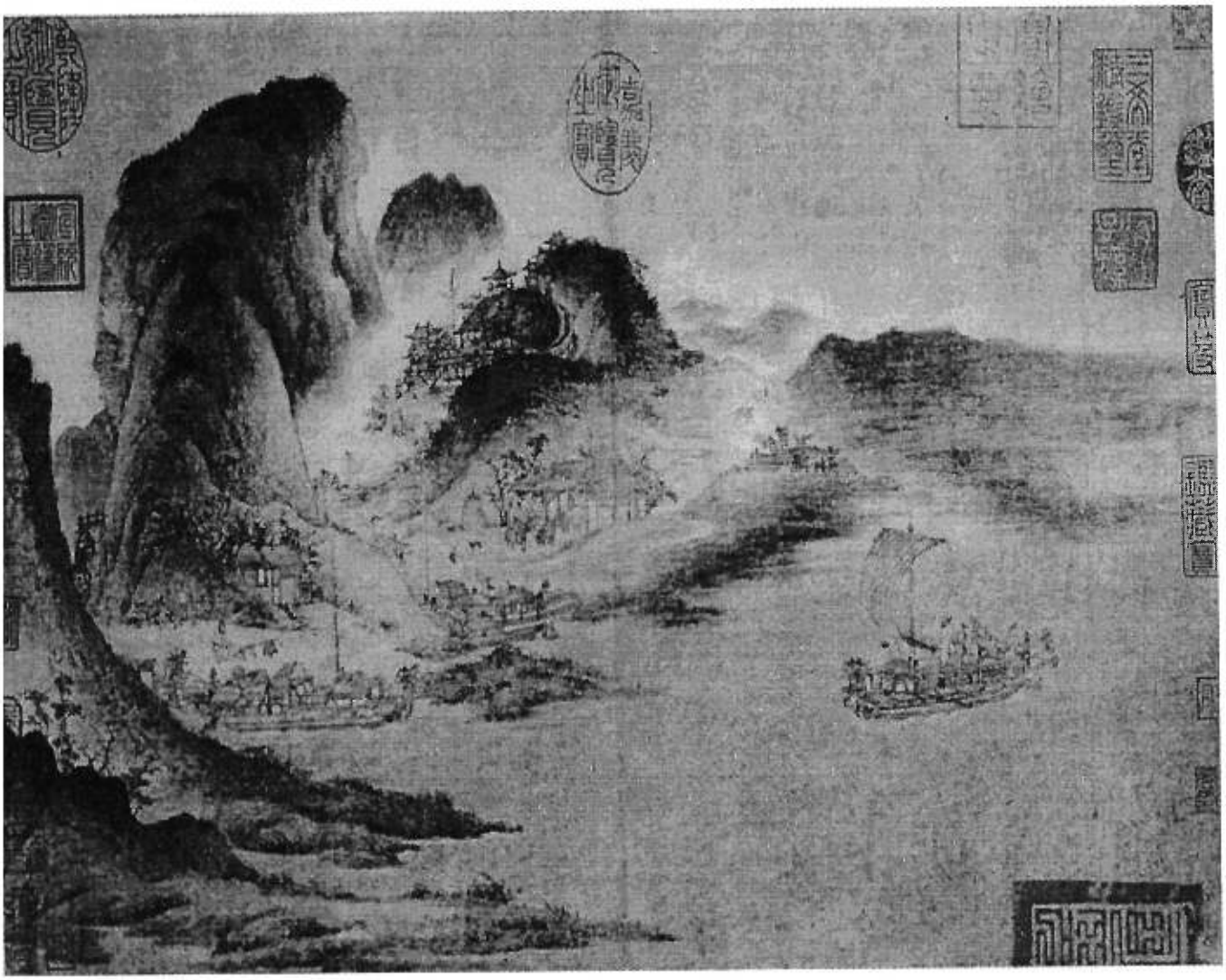

Université de Montréal

Faculté des études supérieures

Cette thèse intitulée:

Time-Dependent Density-Functional Study of Absorption Spectra of Open-Shell Molecules and Alkali Metal Clusters

présentée par:

Jingang Guan

a été évaluée par un jury composé des personnes suivantes:

Tucker Carrington,	président-rapporteur
Dennis R. Salahub,	directeur de recherche
Gilles Durocher,	membre du jury
Fritz Grein,	examinateur externe
John M. Pearson ,	représentant du doyen

Thèse acceptée le: .....

ABSTRACT

Time-dependent density–functional theory (DFT) has been extended by the present work for open-shell applications and coded in the program *deMon-DynaRho* (**de**nsité de **Mon**tréal–**Dyna**mic Response of **Rho**, Rho here stands for the charge density) based on version 2p0 of the previous *deMon-DynaRho*. This version 2p0 could previously only treat closed–shell systems. The present modification and implementation of time-dependent DFT provide a unique practical molecular DFT code capable of treating excited state properties for either open–shell or closed–shell systems. As a case study, six small well–studied open-shell molecules, three neutral molecules (BeH, BeF, CN) and three positive ions (CO^+, N_2^+, CH_2O^+), are chosen to evaluate the quality of time-dependent DFT for the calculation of excitation energies and the prediction of absorption spectra of open-shell molecules. Further applications to predicting and interpreting of absorption spectra of alkali metal clusters (lithium clusters and sodium clusters) from the dimer though the hexamer are presented. With the exception of the lowest two excitation energies (without oscillator strengths) of a few open–shell molecules which recently appeared in the literature [1], the present all-electron calculations of absorption spectra of the six open–shell molecules and alkali metal clusters (the lithium and the sodium clusters) are the first time-dependent DFT study reported in the literature. The quality of the model core potential (MCP) in the applications to excited state properties is assessed against the present all-electron calculations. This MCP provides an efficient tool for the study of larger systems in the future.

The accuracy of DFT calculations depends on the choice of electron exchange-

correlation functional, orbital and auxiliary basis sets, and grids. To ensure the quality of the time-dependent DFT calculations, two exchange-correlation functionals, the local spin density approximation (LSDxc) and the functional proposed by van Leeuwen and Baerends in 1994 (LB94xc), are used respectively at the SCF step, combined with the time-dependent local spin density approximation (TDLSDxc) in the post-SCF step. These functionals used at the SCF step and at the post-SCF step are referred to as LSDxc/TDLSDxc and LB94xc/TDLSDxc functionals. The comparison of excitation energies and oscillator strengths calculated by the two functionals shows that the LSDxc/TDLSDxc functional yields excited state properties in better agreement with available experimental results and high quality conventional *ab initio* methods (e.g. CI). However, the quality deteriorates for higher excitations in the free radical calculations due to the incorrect asymptotic behavior of the LSDxc functional, which leads to a too low ionization threshold compared to measurements. In contrast, the LB94xc/TDLSDxc functional which has the correct asymptotic behavior does give better results for higher excitations in the free radical calculations, but this functional does not give any improvement for the sodium clusters, it yields too larger excitation energies for both low and high excitations in the sodium clusters calculations. The choices of both orbital and auxiliary basis sets have been examined in the present calculations. Excitation energies are sensitive to the orbital basis; it requires a certain number of diffuse and polarization functions to be flexible enough to describe excited state properties. In contrast, excitation energies are less demanding on the auxiliary basis set. The normal auxiliary bases used in ground state property calculations are good enough for the excitation energy calculations. To avoid symmetry breaking, grids need to be carefully chosen in the calculation of excitation energies. The lithium pentamer is found to be a case where a higher quality of grid is needed, requiring a user-defined grid (24832 grid points per atom) for better assignments, whereas other calculations are with the EXTRA-FINE grid (6208 grid points per atom).

Absorption spectra of the open–shell molecules and the alkali metal clusters (lithium and sodium clusters) predicted by the present LSDxc/TDLSDxc calculations coincide nicely with the recorded spectroscopic pattern and are competitive with the *ab initio* CI method. The time-dependent DFT results are better than CIS (single configuration interactions) calculations and give significant improvement from those carried out by traditional DFT "multiplets" and Fritsche approaches, especially for the oscillator strengths. The LB94xc/TDLSDxc functional yields larger excitation energies and with larger errors from the experiments in comparison with the LSDxc/TDLSDxc functional. The deviations of the excitation energies calculated by the LSDxc/TDLSDxc and LB94xc/TDLSDxc functionals can be as large as 1.5 eV or more. Excitation energy collapse compared with available experiments or *ab initio* CI calculations, when excitation energies are larger than the ionization threshold, is observed for the free radicals, but it is not observed for the sodium clusters. On the other hand, excitation energies of the sodium clusters are overestimated, while those of the free radicals are underestimated. This is in contrast to the polarizability calculations which yield underestimations for sodium clusters and overestimations for the small molecules. This observation agrees with the theoretical relationship of excitation energy and polarizability.

The MCP yields similar excitation energies to the all-electron calculations and reasonably reproduces the spectroscopic pattern predicted by the all-electron calculations. However, additional diffuse basis functions are needed for more accurate results and higher excitations.

Key Words: Time-dependent density-functional theory, absorption spectra, open-shell molecules, alkali metal clusters, model core potential.

RÉSUMÉ

La théorie de la fonctionnelle de la densité (DFT) dépendante du temps a été étendue aux applications pour les couches ouvertes et implantée dans le programme *deMon-DynaRho* (**de**nsité de **Mon**tréal-**Dyna**mic Response **Rho**, Rho pour la densité de charge) à partir de la version précédente de *deMon-DynaRho* 2p0. Cette version précédente ne pouvait traiter que les systèmes à couche fermée. La présente modification et implantation de la DFT dépendante du temps, fournit un code DFT moléculaire unique capable de traiter les propriétés dans les états excités pour les molécules a couche fermée et à couche ouverte. Comme cas d'étude, six petites molécules à couche ouverte, trois molécules neutres (BeH, BeF, CN) et trois ions positifs (CO^+, N_2^+, CH_2O^+), sont choisis pour évaluer la qualité de la DFT dépendante du temps pour le calcul d'énergies d'excitation et la prédiction de spectres d'absorption pour les molécules à couche ouverte. Davantage d'applications dans le but de prédire et d'interpréter les spectres d'absorption d'agregats de métaux alcalins (agrégats de lithium et de sodium), à partir de dimères jusqu'aux hexamères sont présentés. Les calculs tous-électrons des spectres d'absorption des six molécules à couche ouverte et des agrégats métalliques alcalins (agrégats de lithium et de sodium) rapportés dans ce travail, représentent la premiére étude DFT dépendante du temps rapportée dans la littérature; bien que les deux énergies d'excitation les plus basses (sans forces oscillatoires) de quelques molécules à couche ouverte soient apparues récemment. La qualité des potentiels modèles de cœur (MCP) dans les calculs de propriétés des états excités est évaluée relativement aux calculs tous-électrons de ce travail. Ces MCP fournissent un outil efficace pour l'étude de plus gros systèmes dans le futur.

La précision des calculs DFT dépend du choix de la fonctionnelle d'échange-corrélation électronique, des bases orbitalaires et auxiliaires, et des grilles. Pour s'assurer de la qualité des calculs de la DFT dépendante du temps, deux fonctionnelles d'échange-corrélation, l'approximation de la densité de spin locale (LSDxc) et la fonctionnelle proposée par van Leeuwen et Baerends en 1994 (LB94xc), sont utilisées respectivement aux itérations SCF, combiné avec l'approximation de densité de spin locale dépendante du temps (TDLSDxc) à l'étape post-SCF. Ces fonctionnelles utilisées à l'étape SCF et à l'étape post-SCF sont représentées par les fonctionnelles LSDxc/TDLSDxc et LB94xc/TDLSDxc. La comparaison des énergies d'excitation et des forces oscillatoires calculées par les deux fonctionnelles montre que la fonctionnelle LSDxc/TDLSDxc donne des propriétés de l'état excité qui correspondent mieux avec les résultats expérimentaux disponibles et les méthodes *ab initio* conventionnelles de haute qualité (e.g. CI). Néanmoins, la qualité se détériore pour des excitations plus élevées dans les calculs de radicaux libres étant donné le comportement asymptotique incorrect de la fonctionnelle LSDxc, qui conduit à un seuil d'ionisation trop faible comparé aux mesures expérimentales. Par contre, la fonctionnelle LB94xc/TDLSDxc, avec le bon comportement asymptotique, apporte une amélioration pour les excitations plus élevées dans le cas des radicaux libres, mais donne des énergies d'excitation trop élevées à la fois pour les basses et hautes excitations dans le cas des agrégats de sodium. Le choix des bases orbitalaires et auxiliaires a été examiné dans les calculs de ce travail. Les énergies d'excitation sont sensibles à la base orbitalaire; elles requièrent un certain nombre de fonctions de polarisation et de diffusion pour être suffisamment flexibles pour décrire les propriétés des états excités. Par contre, les énergies d'excitation sont moins exigeantes sur la base auxiliaire. Les bases auxiliaires normales pour les calculs de propriétés de l'état fondamental sont de qualité suffisante pour le calcul d'énergies d'excitation. Pour éviter une brisure de symétrie, les grilles doivent être choisies avec soin dans les calculs d'énergies d'excitation. Le pentamère de lithium s'est montré être un

cas où une grille de plus grande qualité est nécessaire, demandant une grille définie par l'usager (24832 points de grille par atome) pour des meilleures assignations, tout comme les autres calculs sont faits avec une grille EXTRA-FINE (6208 points de grille par atome). Les spectres d'absorption des molécules à couche ouverte et des agrégats métalliques alcalins (agrégats de lithium et de sodium) prédit par les présent calculs LSDxc/TDLSDxc coïncident bien avec les patrons spectroscopiques mesurés et sont compétitifs avec la méthode *ab initio* CI. Les résultats des calculs avec la DFT dépendante du temps sont meilleurs que ceux obtenus CIS (single configuration interactions) et amènent une amélioration significative relativement aux approches de la DFT "multiplet" et "Fritsche" traditionnelles, particulièrement pour les forces oscillatoires. La fonctionnelle LB94xc/TDLSDxc donne des énergies d'excitation plus élevées et avec de plus grandes erreurs relativement à l'expérience en comparaison avec la fonctionnelle LSDxc/TDLSDxc. Les déviations des énergies d'excitation calculées avec les fonctionnelles LSDxc/TDLSDxc et LB94xc/TDLSDxc peuvent être aussi grandes que 1.5 eV ou plus. Les énergies d'excitation calculées diffèrent de l'expérience et des calculs *ab initio* CI, quand les énergies d'excitation sont supérieures au seuil d'ionisation et cela est observé pour les radicaux libres, mais pas pour les agrégats de sodium. D'autre part, les énergies d'excitation des agrégats de sodium sont surestimées, tandis que celles des radicaux libres sont sous-estimées. Ceci est en contraste au fait que les calculs de polarisabilité sont des sous-estimations pour les agrégats sodium et des surestimations pour les petites molécules. Cette observation correpond à la relation théorique de l'énergie d'excitation et de la polarisabilité.

Les MCP donnent des énergies d'excitation similaires aux calculs tous-électrons. Néanmoins, des fonctions de base diffuses additionnelles sont nécessaires pour des résultats plus précis et des excitations plus élevées.

Mots clefs : théorie de la fonctionnelle de la densité dépendante du temps,

spectre d'absorption, molécules à couche ouverte, agrégats de métaux alcalins, potentiel modèle de cœur.

TABLE OF CONTENTS

LIST OF TABLES

LIST OF FIGURES

LIST OF ABBREVIATIONS

AE *All-electron.*

AEAE *All-electron calculation with all-electron optimized geometry.*

AEMCP *All-electron calculation with model core potential optimized geometry.*

asy *Asymmetric.*

B3LYP *Exchange-correlation functional based on Becke's half and half idea and the original mixed exchange-correlation approximation plus Lee, Yang, and Parr's correlation functional.*

B88x *Becke proposed exchange functional in 1988.*

B88x+P86c *Becke's exchange functional proposed in 1988 plus Perdew's correlation functional proposed in 1986.*

BEPA *Binding energy per atom.*

BLYP *Becke's exchange functional plus Lee, Yang and Parr's correlation functional.*

BHS *Bachelet, Hamann, and Schlüter.*

BRD *Bardsley.*

BSSE *Basis set superposition error.*

CCSD *Coupled cluster single and double excitations.*

CD *Charge density.*

CI *Configuration interaction.*

CPU *Central processing unit.*

DFRT *Density-functional response theory.*

DFT *Density-functional theory.*

DZVP *Double zeta valence plus polarization.*

ECP *Effective core potential.*

F *Fine.*

FF *Finite field.*

FVCI *Full valence configuration interaction.*

GGA *Generalized gradient approximation.*

GTO *Gaussian-type orbital.*

HF *Hartree-Fock.*

HOMO *Highest occupied molecular orbital*

ico *Icosahedral.*

IP *Ionization potential.*

IPA *Independent particle approximation.*

KS *Kohn-Sham.*

LB94xc *van Leeuwen and Baerends proposed exchange-correlation functional in 1994.*

LDAxc *Local density approximation for exchange-correlation functional.*

LSDxc *Local spin density approximation for exchange-correlation functional.*

LYP *Lee, Yang, and Parr proposed correlation functional.*

MCEP *Multiconfiguration electron propagator.*

MCLR *Multiconfigurational linear response theory.*

MCP *Model core potential.*

MCSCF *Multiconfiguration self-consistent field.*

MO *Molecular orbital.*

MP4 *Fourth-order Møller-Plesset perturbation theory.*

MRCI *Multireference configuration interaction.*

MRD-CI *Multireference double excitation configuration interaction.*

NR *NonRandom.*

P86c *Correlation functional proposed by Perdew in 1986.*

PW86x *Perdew and Wang proposed exchange functional in 1986.*

PW86x+P86c *Perdew and Wang's exchange functional plus Perdew's correlation functional.*

R *Random.*

ROCIS *Restricted open-shell single excitation configuration interaction.*

RPA *Random phase approximation.*

SACCI *Symmetry adapted cluster configuration interaction.*

SAPS *Spherically-averaged pseudopotential.*

SCF *Self-consistent field.*

SDCI *Single and double excitation configuration interaction.*

STO *Slater-type orbital.*

STO3G *A Slater-type orbital replaced by three primitive Gaussian functions.*

TDDFRT *Time-dependent density-functional response theory.*

TDDFT *Time-dependent density-functional theory.*

TDLDAx *Time-dependent exchange only local density approximation.*

TDLDAxc *Time-dependent local density approximation.*

TDLSDxc *Time-dependent local spin density approximation.*

UCIS *Unrestricted single excitation configuration interaction.*

UV *Ultraviolet.*

VWN *Vosko, Wilk, and Nusair.*

WDA *Weighted density approximation.*

XC *Exchange-correlation.*

XCIS *Extended single excitation configuration interaction.*

XF *EXTRA-FINE.*

To my parents, my wife, and my son

ACKNOWLEDGEMENTS

I would firstly like to take this opportunity to express my deepest and sincerest appreciation to my supervisor, Professor Dennis R. Salahub, for his knowledgeable guidance, continuous encouragement, constructive criticism, valuable suggestions, and financial support throughout this work, as well as for his countless revision of the drafts of this thesis. During my study at Université de Montréal, I have greatly benefited from his deep understanding in computational chemistry, from his enthusiasm towards science and strive for excellent, from his group which is a unique multidisciplinary research environment. Without him, it would have been impossible to finish my Ph.D study.

I am grateful to fellow colleagues for their friendship and helpful discussions, especially Dr. Mark E. Casida for some useful discussions on time-dependent density-functional theory, some computer technique help, and providing some references of the time-dependent density-functional theory, as well as reading the first two chapters and part of the chapter 3 and part of chapter 4 of this thesis, correcting the English, and giving some comments. Dr. Emil Proynov for some discussions on science. Dr. Suzanne Sirois for providing the model core potential of sodium. A lot of computer technique helps from Pierre-Jean L'Heureux and Benoit Cromp are highly appreciated.

Special thanks to Jean-François Truchon for the help with the French Résumé in this manuscript.

I would like to thank Département de Chimie, Informatiques de l'Université de Montréal, and Université de Montréal for providing excellent services and

computational support.

I am profoundly grateful to my parents, my wife, and my son for constant source of love and encouragement during this endeavor.

CHAPTER 1

INTRODUCTION

Electronic excitation energies and oscillator strengths of metal clusters have been an interesting subject of many experimental and theoretical studies in recent years [17, 18, 19, 20, 21, 22, 23, 24]. Electronic excitation spectra are interesting in their own right and also play a significant role in the description of physical observables in many areas of chemistry, including photochemistry and materials applications. In particular, the oscillator strengths (together with the excitation energies) can be used to calculate the second–order optical properties (e.g. dynamic polarizability). Calculations of the electronic excitation energies and oscillator strengths of metal clusters (with proper assignments) may provide useful information both for characterizing the electronic and nuclear structure of the clusters. They also can be used to understand and design cluster materials with novel optical properties [25]. The problem with existing methods is that they are too costly for large systems and if the level of correlation needed is high. Density-functional theory (DFT), with its simplicity and effective treatment of electron correlation, has been the method of choice for the theoretical treatment of many ground state problems [26, 27, 28]. A real molecular time-dependent DFT formulation has also been developed lately and applied to closed-shell molecules [22, 29, 30, 31, 32, 33, 34, 35, 36, 37], but almost nothing is known about how time-dependent DFT behaves for the open-shell molecules in which electron correlation effects are particularly strong. The extension of the time-dependent DFT to treat open-shell excitation spectra is clearly desirable. A recent time–dependent DFT calculation of the lowest two excitation

energies (without oscillator strengths) of a few free radicals by Hirata and Head–Gordon [1] appeared in the literature. The present work gives a unique modification and implementation of the time-dependent DFT for open–shell systems in the program *deMon-DynaRho*, version 2pX. This implementation provides a new computational tool for the study of excited state properties of open–shell molecules or clusters. As case studies, this new code was applied to calculate excitation spectra of open-shell molecules and alkali metal clusters (lithium and sodium clusters). The use of excitation spectra to help determine equilibrium geometries is also discussed in the present work.

Experimental techniques initially used for obtaining electronic and geometric structure information for metal clusters were ionization potentials [38, 39], molecular beam abundance [40, 41, 42, 43, 44], chemical reactivity [45], and polarizabilities [46]. These techniques only give indirect information. More direct means of structure determination, namely optical absorption spectroscopy, has also been carried out on small metal clusters in the gas phase, particularly metal trimers (lithium, sodium, copper, silver, and nickel, etc.) by laser-induced fluorescence [47, 48, 49, 50] and by multiphoton ionization [51, 52, 53, 54, 55, 56, 57, 58]. Nevertheless, these two experimental techniques failed for large clusters. It is believed the problem comes from insufficient resolution due to short excited state lifetimes [23]. However, the problem is alleviated by the two complementary experimental techniques of electron photodetachment [59, 60, 61, 62, 63] and photodissociation [16, 64, 65, 66, 67, 68, 69] spectroscopies which yield information about negative ions and for cation/neutral clusters, respectively. Photodissociation spectroscopy was first performed for the sodium tetramer [67] and the lithium tetramer [68] by photodepletion. The spectra of large sodium clusters up to forty atoms have been obtained as well by the same technique at visible wavelengths [16, 64, 65, 70, 71]. High resolution spectra covering a large spectral region were also measured for large lithium clusters, up to eight atoms [12, 69] and large sodium clusters, up to twenty atoms [23, 72]. These experimental measurements

offer a good opportunity for theoretical assessments and interpretations.

Theoretical calculations of optical spectra of alkali metal clusters have been carried out with different models. The classical model treats the metal clusters as spheroidal conductors with no atomic structure (droplets), and using surface plasma oscillations to describe the absorption [64, 65, 70, 73]. Quantum effects have been taken into account in the jellium potential model which usually assumes the clusters have spherical topologies [74, 75, 76]. Quantum molecular models considering the molecular nature of the clusters have been performed with effective core potential (ECP) [14, 15, 77] and with all–electron methods [14, 78, 79].

Quantum mechanical *ab initio* methods have been extensively used for studies of optical spectra of atoms [80, 81, 82, 83], molecules [84, 85, 86, 87, 88], clusters [89, 90], and nuclei [91, 92]. The simplest level of quantum mechanical theory for studying electronic spectra is the Tamm-Dancoff approximation (TDA)—single excitation configuration interaction method (CIS) [93, 94, 95]. The TDA is the least computationally demanding of the presently and widely used methods for excited states. The computational cost of the TDA method scales formally as N^6 (for full diagonalization), where N is the number of basis functions used in the calculation. Nevertheless, the TDA fails to describe the states which have significant contributions from double or higher substitutions and the accuracy of the excitation energy calculations in the TDA approach is not satisfactory for most cases (with a few exceptions) [96]. The time-dependent Hartree-Fock (HF) method [97, 98, 99, 100] is another simple theory for treating excited states. Time-dependent HF has more or less the same computational efficiency as the TDA, and the sum of the oscillator strengths satisfies the Thomas-Reiche-Kuhn (TRK) sum rule [101, 102] in the limit of a complete basis set. Both the TDA and the time-dependent HF usually overestimate excitation energies [103, 104]. This may be caused by missing electron correlation effects. Moreover, previous experience [33] has shown that the reliable quantum mechan-

ical treatment of electronic excitations in atoms, molecules, and clusters requires, in general, proper inclusion of static [105, 106] and dynamic [107] electron correlation. Hence a suitable method for obtaining accurate excitation energies should include electron correlation. Methods including such electron correlation are the configuration interaction (CI) method [108, 109, 110] (e.g. the multiple-reference configuration interaction method (MRCI) [111], complete active space plus second order perturbation (CAS-PT2) [112]), and density-functional theory. But the computational cost of the CI (e.g. MRCI) method increases rapidly (formally scaled as N^{12} for double CI with full diagonalization) and the accuracy of calculations decreases as the number of electrons increases [4]. Hence the CI (e.g. MRCI) method is limited to small molecules and small clusters.

Kohn-Sham DFT [26, 113, 114] is structurally similar to the Hartree-Fock method, but it contains the electron correlation effects which Hartree-Fock misses. The computational simplicity of Kohn-Sham DFT with its effective potential based on the charge density which is a function of only three spatial coordinates and spin provides a comparable or even lower computational cost (generally scaling as N^3) compared to the conventional *ab initio* methods (e.g. HF, MRCI, etc). Furthermore, Kohn-Sham DFT has become a powerful and successful state-of-the-art computational tool in the quantitative treatments of time-independent problems (ground state properties) of many-electron systems, such as atoms, molecules, metal clusters, complex systems, solid state, and nuclear physics [26, 27, 115, 116, 117, 118, 119, 120, 121, 122], even very large systems [123, 124]. The ground state properties calculated from DFT with the currently best functionals are usually in very close agreement with configuration interaction calculations [125, 126] although there are some exceptions. These advantages of Kohn-Sham DFT and its successful, impressive, and accurate treatments of stationary systems provide a stimulus for further applications to the interesting area of time-dependent problems.

There are a variety of traditional approaches in time-independent DFT for the calculation of excitation energies and oscillator strengths. The Δ self-consistent field (ΔSCF) procedure [10, 26, 127, 128, 129, 130, 131, 132, 133, 134] is traditionally used for the calculation of excitation energies. This procedure takes the energy difference of ground state electron configuration DFT SCF energy and the excited state electron configuration DFT SCF energy as the excitation energy. It was simplified by Slater [135, 136] who proposed a transition state approximation for calculating ΔSCF energies. Gunnarsson and Lundqvist [137] have shown how ground-state DFT can be rigorously extended to treat the lowest excited states of each symmetry. However, using time-independent Kohn-Sham DFT to tackle excited state properties is notoriously difficult [138, 139]. The second Hohenberg-Kohn theorem is only applicable for the ground state and for lowest states of a given symmetry, hence, the DFT ΔSCF method lacks a solid formal justification. Moreover, excited state DFT SCF calculations can sometimes run into difficulties, such as convergence problems, symmetry breaking, and the multiplets may have the same charge density, but different energies, etc.

Theophilou [140] has given a rigorous extension of DFT for excited states by the subspace theory. Gross, Oliveira, and Kohn [141, 142, 143] gave a more general treatment by ensembles, and they have used an ensemble exchange-correlation potential to calculate the excitation energies. This approach has also been studied by Gáspár [144] and by Nagy [145, 146, 147]. A fundamental difficulty with the extensions of ground state DFT for the excited states based on the Rayleigh-Ritz principle for the lowest eigenstate of each symmetry class [128, 129, 137] or based on a variational principle for ensembles [141, 142, 143, 148, 149, 150], is that the exchange-correlation energy functionals may depend on the symmetry labels of the excited state or on the particular ensemble. The explicit form of the excited state exchange-correlation functionals remains unknown. Furthermore, it has been found that the excitation energies calculated by the ensemble technique vary depending on the value of the weighting factors used [28, 151, 152]. As a

result, subspace theory is not yet a viable candidate for practical calculations.

Time-dependent DFT provides a rigorous alternative for calculating excitation spectra. The generalization of Kohn-Sham DFT to time-dependent DFT has been exploited by many authors [29, 30, 138, 153, 154, 155, 156, 157]. The original model of time-dependent DFT dates back to the time-dependent Thomas-Fermi model proposed by Bloch [158] as early as in 1933. The first significant steps towards a time-dependent DFT were taken by Peuchert [159] and by Zangwill and Soven [160]. They were based on the analogies with the time-dependent HF approach and used the linear response of the density to a time-dependent external potential as the response of the non-interacting electrons to an effective time-dependent potential, and obtained the first time-dependent Kohn-Sham equations. The adiabatic local density approximation was also first applied in the time-dependent DFT by Zangwill and Soven [160]. Important steps toward a rigorous foundation of time-dependent DFT were taken by Deb and Ghosh [155, 161, 162, 163] and by Bartolotti [154, 164, 165, 166]. They successfully proved the fundamental theorems for the time-dependent DFT using a set of restricted external potentials. Deb and Ghosh used a periodic potential (in time) as a time-dependent potential to formulate and to explore Hohenberg–Kohn, and Kohn–Sham type theorems for the time-dependent DFT, while Bartolotti used an adiabatic process. A theoretical breakthrough, giving more general and rather successful proofs of the fundamental theorems (the Hohenberg–Kohn, and Kohn–Sham theorems) for time-dependent DFT was accomplished by Runge and Gross [156]. They used a time-dependent potential which can be expressed in a Taylor's series at initial time to show that the external potential is determined by the charge density up to a time-dependent spatial constant. This provides the theoretical justification for time-dependent DFT and places time-dependent DFT in a parallel footing to time-independent DFT. This also paves the way for time-dependent DFT to tackle many domains which involve time-dependent fields, such as dynamic response properties (dynamic or frequency-dependent po-

larizabilities and hyperpolarizabilities, etc.), electronic excitation energies and oscillator strengths, photoionization cross sections, and the treatment of excited states. Detailed reviews of time-dependent DFT can be found in the literature [138, 139, 167, 168, 169].

Time-dependent DFT provides a practical and useful method for calculating electronic spectra while still maintaining the electron correlation and computational simplicity of time-independent DFT. Indeed, the applications of time-dependent DFT in the calculations of the dynamic response properties have been reported in the literature for atoms [170, 171, 172, 173, 174, 175, 176, 177, 178, 179, 180, 181, 21, 20, 139], molecules [182, 173, 183, 33, 22, 184, 34, 36, 37], clusters [75, 185, 186], metallic surfaces [187, 188, 189], bulk metals [190, 191, 192], bulk semiconductors [176], and solids [177]. The use of time-dependent DFT to calculate excitation spectra is a relatively new feature in quantum chemistry programs. The first excitation energy calculations with time-dependent DFT were done numerically for some atoms using poles of the Kohn-Sham response function by Petersilka, Grossmann, and Gross [21]. Petersilka and Gross [193, 20] calculated excitation energies of atoms with spin multiplets. The atomic applications of time-dependent DFT made use of the spherical symmetry of the system to simplify the calculations. This prevents the algorithm from being applied to molecular systems. Many authors have tried to take advantage of atomic-like algorithms for an extension to the molecular calculations by using a jellium model [194, 195, 196, 197, 198], sphericalized potentials [186, 199, 200], and single-center expansions [182, 173]. Levine and Soven [182, 173], using a single-center formulation, calculated photoemission spectra of some small closed-shell molecules, but this single-center expansion is not suitable for the general treatment of multicenter molecules. Dynamic molecular properties were also explored with time-dependent DFT. Van Gisbergen, Snijders, and Baerends [31, 201, 202] have calculated the frequency-dependent polarizabilities, frequency-dependent hyperpolarizabilities, and van der Waals coefficients. The dynamic hyperpo-

larizabilities were also calculated by Zangwill [203] and by Senatore and Subbaswamy [204]. However, the first real molecular time-dependent DFT algorithm was only recently proposed by several authors [29, 30, 31, 32, 33, 22, 34, 35, 36, 37]. This molecular algorithm has been programmed in a time-dependent DFT program, deMon-DynaRho (**de**nsité de **Mon**tréal–**Dyna**mic Response of **Rho**, Rho here stands for the charge density) which has been recently developed in the Salahub group [29, 30]. The deMon-DynaRho program uses a real molecular time-dependent algorithm. It is based on the idea of using the poles and the residues of the dynamic polarizability to calculate excitation energies and oscillator strengths. Multicenter Gaussian expansions and auxiliary basis functions are used in the program. But it was only available for treating closed-shell molecules prior to the present work.

Bauernschmitt and Ahlrichs [33] have studied excitation energies of closed-shell molecules with several exchange–correlation functionals (local, gradient–corrected and hybrid functionals), they found that the three parameter Lee-Yang-Parr (B3LYP) functional proposed by Becke [205] gives the best excitation energies, and the time-dependent local density approximation gives better results than the traditional *ab initio* methods (TDA and time-dependent HF), but the excitation energies calculated by time-dependent DFT (e.g. local density approximation) are systematically underestimated, with errors of about 0.4 eV. They suggested that the problem caused may come from the use of the adiabatic approximation [33, 22]. Casida *et al.* [183] have shown that the problem actually arises from the incorrect behavior of the exchange-correlation potential, leading to an ionization continuum lying at too low energy. Large molecules have been treated in time–dependent DFT. Yabana and Bertsch [36] have studied excitation energies of C_{60} using a basis–set–free grid method. Stratmann, Scuseria, and Frisch [37] have treated excitation energies of the large closed-shell molecule C_{70} using a minimum basis set. Auxiliary functions offer the possibility of treating larger systems with much more reasonable basis sets than minimum basis

set. This auxiliary basis set expansion technique [206] has been used with time-dependent DFT to calculate the excitation energies of some small closed-shell molecules by Casida *et al.* [29, 207] and by Bauernschmitt, Häser, Treutler, and Ahlrichs [22]. The use of auxiliary basis set expansions reduces the computational costs considerably and makes it possible to calculate relatively large molecules. Bauernschmitt, Häser, Treutler, and Ahlrichs [22] have calculated excitation energies for large molecules such as C_{78} and $Cd_{10}Se_4(SeH)_{12}(PH_3)_4$. Nevertheless, all of the above molecular calculations are limited to closed-shell molecules. The time-dependent DFT study of excitation energies of open-shell molecules has only recently been reported in the literature [1], but only for the lowest two excitation energies and without oscillator strengths. The time-dependent DFT calculations of excitation spectra (please note that not only excitation energies are considered here, but intensities are also considered here) of open–shell molecules have not been found in the literature. Since open-shell molecules are very important in chemistry and astrophysics, it is the time for time–dependent DFT to be further developed for open-shell molecules.

This project extends time-dependent DFT to treat open–shell systems for excited state properties. The time-dependent DFT for open–shell systems is coded in the version 2pX of the program *deMon-DynaRho* [208]. The present modification and implementation of the time-dependent DFT provides a unique practical molecular time-dependent DFT code capable of treating excited state properties for open–shell molecules or clusters. As applications, this new code, version 2pX of the *deMon-DynaRho*, is employed to calculate excitation energies and oscillator strengths of open-shell molecules and alkali metal clusters (lithium and sodium clusters) from the dimer up through the hexamer. With the exception of the lowest two excitation energies (without oscillator strengths) of a few open–shell small molecules which recently appeared in the literature [1], the present all-electron calculations of excitation spectra (excitation energies and oscillator strengths) of open–shell small molecules and alkali metal clusters (the lithium

and the sodium clusters) are the first time-dependent DFT studies reported in the literature. The present work also uses the model core potential (MCP) to perform the time-dependent DFT calculations of electronic excitation spectra for the sodium clusters from the dimer up to the hexamer. The quality of the MCP used in the present study is first assessed for ground state properties against the all-electron calculations of sodium cluster geometric structures, vibrational frequencies, binding energies, and ionization potentials with the LSDxc approximation and gradient-corrected functionals, namely, the 1988 gradient-corrected exchange functional of Becke [209] plus the 1986 gradient-corrected correlation functional of Perdew [210] (B88x+P86c), and the 1986 gradient-corrected exchange functional of Perdew and Wang [211] plus the 1986 gradient-corrected correlation functional of Perdew [210] (PW86x+P86c); and second assessed for excited state properties against the all-electron calculations of excitation spectra of sodium clusters with the local spin density approximation (LSDxc) and the van Leeuwen and Baerends [212] exchange-correlation functional (LB94xc). The accuracy of the calculations of time-dependent DFT is determined by four factors, namely it depends on the choice of the orbital basis sets, auxiliary basis sets, grids, and exchange-correlation functionals. To ensure the accuracy of the present studies, several orbital and auxiliary basis sets have been examined. It is found by the present work that excitation energy calculations require a certain number of diffuse and polarization basis functions in order to be flexible enough to describe excited state properties; in contrast, excitation energies are less demanding on the auxiliary basis set. The normal auxiliary bases employed in ground state property calculations are good enough for the excitation energy calculations. The choice of the grids for the excitation energy calculations is also tested. It seems that carefully choosing a grid can avoid symmetry breaking in the assignments. The exchange-correlation functional plays a significant role in the excitation energy calculations. The present calculations employ the LSDxc functional and the LB94xc functional, respectively, at the SCF-step, combined with

the time-dependent local spin density approximation (TDLSDxc) at the post-SCF step (these functionals used at the SCF step and at the post-SCF step are referred to as LSDxc/TDLSDxc and LB94xc/TDLSDxc functionals). It can be seen from this work that low excitation calculations with the LSDxc/TDLSDxc functional give better results than the LB94xc/TDLSDxc functional does due to the deficiency in the short range behavior of the LB94xc functional. But for the high excitation energy calculations the LB94xc/TDLSDxc functional gives better results, since the LB94xc functional possesses the corrected long range behavior. The present work shows that electron exchange and correlation are important considerations for accurate calculations of excitation spectra. The exchange effects on the excitation energies of sodium trimer can be as large as 1.0 eV, while the correlation effects on the excitation energies can be as much as 0.5 eV in the sodium trimer calculations. This indicates that an appropriate treatment of the exchange and correlation effects plays an essential role for calculations of electronic spectra. This study also shows that the time-dependent DFT calculations of excitation spectra are much closer to the experiments than those of RCIS and UCIS. The accuracy of time-dependent DFT results are very competitive to the CI results.

CHAPTER 2

THEORETICAL BACKGROUND AND METHODOLOGY

2.1 TIME–DEPENDENT PERTURBATION THEORY

In electronic optical spectroscopy, a time-dependent electromagnetic field is applied to a molecule which is initially in its ground stationary state. This perturbation leads to a dynamic response of the charge density in the molecule which is typically described by response properties, such as the dynamic polarizability. Higher frequency perturbations can also lead to electronic excitations which involve electronic transitions to different excited electronic energy states. In order to understand these transitions, the different electronic energy states and their changes with time have to be studied by solving the time-dependent Schrödinger equation. This is harder to solve than the time-independent equation. One commonly used approach to solve the time-dependent Schrödinger equation is time-dependent perturbation theory which is also the basis for time-dependent response theory. The objective of this section is to review this basis in the form used in this thesis. Of course, a more detailed description would include nuclear motion, such as vibrations and rotations, but this is beyond the scope of the present work.

2.1.1 TIME–DEPENDENT PERTURBATION THEORY

A molecule in its ground stationary state satisfies the time-independent Schrödinger equation,

$$\hat{H}^{(0)}\Psi_n^{(0)} = E_n\Psi_n^{(0)}\,. \tag{2.1}$$

Introducing a time-dependent applied electromagnetic field, $\lambda\hat{H}'(t)$, leads to a time-dependent Schrödinger equation (atomic units are used throughout this thesis, unless otherwise mentioned),

$$i\frac{\partial\Psi(t)}{\partial t} = \hat{H}\Psi(t)\,. \tag{2.2}$$

where $\hat{H} = \hat{H}^{(0)} + \lambda\hat{H}'(t)$, and λ is an order parameter used as a measure of the strength of the perturbation. If the molecule is in a stationary state, then

$$\Psi_n(t) = \Psi_n^{(0)}exp(-iE_nt). \tag{2.3}$$

where $\Psi_n^{(0)}$ is a time-independent unperturbed wave function and $exp(-iE_nt)$ is an oscillatory phase factor. If $\lambda = 1$, the time-dependent perturbation is completely turned on.

The time-dependent perturbed function $\Psi(t)$ may be found by expanding it in time-dependent unperturbed wave functions (time-independent unperturbed wave functions times their corresponding oscillatory phase factors) which form a complete set,

$$\begin{aligned}\Psi(t) &= \sum_k c_k(t)\Psi_k(t) \\ &= \sum_k c_k(t)exp(-iE_kt)\Psi_k^{(0)}\,.\end{aligned} \tag{2.4}$$

The expansion coefficients $c_k(t)$ depend upon the form of the perturbation $\hat{H}'(t)$ (note that they depend on time) and upon the initial state $\Psi_n^{(0)}$. These expansion coefficients can be obtained by substituting the above equation (Eq. (2.4)) into the time-dependent Schrödinger equation (Eq. (2.2)). It is straightforward to

obtain

$$i\sum_k \frac{\partial c_k(t)}{\partial t} exp(-iE_k t)\Psi_k^{(0)} = \sum_k c_k(t) exp(-iE_k t)\hat{H}'(t)\Psi_k^{(0)} \tag{2.5}$$

By using the orthonormality relation $\langle \Psi_m^{(0)} | \Psi_k^{(0)} \rangle = \delta_{mk}$ and following some mathematics, the above equation becomes

$$\frac{\partial c_m(t)}{\partial t} = (i)^{-1} \sum_k c_k(t) exp(i\omega_{mk} t) \langle \Psi_m^{(0)} | \hat{H}' | \Psi_k^{(0)} \rangle \,, \tag{2.6}$$

where

$$\omega_{mk} = (E_m - E_k) \,, \tag{2.7}$$

are the excitation frequencies of the system. They are real and positive for excitations to bound states.

It is Eq. (2.6) which will be solved perturbatively. Expanding the $c_m(t)$ as a power series in λ,

$$c_m(t) = c_m^{(0)}(t) + c_m^{(1)}(t)\lambda + c_m^{(2)}(t)\lambda^2 + \cdots \,. \tag{2.8}$$

Substituting this power series into Eq. (2.6), and separating the different orders of λ, leads to the following relations:
to zeroth order (λ^0),

$$\frac{\partial c_m^{(0)}(t)}{\partial t} = 0 \,, \tag{2.9}$$

to first order (λ^1),

$$\frac{\partial c_m^{(1)}(t)}{\partial t} = (i)^{-1} \sum_k c_k^{(0)}(t) \langle \Psi_m^{(0)} | \hat{H}' | \Psi_k^{(0)} \rangle exp(i\omega_{mk} t) \,. \tag{2.10}$$

The zero-order equation [Eq. (2.9)] implies that the zero-order coefficients $c_m^{(0)}(t)$ are independent of time. Physically the system remains in its initial stationary state (n) in the absence of a perturbation. Hence,

$$c_m^{(0)}(t) = \delta_{nm} \,. \tag{2.11}$$

This can be used in the first-order equation [Eq. (2.10)] with the understanding that the perturbation is only turned on at time $t = 0$, to obtain the first-order

coefficients,

$$c_m^{(1)}(t) = (i)^{-1} \int_0^t \langle \Psi_m^{(0)} | \hat{H}'(t') | \Psi_n^{(0)} \rangle exp(i\omega_{mn} t') dt'. \tag{2.12}$$

Hence through first-order,

$$\begin{aligned} \Psi(t) &= \Psi^{(0)}(t) + \Psi^{(1)}(t) \\ &= \Psi_n^{(0)} exp(-iE_n t) \\ &\quad + \sum_k (i)^{-1} \int_0^t [\langle \Psi_k^{(0)} | \hat{H}' | \Psi_n^{(0)} \rangle exp(i\omega_{kn} t)] dt' \exp(-iE_k t) \Psi_k^{(0)} . \end{aligned} \tag{2.13}$$

where the zero-order wave function is

$$\begin{aligned} \Psi^{(0)}(t) &= \sum_k c_k^{(0)}(t) \Psi_k^{(0)} exp(-iE_k t) \\ &= \Psi_n^{(0)} exp(-iE_n t) \end{aligned} \tag{2.14}$$

and the first-order wave function is

$$\begin{aligned} \Psi^{(1)}(t) &= \sum_k c_k^{(1)}(t) \Psi_k^{(0)} exp(-iE_k t) \\ &= \sum_k (i)^{-1} \int_{t=0}^{t=t_1} [\langle \Psi_k^{(0)} | \hat{H}' | \Psi_n^{(0)} \rangle exp(i\omega_{kn} t)] dt \exp(-iE_k t) \Psi_k^{(0)} . \end{aligned} \tag{2.15}$$

The probability of finding the system at time t in the m^{th} stationary state of the initially unperturbed system is, through first order,

$$|\langle \Psi_m^{(0)} | \Psi(t) \rangle|^2 = | \int_0^t dt' \langle \Psi_m^{(0)} | \hat{H}'(t') | \Psi_n^{(0)} \rangle exp(i\omega_{mn} t') |^2 , \tag{2.16}$$

for $m \neq n$. This, of course, is just the probability of observing the excitation $n \rightarrow m$.

2.1.2 APPLICATION TO PHOTOABSORPTION

When a molecule is exposed to electromagnetic radiation, the perturbation is the interaction of electrons of the system with an electric field $\mathcal{E}(t)$ and magnetic

field $\mathbf{B}(t)$. In particular, light is a transverse electromagnetic wave. For light traveling in the z direction and polarized in the (x,y)–plane, the electric field $\mathcal{E}(t)$ and the magnetic field $\mathbf{B}(t)$ are given by

$$\begin{aligned} \mathcal{E}(t) &= \vec{\mathbf{i}}\mathcal{E}_x(t) \\ &= \vec{\mathbf{i}}\mathcal{E}_x^0 \cos(2\pi\nu t - 2\pi\frac{z}{\lambda}) \end{aligned} \tag{2.17}$$

$$\begin{aligned} \mathbf{B}(t) &= \vec{\mathbf{j}}B_y(t) \\ &= \vec{\mathbf{j}}B_y^0 \cos(2\pi\nu t - 2\pi\frac{z}{\lambda}) \end{aligned} \tag{2.18}$$

where $\mathcal{E}_x^0$ and B_y^0 are the amplitude of the electric field $\mathcal{E}$ and the magnetic field $\mathbf{B}$, respectively. $\vec{\mathbf{i}}$ and $\vec{\mathbf{j}}$ are unit vectors. λ is the wavelength which is the distance between two successive crests of $\mathcal{E}$. ν is the frequency which is the number of crests of $\mathcal{E}$ that pass a fixed point in space each second. The relation of the frequency ν and the wavelength λ is

$$\lambda = \frac{c}{\nu} \tag{2.19}$$

where c is the speed of light ($c = 2.9979 \times 10^{10} cm/sec$).

The contribution of the electric field $\mathcal{E}$ and the magnetic field $\mathbf{B}$ to the interaction (time-dependent perturbation) can be estimated from the force $\mathbf{F}$ acting on a particle with charge q and velocity $\mathbf{v}$,

$$\mathbf{F} = q(\mathcal{E} + \mathbf{v} \times \mathbf{B})\,. \tag{2.20}$$

Since the magnitudes of the electric field and the magnetic field of the electromagnetic radiation are related by the speed of light [213],

$$\mathcal{E}_x^{(0)} = cB_y^{(0)}\,, \tag{2.21}$$

the ratio of the magnetic force to the electric force is v/c. For the system of concern (electrons in atoms or molecules), the ratio v/c is a small number, (e.g. for the electron in the ground state of the hydrogen atom, $< v^2 >^{\frac{1}{2}} /c = 1/137$).

This is also the order of magnitude for valence electrons of other atoms. Therefore the magnetic field contributions to the perturbation can be ignored, and one can focus on the electric field contributions. i.e.,

$$\mathbf{F} = q\mathcal{E}\,. \tag{2.22}$$

When the electric field points in the x direction, the force is

$$F_x = q\mathcal{E}_x\,. \tag{2.23}$$

The interaction potential which corresponds to this force can be derived from the following relation,

$$\begin{aligned} \frac{\partial V}{\partial x} &= -F_x \\ &= -q\mathcal{E}_x\,. \end{aligned} \tag{2.24}$$

By integration of the above equation, the interaction potential V is obtained as

$$\begin{aligned} V &= -q\mathcal{E}_x x \\ &= \hat{H}'\,. \end{aligned} \tag{2.25}$$

Extension to a system with several particles (each particle with the charge q) in an electric field pointing in the x direction gives the perturbation term (interaction potential)

$$\begin{aligned} \hat{H}' &= \sum_i q_i x_i \mathcal{E}_x \\ &= -\mathcal{E}_x^0 \sum_i q_i x_i \cos(2\pi\nu t - \frac{2\pi z_i}{\lambda})\,. \end{aligned} \tag{2.26}$$

For a transition between electronic states in an atom and a molecule, the wavelengths λ lie in the ultraviolet region ($\lambda \approx 10^3 \mathring{A}$) which is usually much larger than the size of the system (about $1\mathring{A}$). As far as the electrons confined to move within the molecule are concerned, the spatial variation of the radiation's electric field is negligible,

$$\frac{z_i}{\lambda} \approx 0\,, \tag{2.27}$$

and the perturbation becomes

$$\begin{aligned} \hat{H}' &= -\mathcal{E}_x^0 \cos\omega t \sum_i q_i x_i \\ &= -\mathcal{E}_x^0 \hat{d}_x \cos\omega t \,, \end{aligned} \tag{2.28}$$

where $\omega = 2\pi\nu$ is used, and $\hat{d}_x = \sum_i q_i x_i$ is the x component of the system dipole moment. Substituting the identity

$$\cos\omega t = \frac{1}{2}[exp(i\omega t) + exp(-i\omega t)] \tag{2.29}$$

into Eq. (2.28), the perturbation becomes

$$\hat{H}' = -\mathcal{E}_x^0 \hat{d}_x \frac{1}{2}[exp(i\omega t) + exp(-i\omega t)] \,, \tag{2.30}$$

Substituting this expression for the perturbation into Eq. (2.12), the coefficients $c_m^{(1)}(t)$ become

$$c_m^{(1)}(t) = -\frac{\mathcal{E}_x^0}{2i}\langle\Psi_m^{(0)}|\hat{d}_x|\Psi_n^{(0)}\rangle \int_0^t exp[i(\omega_{mn}+\omega)t'] + exp[i(\omega_{mn}-\omega)t']dt' \,. \tag{2.31}$$

Integration gives

$$\begin{aligned} c_m^{(1)}(t) = -\frac{\mathcal{E}_x^0}{2i}\langle\Psi_m^{(0)}|\hat{d}_x|\Psi_n^{(0)}\rangle \quad \{ & \quad \frac{exp[i(\omega_{mn}+\omega)t]-1}{i(\omega_{mn}+\omega)} \\ & + \quad \frac{exp[i(\omega_{mn}-\omega)t]-1}{i(\omega_{mn}-\omega)}\} \,. \end{aligned} \tag{2.32}$$

From Eq. (2.32), the probability of a transition from state n to state m is maximized when

$$\omega_{mn} = \omega \,. \tag{2.33}$$

The transition probability is not infinite here because the second fraction in Eq. (2.32) is finite in the limit $(\omega_{mn} - \omega \approx 0)$

$$\begin{aligned} \lim_{\omega\to\omega_{mn}} \frac{exp[i(\omega_{mn}-\omega)t]-1}{i(\omega_{mn}-\omega)} &= \lim_{\omega\to\omega_{mn}} \frac{1+i(\omega_{mn}-\omega)t-1}{i(\omega_{mn}-\omega)} \\ &= t \,. \end{aligned} \tag{2.34}$$

This indicates that the probability of a transition from state n to state m is directly proportional to the exposure time t. Since the second term in Eq. (2.32)

dominates at $\omega_{mn} - \omega \approx 0$, the first fraction can be neglected in absorption spectra. Moreover, the first term is rapidly oscillating and so it will average to zero over any significant time interval. The probability of the transition from state n to state m depends also on the dipole moment integrals in electric-dipole transitions,

$$d_{mn} = \langle \Psi_m^{(0)} | \hat{d}_x | \Psi_n^{(0)} \rangle \,. \tag{2.35}$$

If the dipole moment integrals d_{mn} vanish, the transition between state n and state m is forbidden. The conditions which lead to nonzero dipole moment integrals are called selection rules, these rules specify the allowed transitions. More details are given in Ref. 214, 215.

2.2 DENSITY-FUNCTIONAL THEORY

Density-functional theory (in its original time-independent form) has become an accepted computational tool for the description of the ground state properties of atoms, molecules, and solids [26, 27, 28]. The computational simplicity of the Kohn-Sham formalism and the availability of reliable exchange-correlation functionals allow accurate calculations even for large systems [123, 124]. A brief review of the density-functional theory is given here, detailed reviews can be found in the literature[26, 27, 216, 118, 120, 217, 218, 28].

2.2.1 HOHENBERG–KOHN THEOREMS

Traditional density-functional theory (DFT) is based on two theorems of Hohenberg and Kohn [113] which indicate that the N–electron wave function, Ψ, may be replaced by the charge density, n, as the foundamental quantity of an electronic structure theory. These theorems and their proofs are reviewed in this section.

The key to the Hohenberg–Kohn theorems is the recognition that the total energy can be divided into two parts, one containing the external potential and the charge density and another independent of the external potential. In particular, Hohenberg and Kohn considered a non-relativistic N-electron system where the electrons are moving under the influence of a local external potential, V_{ext}. The Hamiltonian of this system can be written as,

$$\hat{H} = \hat{T} + \hat{V}_{ext} + \hat{U}\,, \tag{2.36}$$

where $\hat{T}$ is the kinetic energy operator,

$$\hat{T} = -\frac{1}{2}\sum_j \nabla_j^2 \tag{2.37}$$

$\hat{V}_{ext}$ is an external potential operator, normally just the interaction between the nuclei with charges Z_a and the electrons,

$$\begin{aligned} \hat{V}_{ext} &= \sum_j v(\mathbf{r_j}) \\ &= -\sum_j \sum_a \frac{Z_a}{\mathbf{R}_a - \mathbf{r}_j} \end{aligned} \tag{2.38}$$

this external potential may also include an additional applied electric field. $\hat{U}$ is the electron-electron repulsion operator,

$$\hat{U} = \frac{1}{2}\sum_{i,j}^{i\neq j} \frac{1}{r_{ij}}\,. \tag{2.39}$$

The total energy of the system is the expectation value of the system Hamiltonian,

$$\begin{aligned} E[n] &= \langle \Psi | \hat{H} | \Psi \rangle \\ &= \int d\mathbf{r}_1 d\sigma_1 d\mathbf{r}_2 d\sigma_2 \cdots d\mathbf{r}_n d\sigma_n \Psi(\mathbf{r}_1, \sigma_1, \mathbf{r}_2, \sigma_2, \cdots, \mathbf{r}_n, \sigma_n) \\ &\quad \times \hat{H}(\mathbf{r}_1, \sigma_1, \mathbf{r}_2, \sigma_2, \cdots, \mathbf{r}_n, \sigma_n) \Psi(\mathbf{r}_1, \sigma_1, \mathbf{r}_2, \sigma_2, \cdots, \mathbf{r}_n, \sigma_n)\,. \end{aligned} \tag{2.40}$$

Since the expression for the electronic kinetic energy and electron-electron repulsion energy are identical for any N-electron system, these two energies may be combined as a new functional, the so–called "universal functional", F[n], of

Hohenberg and Kohn. The remaining electron external potential energy can also be written as a functional of the electron density. Thus the total energy can be rewritten as

$$\begin{aligned} E[n] &= \langle\Psi|\hat{T}+\hat{U}|\Psi\rangle + \langle\Psi|\hat{V}_{ext}|\Psi\rangle \\ &= F[n] + \int d\mathbf{r} n(\mathbf{r}) v(\mathbf{r}), \end{aligned} \tag{2.41}$$

where $n(\mathbf{r})$ is charge density which is defined by the following equation

$$n(\mathbf{r_1}) = \int \cdots \int d\mathbf{r_2} d\mathbf{r_3} \cdots d\mathbf{r_n} \Psi^*(\mathbf{r_1}, \mathbf{r_2}, \cdots, \mathbf{r_n}) \Psi(\mathbf{r_1}, \mathbf{r_2}, \cdots, \mathbf{r_n}). \tag{2.42}$$

Hohenberg and Kohn [113] pointed out in their theorem (the first Hohenberg–Kohn theorem) that the external potential, V_{ext}, is determined by the knowledge of the electron density, $\mathbf{n(r)}$, up to a trivial additive constant. This first Hohenberg–Kohn theorem can be proven by a *reductio ad absurdum* procedure (seeking a contradiction). Suppose that there exists another external potential, $v'(\mathbf{r})$, which is different from the original external potential, $v(\mathbf{r})$,

$$v(\mathbf{r}) \neq v'(\mathbf{r}) + const. \tag{2.43}$$

and it gives the same charge density, $n(\mathbf{r})$, as the original external potential. In other words, there are two different external potentials, $v(\mathbf{r})$ and $v'(\mathbf{r})$, leading to two different Hamiltonians, $\hat{H}$ and $\hat{H}'$ and consequently to two different ground state wave functions, Ψ and Ψ', corresponding to the two different ground state energies, $E[n]$ and $E'[n]$. According to the Rayleigh–Ritz variational principle [219], the total energy of the system,$E[n]$, obeys the equation,

$$\begin{aligned} E[n] &= \langle\Psi|\hat{H}|\Psi\rangle \\ &< \langle\Psi'|\hat{H}|\Psi'\rangle \\ &= \langle\Psi'|\hat{H}'|\Psi'\rangle + \langle\Psi'|\hat{H}-\hat{H}'|\Psi'\rangle \\ &= E'[n] + \int d\mathbf{r} n(\mathbf{r})[v(\mathbf{r}) - v'(\mathbf{r})]. \end{aligned} \tag{2.44}$$

Similarly, the total energy, $E'[n]$, can be written as,

$$E'[n] = \langle\Psi'|\hat{H}'|\Psi'\rangle$$

$$
\begin{aligned}
&< \langle \Psi | \hat{H}' | \Psi \rangle \\
&= \langle \Psi | \hat{H} | \Psi \rangle + \langle \Psi | \hat{H}' - \hat{H} | \Psi \rangle \\
&= E[n] + \int d\mathbf{r} n(\mathbf{r}) [v'(\mathbf{r}) - v(\mathbf{r})] \,. \qquad (2.45)
\end{aligned}
$$

Summing over Eq.(2.44) and Eq.(2.45), the result is an obvious contradiction,

$$E[n] + E'[n] < E[n] + E'[n] \,, \qquad (2.46)$$

therefore, the conclusion can be drawn that the charge density of the system determines the external potential up to an additive constant. This means that if the electron density is fixed, then the external potential and, consequently, the system Hamiltonian, are uniquely determined. Therefore, all the observable quantities are also determined. Wilson [220] also pointed out that in a system without external perturbations, the cusps of the charge density give the positions of the nuclei, the nuclear charges can be gotten from the gradient of the charge density at the cusps, and the integration of the charge density determines the total number of electrons in the system. Hence, the density does determine the external potential in this instance. However, Wilson's argument is not obvious for a system with a general external potential.

Hohenberg and Kohn pointed out that the exact charge density of the system minimizes the total energy of the system which is a functional of the charge density. This is the second Hohenberg–Kohn theorem. It is also proven based on the variational principle. Suppose there is any trial charge density, $\tilde{n}$, which determines the trial external potential, $\tilde{v}$, and consequently the trial system Hamiltonian, $\hat{\tilde{H}}$, and the trial wave function, $\tilde{\Psi}$. According to the variational principle,

$$
\begin{aligned}
E[n] &= \langle \Psi | \hat{H} | \Psi \rangle \leq \langle \tilde{\Psi} | \hat{H} | \tilde{\Psi} \rangle \\
&= F[n] + \int d\mathbf{r} v(\mathbf{r}) n(\mathbf{r}) \leq F[\tilde{n}] + \int d\mathbf{r} v(\mathbf{r}) \tilde{n}(\mathbf{r}) \,. \qquad (2.47)
\end{aligned}
$$

This is true only for the ground state. In practice, the charge density, $n(\mathbf{r})$, at a known external potential, $v(\mathbf{r})$, is obtained by minimizing the total energy of the system, but using approximate exchange–correlation functionals.

2.2.2 KOHN-SHAM THEORY

The Kohn-Sham equation is the corner stone of practical density-functional theory. Kohn and Sham map the real system of interacting electrons to a fictitious system of noninteracting particles, with an effective potential. This fictitious system of noninteracting particles has the same charge density as that of the real system.

Kohn and Sham rewrote the total energy of the real interacting particle system as

$$\begin{aligned} E[n] &= T_s[n] + U[n] + V_{ext}[n] + T_c[n] \\ &= T_s[n] + U[n] + T_c[n] + \int d\mathbf{r} n(\mathbf{r}) v(\mathbf{r}) \end{aligned} \tag{2.48}$$

where $T_s[n]$ is the kinetic energy for the fictitious system of noninteracting particles,

$$T_s[n] = \sum_j \langle \psi_{sj} | -\frac{1}{2}\nabla^2 | \psi_{sj} \rangle \,, \tag{2.49}$$

$T_c[n]$ is the kinetic energy difference between the exact kinetic energy of the real interacting system, $T[n]$, and the kinetic energy of the noninteracting system, $T_s[n]$,

$$T_c[n] = T[n] - T_s[n] \,. \tag{2.50}$$

The electron-electron repulsion energy, $U[n]$, and the difference of the kinetic energy, $T_c[n]$, are rewritten as

$$\begin{aligned} U[n] + T_c[n] &= \frac{1}{2}\int\int d\mathbf{r} d\mathbf{r}' \frac{n(\mathbf{r})n(\mathbf{r}')}{|\mathbf{r} - \mathbf{r}'|} + E_{xc}[n] \\ &= J[n] + E_{xc}[n] \end{aligned} \tag{2.51}$$

which defines the electron exchange-correlation energy $E_{xc}[n]$. Note that this exchange-correlation energy includes the residual of the electron-electron repulsion energy minus the electron-electron Coulomb interaction energy and the difference of the true kinetic energy of the real system and the kinetic energy of the

noninteracting particle system. The total energy can then be rewritten as

$$E[n] = T_s[n] + J[n] + E_{xc}[n] + \int d\mathbf{r} n(\mathbf{r}) v(\mathbf{r}) \,. \tag{2.52}$$

According to the variational principle, the variation of the above total energy with respect to the charge density gives the Euler equation,

$$\begin{aligned} \mu &= \frac{\delta E[n]}{\delta n(\mathbf{r})} \\ &= \frac{\delta T_s[n]}{\delta n(\mathbf{r})} + \frac{\delta J[n]}{\delta n(\mathbf{r})} + \frac{\delta E_{xc}[n]}{\delta n(\mathbf{r})} + v(\mathbf{r}) \\ &= \frac{\delta T_s[n]}{\delta n(\mathbf{r})} + v_J(\mathbf{r}) + v_{xc}(\mathbf{r}) + v(\mathbf{r}) \\ &= \frac{\delta T_s[n]}{\delta n(\mathbf{r})} + v_{eff}(\mathbf{r}) \,, \end{aligned} \tag{2.53}$$

where the μ is the electron chemical potential, $v_{eff}(\mathbf{r})$ is the Kohn-Sham effective potential (also called Kohn-Sham potential),

$$v_{eff}(\mathbf{r}) = v_J(\mathbf{r}) + v_{xc}(\mathbf{r}) + v(\mathbf{r}) \,, \tag{2.54}$$

in which the $v_J(\mathbf{r})$ is the electron Coulomb potential,

$$\begin{aligned} v_J(\mathbf{r}) &= \frac{\delta J[n]}{\delta n(\mathbf{r})} \\ &= \int d\mathbf{r}' \frac{n(\mathbf{r}')}{|\mathbf{r} - \mathbf{r}'|} \,, \end{aligned} \tag{2.55}$$

and $v_{xc}(\mathbf{r})$ is the electron exchange-correlation potential,

$$v_{xc}(\mathbf{r}) = \frac{\delta E_{xc}[n]}{\delta n(\mathbf{r})} \,, \tag{2.56}$$

and $v(\mathbf{r})$ is the external potential.

The total energy of the system can also be written as a function of one electron orbitals, ψ_i,

$$\begin{aligned} E[n] = &- \frac{1}{2} \sum_{i=1}^{N^\sigma} \langle \psi_i(\mathbf{r}) | \nabla^2 | \psi_i(\mathbf{r}) \rangle + \int d\mathbf{r} [v_{ext}(\mathbf{r}) n(\mathbf{r})] \\ &+ \frac{1}{2} \int \int d\mathbf{r} d\mathbf{r}' \frac{n(\mathbf{r}) n(\mathbf{r}')}{|\mathbf{r} - \mathbf{r}'|} + E_{xc}[n] \,. \end{aligned} \tag{2.57}$$

Minimization of the total energy subject to the constraint of orbital orthonormality leads to the famous Kohn-Sham equation,

$$(-\frac{1}{2}\nabla^2 + v_{eff})\psi_i = \epsilon_i \psi_i \,, \tag{2.58}$$

where the kinetic energy operator and the effective potential make up the Kohn-Sham operator,

$$\hat{F}^{KS} = -\frac{1}{2}\nabla^2 + v_{eff} \,. \tag{2.59}$$

The Kohn-Sham equation indicates that the motion of the interacting electrons can be treated exactly the same way as for the noninteracting particle system. The electrons can be considered as if they move in the effective local potential, and the Kohn-Sham equation is exact if the effective potential is known exactly. The Kohn-Sham equation also includes all the effects of the correlations among the electrons of the system. These are some of the advantages of the density-functional theory. Since the effective potential also depends on the charge density, the Kohn-Sham equation must be solved self-consistently.

If the electron spin is considered, the spin-dependent total energy is

$$\begin{aligned} E[n^{\uparrow}, n^{\downarrow}] = & - \frac{1}{2}\sum_{\sigma}^{spin}\sum_{i=1}^{N^{\sigma}} \langle \psi_i^{\sigma} | \nabla^2 | \psi_i^{\sigma} \rangle + \int v_{ext}(\vec{r}) n(\vec{r})\, d\vec{r} \\ & + \frac{1}{2}\int\int \frac{n(\vec{r}_1) n(\vec{r}_2)}{r_{12}}\, d\vec{r}_1 d\vec{r}_2 + E_{xc}[n^{\uparrow}, n^{\downarrow}] \,. \end{aligned} \tag{2.60}$$

and the spin-polarized Kohn-Sham equation can be written as [221, 28]

$$\left[-\frac{1}{2}\nabla^2 + v_{eff}^{\sigma}(\mathbf{r})\right] \psi_i^{\sigma}(\mathbf{r}) = \epsilon_i^{\sigma} \psi_i^{\sigma}(\mathbf{r}) \,, \tag{2.61}$$

where the spin-polarized Kohn-Sham operator is

$$\hat{F}_{\sigma}^{KS} = -\frac{1}{2}\nabla^2 + v_{eff}^{\sigma}(\mathbf{r}) \,, \tag{2.62}$$

and here σ stands for spin up (α spin) and spin down (β spin). The total charge density becomes the sum of the spin-up and spin-down electron densities,

$$n(\mathbf{r}) = n^{\uparrow}(\mathbf{r}) + n^{\downarrow}(\mathbf{r}) \tag{2.63}$$

and the spin-polarized effective potential, $v^{\sigma}_{eff}(\mathbf{r})$, can be written as

$$v^{\sigma}_{eff}(\mathbf{r}) = v_{\sigma}(\mathbf{r}) + \int d\mathbf{r}' \frac{n(\mathbf{r}')}{|\mathbf{r} - \mathbf{r}'|} + v_{xc\sigma}(\mathbf{r}) \,, \tag{2.64}$$

in which the spin dependent exchange-correlation potential, $v_{xc\sigma}(\mathbf{r})$, is

$$v_{xc\sigma}(\mathbf{r}) = \frac{\delta E_{xc}[n^{\uparrow}, n^{\downarrow}]}{\delta n_{\sigma}(\mathbf{r})} \,, \tag{2.65}$$

and the spin-polarized external potential, $v_{\sigma}(\mathbf{r})$, may have two different parts of spin-up and spin-down external potentials dependent on the additional applied field (e.g. inclusion of certain types of magnetic field effects). Spin-polarized density-functional theory provides a better description of many systems, especially for open-shell systems, such as open-shell atoms, open-shell molecules, and open-shell clusters, etc. The spin-dependent density-functional theory is also capable of describing certain properties of a system in the presence of a magnetic field [221]. It also provides the possibility for electrons with different spin to have different spatial orbitals.

The effective potential includes the Coulomb electron-electron interaction potential (the Hartree potential), the external potential (nuclear-electron attraction potential and possibly an applied perturbation), and the exchange-correlation potential. The latter is a functional of the charge density, but the exact practical form is unknown. The accuracy of density-functional theory calculations mainly depends on the quality of the approximation made for the exchange-correlation functional.

2.2.3 EXCHANGE-CORRELATION FUNCTIONALS

Density-functional theory is in principle exact. Unfortunately the exact formulation of the electron exchange-correlation functional is so far unknown. In practice, density-functional theory calculations have to be done with approximate exchange-correlation functionals. Various approximations characterize different schemes of density-functional theory and are of different accuracy.

Numerous proposed exchange-correlation functionals have been reported in the literature [222, 223, 224, 225, 226, 227, 228, 229, 230, 231], such as the local density approximation [97, 223, 232, 233], gradient–corrected approximations (also called non-local approximations or generalized gradient approximations) [234, 235, 236, 210, 237, 211, 238, 239, 209, 240, 27] and weighted density approximations (WDA) [241, 242]. The simplest and the most commonly used exchange-correlation approximation [243] is the local spin density approximation (LSDxc).

2.2.3.1 LOCAL SPIN DENSITY APPROXIMATION

The LSDxc approximation was the first approximation used for the exchange-correlation functional in density-functional theory. This approximation is based on the theory of the homogeneous electron gas in that it is supposed that an inhomogeneous system can be described locally as a homogeneous electron gas with density equal to the local density at that point in the inhomogeneous system. The exchange-correlation effects in the homogeneous electron gas are well understood by now [243], and the exchange energy is known exactly. The specific forms of the exchange energy and correlation energy depend on the treatment of exchange and correlation used in the calculations of the homogeneous electron gas [115].

In the LSDxc approximation, the exchange-correlation energy may be written as

$$E_{xc}^{LSDxc}[n^{\uparrow}, n^{\downarrow}] = \int d\mathbf{r}[n(\mathbf{r})\epsilon_{xc}(n^{\uparrow}(\mathbf{r}), n^{\downarrow}(\mathbf{r}))] \tag{2.66}$$

where $\epsilon_{xc}(n^{\uparrow}(\mathbf{r}), n^{\downarrow}(\mathbf{r}))$ is the exchange-correlation energy density of a homogeneous electron gas with spin densities $n^{\uparrow}$ and $n^{\downarrow}$. The exchange-correlation energies of the homogeneous electron gas have been accurately determined by Monte Carlo simulations [244] and various convenient parametrizations have been reported in the literature [232, 226, 231]. The exchange-correlation energy can be

divided into the exchange (E_x) and the correlation energy (E_c),

$$E_{xc} = E_x + E_c \,. \tag{2.67}$$

Since the exchange energy is the dominant component of the exchange-correlation energy, it should be treated with more accuracy. For a homogeneous electron gas, the exchange energy can be written as

$$E_x[n^\uparrow, n^\downarrow] = \int d\mathbf{r}[n(\mathbf{r})\epsilon_x(n^\uparrow, n^\downarrow)] \,. \tag{2.68}$$

The exchange energy density, $\epsilon_x(n^\uparrow, n^\downarrow)$, was first obtained by Dirac [97],

$$\epsilon_x(n^\uparrow, n^\downarrow) = -\frac{3}{4}(\frac{3}{\pi})^{1/3} \sum_\sigma n^\sigma(\mathbf{r})^{1/3} \tag{2.69}$$

The exchange energy density was also derived by Slater [245, 135], Gáspár [246], and Kohn and Sham [114]. Since they obtained the exchange energy density in different ways (e.g. Slater exchange was derived from the one-electron Hartree-Fock equations by averaging the Fermi hole and introducing the LSDxc approximation, Gáspár made these approximations in the Hartree-Fock total energy expression and then appied the variation principle, yielding the exchange potential), their expressions differ by a constant factor [115]. This constant factor is used as a semiempirical parameter in the X_α method [136].

The correlation energy functional

$$E_c[n^\uparrow, n^\downarrow] = E_{xc}[n^\uparrow, n^\downarrow] - E_x[n^\uparrow, n^\downarrow] \tag{2.70}$$

is more difficult to obtain. The exact analytical form is unknown even for the homogeneous electron gas. Approximations have to be used for the correlation energy (density). The most widely used correlation energy density is from the work of Vosko, Wilk, and Nusair (VWN) [232]. It is a Padé approximate parametrization of Ceperley and Alder's accurate Green's function Monte Carlo calculations for the homogeneous electron gas [244]. The VWN correlation energy density is given as the following formula,

$$\epsilon_c(r_s, \xi) = \epsilon_c^0(r_s) + \alpha(r_s)[\frac{f(\xi)}{f''(0)}][1 + \beta(r_s)\xi^4] \,, \tag{2.71}$$

where

$$r_s = (\frac{3}{4\pi n})^{1/3}\,, \tag{2.72}$$

$$\xi = \frac{n^{\uparrow} - n^{\downarrow}}{n^{\uparrow} + n^{\downarrow}} = \frac{n^{\uparrow} - n^{\downarrow}}{n}\,, \tag{2.73}$$

$$f(\xi) = \frac{1}{2(2^{1/3}-1)}[(1+\xi)^{4/3} + (1-\xi)^{4/3} - 2]\,, \tag{2.74}$$

$$\beta(r_s) = [\epsilon_c^1(r_s) - \epsilon_c^0(r_s)]\frac{f''(0)}{\alpha(r_s)} - 1\,, \tag{2.75}$$

and

$$\alpha(r_s) = A_\alpha \ln r_s + C_\alpha\,, \tag{2.76}$$

in which

$$A_\alpha = -\frac{1}{3\pi^2}\,, \tag{2.77}$$

and

$$C_\alpha = \frac{\ln(16\pi/\alpha) - 3 + \langle \ln R\rangle_{av}}{3\pi^2}\,, \tag{2.78}$$

where

$$\langle \ln R\rangle_{av} = 0.531504\,, \tag{2.79}$$

and

$$\alpha = (4/9\pi)^{1/3}\,. \tag{2.80}$$

The para- and ferro-magnetic state correlation energy densities, $\epsilon_c^0(x)$ and $\epsilon_c^1(x)$, are given by

$$\begin{aligned}\epsilon_c^{0,1}(x) = \quad & A \quad \{\ln\frac{x^2}{X(x)} + \frac{2b}{Q}\tan^{-1}\frac{Q}{2x+b} - \frac{bx_0}{X(x_0)}[\ln\frac{(x-x_0)^2}{X(x)} \\ & + \quad \frac{2(b+2x_0)}{Q}\tan^{-1}\frac{Q}{2x+b}]\}\,,\end{aligned} \tag{2.81}$$

where $x = r_s^{1/2}$, $X(x)$ is expressed as

$$X(x) = x^2 + bx + c\,, \tag{2.82}$$

and $Q = (4c - b^2)^{1/2}$, x_0 is the root of the expression, $(1 + b_1 x + b_2 x^2 + b_3 x^3)$, A, x_0, b, and c are parameters either equal to $A = 0.0621814, x_0 = -0.10498, b = 3.72744$, and $c = 12.9352$ in the case of spin unpolarized $[\epsilon_c^0(x)]$ or equal to

$A = 0.0310907, x_0 = -0.325000, b = 7.06042$, and $c = 18.0578$ in the case of spin polarized $[\epsilon_c^1(x)]$ by fitting to the results of Ceperley and Alder. This functional is believed to represent closely the limit of the LSDxc approximation.

It is well–known that the correlation energy in the LSDxc approximation is normally overestimated by a factor of 2 [210] and the sign of the error in exchange energy is opposite to that of the correlation energy, which is underestimated by about 10% [209]. Until now there is no rigorous way to correct these inherent errors. Nevertheless, these two errors are believed, in practice, to cancel each other in the applications of the LSDxc approximation. Reasonable accuracy should be obtained for systems with the density varying slowly (such as some metals), but not for the systems with the density varying rapidly (such as molecules) [26, 27]. However, although it underbinds the core electrons in an atom and overbinds the atoms in a molecule or solid, the satisfying results for many properties of different systems (even for molecules) have been obtained by the LSDxc approximation and some successful applications of the LSDxc approximation to electronic properties of the complex systems and solid state systems have been reported [115, 226], including geometric structures and vibrational frequencies, but the LSDxc approximation poorly describes binding energies, dissociation energies, hydrogen bonds, negative ions, and properties which are sensitively dependent on the behavior of the exchange-correlation potential [247, 248, 216, 249, 250, 212, 28]. The reasons behind these poor descriptions may come from the deficiencies of the LSDxc approximation, in particular, it may come from the imperfect cancellation of self-interaction effects, which leads to the incorrect asymptotic decay of the local density exchange–correlation potential [251, 212].

There are some other local approximations also, such as the Gombás–Lie–Clementi approximation [252, 253], and the local Wigner correlation functional parametrized by Wilson and Levy [254], that of Lee and Parr [255], and that of Süle and Nagy [256].

2.2.3.2 BEYOND THE LOCAL SPIN DENSITY APPROXIMATION

To improve the LSDxc approximation, the inherent errors of the LSDxc approximation have to be corrected. There are several alternative approaches already proposed to improve the LSDxc approximation in the literature [257, 235, 258, 236, 211, 210, 237, 259, 209]. The generalized gradient approximation (GGA) is the most commonly recognized approach to improve the LSDxc approximation. The GGA is based on the theory of the inhomogeneous electron gas and on the analysis of the exchange-correlation hole and takes into account the gradient of the density.

The exchange-correlation energy at the GGA can be written as

$$E_{xc}^{GGA}[n^{\uparrow}, n^{\downarrow}] = \int d\mathbf{r} f[n^{\uparrow}(\mathbf{r}), n^{\downarrow}(\mathbf{r}), \nabla n^{\uparrow}(\mathbf{r}), \nabla n^{\downarrow}(\mathbf{r})] \,. \tag{2.83}$$

The GGA was originally constructed by Langreth and coworkers [257, 235] using a cutoff of the spurious small wave vector contribution to the Fourier transform of the second-order density gradient expansion for the exchange-correlation hole around an electron [260]. The exchange energy construction is believed to be a major source of the errors in the LSDxc approximation. In the GGA it is constructed with the ansatz,

$$E_x^{GGA} = -\frac{3}{4}(\frac{3}{\pi})^{1/3} \int d\mathbf{r} n^{4/3}(\mathbf{r}) F^{GGA}[s(\mathbf{r})] \,, \tag{2.84}$$

where the scaled density gradient, s, is

$$s(\mathbf{r}) = \frac{|\nabla n(\mathbf{r})|}{2k_F(\mathbf{r})n(\mathbf{r})} \,. \tag{2.85}$$

The local Fermi wave vector, k_F, is

$$k_F(\mathbf{r}) = (3\pi^2 n(\mathbf{r}))^{1/3} \,. \tag{2.86}$$

Perdew and Wang [211] have based their exchange functional on the gradient expansion of the exchange hole with a real space cutoff of the spurious long-range contributions to guarantee that the exchange hole be negative everywhere

and represents a deficit of one electron. They proposed the explicit form for the function, $F^{GGA}(s)$,

$$F^{GGA}_{PW86x}(s) = (1 + 1.296s^2 + 14s^4 + 0.2s^6)^{1/15}\,. \tag{2.87}$$

Becke [209] emphasized reproducing the correct asymptotic behavior of the exchange energy density and proposed a one parameter exchange energy functional,

$$E^{GGA}_{B88x} = E^{LSDxc}_x - \beta \sum_\sigma \int d\mathbf{r} n^{4/3}_\sigma(\mathbf{r}) \frac{\chi^2_\sigma(\mathbf{r})}{1 + 6\beta\chi_\sigma(\mathbf{r}) sinh^{-1}\chi_\sigma(\mathbf{r})}\,, \tag{2.88}$$

where χ_σ is the dimensionless ratio,

$$\chi_\sigma(\mathbf{r}) = \frac{|\nabla n_\sigma(\mathbf{r})|}{n^{4/3}_\sigma(\mathbf{r})}\,, \tag{2.89}$$

and β is a constant parameter which is known from fitting the exact Hartree-Fock exchange energies of six noble gas atoms, helium through radon, with a value of $\beta = 0.0042 a.u.$

The correlation error of the LSDxc approximation in molecules is believed to come primarily from the part of the correlation between electrons of the same spin [261, 216], since the correlation between electrons of the same spin in finite systems is much smaller than that in the homogeneous electron gas. A few ways have been proposed [261, 262, 210, 237] to overcome the drawback of the LSDxc approximation. Stoll and coworkers [261] have proposed a correlation functional which has eliminated the correlation between electrons of the same spin. Perdew [210] also proposed a correlation energy functional based on the work of Langreth and coworkers [257, 235, 258, 263], which includes inhomogeneity effects beyond the random-phase approximation,

$$\begin{aligned} E_c[n^\uparrow, n^\downarrow] &= \int d\mathbf{r} n(\mathbf{r}) \epsilon^{LSDxc}(n^\uparrow(\mathbf{r}), n^\downarrow(\mathbf{r})) \\ &\quad + \int d\mathbf{r} d^{-1} e^{-\Phi}(\mathbf{r}) C[n(bfr)] |\nabla n(\mathbf{r})|^2 / n^{4/3}(\mathbf{r})\,, \end{aligned} \tag{2.90}$$

where

$$d = 2^{1/3} \{ [\frac{1+\xi}{2}]^{5/3} + [\frac{1-\xi}{2}]^{5/3} \}^{1/2}\,, \tag{2.91}$$

defines the spin polarization with $\xi = (n^{\uparrow} - n^{\downarrow})/n$, and $n = n^{\uparrow} + n^{\downarrow}$. Here Φ is given as

$$\Phi = 1.745\tilde{f}[C(\infty)/C(n)]\frac{|\nabla n|^2}{n^{7/6}}, \tag{2.92}$$

and the cutoff parameter,$\tilde{f} = 0.11$, is obtained by fitting the exact correlation energy of the neon atom. The correlation energy gradient coefficient, $C(n)$, is

$$C(n) = 0.001667 + \frac{0.002568 + \alpha r_s + \beta r_s^2}{1 + \gamma r_s + \delta r_s^2 + 10^4 \beta r_s^3} \tag{2.93}$$

in which $n = (4\pi r_s^3/3)^{-1}$ and $\alpha = 0.023266, \beta = 7.389 \times 10^{-6}, \gamma = 8.723$, and $\delta = 0.472$. When Perdew's correlation functional is combined with Becke's [209] exchange functional, it is normally called the Becke-Perdew exchange-correlation functional (B88x+P86c). When Perdew's correlation functional is combined with Perdew and Wang's [211] exchange functional, it is usually called the Perdew-Perdew exchange-correlation functional (PW86x+P86c).

The other commonly used correlation functional is from the work of Lee, Yang, and Parr [240]. Lee, Yang, and Parr based their work on that of Colle and Salvetti [264, 265, 266, 267, 268]. They converted the correlation energy formula of Colle and Salvetti (in which the correlation energy density is expressed in terms of the electron and a Laplacian of the second-order Hartree-Fock density matrix) into a density-functional formula for closed and open shells, respectively,

$$\begin{aligned} E_c = & - a\int d\mathbf{r}\frac{1}{1 + dn^{-1/3}(\mathbf{r})}\{n(\mathbf{r}) + bn^{-2/3}(\mathbf{r})[C_F n^{5/3}(\mathbf{r}) - 2t_W(\mathbf{r}) \\ & + (\frac{1}{9}t_W(\mathbf{r}) + \frac{1}{18}\nabla^2 n(\mathbf{r}))]e^{-cn^{-1/3}(\mathbf{r})}\}, \end{aligned} \tag{2.94}$$

and

$$\begin{aligned} E_c = & - a\int d\mathbf{r}\frac{\gamma(\mathbf{r})}{1 + dn^{-1/3}(\mathbf{r})}\{n(\mathbf{r}) + 2bn^{-5/3}(\mathbf{r})[2^{2/3}C_F n^{\uparrow 8/3}(\mathbf{r}) \\ & + 2^{2/3}C_F n^{\downarrow 8/3}(\mathbf{r}) - n(\mathbf{r})t_W(\mathbf{r}) + \frac{1}{9}(n^{\uparrow}(\mathbf{r})t_W^{\uparrow}(\mathbf{r}) + n^{\downarrow}(\mathbf{r})t_W^{\downarrow}(\mathbf{r})) \\ & + \frac{1}{18}(n^{\uparrow}(\mathbf{r})\nabla^2 n^{\uparrow}(\mathbf{r}) + n^{\downarrow}(\mathbf{r})\nabla^2 n^{\downarrow}(\mathbf{r}))]e^{-cn^{-1/3}(\mathbf{r})}\}, \end{aligned} \tag{2.95}$$

where $\gamma(\mathbf{r})$ is expressed as,

$$\gamma(\mathbf{r}) = 2[1 - \frac{n^{\uparrow 2}(\mathbf{r}) + n^{\downarrow 2}(\mathbf{r})}{n^2(\mathbf{r})}], \tag{2.96}$$

and the constant parameters, $a = 0.04918, b = 0.132, c = 0.2533$, and $d = 0.349$, are obtained by a fitting procedure using only the Hartree-Fock orbital for the helium atom. $C_F = \frac{3}{10}(3\pi^2)^{2/3}$, and the local "Weizsäcker" kinetic energy density is given as

$$t_W(\mathbf{r}) = \frac{1}{8}\frac{|\nabla n(\mathbf{r})|^2}{n(\mathbf{r})} - \frac{1}{8}\nabla^2 n(\mathbf{r}), \tag{2.97}$$

When Lee, Yang and Parr's correlation functional (LYP) is combined with Becke's exchange functional [209], the resultant functional is commonly called the Becke-Lee-Yang-Parr exchange-correlation functional (BLYP). The BLYP exchange-correlation functional has been widely used in the calculations of electronic properties of atoms and molecules [269, 270, 271, 35, 28].

There is another combination of the exchange and correlation functional (hybrid functional) which is also commonly used, namely the B3LYP exchange-correlation functional [272, 273]. The B3LYP exchange-correlation functional is based on Becke's half and half idea [274] and the original mixed exchange-correlation approximation proposed by Becke [205], it was first programmed in Gaussian92/DFT [272] and takes the form,

$$E_{xc} = (1 - a_0)E_x^{LSDxc} + a_0 E_x^{exact} + a_x \Delta E_x^{B88} + a_c E_c^{LYP} + (1 - a_c)E_c^{VWN}, \tag{2.98}$$

where the $a_0 = 0.20$, $a_x = 0.72$, and $a_c = 0.81$ are semiempirical coefficients obtained by a linear least-squares fit to the experimental data of some properties of a variety of atoms [275], E_x^{LSDxc} is the exchange energy of the LSDxc approximation, E_x^{exact} is the exact exchange energy, ΔE_x^{B88} is Becke's 1988 gradient correction to the exchange functional, E_c^{LYP} is Lee, Yang, and Parr's correlation functional which has replaced the original Perdew-Wang gradient correction to the correlation functional [276, 277] proposed by Becke [205], and E_c^{VWN} is the VWN correlation functional expression at the LSDxc approximation.

Recently van Leeuwen and Baerends [212] analyzed the asymptotic behavior of the exchange-correlation potential instead of exchange-correlation energy or exchange-correlation hole potential and by comparing to the exact Kohn-Sham

potential proposed an exchange-correlation potential (LB94xc) which corrects the LSDxc potential. The exchange-correlation potential of van Leeuwen and Baerends has the form,

$$v_{xc}^{\sigma}(\mathbf{r}) = -\beta n_{\sigma}^{1/3}(\mathbf{r}) \frac{\chi_{\sigma}^{2}}{1 + 3\beta\chi_{\sigma} sinh^{-1}(\chi_{\sigma})}, \tag{2.99}$$

in which the dimensionless parameter, χ_{σ}, is

$$\chi_{\sigma} = \frac{|\nabla n_{\sigma}|}{n_{\sigma}^{4/3}}. \tag{2.100}$$

The parameter $\beta = 0.05$ is obtained by fitting to the exact potential for the beryllium atom. The van Leeuwen and Baerends potential represents the intershell peak fairly well and the asymptotic behavior essentially correctly. The application of the van Leeuwen and Baerends potential shows that it considerably improves the LSDxc eigenvalues and yields bound state solutions for the negative ions [212].

2.3 LINEAR COMBINATION OF GAUSSIAN TYPE ORBITALS AND THE PROGRAM deMon–KS

deMon–KS (**de**nsity of **Mon**treal–Kohn–Sham) has been developed as a linear combination of Gaussian–type orbital–model core potential–Kohn–Sham density–functional program [278, 279, 280]. The linear combination of Gaussian–type orbitals, auxiliary basis sets, grid, and model core potential techniques implemented in the deMon–KS program will be reviewed in this section.

2.3.1 LINEAR COMBINATION OF GAUSSIAN TYPE ORBITALS

The Kohn-Sham equation (Eq. 2.58) can be efficiently solved by expanding the molecular orbitals in an orbital basis set. Several different types of orbital

basis sets have been used in different DFT programs, including numerical basis sets (DMol [281], NUMOL [282, 283, 284]), plane waves basis sets (Car-Parrinello [285], CORNING [286]), Slater-type orbital (STO) [287] basis sets (AMol or ADF [288, 289, 290]), and Gaussian-type orbital (GTO) [291, 292, 293, 294, 295] basis sets (deMon–KS [278, 279, 280], DGauss [296, 297], GAUSSIAN [298], CADPAC [299], TurboMol [300, 301, 302]). Each choice has its own set of advantages and disadvantages. GTO basis sets tend to be the more popular choice. Although larger orbital basis sets are needed when Gaussians are used, there is a net gain in computational efficiency because the necessary integrals can be evaluated analytically. The GTOs also make it possible to accurately calculate analytic energy gradients (for geometry optimizations) and density gradients (for corrections of the exchange-correlation functional beyond the LSDxc approximation). A more detailed review of the advantages of using GTOs in the DFT can be found in the literature [303, 120]. For these reasons, the GTOs are most widely used in the contemporary computational chemistry and physics.

The expansion of Kohn-Sham molecular orbitals, $\psi_i^\sigma(\mathbf{r})$, into the GTOs,

$$\psi_i^\sigma(\mathbf{r}) = \sum_j C_{ji}^\sigma \chi_j(\mathbf{r}) \,, \tag{2.101}$$

leads to the Kohn-Sham secular equations,

$$\sum_l (H_{kl}^\sigma - \epsilon_i^\sigma S_{kl}) C_{li}^\sigma = 0 \,, \tag{2.102}$$

where the C_{li}^σ are expansion coefficients for the i orbital,

$$H_{kl}^\sigma = \int d\mathbf{r} \chi_k^*(\mathbf{r}) \hat{h}^{\sigma,KS} \chi_l(\mathbf{r}) \,, \tag{2.103}$$

and

$$S_{kl} = \int d\mathbf{r} \chi_k^*(\mathbf{r}) \chi_l(\mathbf{r}) \,. \tag{2.104}$$

Here $\hat{h}^{\sigma,KS}$ is the Kohn-Sham operator, and the $\chi_l(\mathbf{r})$ are contracted Gaussian-type basis functions. The basis sets are normally described in "deMon-KS terminology" (Huzinaga notation) in the form [304, 280],

$$(\chi_s^1, \chi_s^2, \cdots, \chi_s^{Ks} / \chi_p^1, \chi_p^2, \cdots, \chi_p^{Kp} / \chi_d^1, \chi_d^2, \cdots, \chi_d^{Kd})$$

which indicates that there are Ks contracted s type Gaussian functions comprised respectively by $\chi_s^1, \chi_s^2, \cdots, \chi_s^{Ks}$ Gaussian primitives in the basis set, Kp contracted p type Gaussian functions constituted respectively by $\chi_p^1, \chi_p^2, \cdots, \chi_p^{Kp}$ Gaussian primitives, and Kd contracted d type Gaussian functions constructed respectively by $\chi_d^1, \chi_d^2, \cdots, \chi_d^{Kd}$ Gaussian primitives.

2.3.2 AUXILIARY FUNCTION METHOD

Calculations involving coulomb and exchange-correlation integrals are simplified in *deMon–KS* by the use of auxiliary basis functions. Following the work of Samble and Felton [305] and that of Dunlap, Connolly, and Sabin [306, 307], the charge density, $n(\mathbf{r})$, is expanded as a linear combination of auxiliary basis functions, f_i,

$$\tilde{n}(\mathbf{r}) = \sum_i a_i f_i(\mathbf{r}) \,, \tag{2.105}$$

consisting of atom-centered GTO primitives. The exchange-correlation potential is expanded in another auxiliary basis set of GTO functions (also consisting of atom-centered GTO primitives), g_i, and

$$\tilde{v}_{xc}^{\sigma}(\mathbf{r}) = \sum_i b_i^{\sigma} g_i(\mathbf{r}) \,. \tag{2.106}$$

where a_i and b_i^{σ} are fitting coefficients. The tilde used here emphasizes that these fitted quantities may differ from the corresponding exact quantities due to use of an incomplete set of Gaussian functions. The auxiliary basis sets used in the program *deMon–KS* are abbreviated by $(n_s, n_{spd}; v_s, v_{spd})$, where n_s and v_s are the number of s-type Gaussian primitives used, and n_{spd} and the v_{spd} are the number of sets of s-, p-, and d-type Gaussian primitives with shared exponents used for fitting the charge density and the exchange-correlation potential, respectively.

The charge density fitting coefficients, a_i, are obtained by a least squares fitting procedure to minimize the Coulomb repulsion energy difference between the fitted density and original density [306, 307],

$$\langle n - \tilde{n}|\tfrac{1}{|\mathbf{r}-\mathbf{r}'|}|n - \tilde{n}\rangle$$

subject to the normalization constraint,

$$\int d\mathbf{r}\tilde{n}(\mathbf{r}) = N\,, \tag{2.107}$$

where N is the total number of electrons. This constrained minimization leads to

$$a_k = \sum_I S^{-1}_{ki}\langle f_i|\frac{1}{|\mathbf{r}-\mathbf{r}'|}|n\rangle + \lambda\int d\mathbf{r} f_i \tag{2.108}$$

where the charge density overlap matrix is defined as

$$S_{ki} = \langle f_k|\frac{1}{|\mathbf{r}-\mathbf{r}'|}|f_i\rangle\,. \tag{2.109}$$

The Lagrange multiplier, λ, obtained by the normalization constraint (Eq. 2.107) is

$$\lambda = \frac{N - \sum ij(\int d\mathbf{r} f_j(\mathbf{r})S^{-1}_{ji}\langle f_i(\mathbf{r})|\frac{1}{|\mathbf{r}-\mathbf{r}'|}|n(\mathbf{r})\rangle}{\sum_{ij}(\int d\mathbf{r} f_j(\mathbf{r})S^{-1}_{ji}(\int d\mathbf{r} f_i(\mathbf{r})}\,, \tag{2.110}$$

The Coulomb part of the total energy is calculated as

$$\langle n|\tfrac{1}{\mathbf{r}-\mathbf{r}'}|\tilde{n}\rangle - \tfrac{1}{2}\langle\tilde{n}|\tfrac{1}{\mathbf{r}-\mathbf{r}'}|\tilde{n}\rangle\,,$$

which differs from the true value

$$\tfrac{1}{2}\langle n|\tfrac{1}{\mathbf{r}-\mathbf{r}'}|n\rangle\,,$$

by half the fitting error,

$$\frac{1}{2}\langle n|\frac{1}{\mathbf{r}-\mathbf{r}'}|n\rangle - \{\langle n|\frac{1}{\mathbf{r}-\mathbf{r}'}|\tilde{n}\rangle - \frac{1}{2}\langle\tilde{n}|\frac{1}{\mathbf{r}-\mathbf{r}'}|\tilde{n}\rangle\} = \frac{1}{2}\langle n-\tilde{n}|\frac{1}{\mathbf{r}-\mathbf{r}'}|n-\tilde{n}\rangle\,. \tag{2.111}$$

The exchange-correlation fitting coefficients, b_i^σ, are difficult to obtain analytically (see however Ref. [308]). Instead they are obtained numerically in *deMon–KS* by minimizing the numerical integral,

$$\sum_I [v_{xc}^\sigma(I) - \tilde{v}_{xc}^\sigma(I)]^2 W(I)$$

where the summation weighted by $W(I)$ is over the grid points, and $W(I)$ is proportional to the volume of space of the related grid point. Minimizing

$$\frac{\partial}{\partial b_i^\sigma}\{v_{xc}^\sigma(I) - \sum_i b_i^\sigma g_i(I)]^2 W(I)\} = 0 \tag{2.112}$$

leads to

$$b_i^\sigma = \sum_j Sxc_{ij}^{-1} \sum_I g_j(I) v_{xc}^\sigma(I) W(I) \tag{2.113}$$

where the exchange-correlation fitting overlap matrix is

$$Sxc_{ij} = \sum_I g_i(I) g_j(I) W(I)\,. \tag{2.114}$$

It is obvious that the auxiliary–function method (the linear combination of GTOs for the expansion of the charge density and exchange-correlation potential) reduces four–center two–electron integrals to three–center two–electron integrals, simplifying the necessary calculations and gaining computational efficiency. The Coulomb integrals become

$$\sum_i \int\int d\mathbf{r} d\mathbf{r}' \frac{\chi_k^*(\mathbf{r})\chi_l(\mathbf{r}) f_i(\mathbf{r}') a_i}{|\mathbf{r}-\mathbf{r}'|}\,,$$

and the exchange-correlation integrals become

$$\sum_i \int d\mathbf{r} \chi_k^*(\mathbf{r})\chi_l(\mathbf{r}) f_i(\mathbf{r}) b_i^\sigma\,,$$

2.3.3 GRID

A grid is commonly used in the numerical integrations in density-functional theory programs, such as deMon–KS [278, 279, 280], Amol (ADF) [288, 289, 290], DMol [281], NUMOL [282, 283, 284], CADPAC [299], DGauss [296, 297], GAUSSIAN/DFT [298], and Q-CHEM [309]. As normally practiced, multicenter molecular integrals are partitioned into a sum of atomic–like single center integrals using a nuclear weight function algorithm [310, 311, 281, 312] or the molecular space is separated into atomic spheres [313, 314, 315, 316]. In deMon–KS, the nuclear weight function approach has been used, but the original Gauss-Chebyshev quadrature [317] has been replaced by Gauss-Legendre quadrature [318]. In addition to this radial grid, a suitable angular grid also needs to be chosen for the quadrature of each unit sphere. A few kinds of angular grids have been proposed in the literature [319, 320, 321, 322, 323, 324, 325, 326]. Version 1.2 of deMon–KS employs the Lebedev angular grid with 6, 12, 26, 50, 110, 194 angular grid points [321, 322, 323, 324, 325, 311]. All grid options in this version use 32 radial grid points. If proportional angular grid points are used it is the FINE grid (in *deMon–KS*, the radial grid, G_R is partitioned into five regions, the first region, 0.0–0.4G_R, with 50 angular grid points, the second region, 0.4G_R–0.5G_R, with 110 angular grid points, the third region, 0.5G_R–0.7G_R, with 194 angular grid points, the fourth region, 0.7G_R–0.8G_R, with 110 angular grid points, and the fifth region, 0.8G_R–1.0G_R, with 50 angular grid points). If 194 angular grid points are used in each unit shell it is called EXTRA-FINE grid. Later it was improved to include a user defined grid [327] which allows the user to choose as many radial grid points as needed and to vary the angular grid points.

2.3.4 MODEL CORE POTENTIAL

Model core potentials (MCPs) are a technique used to reduce computational cost. In this technique, the inert core electrons are not treated explicitly but

rather are replaced with an analytical core potential. Only the valence electrons which move in the core potential are considered. The use of MCPs can reduce basis set superposition error and include some relativistic effects by building relativistic effects into the MCPs [279]. MCPs also make it possible to treat larger molecules and clusters than would otherwise be possible.

An MCP for atom A with nuclear charge Z and N_c core electrons is introduced by replacing the all-electron nuclear attraction term as follows:

$$-\frac{Z}{|\mathbf{r}-\mathbf{r}_A|} \longrightarrow -V_{MCP}(\mathbf{r}-\mathbf{r}_A)+\hat{P}_A^{\sigma}\,. \tag{2.115}$$

Here

$$V_{MCP}(\mathbf{r})=\sum_i A_i \frac{exp(-\alpha_i \mathbf{r}^2)}{\mathbf{r}}(\frac{\alpha_i}{\pi})^{3/2}, \tag{2.116}$$

is the actual core potential whose exponents, α_i, coefficients, A_i, are adjusted to minimize the least square error between the MCP valence and exact numerical valence atomic orbitals. The coefficients are normalized so that

$$\sum_i A_i = N_c\,. \tag{2.117}$$

In order to avoid variational collapse of the valence electrons into the core, a projector

$$P^{\sigma}=\sum_{c,\sigma} 2\epsilon_c^{\sigma}|\psi_c^{\sigma}><\psi_c^{\sigma}|\,, \tag{2.118}$$

is introduced to lift the core orbital energies up above the valence orbital energies. The ϵ_c^{σ} and ψ_c^{σ} are respectively the core orbital energies and orbitals for atom A. More details will be given in chapter 4.

2.4 TIME-DEPENDENT DENSITY-FUNCTIONAL THEORY

Traditionally Kohn–Sham density-functional theory is restricted to time-independent ground-state problems. It has difficulty to treat excited state properties and time-dependent problems, hence a time-dependent theory is needed.

A number of authors [159, 153, 160, 154, 155, 156, 166, 157, 138] have tried to develop time-dependent density-functional theory. Initial work towards time-dependent DFT was achieved by Peuckert [159] and by Zangwill and Soven [160]. Zangwill and Soven [160] were the first to use the adiabatic approximation with the local density approximation (LDAxc) to treat the time-dependent exchange-correlation potential in their calculations of photoabsorption of noble gases. An important step toward a rigorous foundation of time-dependent DFT was taken by Deb and Ghosh [155, 161, 162, 163] and by Bartolotti [154, 164, 165]. They formulated time-dependent DFT with a set of external potentials. A solid theoretical framework for the time–dependent DFT was given by Runge and Gross [156] who proved fundamental theorems of the time-dependent DFT for a more general external potential. A brief review of time-dependent density-functional theory is given in this section. Detailed reviews can be found in the literature [167, 138, 168, 139, 169, 328, 329].

2.4.1 ANALOGUES OF THE HOHENBERG–KOHN THEOREMS

A fundamental challenge in time-dependent density-functional theory has been to find a suitable analogue of the Hohenberg-Kohn theorems [113]. In the time-independent case, the existence of an exact mapping between the charge density and single particle external potential are proved based upon the Rayleigh-Ritz minimum principle for the energy. Straightforward extension of this approach to the time-dependent situation is not possible owing to the lack of a suitable minimum principle. Nevertheless, Runge and Gross [156] have been able to show that the time-dependent charge density determines the time-dependent external potential for the case of external potentials which can be expressed as a Taylor series about some initial time t_0,

$$v(t) = \sum_{i=0}^{\infty} \frac{1}{i!} \frac{\partial v^i(t_0)}{\partial t^i} (t - t_0)^i \,. \tag{2.119}$$

Note that the external potential $v(t)$ is assumed to be a constant at $t < t_0$ and the initial time t_0 is assumed to be finite, since at $t_0 = -\infty$ there is an essential singularity in the Taylor expansion. In the formal proof of Runge and Gross, the current density is used, which is beyond the scope of this thesis. Hence only the basic idea of the Runge-Gross proof is given here.

In the time-dependent domain, a system is described by the time-dependent Schrödinger equation (atomic units are used),

$$i\frac{\partial\Psi(t)}{\partial t} = \hat{H}\Psi(t) \tag{2.120}$$

where the Hamiltonian in the above equation is

$$\begin{aligned}\hat{H} &= -\frac{1}{2}\sum_i \nabla_i^2 + \sum_{i<j}\frac{1}{|r_i - r_j|} + \sum_i v(r_i, t) \\ &= \hat{T} + \hat{U} + \hat{V}_{ext}(t)\,,\end{aligned} \tag{2.121}$$

note that the external potential

$$\hat{V}_{ext}(t) = \sum_j^N v(\mathbf{r}_j, t) \tag{2.122}$$

may include a time-dependent perturbation (e.g. a time-dependent electrical field).

In order to prove the analogue of the time-independent first Hohenberg–Kohn theorem, the solutions of the time-dependent Schrödinger equation are only considered for $t > t_0$, subject to the initial condition that $\Psi(t_0) = \Psi_0$. In the Runge and Gross proof [156], they suppose that there are two external potentials which differ by more than a time-dependent constant function,

$$v'(t) - v(t) \neq C(t)\,, \tag{2.123}$$

and that both of the potentials can also be expanded in a Taylor series around initial time t_0

$$v(t) = \sum_{i=0}^{\infty}\frac{1}{i!}\frac{\partial^i}{\partial t^i}v(t)(t - t_0)^i \tag{2.124}$$

and

$$v'(t) = \sum_{i=0}^{\infty} \frac{1}{i!} \frac{\partial^i}{\partial t^i} v'(t)(t - t_0)^i \,. \tag{2.125}$$

Suppose also that these two external potentials lead to the same time-dependent charge density, $n(t)$. Runge and Gross [156] found the contradiction by first proving that the current densities corresponding to the above two external potentials are different. They then showed that the two time-dependent charge densities corresponding to the above two external potentials are also different by using the continuity boundary conditions between time-dependent charge density and current density. This contradicts the original assumption that the two external potentials lead to the same time-dependent charge density, hence proving the **Runge–Gross Theorem** (an analogue of the time-independent first Hohenberg–Kohn theorem in the time-dependent case). *Under the conditions discussed above, the time-dependent charge density determines the external potential uniquely up to an additive time-dependent constant.*

According to the Runge–Gross theorem, it can be concluded that expectation values of any quantum mechnical operators and the time-dependent wave function are also functionals of the time-dependent charge density. Since, if the two applied external potentials differ by only an additive time-dependent constant $C(t)$,

$$v'(t) = v(t) + C(t) \,, \tag{2.126}$$

by solving the time-dependent Schrödinger equation (Eq. 2.120), one can show that the corresponding time-dependent wave functions differ by only a time-dependent phase factor $exp[-i\alpha(t)]$ (where $\alpha(t) = \int dt C(t)$).

$$\Psi'(t) = \Psi(t) exp[-i\alpha(t)] \,. \tag{2.127}$$

Hence, the time-dependent external potential determines the time-dependent wave functions uniquely up to a time-dependent phase factor. This phase factor cancels out in the charge density

$$n(\mathbf{r}, t) = N \int ds_1 \int d\tau_2 \cdots \int d\tau_N |\Psi(t)|^2 \,, \tag{2.128}$$

and the expectation values of any quantum mechanical operator $\hat{A}(t)$,

$$\langle \Psi(t)|\hat{A}(t)|\Psi(t)\rangle = A(t)\,, \tag{2.129}$$

if the operator $\hat{A}(t)$ contains no time derivatives or time intergals. Therefore, they lead to the same charge density and the same expectation values. Note that the Runge–Gross theorem indicates that the time-dependent charge density uniquely determines the external potential up to an additive time-dependent constant, and the external potential uniquely determines the time-dependent wave function up to a phase factor, then the time-dependent wave function must also be a functional of the time-dependent charge density, even though the explicit dependence of the wave function on the charge density is unknown yet.

$$\Psi(t) = \Psi[n](t)exp[-i\alpha(t)]\,. \tag{2.130}$$

Consequently the expectation value is also a functional of the charge density.

$$\begin{aligned} A(t) &= \langle \Psi(t)|\hat{A}(t)|\Psi(t)\rangle \\ &= \langle \Psi[n](t)|\hat{A}(t)|\Psi[n](t)\rangle \\ &= A(n,t)\,. \end{aligned} \tag{2.131}$$

This indicates that any observable quantities are functionals of the time-dependent charge density. It does, however, have an implicit dependence on the initial state Ψ_0. This dependence can be an immaterial when the initial state is just the ground stationary state of a system (with a static external potential). Specifically, observables depend only on the charge density when the initial state is specified in terms of the charge density. Since according to the first Hohenberg and Kohn theorem [113], if the initial state is a non-degenerate ground state, it is an unique functional of the ground state charge density. So the expectation value can be considered as a unique functional of the charge density.

In the time-independent case, the second Hohenberg–Kohn theorem stated that the true charge density minimized the total energy. In the time-dependent

case, there is no explicit energy in the time-dependent Schrödinger equation, so the energy minimum principle is not applicable in time–dependent DFT. Hence the action has to be used.

$$\mathcal{A} = \int_{t_0}^{t_1} dt \langle \Psi(t) | i\frac{\partial}{\partial t} - \hat{H}(t) | \Psi(t) \rangle \tag{2.132}$$

Since there is a mapping between the time-dependent wave function and the time-dependent charge density, the above action integral is also a functional of time-dependent charge density.

$$\mathcal{A}(n) = \int_{t_0}^{t_1} dt \langle \Psi[n](t) | i\frac{\partial}{\partial t} - \hat{H}(t) | \Psi[n](t) \rangle \,, \tag{2.133}$$

which has a stationary point at the true time-dependent charge density. This true time-dependent charge density of the system can be obtained by making the action $\mathcal{A}$ stationary, namely the Euler equation,

$$\begin{aligned} \frac{\delta \mathcal{A}}{\delta n(\mathbf{r},t)} &= \int_{t_0}^{t_1} dt' [\langle \frac{\delta \Psi(t')}{\delta n(\mathbf{r},t)} | i\frac{\partial}{\partial t'} - \hat{H}(t') | \Psi(t') \rangle \\ &+ \langle \Psi(t') | i\frac{\partial}{\partial t'} - \hat{H}(t') | \frac{\delta \Psi(t')}{\delta n(\mathbf{r},t)} \rangle] \\ &= 0 \end{aligned} \tag{2.134}$$

The phase factor in the wave function makes no contribution in the action defined in Eq (2.132) despite the presence of the time derivative operator, since the phase factor only gives an additive constant. The above discussions give the important **stationary action principle**. *When the action [Eq. (2.132)] is expressed as a functional of the time-dependent charge density [Eq. (2.133)], it must have a stationary point at the true time-dependent charge density which can be obtained by solving the Euler equation [Eq. (2.134)].* This is the time-dependent analogue of the second Hohenberg–Kohn theorem in time-independent DFT. It is notable that most quantum chemical treatments of the time-dependent problem are based on some stationary action principle (usually the Frenkel principle [330]). In time-dependent DFT, this action principle is not without subtleties, a recent example

of which is van Leeuwen's redefinition of the action in time-dependent DFT to resolve a paradox regarding causality and symmetry in the response kernel [331]. Nevertheless, van Leeuwen's redefinition of the action is not considered in this thesis, the traditional definition of the action will be used throughout this thesis to avoid introducing tedious and confusing (though technically important) details.

2.4.2 TIME-DEPENDENT KOHN–SHAM EQUATION

Since the energy minimum principle is not applicable in the time-dependent case, the stationary action principle has to be used to derive the time-dependent Kohn-Sham equation. The action is a unique functional of the time-dependent charge density $n(\mathbf{r},t)$,

$$\mathcal{A}[n] = \int_{t_0}^{t_1} dt \langle \Psi[n](t)| i\frac{\partial}{\partial t} - \hat{H}(t)|\Psi[n](t)\rangle \,. \tag{2.135}$$

Analogously to time-independent density-functional theory, the action can also be written as the sum of a universal functional $B[n]$, and an external action $\mathcal{A}_{ext}[n]$. The universal functional $B[n]$ is given by

$$B[n] = \int_{t_0}^{t_1} dt \langle \Psi[n](t)| i\frac{\partial}{\partial t} - \hat{T} - \hat{U}|\Psi[n](t)\rangle \,, \tag{2.136}$$

which is independent of the external potential and plays the role of the Hohenberg–Kohn universal functional $F[n]$ in the time-independent DFT theory [26]. The external action $\mathcal{A}_{ext}[n]$ is defined as,

$$\mathcal{A}_{ext}[n] = -\int_{t_0}^{t_1} dt \int d\mathbf{r}[v(\mathbf{r},t)n(\mathbf{r},t)] \,. \tag{2.137}$$

Hence, the action can be rewritten as

$$\begin{aligned} \mathcal{A}[n] &= B[n] + \mathcal{A}_{ext}[n] \\ &= B[n] - \int_{t_0}^{t_1} dt \int d\mathbf{r}[v(\mathbf{r},t)n(\mathbf{r},t)] \,. \end{aligned} \tag{2.138}$$

Introducing a non-interacting system universal functional B_s,

$$B_s[n] = \int_{t_0}^{t_1} dt \langle \Psi_s[n](t)| i\frac{\partial}{\partial t} - \hat{T}|\Psi_s[n](t)\rangle \,, \tag{2.139}$$

allows the action $\mathcal{A}$ to be rewritten as

$$\begin{aligned} \mathcal{A}[n] &= B_s[n] - \int_{t_0}^{t_1} dt \int dr[v(\mathbf{r},t)n(\mathbf{r},t)] \\ &- \frac{1}{2}\int_{t_0}^{t_1} dt \int d\mathbf{r} \int d\mathbf{r}' \frac{n(\mathbf{r},t)n(\mathbf{r}',t)}{|\mathbf{r}-\mathbf{r}'|} - \mathcal{A}_{xc}[n] \,, \end{aligned} \tag{2.140}$$

where $\mathcal{A}_{xc}[n]$ is the exchange-correlation action. By comparing Eq. (2.138) and Eq. (2.140), $\mathcal{A}_{xc}[n]$ is

$$\mathcal{A}_{xc}[n] = B_s[n] - \frac{1}{2}\int_{t_0}^{t_1} dt \int d\mathbf{r} \int d\mathbf{r}' \frac{n(\mathbf{r},t)n(\mathbf{r}',t)}{|\mathbf{r}-\mathbf{r}'|} - B[n] \,. \tag{2.141}$$

If the external potential of a non-interacting system can be found, it must be unique due to the Runge–Kohn theorem, this potential also makes the non-interacting system charge density identical with the interacting system charge density (i.e. the charge density is "v–representable"), the charge density may be written in terms of a set of orbitals,

$$n(\mathbf{r},t) = \sum_{i=1}^{N} n_i |\psi_i(\mathbf{r},t)|^2 \tag{2.142}$$

where the n_i are the occupation numbers. Applying the stationary action principle [Eq (2.134)] with the constraint [Eq (2.142)], the time-dependent Kohn-Sham equation can be obtained as

$$i\frac{\partial \psi_i(\mathbf{r},t)}{\partial t} = [-\frac{1}{2}\nabla^2 + v_{eff}(\mathbf{r},t)]\psi_i(\mathbf{r},t) \tag{2.143}$$

where the effective potential (also called time-dependent Kohn–Sham potential) is

$$\begin{aligned} v_{eff}(\mathbf{r},t) &= v_{ext}(\mathbf{r},t) + \int d\mathbf{r}' \frac{n(\mathbf{r}',t)}{|\mathbf{r}-\mathbf{r}'|} + \frac{\delta \mathcal{A}_{xc}[n]}{\delta n(\mathbf{r},t)} \,, \\ &= v_{ext}(\mathbf{r},t) + v_{SCF}(\mathbf{r},t) \end{aligned} \tag{2.144}$$

evidently the self-consistent field potential is

$$\begin{aligned} v_{SCF}(\mathbf{r},t) &= \int d\mathbf{r}' \frac{n(\mathbf{r}',t)}{|\mathbf{r}-\mathbf{r}'|} + \frac{\delta \mathcal{A}_{xc}[n]}{\delta n(\mathbf{r},t)}, \\ &= \int d\mathbf{r}' \frac{n(\mathbf{r}',t)}{|\mathbf{r}-\mathbf{r}'|} + v_{xc}(\mathbf{r},t) \end{aligned} \tag{2.145}$$

where $v_{xc}(\mathbf{r},t)$ is the time-dependent exchange-correlation potential and given by

$$v_{xc}(\mathbf{r},t) = \frac{\delta \mathcal{A}_{xc}[n]}{\delta n(\mathbf{r},t)} \tag{2.146}$$

2.4.3 THE ADIABATIC APPROXIMATION

The time-dependent exchange-correlation action $\mathcal{A}_{xc}[n]$ is the time-dependent analogue of the time-independent exchange-correlation energy $E_{xc}[n]$, but $\mathcal{A}_{xc}[n]$ is a functional of the time-dependent charge density $n(\mathbf{r},t)$, whereas $E_{xc}[n]$ depends only on the stationary charge density $n(\mathbf{r})$. Several approximations are known for the time-independent exchange-correlation energy. However, no time-dependent exchange-correlation action form $\mathcal{A}_{xc}[n]$ is known yet. Hence approximations are needed. Peuckert [159] suggested an iterative scheme for the calculation of the exchange-correlation potential. Zangwill and Soven [160] applied the adiabatic approximation which used a static exchange-correlation potential in the local density approximation to calculate the photoabsorption of the rare gases. This adiabatic approximation is the most well known and the most commonly used in the calculation of the exchange-correlation potential in time-dependent DFT. Simply speaking this approximation uses the static DFT exchange-correlation functional expression (e.g. LSDxc) with a time-dependent charge density.

$$\mathcal{A}_{xc}[n](\mathbf{r},t) = \int_{t_0}^{t} dt' E_{xc}[n_{t'}], \tag{2.147}$$

where

$$n_t(\mathbf{r}) = n(\mathbf{r},t). \tag{2.148}$$

This equation indicates that the charge density is evaluated at a certain time t [e.g. the initial charge density $n_0(\mathbf{r}) = n(\mathbf{r}, t_0)$]. The exchange-correlation action changes when the charge density changes

$$\mathcal{A}_{xc}(n+\delta n) - \mathcal{A}_{xc}[n] = \int_{t_0}^{t} dt' \{E_{xc}[n_{t'} + \delta n_{t'}] - E_{xc}[n_{t'}]\}\,, \tag{2.149}$$

hence,

$$\begin{aligned} \delta\mathcal{A}_{xc}[n] &= \int_{t_0}^{t} dt' \delta E_{xc}[n_{t'}] \\ &= \int_{t_0}^{t} dt' \{\int d\mathbf{r} \frac{\delta E_{xc}[n_{t'}]}{\delta n_{t'}} n_{t'}(\mathbf{r})\} \\ &= \int_{t_0}^{t} dt' \int d\mathbf{r} \frac{\delta E_{xc}[n_{t'}]}{\delta n_{t'}} n(\mathbf{r}, t')\,. \end{aligned} \tag{2.150}$$

So, in the adiabatic approximation,

$$\frac{\delta\mathcal{A}_{xc}[n]}{\delta n(\mathbf{r}, t)} = \frac{\delta E_{xc}(n_t)}{\delta n_t(\mathbf{r})}\,. \tag{2.151}$$

According to Eq. (2.146), the time-dependent exchange-correlation potential is

$$\begin{aligned} v_{xc}(\mathbf{r}, t) &= \frac{\delta\mathcal{A}_{xc}[n]}{\delta n(\mathbf{r}, t)} \\ &= \frac{\delta E_{xc}[n_t]}{\delta n_t(\mathbf{r})}\,, \end{aligned} \tag{2.152}$$

i.e.

$$v_{xc}[n](\mathbf{r}, t) = v_{xc}[n_t](\mathbf{r})\,. \tag{2.153}$$

This adiabatic approximation equates the time-dependent exchange-correlation potential to that of the time-independent theory, but with the charge density evaluated at a certain time t.

2.5 TIME-DEPENDENT RESPONSE THEORY

The general wave function time-dependent response theory has been well developed. It is a useful tool in the development of time-dependent density–functional response theory. A brief review is given in this section.

The expectation value of an operator $\hat{A}$ can be written in the second quantization [332, 26] form,

$$\begin{aligned} A(t) &= \langle\Psi(t)|\hat{A}(t)|\Psi(t)\rangle \\ &= \sum_{pq\sigma} A_{pq\sigma}\langle\Psi(t)|\hat{p}_\sigma^+\hat{q}_\sigma|\Psi(t)\rangle \\ &= \sum_{pq\sigma} A_{pq\sigma}P_{qp\sigma} \\ &= tr(\mathcal{AP}) \end{aligned} \tag{2.154}$$

where $\hat{A}(t) = \sum_{pq\sigma} A_{pq\sigma}\hat{p}_\sigma^+\hat{q}_\sigma$ is the second quantization expression for the operator $\hat{A}$, the $\hat{p}_\sigma^+$ are fermion creation operators, and the $\hat{q}_\sigma$ are fermion annihilation operators, $\mathcal{A}$ represents the matrix of the operator $\hat{A}$, and $\mathcal{P}$ represents the density matrix with the elements $P_{qp\sigma}$. The Roman letters p and q refer to space indices and the Greek letter σ indicates the spin index. Trace (tr) means to sum over all of the diagonal elements of the matrix. If the system wave function is cut off at first order [Eq. (2.13)], the expectation value of the operator $\hat{A}$ (Eq. (2.154)) becomes

$$\begin{aligned} A(t) &= tr(\mathcal{AP}) \\ &= \sum_{pq\sigma} A_{pq\sigma}\langle\Psi^{(0)}(t) + \Psi^{(1)}(t)|\hat{p}_\sigma^+\hat{q}_\sigma|\Psi^{(0)}(t) + \Psi^{(1)}(t)\rangle \\ &= \sum_{pq\sigma} A_{pq\sigma}[P_{qp\sigma}^{(0)}(t) + P_{qp\sigma}^{(1)}(t) + P_{qp\sigma}^{(2)}(t)] \\ &= tr(\mathcal{AP}^{(0)}) + tr(\mathcal{AP}^{(1)}) + tr(\mathcal{AP}^{(2)}) \\ &= A^{(0)} + A^{(1)} + A^{(2)} \end{aligned} \tag{2.155}$$

where the zeroth order part of the expectation value $A^{(0)} = tr(\mathcal{AP}^{(0)})$ with the zeroth order density matrix,

$$P_{qp\sigma}^{(0)}(t) = \langle\Psi^{(0)}(t)|\hat{p}_\sigma^+\hat{q}_\sigma|\Psi^{(0)}(t)\rangle\,; \tag{2.156}$$

the first order part of the expectation value (the linear response of the expectation value A) is $A^{(1)} = tr(\mathcal{AP}^{(1)})$ with the first order density matrix

$$P_{qp\sigma}^{(1)}(t) = \langle\Psi^{(1)}(t)|\hat{p}_\sigma^+\hat{q}_\sigma|\Psi^{(0)}(t)\rangle + \langle\Psi^{(0)}(t)|\hat{p}_\sigma^+\hat{q}_\sigma|\Psi^{(1)}(t)\rangle\,; \tag{2.157}$$

and part of the second order of the expectation value $A^{(2)} = tr(\mathcal{A}\mathcal{P}^{(2)})$ where the part of the second order density matrix is

$$P^{(2)}_{qp\sigma}(t) = \langle \Psi^{(1)}(t)|\hat{p}^{+}_{\sigma}\hat{q}_{\sigma}|\Psi^{(1)}(t)\rangle\,. \tag{2.158}$$

Substituting the first order wave function [Eq. (2.15)] into the linear response of the density matrix, $P^{(1)}_{qp\sigma}(t)$, one gets

$$\begin{aligned} P^{(1)}_{qp\sigma}(t) &= \langle \sum_{k}(i)^{-1}\int_{-\infty}^{t} dt[\langle \Psi^{(0)}_{k}|\hat{H}'|\Psi^{(0)}_{n}\rangle \\ &\quad \times exp(i\omega_{kn}t)]\exp(-iE_kt)\Psi^{(0)}_{k}|\hat{p}^{+}_{\sigma}\hat{q}_{\sigma}|\Psi^{(0)}(t)\rangle \\ &\quad +\langle \Psi^{(0)}(t)|\hat{p}^{+}_{\sigma}\hat{q}_{\sigma}|\sum_{k}(i)^{-1}\int_{-\infty}^{t} dt[\langle \Psi^{(0)}_{k}|\hat{H}'|\Psi^{(0)}_{n}\rangle exp(i\omega_{kn}t)] \\ &\quad \times \exp(-iE_kt)\Psi^{(0)}_{k}\rangle\,. \end{aligned} \tag{2.159}$$

The time integrals in the above equation [Eq. (2.159)] do not converge at time equal to minus infinity, due to the oscillating term $exp(i\omega_{kn}t) = \cos(\omega_{kn}t) - i\sin(\omega_{kn}t)$. To assure the convergence of the above time integrals, the perturbation operator $\hat{H}'$ is set to

$$\begin{aligned} \hat{H}'(t) &= \exp[-\xi(t-t')]\hat{H}'(t) \\ &= \begin{cases} \hat{H}'(t) & ;\,\text{at}\,t' = t \\ 0 & ;\,\text{at}\,t' = -\infty \end{cases} \end{aligned} \tag{2.160}$$

where ξ is a positive infinitesimal. Substituting Eq. (2.160) and the zeroth order wave function $\Psi^{(0)}(t) = \exp(-iE_nt)\Psi^{(0)}_{n}$ into Eq. (2.159), the linear response of the density matrix becomes

$$\begin{aligned} P^{(1)}_{qp\sigma}(t) &= \frac{1}{i}\int_{-\infty}^{t} dt' \sum_{k}\{\langle \Psi^{(0)}_{n}|\hat{p}^{+}_{\sigma}\hat{q}_{\sigma}|\Psi^{(0)}_{k}\rangle\langle \Psi^{(0)}_{k}|\hat{H}'|\Psi^{(0)}_{n}\rangle \\ &\quad \times exp[-i(E_k - E_n - i\xi)(t-t')] - \langle \Psi^{(0)}_{n}|\hat{H}'|\Psi^{(0)}_{k}\rangle\langle \Psi^{(0)}_{k}|\hat{p}^{+}_{\sigma}\hat{q}_{\sigma}|\Psi^{(0)}_{n}\rangle \\ &\quad \times exp[-i(E_n - E_k - i\xi)(t-t')]\}\,. \end{aligned} \tag{2.161}$$

Using the second quantization notation for the perturbation operator $\hat{H}'$,

$$\hat{H}'(t) = \sum_{sr\tau} H'_{sr\tau}\hat{s}^{+}_{\tau}\hat{r}_{\tau} \tag{2.162}$$

substituting this equation [Eq. (2.162)] into Eq. (2.161), then

$$\begin{aligned} P^{(1)}_{qp\sigma}(t) &= \sum_{sr\tau} \int_{-\infty}^{t} dt' \{ \frac{1}{i} \sum_{k} [\langle \Psi^{(0)}_{n} | \hat{p}^{+}_{\sigma} \hat{q}_{\sigma} | \Psi^{(0)}_{k} \rangle \langle \Psi^{(0)}_{k} | \hat{s}^{+}_{\tau} \hat{r}_{\tau} | \Psi^{(0)}_{n} \rangle \\ &\times exp[-i(E_k - E_n - i\xi)(t - t')] - \langle \Psi^{(0)}_{n} | \hat{s}^{+}_{\tau} \hat{r}_{\tau} | \Psi^{(0)}_{k} \rangle \langle \Psi^{(0)}_{k} | \hat{p}^{+}_{\sigma} \hat{q}_{\sigma} | \Psi^{(0)}_{n} \rangle \\ &\times exp[-i(E_n - E_k - i\xi)(t - t')]] H'_{sr\tau}(t') \} . \end{aligned} \tag{2.163}$$

In order to change the integration limit from t to ∞, the Heaviside function Θ is introduced,

$$\Theta(t - t') = \begin{cases} 1 & ; \quad t > t' \\ 0 & ; \quad t < t' \end{cases} \tag{2.164}$$

This allows the above Eq. (2.163) to be rewritten as

$$\begin{aligned} P^{(1)}_{qp\sigma}(t) &= \sum_{sr\tau} \int_{-\infty}^{\infty} dt' \{ \frac{1}{i} \Theta(t - t') \sum_{k} [\langle \Psi^{(0)}_{n} | \hat{p}^{+}_{\sigma} \hat{q}_{\sigma} | \Psi^{(0)}_{k} \rangle \langle \Psi^{(0)}_{k} | \hat{s}^{+}_{\tau} \hat{r}_{\tau} | \Psi^{(0)}_{n} \rangle \\ &\times exp[-i(E_k - E_n - i\xi)(t - t')] - \langle \Psi^{(0)}_{n} | \hat{s}^{+}_{\tau} \hat{r}_{\tau} | \Psi^{(0)}_{k} \rangle \langle \Psi^{(0)}_{k} | \hat{p}^{+}_{\sigma} \hat{q}_{\sigma} | \Psi^{(0)}_{n} \rangle \\ &\times exp[-i(E_n - E_k - i\xi)(t - t')]] H'_{sr\tau}(t') \} . \end{aligned} \tag{2.165}$$

This time-dependent linear response of the density matrix can be written as frequency-dependent by using the Fourier transform,

$$\Psi^{(1)}_{qp\sigma}(\omega) = \int_{-\infty}^{\infty} dt \, \exp(i\omega t) \Psi^{(1)}_{qp\sigma}(t) . \tag{2.166}$$

It follows that

$$\begin{aligned} P^{(1)}_{qp\sigma}(\omega) &= \sum_{sr\tau} \sum_{k} \frac{1}{i} \{ \langle \Psi^{(0)}_{n} | \hat{p}^{+}_{\sigma} \hat{q}_{\sigma} | \Psi^{(0)}_{k} \rangle \langle \Psi^{(0)}_{k} | \hat{s}^{+}_{\tau} \hat{r}_{\tau} | \Psi^{(0)}_{n} \rangle \\ &\times \int_{-\infty}^{\infty} dt' H'_{sr\tau}(t') exp(i\omega t') \int_{-\infty}^{\infty} d(t - t') \Theta(t - t') \\ &\times exp[i(\omega - \omega_{kn} + i\xi)(t - t')] - \langle \Psi^{(0)}_{n} | \hat{s}^{+}_{\tau} \hat{r}_{\tau} | \Psi^{(0)}_{k} \rangle \langle \Psi^{(0)}_{k} | \hat{p}^{+}_{\sigma} \hat{q}_{\sigma} | \Psi^{(0)}_{n} \rangle \\ &\times \int_{-\infty}^{\infty} dt' H'_{sr\tau}(t') exp(i\omega t') \int_{-\infty}^{\infty} d(t - t') \Theta(t - t') \\ &\times exp[i(\omega - \omega_{nk} + i\xi)(t - t')] \end{aligned} \tag{2.167}$$

using properties of the Heaviside function $\Theta(t-t')$, which can be eliminated by changing the integration limit.

$$\begin{aligned} P^{(1)}_{qp\sigma}(\omega) &= \sum_{sr\tau}\sum_{k}\frac{1}{i}\{\langle\Psi^{(0)}_n|\hat{p}^+_\sigma\hat{q}_\sigma|\Psi^{(0)}_k\rangle\langle\Psi^{(0)}_k|\hat{s}^+_\tau\hat{r}_\tau|\Psi^{(0)}_n\rangle \\ &\times\int_{-\infty}^{\infty}dt'H'_{sr\tau}(t')exp(i\omega t')\int_0^{\infty}d(t-t') \\ &\times exp[i(\omega-\omega_{kn}+i\xi)(t-t')]-\langle\Psi^{(0)}_n|\hat{s}^+_\tau\hat{r}_\tau|\Psi^{(0)}_k\rangle\langle\Psi^{(0)}_k|\hat{p}^+_\sigma\hat{q}_\sigma|\Psi^{(0)}_n\rangle \\ &\times\int_{-\infty}^{\infty}dt'H'_{sr\tau}(t')exp(i\omega t')\int_0^{\infty}d(t-t') \\ &\times exp[i(\omega-\omega_{nk}+i\xi)(t-t')] \end{aligned} \tag{2.168}$$

Integrating over $(t-t')$ and doing the Fourier transform,

$$\begin{aligned} P^{(1)}_{qp\sigma}(\omega) &= \sum_{sr\tau}\sum_{k}H'_{sr\tau}(\omega)\{\frac{\langle\Psi^{(0)}_n|\hat{p}^+_\sigma\hat{q}_\sigma|\Psi^{(0)}_k\rangle\langle\Psi^{(0)}_k|\hat{s}^+_\tau\hat{r}_\tau|\Psi^{(0)}_n\rangle}{\omega-\omega_{kn}+i\xi} \\ &- \frac{\langle\Psi^{(0)}_n|\hat{s}^+_\tau\hat{r}_\tau|\Psi^{(0)}_k\rangle\langle\Psi^{(0)}_k|\hat{p}^+_\sigma\hat{q}_\sigma|\Psi^{(0)}_n\rangle}{\omega-\omega_{nk}+i\xi}\}. \end{aligned} \tag{2.169}$$

It is convenient to introduce the generalized susceptibility χ defined by,

$$P^{(1)}_{qp\sigma}(\omega)=\sum_{sr\tau}\chi_{qp\sigma,sr\tau}(\omega)H'_{sr\tau}(\omega). \tag{2.170}$$

By comparing Eq. (2.169) and Eq. (2.170), the frequency-dependent generalized susceptibility χ is seen to be

$$\begin{aligned} \chi_{qp\sigma,sr\tau}(\omega) &= \sum_{k}\{\frac{\langle\Psi^{(0)}_n|\hat{p}^+_\sigma\hat{q}_\sigma|\Psi^{(0)}_k\rangle\langle\Psi^{(0)}_k|\hat{s}^+_\tau\hat{r}_\tau|\Psi^{(0)}_n\rangle}{\omega-\omega_{kn}+i\xi} \\ &- \frac{\langle\Psi^{(0)}_n|\hat{s}^+_\tau\hat{r}_\tau|\Psi^{(0)}_k\rangle\langle\Psi^{(0)}_k|\hat{p}^+_\sigma\hat{q}_\sigma|\Psi^{(0)}_n\rangle}{\omega+\omega_{kn}+i\xi}\}. \end{aligned} \tag{2.171}$$

The frequency dependence of the linear response of the expectation value $A^{(1)}(\omega)$ can also be obtained with the Fourier transform [Eq. (2.166)]

$$\begin{aligned} A^{(1)}(\omega) &= \int_{-\infty}^{\infty}dt[exp(i\omega t)A^{(1)}(t)] \\ &= \int_{-\infty}^{\infty}dt[exp(i\omega t)tr(\mathcal{A}\mathcal{P}^{(1)}(t))] \end{aligned}$$

$$
\begin{aligned}
&= \sum_{pq\sigma} A_{pq\sigma} P^{(1)}_{qp\sigma}(\omega) \\
&= \sum_{pq\sigma}\sum_{sr\tau} A_{pq\sigma}\chi_{pq\sigma,sr\tau}(\omega) H'_{sr\tau}(\omega) \qquad (2.172)
\end{aligned}
$$

where the time (or frequency) independence of the $A_{pq\sigma}$ is assumed and Eq. (2.170) is used in the above equation. Since the operator for the y component of the dipole moment is

$$\hat{\mu}_y = -ey = -y \qquad (2.173)$$

If the perturbation is considered as an electric field $\mathcal{E}$ turned on in the z direction, $H'_{sr\tau}(\omega) = z_{sr\tau}\mathcal{E}_z(\omega)$, then according to the Eq. (2.172), the linear response of the dipole moment (induced dipole moment) y-component can be expressed as

$$\mu^{(1)}_y(\omega) = -\sum_{pq\sigma} y_{pq\sigma} P^{(1)}_{qp\sigma}(\omega) \qquad (2.174)$$

or

$$\mu^{(1)}_y(\omega) = -\sum_{pq\sigma}\sum_{sr\tau} y_{pq\sigma}\chi_{qp\sigma,sr\tau}(\omega) z_{sr\tau}\mathcal{E}_z(\omega) \qquad (2.175)$$

Conventionally, the dipole moment $\mu(t)$ can be expanded in the series

$$\mu_y(t) = \mu^{(0)}_y + \int dt' \alpha_{yz}(t-t')\mathcal{E}_z(t') + \cdots . \qquad (2.176)$$

By Fourier transform

$$F(t) = \frac{1}{2\pi}\int_{-\infty}^{\infty} d\omega[exp(-i\omega t)F(\omega)]\,, \qquad (2.177)$$

the dipole moment expansion [Eq. (2.176)] can be written as

$$\mu_y(t) = \mu^{(0)}_y + \frac{1}{2\pi}\int_{-\infty}^{\infty} d\omega[\alpha_{yz}(\omega)\mathcal{E}_z(\omega)exp(-i\omega t)] + \cdots \qquad (2.178)$$

Therefore the linear response of the dipole moment (induced dipole moment) is given as

$$
\begin{aligned}
\mu^{(1)}_y(t) &= \mu_y(t) - \mu^{(0)}_y \\
&= \frac{1}{2\pi}\int_{-\infty}^{\infty} d\omega[\alpha_{yz}(\omega)\mathcal{E}_z(\omega)exp(-i\omega t)]\,. \qquad (2.179)
\end{aligned}
$$

According to the Fourier transform [Eq. (2.177)] the linear response of the dipole moment (induced dipole moment) can also be rewritten as

$$\mu_y^{(1)}(t) = \frac{1}{2\pi} \int_{-\infty}^{\infty} d\omega [\mu_y^{(1)}(\omega) exp(-i\omega t)] \,. \tag{2.180}$$

By comparing the two equations [Eq. (2.179) and Eq. (2.180)], the frequency-dependent linear response dipole moment is

$$\mu_y^{(1)}(\omega) = \alpha_{yz}(\omega)\mathcal{E}_z(\omega) \,. \tag{2.181}$$

Therefore the frequency-dependent polarizability is given by

$$\alpha_{yz}(\omega) = \frac{\mu_y^{(1)}(\omega)}{\mathcal{E}_z(\omega)} \,. \tag{2.182}$$

Substituting Eq. (2.174) (i.e. the linear response of the dipole moment) into the above equation [Eq. (2.182)], the dynamic polarizability (y,z)–component can be rewritten as

$$\alpha_{yz}(\omega) = -\sum_{pq\sigma} \frac{y_{pq\sigma} P^{(1)}_{qp\sigma}(\omega)}{\mathcal{E}_z(\omega)} \tag{2.183}$$

or inserting Eq. (2.175) into Eq. (2.182), the dynamic polarizability (y,z)-component is

$$\begin{aligned} \alpha_{yz}(\omega) &= \frac{-\sum_{pq\sigma}\sum_{sr\tau} y_{pq\sigma}\chi_{qp\sigma,sr\tau}(\omega) z_{sr\tau}\mathcal{E}_z(\omega)}{\mathcal{E}_z(\omega)} \\ &= \sum_k \frac{2\omega_{kn}\langle\Psi_n^{(0)}|\hat{y}|\Psi_k^{(0)}\rangle\langle\Psi_k^{(0)}|\hat{z}|\Psi_n^{(0)}\rangle}{\omega_{kn}^2 - \omega^2} \,, \end{aligned} \tag{2.184}$$

where the generalized susceptibility $\chi_{pq\sigma,sr\tau}$ is replaced by Eq. (2.171), the infinitesimal ξ has been set to zero, and the expression

$$\langle\Psi_n|\hat{y}|\Psi_k\rangle\langle\Psi_k|\hat{z}|\Psi_n\rangle = \langle\Psi_n|\hat{z}|\Psi_k\rangle\langle\Psi_k|\hat{y}|\Psi_n\rangle \tag{2.185}$$

has been used in the above derivation (i.e. the matrix elements are assumed to be real). The mean polarizability $\bar{\alpha}$ is given by

$$\begin{aligned} \bar{\alpha}(\omega) &= \frac{1}{3}[\alpha_{xx}(\omega) + \alpha_{yy}(\omega) + \alpha_{zz}(\omega)] \\ &= \sum_k \frac{f_k}{\omega_{kn}^2 - \omega^2} \end{aligned} \tag{2.186}$$

where the poles are excitation energies,

$$\omega_{kn} = E_k - E_n \tag{2.187}$$

and the residues are the oscillator strengths,

$$f_k = \frac{2}{3}\omega_{kn}[|\langle\Psi_n|\hat{x}|\Psi_k\rangle|^2 + |\langle\Psi_n|\hat{y}|\Psi_k\rangle|^2 + |\langle\Psi_n|\hat{z}|\Psi_k\rangle|^2]\,. \tag{2.188}$$

Eq. (2.186) is the famous sum-over-states (SOS) theorem of optics which is the basis for extracting excitation spectra from time-dependent DFT.

2.6 TIME-DEPENDENT DENSITY-FUNCTIONAL RESPONSE THEORY

Time-dependent density–functional response theory (DFRT) is an important tool for calculating excitation spectra [29, 207, 328, 329]. A detailed description of how to calculate excitation energies and oscillator strengths for open–shell molecules by the time–dependent DFRT are given in this section.

In the time-dependent response theory section, the linear response of the density matrix was obtained as

$$P^{(1)}_{qp\sigma}(\omega) = \sum_{sr\tau} \chi_{qp\sigma,sr\tau}(\omega) H'_{sr\tau}(\omega)\,. \tag{2.189}$$

where the generalized susceptibility is

$$\begin{aligned}\chi_{qp\sigma,sr\tau}(\omega) &= \sum_k \{ \frac{\langle\Psi^{(0)}_n|\hat{p}^+_\sigma\hat{q}_\sigma|\Psi^{(0)}_k\rangle\langle\Psi^{(0)}_k|\hat{s}^+_\tau\hat{r}_\tau|\Psi^{(0)}_n\rangle}{\omega - \omega_{kn} + i\xi} \\ &- \frac{\langle\Psi^{(0)}_n|\hat{s}^+_\tau\hat{r}_\tau|\Psi^{(0)}_k\rangle\langle\Psi^{(0)}_k|\hat{p}^+_\sigma\hat{q}_\sigma|\Psi^{(0)}_n\rangle}{\omega + \omega_{kn} + i\xi} \}\,.\end{aligned} \tag{2.190}$$

Since the Kohn-Sham equation has a quasi–independent particle nature, it is convenient to begin with a discussion of the linear response of the density matrix for an independent particle system.

For such a single particle system, the initial ground state wave function $\Psi_n^{(0)} = \psi_{i\nu}$ and corresponding energy $E_n = \varepsilon_{i\nu}$ satisfy the Schrödinger equation

$$\hat{h}\psi_{i\nu} = \varepsilon_{i\nu}\psi_{i\nu} \,. \tag{2.191}$$

In this special case, the generalized susceptibility is just

$$\begin{aligned} \chi_{qp\sigma,sr\tau}(\omega) &= \sum_{k,\sigma'}\{\frac{\langle\psi_{i\nu}|\hat{p}_\sigma^+\hat{q}_\sigma|\psi_{k\sigma'}\rangle\langle\psi_{k\sigma'}|\hat{s}_\tau^+\hat{r}_\tau|\psi_{i\nu}\rangle}{\omega - \omega_{k\sigma',i\nu} + i\xi} \\ &- \frac{\langle\psi_{i\nu}|\hat{s}_\tau^+\hat{r}_\tau|\psi_{k\sigma'}\rangle\langle\psi_{k\sigma'}|\hat{p}_\sigma^+\hat{q}_\sigma|\psi_{i\nu}\rangle}{\omega + \omega_{k\sigma',i\nu} + i\xi}\} \,. \end{aligned} \tag{2.192}$$

After some mathematics, the single particle generalized susceptibility simplifies to

$$\chi_{qp\sigma,sr\tau}(\omega) = \frac{\delta_{\sigma\nu}\delta_{\sigma\tau}\delta_{qs}\delta_{pr}}{\omega - \omega_{q\sigma,p\sigma} + i\xi}(\delta_{pi} - \delta_{qi}) \tag{2.193}$$

where $\omega_{q\sigma,p\sigma} = \varepsilon_{q\sigma} - \varepsilon_{p\sigma}$.

This single particle generalized susceptibility can be generalized to a system of many independent particles. Since the occupation number $n_{i\nu}$ of each orbital indicates the portion of the contribution to the generalized susceptibility from each orbital, the $\chi_{pq\sigma,sr\tau}(\omega)$ of the system with many independent particles is the sum of each orbital's contribution to the generalized susceptibility,

$$\begin{aligned} \chi_{qp\sigma,sr\tau}(\omega) &= \sum_{i\nu} n_{i\nu}\frac{\delta_{\sigma\nu}\delta_{\sigma\tau}\delta_{qs}\delta_{pr}}{\omega - \omega_{q\sigma,p\sigma} + i\xi}(\delta_{pi} - \delta_{qi}) \\ &= \frac{\delta_{\sigma\tau}\delta_{qs}\delta_{pr}}{\omega - \omega_{q\sigma,p\sigma} + i\xi}(n_{p\sigma} - n_{q\sigma}) \end{aligned} \tag{2.194}$$

The nature of the quasi-independent particles of the Kohn-Sham equation permits one to use the linear response of the density matrix of the independent particle system (or the generalized susceptibility of the independent particle system). However there is now an effective perturbation $\hat{H}'^{eff}$ which contains both the applied perturbation $\hat{H}'$ and the linear response of the self-consistent field $v^{(1)SCF}$ induced by the response of the charge density. The linear response of the

Kohn-Sham density matrix is

$$\begin{aligned} P^{(1)}_{qp\sigma}(\omega) &= \sum_{sr\tau} \chi_{qp\sigma,sr\tau}(\omega) H'^{eff}_{sr\tau}(\omega) \\ &= \sum_{sr\tau} \frac{\delta_{\sigma\tau}\delta_{qs}\delta_{pr}}{\omega - \omega_{q\sigma,p\sigma} + i\xi}(n_{p\sigma} - n_{q\sigma}) H'^{eff}_{sr\tau}(\omega) \\ &= \frac{n_{p\sigma} - n_{q\sigma}}{\omega - \omega_{q\sigma,p\sigma}} H'^{eff}_{qp\sigma}(\omega) \end{aligned} \tag{2.195}$$

where the generalized susceptibility of the many independent–particle system has been used, the infinitesimal ξ has been set to zero and the effective perturbation is

$$\hat{H}'^{eff}(\mathbf{r},t) = \hat{H}'(\mathbf{r},t) + v^{(1)SCF}(\mathbf{r},t)\,. \tag{2.196}$$

Although Eq. (2.195) does not give the correct response of the true density matrix, it does give the correct response of the charge density which is enough to be able to treat many properties.

The first order of the self-consistent field $v^{(1)SCF}$ is related to the linear response of the density matrix $P^{(1)}_{qp\sigma}(\omega)$ by the coupling matrix $K_{qp\sigma,sr\tau}(\omega)$,

$$v^{(1)SCF}_{qp\sigma}(\omega) = \sum_{sr\tau} K_{qp\sigma,sr\tau}(\omega) P^{(1)}_{sr\tau}(\omega)\,. \tag{2.197}$$

Therefore the coupling matrix is given by

$$\begin{aligned} K_{qp\sigma,sr\tau}(\omega) &= \frac{\partial v^{SCF}_{qp\sigma}(\omega)}{\partial P_{sr\tau}(\omega)} \\ &= \int_{-\infty}^{\infty} d(t-t')exp[i\omega(t-t')] \frac{\partial v^{SCF}_{qp\sigma}(t)}{\partial P_{sr\tau}(t')}\,. \end{aligned} \tag{2.198}$$

The self-consistent potential is a functional of the charge density. According to the chain rule, the above equation can be rewritten as

$$K_{qp\sigma,sr\tau}(\omega) = \int_{-\infty}^{\infty} d(t-t')exp[i\omega(t-t')]\{\sum_{\gamma} \int d\mathbf{r}' \int dt'' \frac{\delta v^{SCF}_{qp\sigma}(t)}{\delta n_\gamma(\mathbf{r}',t'')} \frac{\partial n_\gamma(\mathbf{r}',t'')}{\partial P_{sr\tau}(t')}\}\,. \tag{2.199}$$

From the time-dependent density-functional theory section, the self-consistent potential consists of the Coulomb potential and the exchange-correlation potential

[Eq. (2.145)],

$$\begin{aligned}\frac{\delta v_{qp\sigma}^{SCF}(t)}{\delta n_\gamma(\mathbf{r}',t'')} &= \frac{\delta}{\delta n_\gamma(\mathbf{r}',t'')}\left(\int d\mathbf{r}'\frac{n_\sigma(\mathbf{r}',t)}{|\mathbf{r}-\mathbf{r}'|}+v_{xc}^{\sigma}(\mathbf{r},t)\right)\\ &= \left(\frac{\delta(t''-t)\delta_{\sigma\gamma}}{|\mathbf{r}-\mathbf{r}'|}+\frac{\delta v_{xc}^{\sigma}(\mathbf{r},t)}{\delta n_\gamma(\mathbf{r}',t'')}\right). \qquad (2.200)\end{aligned}$$

The relation between the charge density and the density matrix

$$n_\tau(\mathbf{r}',t') = \sum_s\sum_r P_{sr\tau}(\mathbf{r}',t')\psi_{r\tau}^*(\mathbf{r}')\psi_{s\tau}(\mathbf{r}'), \qquad (2.201)$$

is used to obtain the derivative of the charge density with respect to the density matrix,

$$\frac{\partial n_\gamma(\mathbf{r}'t'')}{\partial P_{sr\tau}(t')} = \delta(t''-t')\delta_{\gamma\tau}\psi_{r\tau}^*(\mathbf{r}')\psi_{s\tau}(\mathbf{r}'). \qquad (2.202)$$

Substituting Eq. (2.200) and Eq. (2.202) into Eq. (2.199), the coupling matrix becomes

$$\begin{aligned}K_{qp\sigma,sr\tau}(\omega) = &\int_{-\infty}^{\infty} d(t-t')exp[i\omega(t-t')]\{\int d\mathbf{r}\int d\mathbf{r}'\frac{\psi_{q\sigma}^*(\mathbf{r})\psi_{r\tau}^*(\mathbf{r}')\psi_{s\tau}(\mathbf{r}')\psi_{p\sigma}(\mathbf{r})}{|\mathbf{r}-\mathbf{r}'|}\\ &+\int d\mathbf{r}\int d\mathbf{r}'\psi_{q\sigma}^*(\mathbf{r})\psi_{r\tau}^*(\mathbf{r}')\frac{\delta v_{xc}^{\sigma}(\mathbf{r},t)}{\delta n_\tau(\mathbf{r}',t')}\psi_{p\sigma}(\mathbf{r})\psi_{s\tau}(\mathbf{r}')\}, \qquad (2.203)\end{aligned}$$

where the time-dependent exchange-correlation potential in the adiabatic approximation is

$$\begin{aligned}v_{xc}(\mathbf{r},t) &= \frac{\delta A_{xc}[n]}{\delta n(\mathbf{r},t)}\\ &= \frac{\delta E_{xc}[n_t]}{\delta n_t(\mathbf{r})}. \qquad (2.204)\end{aligned}$$

Hence, the derivative of the time-dependent exchange-correlation potential with respect to the charge density can be evaluated as

$$\begin{aligned}\frac{\delta v_{xc}^{\sigma}(\mathbf{r},t)}{\delta n_\tau(\mathbf{r}',t')} &= \frac{\delta^2 E_{xc}[n_\sigma(\mathbf{r},t)]}{\delta n_\sigma(\mathbf{r},t)\delta n_\tau(\mathbf{r}',t')}\\ &= \frac{\delta^2 E_{xc}[n_\sigma(\mathbf{r})]}{\delta n_\sigma(\mathbf{r})\delta n_\tau(\mathbf{r}')}\delta(t-t'). \qquad (2.205)\end{aligned}$$

This makes the coupling matrix in the adiabatic approximation independent of omega. It is obvious that the coupling matrix has the following symmetry properties,

$$K_{qp\sigma,sr\tau}(\omega) = K_{pq\sigma,sr\tau}(\omega) = K_{pq\sigma,rs\tau}(\omega) = K_{qp\sigma,rs\tau}(\omega), \qquad (2.206)$$

and

$$K_{qp\sigma,sr\tau}(\omega) = [K_{sr\tau,qp\sigma}(-\omega)]^* . \tag{2.207}$$

Note that the minus omega comes from the Fourier transform.

If one inserts the coupling matrix [Eq. (2.197)] with Eq. (2.196) into the density matrix [Eq. (2.195)], one gets

$$\begin{aligned} \frac{\omega - \omega_{q\sigma,p\sigma}}{n_{p\sigma} - n_{q\sigma}} P^{(1)}_{qp\sigma}(\omega) &= H'_{qp\sigma}(\omega) + v^{(1)SCF}_{qp\sigma} \\ &= H'_{qp\sigma}(\omega) + \sum_{sr\tau} K_{qp\sigma,sr\tau}(\omega) P^{(1)}_{sr\tau}(\omega) . \end{aligned} \tag{2.208}$$

By reordering the above equation, the density matrix can be rewritten as

$$\begin{aligned} \frac{\omega - \omega_{q\sigma,p\sigma}}{n_{p\sigma} - n_{q\sigma}} P^{(1)}_{qp\sigma}(\omega) - \sum_{sr\tau} K_{qp\sigma,sr\tau}(\omega) P^{(1)}_{sr\tau}(\omega) &= H'_{qp\sigma}(\omega) \\ \sum_{sr\tau}^{n_{p\sigma}-n_{q\sigma}\neq 0} [\delta_{\sigma\tau}\delta_{qs}\delta_{pr} \frac{\omega - \omega_{q\sigma,p\sigma}}{n_{p\sigma} - n_{q\sigma}} - K_{qp\sigma,sr\tau}(\omega)] P^{(1)}_{sr\tau}(\omega) &= H'_{qp\sigma}(\omega) . \end{aligned} \tag{2.209}$$

This density matrix (or the applied perturbation matrix) includes both the particle-hole ($n_{q\sigma} > n_{p\sigma}$) and the hole-particle ($n_{q\sigma} < n_{p\sigma}$) elements if the orbitals are ordered like $q < p$ ($n_{q\sigma} \geq n_{p\sigma}$). This equation, however, can be separated into two parts, the particle-hole and hole-particle equations of the applied perturbation matrix. For the particle-hole part of the applied perturbation $H'_{qp\sigma}(\omega)$ ($n_{q\sigma} > n_{p\sigma}$), the equation is

$$\begin{aligned} H'_{qp\sigma}(\omega) &= \sum_{sr\tau}^{n_{s\tau}-n_{r\tau}>0} [\delta_{\sigma\tau}\delta_{qs}\delta_{pr} \frac{\omega - \omega_{s\sigma,r\sigma}}{n_{r\sigma} - n_{s\sigma}} - K_{qp\sigma,sr\tau}(\omega)] P^{(1)}_{sr\tau}(\omega) \\ &\quad + \sum_{sr\tau}^{n_{s\tau}-n_{r\tau}<0} [\delta_{\sigma\tau}\delta_{qs}\delta_{pr} \frac{\omega - \omega_{s\sigma,r\sigma}}{n_{r\sigma} - n_{s\sigma}} - K_{qp\sigma,sr\tau}(\omega)] P^{(1)}_{sr\tau}(\omega) \\ &= \sum_{sr\tau}^{n_{s\tau}-n_{r\tau}>0} [\delta_{\sigma\tau}\delta_{qs}\delta_{pr} \frac{\omega - \omega_{s\sigma,r\sigma}}{n_{r\sigma} - n_{s\sigma}} - K_{qp\sigma,sr\tau}(\omega)] P^{(1)}_{sr\tau}(\omega) \\ &\quad + \sum_{sr\tau}^{n_{s\tau}-n_{r\tau}>0} [\delta_{\sigma\tau}\delta_{qr}\delta_{ps} \frac{\omega - \omega_{s\sigma,r\sigma}}{n_{r\sigma} - n_{s\sigma}} - K_{qp\sigma,rs\tau}(\omega)] P^{(1)}_{rs\tau}(\omega) \\ &= \sum_{sr\tau}^{n_{s\tau}-n_{r\tau}>0} [\delta_{\sigma\tau}\delta_{qs}\delta_{pr} \frac{\omega - \omega_{s\sigma,r\sigma}}{n_{r\sigma} - n_{s\sigma}} - K_{qp\sigma,sr\tau}(\omega)] P^{(1)}_{sr\tau}(\omega) \\ &\quad - \sum_{sr\tau}^{n_{s\tau}-n_{r\tau}>0} K_{qp\sigma,rs\tau}(\omega) P^{(1)}_{rs\tau}(\omega) . \end{aligned} \tag{2.210}$$

In the last step of the derivation of the above equation, $\delta_{qr} = 0$ and $\delta_{ps} = 0$ are used. Since $n_{q\sigma} > n_{p\sigma}$ and $n_{s\tau} > n_{r\tau}$, the q orbital and the s orbital are occupied and the p orbital and the r orbital are unoccupied. Therefore, the q and the r will not be the same, so $\delta_{qr} = 0$ and $\delta_{ps} = 0$. For the hole-particle part, the equation is

$$\begin{aligned} H'_{pq\sigma}(\omega) &= \sum_{s\tau}^{n_{s\tau}-n_{r\tau}>0} [\delta_{\sigma\tau}\delta_{qs}\delta_{pr}\frac{\omega-\omega_{r\sigma,s\sigma}}{n_{s\sigma}-n_{r\sigma}} - K_{pq\sigma,rs\tau}(\omega)]P^{(1)}_{rs\tau}(\omega) \\ &\quad + \sum_{s\tau}^{n_{s\tau}-n_{r\tau}<0} [\delta_{\sigma\tau}\delta_{qs}\delta_{pr}\frac{\omega-\omega_{r\sigma,s\sigma}}{n_{s\sigma}-n_{r\sigma}} - K_{pq\sigma,rs\tau}(\omega)]P^{(1)}_{rs\tau}(\omega) \\ &= \sum_{s\tau}^{n_{s\tau}-n_{r\tau}>0} [\delta_{\sigma\tau}\delta_{qs}\delta_{pr}\frac{\omega-\omega_{r\sigma,s\sigma}}{n_{s\sigma}-n_{r\sigma}} - K_{pq\sigma,rs\tau}(\omega)]P^{(1)}_{rs\tau}(\omega) \\ &\quad + \sum_{s\tau}^{n_{s\tau}-n_{r\tau}>0} [\delta_{\sigma\tau}\delta_{qr}\delta_{ps}\frac{\omega-\omega_{s\sigma,r\sigma}}{n_{r\sigma}-n_{s\sigma}} - K_{pq\sigma,sr\tau}(\omega)]P^{(1)}_{sr\tau}(\omega) \\ &= \sum_{s\tau}^{n_{s\tau}-n_{r\tau}>0} [\delta_{\sigma\tau}\delta_{qs}\delta_{pr}\frac{\omega-\omega_{r\sigma,s\sigma}}{n_{s\sigma}-n_{r\sigma}} - K_{pq\sigma,rs\tau}(\omega)]P^{(1)}_{rs\tau}(\omega) \\ &\quad - \sum_{s\tau}^{n_{s\tau}-n_{r\tau}>0} K_{pq\sigma,sr\tau}(\omega)]P^{(1)}_{sr\tau}(\omega)\,. \end{aligned} \tag{2.211}$$

Combining the particle–hole [Eq. (2.210)] and the hole–particle [Eq. (2.211)] of the two equations, one gets a single matrix equation,

$$\begin{aligned} &\left\{ \begin{pmatrix} \mathcal{A}(\omega) & \mathcal{B}(\omega) \\ \mathcal{B}(\omega) & \mathcal{A}(\omega) \end{pmatrix} - \omega \begin{pmatrix} \mathcal{C}(\omega) & 0 \\ 0 & -\mathcal{C}(\omega) \end{pmatrix} \right\} \begin{pmatrix} \mathbf{P}^{(1)}(\omega) \\ \mathbf{P}^{*(1)}(\omega) \end{pmatrix} \\ &= \begin{pmatrix} \mathbf{H}'(\omega) \\ \mathbf{H}^{*\prime}(\omega) \end{pmatrix}, \end{aligned} \tag{2.212}$$

where

$$\mathcal{A}_{qp\sigma,sr\tau} = \delta_{\sigma\tau}\delta_{qs}\delta_{pr}\frac{\omega_{s\tau,r\tau}}{n_{s\tau}-n_{r\tau}} - K_{qp\sigma,sr\tau}(\omega)\,, \tag{2.213}$$

$$\mathcal{B}_{qp\sigma,sr\tau} = -K_{qp\sigma,rs\tau}(\omega)\,, \tag{2.214}$$

and

$$\mathcal{C}_{qp\sigma,sr\tau} = \frac{\delta_{\sigma\tau}\delta_{qs}\delta_{pr}}{n_{s\tau}-n_{r\tau}}\,. \tag{2.215}$$

The linear response of the density matrix contains real and imaginary parts; the real part is used to calculate response properties (i.e. polarizabilities, excitation energies). In order to separate the real and the imaginary parts of the linear

response of the density matrix, it is necessary to do a unitary transformation of the matrix equation [Eq. (2.212)] yielding the form,

$$\left\{\begin{pmatrix} \mathcal{A}+\mathcal{B} & 0 \\ 0 & \mathcal{A}-\mathcal{B} \end{pmatrix} - \omega \begin{pmatrix} 0 & -\mathcal{C} \\ -\mathcal{C} & 0 \end{pmatrix}\right\} \begin{pmatrix} \mathbf{P}^{(1)}+\mathbf{P}^{(1)*} \\ -\mathbf{P}^{(1)}+\mathbf{P}^{(1)*} \end{pmatrix} = \begin{pmatrix} \mathbf{H}'+\mathbf{H}'^{*} \\ -\mathbf{H}'+\mathbf{H}'^{*} \end{pmatrix} . \tag{2.216}$$

If the linear response of the density matrix $\mathbf{P}^{(1)}$ is written in terms of the real (Rel) and imaginary (Img) parts, and similarly for the applied perturbation $\mathbf{H}'$, then the above equation can be rewritten as

$$\begin{pmatrix} \mathcal{A}+\mathcal{B} & \omega\mathcal{C} \\ \omega\mathcal{C} & \mathcal{A}-\mathcal{B} \end{pmatrix} \begin{pmatrix} \mathsf{Rel}\mathbf{P}^{(1)} \\ -i\mathsf{Img}\mathbf{P}^{(1)} \end{pmatrix} = \begin{pmatrix} \mathsf{Rel}\mathbf{H}' \\ -i\mathsf{Img}\mathbf{H}' \end{pmatrix} . \tag{2.217}$$

Separating the above matrix equation [Eq. (2.217)] into two equations gives

$$(\mathcal{A}+\mathcal{B})\mathsf{Rel}\mathbf{P}^{(1)} - i\omega\mathcal{C}\mathsf{Img}\mathbf{P}^{(1)} = \mathsf{Rel}\mathbf{H}' \tag{2.218}$$

and

$$\omega\mathcal{C}\mathsf{Rel}\mathbf{P}^{(1)} - i(\mathcal{A}-\mathcal{B})\mathsf{Img}\mathbf{P}^{(1)} = -i\mathsf{Img}\mathbf{H}' . \tag{2.219}$$

with some algebra, one can separate the equations for the real and imaginary parts of the linear response of the density matrix ($\mathbf{P}^{(1)}$). The real part of $\mathbf{P}^{(1)}$ is

$$[(\mathcal{A}+\mathcal{B}) - \omega^2\mathcal{C}(\mathcal{A}-\mathcal{B})^{-1}\mathcal{C}]\mathsf{Rel}\mathbf{P}^{(1)} = \mathsf{Rel}\mathbf{H}' + i\omega\mathcal{C}(\mathcal{A}+\mathcal{B})^{-1}\mathsf{Img}\mathbf{H}' \tag{2.220}$$

and the imaginary part of $\mathbf{P}^{(1)}$ is

$$[(\mathcal{A}-\mathcal{B}) - \omega^2\mathcal{C}(\mathcal{A}+\mathcal{B})^{-1}\mathcal{C}]\mathsf{Img}\mathbf{P}^{(1)} = \mathsf{Img}\mathbf{H}' - i\omega\mathcal{C}(\mathcal{A}+\mathcal{B})^{-1}\mathsf{Rel}\mathbf{H}' . \tag{2.221}$$

If the applied perturbation is real (e.g. an electric field), the imaginary part of the applied perturbation is zero ($\mathsf{Img}\mathbf{H}' = 0$). Then the real part of the linear response of the density matrix can be obtained as

$$\mathsf{Rel}\mathbf{P}^{(1)} = [(\mathcal{A}+\mathcal{B}) - \omega^2\mathcal{C}(\mathcal{A}-\mathcal{B})^{-1}\mathcal{C}]^{-1}\mathsf{Rel}\mathbf{H}' , \tag{2.222}$$

This real part of the linear response of the density matrix can be rewritten as

$$\mathsf{Rel}\mathbf{P}^{(1)} = [(\mathcal{A}+\mathcal{B}) + \omega^2\mathcal{S}]^{-1}\mathsf{Rel}\mathbf{H}'$$

$$
\begin{aligned}
&= [(\mathcal{A}+\mathcal{B})+\mathcal{S}^{1/2}\omega^2\mathcal{S}^{1/2}]^{-1}\mathsf{Rel}\mathbf{H}^{'} \\
&= [\mathcal{S}^{1/2}\mathcal{S}^{-1/2}(\mathcal{A}+\mathcal{B})\mathcal{S}^{-1/2}\mathcal{S}^{1/2}+\mathcal{S}^{1/2}\omega^2\mathcal{S}^{1/2}]^{-1}\mathsf{Rel}\mathbf{H}^{'} \\
&= \mathcal{S}^{-1/2}(\omega^2-\Omega)^{-1}\mathcal{S}^{-1/2}\mathsf{Rel}\mathbf{H}^{'}\,, \qquad (2.223)
\end{aligned}
$$

with

$$\mathcal{S} = -\mathcal{C}(\mathcal{A}-\mathcal{B})^{-1}\mathcal{C}\,, \qquad (2.224)$$

and

$$\Omega = -\mathcal{S}^{-1/2}(\mathcal{A}+\mathcal{B})\mathcal{S}^{-1/2}\,, \qquad (2.225)$$

The real part of the linear response of the density matrix is used in the response property calculations, such as dynamic polarizabilities. In the dynamic polarizability expression [Eq. (2.183) and Eq. (2.184)], since the coordinates ($y_{pq\sigma}$, $z_{sr\tau}$), electric field ($\mathcal{E}$), and the generalized susceptibility [$\chi_{qp\sigma,sr\tau}(\omega)$, see Eq. (2.193)] are real, then, the linear response of the density matrix ($P^{(1)}_{qp\sigma}(\omega)$) in Eq. (2.183) must also be real [compare Eq. (2.183) and Eq. (2.184)]. Thus dynamic polarizability is only related to the real part of the linear response of the density matrix [$\mathsf{RelP}^{(1)}(\omega)$] and Eq. (2.183) can be rewritten as

$$\alpha_{yz}(\omega) = -\sum_{pq\sigma}\frac{y_{pq\sigma}RelP^{(1)}_{qp\sigma}(\omega)}{\mathcal{E}_z(\omega)}\,. \qquad (2.226)$$

Inserting the $\mathsf{Rel}P^{(1)}_{qp\sigma}(\omega)$ [Eq. (2.223)] into the above equation [Eq. (2.226)]

$$
\begin{aligned}
\alpha_{yz}(\omega) &= -\sum_{pq\sigma} y_{pq\sigma}\mathcal{S}^{-1/2}_{qp\sigma}(\omega^2-\Omega_{qp\sigma})^{-1}\mathcal{S}^{-1/2}_{qp\sigma}\frac{\mathsf{Rel}\mathbf{H}^{'}_{qp\sigma}}{\mathcal{E}_z(\omega)} \\
&= -2\sum_{p>q,\sigma} y_{pq\sigma}\mathcal{S}^{-1/2}_{qp\sigma}(\omega^2-\Omega_{qp\sigma})^{-1}\mathcal{S}^{-1/2}_{qp\sigma}\frac{\mathsf{Rel}\mathbf{H}^{'}_{qp\sigma}}{\mathcal{E}_z(\omega)}\,. \qquad (2.227)
\end{aligned}
$$

In Eq. (2.184), knowing that the pole of the polarizability $\alpha_{yz}(\omega)$ is the excitation energy, and comparing Eq. (2.227) with Eq. (2.184), it is seen that the excitation energies may be calculated from the equation,

$$\Omega(\omega)\mathbf{F}_K = \omega^2_K\mathbf{F}_K\,, \qquad (2.228)$$

where ω_K is an excitation energy, and Ω is defined in Eq. (2.225). Its explicit expression in time-dependent density-functional theory is given by

$$\begin{aligned}\Omega_{qp\sigma,sr\tau}(\omega) &= -\sum_{q'p'\sigma',s'r'\tau'} \mathcal{S}^{-1/2}_{qp\sigma,q'p'\sigma'}(\mathcal{A}+\mathcal{B})_{q'p'\sigma',s'r'\tau'}\mathcal{S}^{-1/2}_{s'r'\tau',sr\tau} \\ &= \delta_{qs}\delta_{pr}\delta_{\sigma\tau}\omega^2_{r\tau,s\tau} \\ &\quad +2\sqrt{(n_{q\sigma}-n_{p\sigma})\omega_{p\sigma,q\sigma}}K_{qp\sigma,sr\tau}(\omega)\sqrt{(n_{s\tau}-n_{r\tau})\omega_{r\tau,s\tau}} \quad (2.229)\end{aligned}$$

and the $\mathbf{S}$ is given by

$$S_{qp\sigma,sr\tau} = \frac{\delta_{\sigma\tau}\delta_{qs}\delta_{pr}}{(n_{s\tau}-n_{r\tau})\omega_{r\tau,s\tau}}\,. \quad (2.230)$$

In the adiabatic approximation, K and Ω are ω–independent. By diagonalizing the Ω matrix, the excitation energies are obtained. The eigenvectors F_k in Eq. (2.228) can be normalized by multiplying $F_k^\dagger$ and taking the summation on both sides of the equation,

$$\Omega(\omega)\sum_K \mathbf{F}_K\mathbf{F}_K^\dagger = \sum_K \omega_K^2\mathbf{F}_K\mathbf{F}_K^\dagger\,. \quad (2.231)$$

Since $\sum_K \mathbf{F}_K\mathbf{F}_K^\dagger = 1$, then

$$\Omega(\omega) = \sum_K \omega_K^2\mathbf{F}_K\mathbf{F}_K^\dagger\,. \quad (2.232)$$

Subtracting both sides of the equation from ω^2, gives

$$\omega^2 - \Omega(\omega) = \sum_K(\omega^2-\omega_K^2)\mathbf{F}_K\mathbf{F}_K^\dagger\,. \quad (2.233)$$

If the vector F_K is not normalized, the normalization factor R_K is introduced into the above equation,

$$\omega^2 - \Omega(\omega) = \sum_K(\omega^2-\omega_K^2)\frac{\mathbf{F}_K\mathbf{F}_K^\dagger}{R_K}\,. \quad (2.234)$$

It follows that

$$[\omega^2 - \Omega(\omega)]^{-1} = \sum_K(\omega^2-\omega_K^2)^{-1}R_K\mathbf{F}_K\mathbf{F}_K^\dagger\,. \quad (2.235)$$

Rearranging the above equation, the normalization factor R_K is given by

$$R_K^{-1} = \mathbf{F}_K^\dagger\frac{\omega^2-\Omega(\omega)}{\omega^2-\omega_K^2}\mathbf{F}_K\,. \quad (2.236)$$

In the limit ($\omega = \omega_K$), the Eq. (2.236) can be rewritten as

$$\begin{aligned} R_K^{-1} &= \lim_{\omega \to \omega_K} \mathbf{F}_K^{\dagger} \frac{\omega^2 - \Omega(\omega)}{\omega^2 - \omega_K^2} \mathbf{F}_K \\ &= \mathbf{F}_K^{\dagger} [\frac{\partial(\omega^2 - \Omega(\omega))}{\partial \omega^2}]_{\omega=\omega_K} \mathbf{F}_K \\ &= \mathbf{F}_K^{\dagger} \{1 - [\frac{\partial \Omega(\omega)}{\partial \omega^2}]_{\omega=\omega_K}\} \mathbf{F}_K \,. \end{aligned} \tag{2.237}$$

Inserting Eq. (2.235) and setting $\mathsf{Re}H'_{qp\sigma}(\omega) = z_{qp\sigma}\mathcal{E}_z(\omega)$ in Eq. (2.227), the polarizability can be rewritten as

$$\alpha_{yz}(\omega) = \sum_{pq\sigma} y_{pq\sigma} \mathcal{S}_{qp\sigma}^{-1/2} (\omega_{qp\sigma}^2 - \omega^2)^{-1} R_K \mathbf{F}_K \mathbf{F}_K^{\dagger} \mathcal{S}_{qp\sigma}^{-1/2} z_{qp\sigma} \,. \tag{2.238}$$

By comparing this equation with the sum over states polarizability expression Eq. (2.184), the following equation holds,

$$\sum_{pq\sigma} y_{pq\sigma} \mathcal{S}_{qp\sigma}^{-1/2} R_K^{1/2} \mathbf{F}_K = \omega_{kn}^{1/2} \langle \Psi_n^{(0)} | \hat{y} | \Psi_k^{(0)} \rangle \,. \tag{2.239}$$

Substituting Eq. (2.239) into the oscillator strength expression Eq. (2.188) and similarly for the x and the z components, the oscillator strength is given by

$$f_K = \frac{2}{3} R_K (\sum_{pq\sigma} x_{pq\sigma} \mathcal{S}_{qp\sigma}^{-1/2} \mathbf{F}_K)^2 + (\sum_{pq\sigma} y_{pq\sigma} \mathcal{S}_{qp\sigma}^{-1/2} \mathbf{F}_K)^2 + (\sum_{pq\sigma} z_{pq\sigma} \mathcal{S}_{qp\sigma}^{-1/2} \mathbf{F}_k)^2 \,. \tag{2.240}$$

CHAPTER 3

NEW CONTRIBUTIONS TO THE PROGRAM *deMon–DynaRho*

deMon-DynaRho (**den**sité de **Mon**tréal–**Dyna**mic Response of **Rho**, Rho here stands for the charge density) has been developed as a post-*deMon–KS* program [29, 183]. The *deMon-DynaRho* program performs molecular time-dependent density-functional response theory (DFRT) calculations using multi-center Gaussian expansions and auxiliary basis functions. The program is based on the idea of extracting the poles and the residues of the dynamic polarizability, using a one-particle density matrix–based algorithm to calculate the excitation energies and oscillator strengths. It is also able to calculate dynamic polarizabilities. But all of these calculations were only available for closed-shell molecules prior to the present work. Since there are many interesting open-shell systems, such as simple metal clusters (lithium clusters and sodium clusters) with an odd number of atoms, free radicals, etc., calculations of excitation spectra and dynamic response properties are desired not only for closed-shell systems, but also for open-shell systems. For this reason, the time-dependent unrestricted DFRT has been modified for the open-shell case and implemented in the program, *deMon-DynaRho*, version 2pX, in the present study.

Applying time-dependent unrestricted DFRT to an open-shell system, spin α and spin β have to be treated explicitly. Hence *deMon–DynaRho* needs to be modified from the original program (version 2p0) for only the closed-shell systems to handle both α and β spins. This makes the construction of the Ω matrix (see

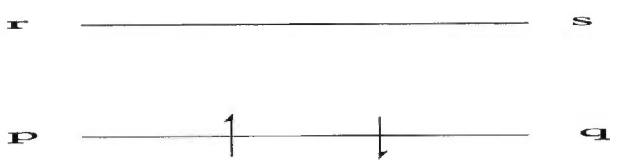

Figure 1. Two electron closed–shell configuration.

Chapter 2 of this thesis for details) more complicated than for the closed-shell case. For a two–electron closed-shell system (Fig. 1), the Ω matrix is a simple two by two matrix,

$$\begin{pmatrix} \Omega_{1,1} & \Omega_{1,2} \\ \Omega_{2,1} & \Omega_{2,2} \end{pmatrix} \tag{3.1}$$

where

$$\begin{aligned} \Omega_{1,1} &= \delta_{pq}\delta_{rs}\omega_{s,q}^2 + 2\sqrt{\omega_{r,p}}K_{pr\uparrow,qs\uparrow}\sqrt{\omega_{s,q}}\,, \\ \Omega_{1,2} &= 2\sqrt{\omega_{r,p}}K_{pr\uparrow,qs\downarrow}\sqrt{\omega_{s,q}}\,, \\ \Omega_{2,1} &= 2\sqrt{\omega_{r,p}}K_{pr\downarrow,qs\uparrow}\sqrt{\omega_{s,q}}\,, \\ \Omega_{2,2} &= \delta_{pq}\delta_{rs}\omega_{s,q}^2 + 2\sqrt{\omega_{r,p}}K_{pr\downarrow,qs\downarrow}\sqrt{\omega_{s,q}}\,, \end{aligned} \tag{3.2}$$

in which $\omega_{i,j} = \varepsilon_i - \varepsilon_j$. The Ω matrix is much more complicated for an open–shell system than for the closed–shell case. For example, for a simple three–electron system (Fig. 2), the Ω matrix becomes

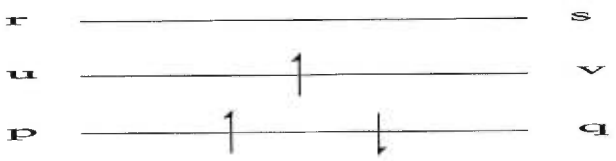

Figure 2. Three electron open–shell configuration.

$$\begin{pmatrix} \Omega_{1,1} & \Omega_{1,2} & \Omega_{1,3} & \Omega_{1,4} \\ \Omega_{2,1} & \Omega_{2,2} & \Omega_{2,3} & \Omega_{2,4} \\ \Omega_{3,1} & \Omega_{3,2} & \Omega_{3,3} & \Omega_{3,4} \\ \Omega_{4,1} & \Omega_{4,2} & \Omega_{4,3} & \Omega_{4,4} \end{pmatrix} \tag{3.3}$$

where

$$\Omega_{1,1} = \delta_{sr}\delta_{uv}\omega^2_{s\uparrow,v\uparrow} + 2\sqrt{\omega_{r\uparrow,u\uparrow}}K_{ur\uparrow,vs\uparrow}\sqrt{\omega_{s\uparrow,v\uparrow}}\,,$$

$$\Omega_{1,2} = 2\sqrt{\omega_{r\uparrow,u\uparrow}}K_{ur\uparrow,qv\downarrow}\sqrt{\omega_{v\downarrow,q\downarrow}}\,,$$

$$\Omega_{1,3} = 2\sqrt{\omega_{r\uparrow,u\uparrow}}K_{ur\uparrow,qs\uparrow}\sqrt{\omega_{s\uparrow,q\uparrow}}\,,$$

$$\Omega_{1,4} = 2\sqrt{\omega_{r\uparrow,u\uparrow}}K_{ur\uparrow,qs\downarrow}\sqrt{\omega_{s\downarrow,q\downarrow}}\,,$$

$$\Omega_{2,1} = 2\sqrt{\omega_{u\downarrow,p\downarrow}}K_{pu\downarrow,vs\uparrow}\sqrt{\omega_{s\uparrow,v\uparrow}}\,,$$

$$\Omega_{2,2} = \delta_{pq}\delta_{uv}\omega^2_{v\downarrow,q\downarrow} + 2\sqrt{\omega_{u\downarrow,p\downarrow}}K_{pu\downarrow,qv\downarrow}\sqrt{\omega_{v\downarrow,q\downarrow}}\,,$$

$$\Omega_{2,3} = 2\sqrt{\omega_{u\downarrow,p\downarrow}}K_{pu\downarrow,qs\uparrow}\sqrt{\omega_{s\uparrow,q\uparrow}}\,,$$

$$\Omega_{2,4} = 2\sqrt{\omega_{u\downarrow,p\downarrow}}K_{pu\downarrow,qs\downarrow}\sqrt{\omega_{s\downarrow,q\downarrow}}\,,$$

$$\Omega_{3,1} = 2\sqrt{\omega_{r\uparrow,p\uparrow}}K_{pr\uparrow,vs\uparrow}\sqrt{\omega_{s\uparrow,v\uparrow}}\,,$$

$$\Omega_{3,2} = 2\sqrt{\omega_{r\uparrow,p\uparrow}}K_{pr\uparrow,qv\downarrow}\sqrt{\omega_{v\downarrow,q\downarrow}}\,,$$

$$\Omega_{3,3} = \delta_{pq}\delta_{rs}\omega^2_{s\uparrow,q\uparrow} + 2\sqrt{\omega_{r\uparrow,p\uparrow}}K_{pr\uparrow,qs\uparrow}\sqrt{\omega_{s\uparrow,q\uparrow}}\,,$$

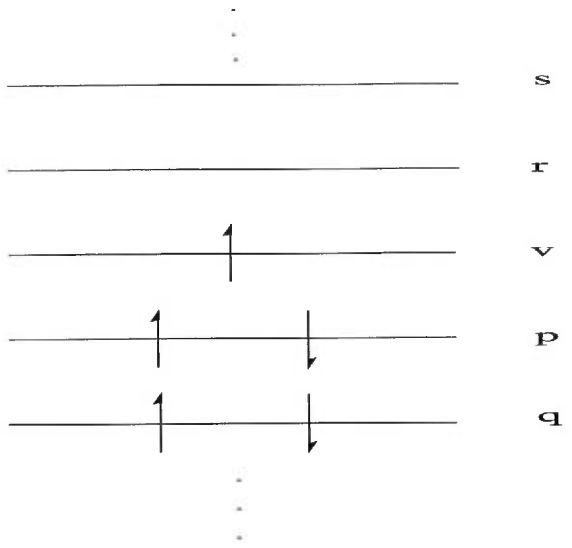

Figure 3. The open–shell system electron configuration with N electrons and one open-shell case.

$$\Omega_{3,4} = 2\sqrt{\omega_{r\uparrow,p\uparrow}}K_{pr\uparrow,qs\downarrow}\sqrt{\omega_{s\downarrow,q\downarrow}}\,,$$

$$\Omega_{4,1} = 2\sqrt{\omega_{r\downarrow,p\downarrow}}K_{pr\downarrow,vs\uparrow}\sqrt{\omega_{s\uparrow,v\uparrow}}\,,$$

$$\Omega_{4,2} = 2\sqrt{\omega_{r\downarrow,p\downarrow}}K_{pr\downarrow,qv\downarrow}\sqrt{\omega_{v\downarrow,q\downarrow}}\,,$$

$$\Omega_{4,3} = 2\sqrt{\omega_{r\downarrow,p\downarrow}}K_{pr\downarrow,qs\uparrow}\sqrt{\omega_{s\uparrow,q\uparrow}}\,,$$

$$\Omega_{4,4} = \delta_{pq}\delta_{rs}\omega^2_{s\downarrow,q\downarrow} + 2\sqrt{\omega_{r\downarrow,p\downarrow}}K_{pr\downarrow,qs\downarrow}\sqrt{\omega_{s\downarrow,q\downarrow}}\,, \tag{3.4}$$

where $\omega_{i\sigma,j\tau} = \varepsilon_{i\sigma} - \varepsilon_{j\tau}$. This Ω matrix can be generalized for an N electron open-shell system with one open-shell having the configuration shown in Fig. 3. The Ω matrix for this N electron one open-shell system can be written out explicitly as

$$\begin{pmatrix}
\Omega_{rv\uparrow,rv\uparrow} & \Omega_{rv\uparrow,sv\uparrow} & \Omega_{rv\uparrow,vp\downarrow} & \Omega_{rv\uparrow,vq\downarrow} & \Omega_{rv\uparrow,rp\uparrow} & \Omega_{rv\uparrow,rp\downarrow} & \Omega_{rv\uparrow,sp\uparrow} & \Omega_{rv\uparrow,sp\downarrow} & \Omega_{rv\uparrow,rq\uparrow} & \Omega_{rv\uparrow,rq\downarrow} & \Omega_{rv\uparrow,sq\uparrow} & \Omega_{rv\uparrow,sq\downarrow} \\
\Omega_{sv\uparrow,rv\uparrow} & \Omega_{sv\uparrow,sv\uparrow} & \Omega_{sv\uparrow,vp\downarrow} & \Omega_{sv\uparrow,vq\downarrow} & \Omega_{sv\uparrow,rp\uparrow} & \Omega_{sv\uparrow,rp\downarrow} & \Omega_{sv\uparrow,sp\uparrow} & \Omega_{sv\uparrow,sp\downarrow} & \Omega_{sv\uparrow,rq\uparrow} & \Omega_{sv\uparrow,rq\downarrow} & \Omega_{sv\uparrow,sq\uparrow} & \Omega_{sv\uparrow,sq\downarrow} \\
\Omega_{vp\downarrow,rv\uparrow} & \Omega_{vp\downarrow,sv\uparrow} & \Omega_{vp\downarrow,vp\downarrow} & \Omega_{vp\downarrow,vq\downarrow} & \Omega_{vp\downarrow,rp\uparrow} & \Omega_{vp\downarrow,rp\downarrow} & \Omega_{vp\downarrow,sp\uparrow} & \Omega_{vp\downarrow,sp\downarrow} & \Omega_{vp\downarrow,rq\uparrow} & \Omega_{vp\downarrow,rq\downarrow} & \Omega_{vp\downarrow,sq\uparrow} & \Omega_{vp\downarrow,sq\downarrow} \\
\Omega_{vq\downarrow,rv\uparrow} & \Omega_{vq\downarrow,sv\uparrow} & \Omega_{vq\downarrow,vp\downarrow} & \Omega_{vq\downarrow,vq\downarrow} & \Omega_{vq\downarrow,rp\uparrow} & \Omega_{vq\downarrow,rp\downarrow} & \Omega_{vq\downarrow,sp\uparrow} & \Omega_{vq\downarrow,sp\downarrow} & \Omega_{vq\downarrow,rq\uparrow} & \Omega_{vq\downarrow,rq\downarrow} & \Omega_{vq\downarrow,sq\uparrow} & \Omega_{vq\downarrow,sq\downarrow} \\
\Omega_{rp\uparrow,rv\uparrow} & \Omega_{rp\uparrow,sv\uparrow} & \Omega_{rp\uparrow,vp\downarrow} & \Omega_{rp\uparrow,vq\downarrow} & \Omega_{rp\uparrow,rp\uparrow} & \Omega_{rp\uparrow,rp\downarrow} & \Omega_{rp\uparrow,sp\uparrow} & \Omega_{rp\uparrow,sp\downarrow} & \Omega_{rp\uparrow,rq\uparrow} & \Omega_{rp\uparrow,rq\downarrow} & \Omega_{rp\uparrow,sq\uparrow} & \Omega_{rp\uparrow,sq\downarrow} \\
\Omega_{rp\downarrow,rv\uparrow} & \Omega_{rp\downarrow,sv\uparrow} & \Omega_{rp\downarrow,vp\downarrow} & \Omega_{rp\downarrow,vq\downarrow} & \Omega_{rp\downarrow,rp\uparrow} & \Omega_{rp\downarrow,rp\downarrow} & \Omega_{rp\downarrow,sp\uparrow} & \Omega_{rp\downarrow,sp\downarrow} & \Omega_{rp\downarrow,rq\uparrow} & \Omega_{rp\downarrow,rq\downarrow} & \Omega_{rp\downarrow,sq\uparrow} & \Omega_{rp\downarrow,sq\downarrow} \\
\Omega_{sp\uparrow,rv\uparrow} & \Omega_{sp\uparrow,sv\uparrow} & \Omega_{sp\uparrow,vp\downarrow} & \Omega_{sp\uparrow,vq\downarrow} & \Omega_{sp\uparrow,rp\uparrow} & \Omega_{sp\uparrow,rp\downarrow} & \Omega_{sp\uparrow,sp\uparrow} & \Omega_{sp\uparrow,sp\downarrow} & \Omega_{sp\uparrow,rq\uparrow} & \Omega_{sp\uparrow,rq\downarrow} & \Omega_{sp\uparrow,sq\uparrow} & \Omega_{sp\uparrow,sq\downarrow} \\
\Omega_{sp\downarrow,rv\uparrow} & \Omega_{sp\downarrow,sv\uparrow} & \Omega_{sp\downarrow,vp\downarrow} & \Omega_{sp\downarrow,vq\downarrow} & \Omega_{sp\downarrow,rp\uparrow} & \Omega_{sp\downarrow,rp\downarrow} & \Omega_{sp\downarrow,sp\uparrow} & \Omega_{sp\downarrow,sp\downarrow} & \Omega_{sp\downarrow,rq\uparrow} & \Omega_{sp\downarrow,rq\downarrow} & \Omega_{sp\downarrow,sq\uparrow} & \Omega_{sp\downarrow,sq\downarrow} \\
\Omega_{rq\uparrow,rv\uparrow} & \Omega_{rq\uparrow,sv\uparrow} & \Omega_{rq\uparrow,vp\downarrow} & \Omega_{rq\uparrow,vq\downarrow} & \Omega_{rq\uparrow,rp\uparrow} & \Omega_{rq\uparrow,rp\downarrow} & \Omega_{rq\uparrow,sp\uparrow} & \Omega_{rq\uparrow,sp\downarrow} & \Omega_{rq\uparrow,rq\uparrow} & \Omega_{rq\uparrow,rq\downarrow} & \Omega_{rq\uparrow,sq\uparrow} & \Omega_{rq\uparrow,sq\downarrow} \\
\Omega_{rq\downarrow,rv\uparrow} & \Omega_{rq\downarrow,sv\uparrow} & \Omega_{rq\downarrow,vp\downarrow} & \Omega_{rq\downarrow,vq\downarrow} & \Omega_{rq\downarrow,rp\uparrow} & \Omega_{rq\downarrow,rp\downarrow} & \Omega_{rq\downarrow,sp\uparrow} & \Omega_{rq\downarrow,sp\downarrow} & \Omega_{rq\downarrow,rq\uparrow} & \Omega_{rq\downarrow,rq\downarrow} & \Omega_{rq\downarrow,sq\uparrow} & \Omega_{rq\downarrow,sq\downarrow} \\
\Omega_{sq\uparrow,rv\uparrow} & \Omega_{sq\uparrow,sv\uparrow} & \Omega_{sq\uparrow,vp\downarrow} & \Omega_{sq\uparrow,vq\downarrow} & \Omega_{sq\uparrow,rp\uparrow} & \Omega_{sq\uparrow,rp\downarrow} & \Omega_{sq\uparrow,sp\uparrow} & \Omega_{sq\uparrow,sp\downarrow} & \Omega_{sq\uparrow,rq\uparrow} & \Omega_{sq\uparrow,rq\downarrow} & \Omega_{sq\uparrow,sq\uparrow} & \Omega_{sq\uparrow,sq\downarrow} \\
\Omega_{sq\downarrow,rv\uparrow} & \Omega_{sq\downarrow,sv\uparrow} & \Omega_{sq\downarrow,vp\downarrow} & \Omega_{sq\downarrow,vq\downarrow} & \Omega_{sq\downarrow,rp\uparrow} & \Omega_{sq\downarrow,rp\downarrow} & \Omega_{sq\downarrow,sp\uparrow} & \Omega_{sq\downarrow,sp\downarrow} & \Omega_{sq\downarrow,rq\uparrow} & \Omega_{sq\downarrow,rq\downarrow} & \Omega_{sq\downarrow,sq\uparrow} & \Omega_{sq\downarrow,sq\downarrow}
\end{pmatrix} \tag{3.5}$$

All of the elements of the Ω matrix [Eq. (3.5)] can be written out according to Eq. (2.229), here, only the first column elements are written out as an example, other elements can be written out similarly,

$$\begin{aligned}
\Omega_{rv\uparrow,rv\uparrow} &= 2\sqrt{\omega_{r\uparrow,v\uparrow}}K_{rv\uparrow,rv\uparrow}\sqrt{\omega_{r\uparrow,v\uparrow}} + \omega^2_{r\uparrow,v\uparrow} \\
\Omega_{sv\uparrow,rv\uparrow} &= 2\sqrt{\omega_{s\uparrow,v\uparrow}}K_{sv\uparrow,rv\uparrow}\sqrt{\omega_{r\uparrow,v\uparrow}} \\
\Omega_{vp\downarrow,rv\uparrow} &= 2\sqrt{\omega_{v\downarrow,p\downarrow}}K_{vp\downarrow,rv\uparrow}\sqrt{\omega_{r\uparrow,v\uparrow}} \\
\Omega_{vq\downarrow,rv\uparrow} &= 2\sqrt{\omega_{v\downarrow,q\downarrow}}K_{vq\downarrow,rv\uparrow}\sqrt{\omega_{r\uparrow,v\uparrow}} \\
\Omega_{rp\uparrow,rv\uparrow} &= 2\sqrt{\omega_{r\uparrow,p\uparrow}}K_{rp\uparrow,rv\uparrow}\sqrt{\omega_{r\uparrow,v\uparrow}} \\
\Omega_{rp\downarrow,rv\uparrow} &= 2\sqrt{\omega_{r\downarrow,p\downarrow}}K_{rp\downarrow,rv\uparrow}\sqrt{\omega_{r\uparrow,v\uparrow}} \\
\Omega_{sp\uparrow,rv\uparrow} &= 2\sqrt{\omega_{s\uparrow,p\uparrow}}K_{sp\uparrow,rv\uparrow}\sqrt{\omega_{r\uparrow,v\uparrow}} \\
\Omega_{sp\downarrow,rv\uparrow} &= 2\sqrt{\omega_{s\downarrow,p\downarrow}}K_{sp\downarrow,rv\uparrow}\sqrt{\omega_{r\uparrow,v\uparrow}} \\
\Omega_{rq\uparrow,rv\uparrow} &= 2\sqrt{\omega_{r\uparrow,q\uparrow}}K_{rq\uparrow,rv\uparrow}\sqrt{\omega_{r\uparrow,v\uparrow}} \\
\Omega_{rq\downarrow,rv\uparrow} &= 2\sqrt{\omega_{r\downarrow,q\downarrow}}K_{rq\downarrow,rv\uparrow}\sqrt{\omega_{r\uparrow,v\uparrow}} \\
\Omega_{sq\uparrow,rv\uparrow} &= 2\sqrt{\omega_{s\uparrow,q\uparrow}}K_{sq\uparrow,rv\uparrow}\sqrt{\omega_{r\uparrow,v\uparrow}} \\
\Omega_{sq\downarrow,rv\uparrow} &= 2\sqrt{\omega_{s\downarrow,q\downarrow}}K_{sq\downarrow,rv\uparrow}\sqrt{\omega_{r\uparrow,v\uparrow}} \,. \qquad (3.6)
\end{aligned}$$

The above Ω matrix [Eq. (3.5)] is for a single open-shell systems. It is not difficult to generalize the above Ω matrix to two open-shell systems (e.g. O_2) or more open-shell cases by adding the extra singly occupied electron transitions to the virtual orbitals and doubly occupied electron transitions to the extra singly occupied orbitals.

The difference between the closed-shell systems and open-shell systems in constructing the Ω matrix can be seen by comparing the two–electron closed–shell Ω matrix elements [Eq. (3.2)] and the three–electron open-shell Ω matrix elements [Eq. (3.4)]. It can be seen that in closed-shell cases (*deMon* – *DynaRho*, prior to the present study), only considered α orbital energies in the construction of the Ω matrix, and only constructed the $\alpha\alpha$ block and the $\alpha\beta$ block of the coupling K matrix (see Chapter 2 of this thesis for details), since the $\alpha\alpha$ block and the

$\beta\beta$ block of the K matrix are the same in the closed-shell case, as well as the $\alpha\beta$ block and the $\beta\alpha$ block. But for an open–shell system, the $\alpha\alpha$ block and the $\beta\beta$ block of the coupling K matrix are no longer the same. Hence, the present study extends *deMon-DynaRho* to open–shell systems by constructing the new $\beta\beta$ and $\beta\alpha$ blocks. It is known that the K matrix includes two parts (see Chapter 2 of this thesis), one is the Coulomb potential contribution [the first term in Eq. (2.203)], another part is exchange-correlation potential contribution [the second part in Eq. (2.203)]. The key step to construct the K matrix is to evaluate the derivative of the exchange-correlation potential with respect to charge density under the adiabatic approximation. In open-shell case, constructing the $\beta\beta$ and the $\beta\alpha$ blocks of the K matrix need the derivatives of β electron exchange-correlation potential with respect to β electron charge density and with respect to α electron charge density, these derivatives were not evaluated in closed-shell case. The β electron exchange-correlation potential is

$$\begin{aligned} v_{xc}^{\uparrow} &= \frac{\delta\{\int d\mathbf{r}\epsilon_{xc}[n^{\uparrow}(\mathbf{r}), n^{\downarrow}(\mathbf{r})]n(\mathbf{r})\}}{\delta n^{\uparrow}} \\ &= n(\mathbf{r})\frac{\delta\epsilon_{xc}[n^{\uparrow}(\mathbf{r}), n^{\downarrow}(\mathbf{r})]}{\delta n^{\uparrow}} + \epsilon_{xc}[n^{\uparrow}(\mathbf{r}), n^{\downarrow}(\mathbf{r})]\,. \end{aligned} \tag{3.7}$$

The exchange and correlation energy densities are known which are given in Eq. (2.69) and Eq. (2.71). It can be seen from these equations [Eq. (2.69) and Eq. (2.71)] that the derivative of the exchange potential with respect to the charge density is easy to evaluate, but the derivative of the correlation potential with respect to the charge density needs to be evaluated as

$$\frac{\delta v_c^{\sigma}}{\delta n^{\tau}} = \frac{\delta\epsilon_c}{\delta n^{\sigma}} + \frac{\delta\epsilon_c}{\delta n^{\tau}} + n\frac{\delta^2\epsilon_c}{\delta n^{\sigma}\delta n^{\tau}}\,. \tag{3.8}$$

Constructing the $\beta\beta$ and the $\beta\alpha$ blocks need to evaluate $\frac{\delta v_c^{\downarrow}}{\delta n^{\downarrow}}$ and $\frac{\delta v_c^{\downarrow}}{\delta n^{\uparrow}}$ which can be obtained from

$$\begin{matrix} \frac{\delta^2\epsilon_c}{\delta x^2} & \frac{\delta^2\epsilon_c}{\delta x\delta\xi} \\ \frac{\delta^2\epsilon_c}{\delta\xi\delta x} & \frac{\delta^2\epsilon_c}{\delta\xi^2} \end{matrix} \tag{3.9}$$

This is much more complicated than in closed-shell case, since in the closed-shell case, the spin-polarization parameter, ξ, is zero. Moreover, the present work also

Table I. Descriptions of exchange-correlation functionals used in deMon-KS and in deMon–DynaRho with different electron-electron interaction terms.

	deMon-KS			
Interaction terms	Core	Hartree	LSDx	LSDxc
Coulomb	NO	YES	YES	YES
Exchange	NO	NO	YES	YES
Correlation	NO	NO	NO	YES
	deMon-DynaRho			
Interaction terms	IPA	RPA	TDLDAx	TDLDAxc
Coulomb	NO	YES	YES	YES
Exchange	NO	NO	YES	YES
Correlation	NO	NO	NO	YES

considers both α and β orbital energies in the construction of the Ω matrix in the *deMon – DynaRho*. This is also different from the closed-shell case which only considered α orbital energies.

Oscillator strength calculations are also modified, since the contributions of α and β electrons to the oscillator strengths are no longer the same. Specifically, the S matrix has to be calculated explicitly for α and β electron contributions.

Since *deMon–DynaRho* is a post–SCF program, it is possible to use different exchange–correlation functionals in the calculations during the SCF step and post-SCF (time-dependent DFRT) step. The exchange-correlation functionals used in the two steps are summarized in Table I. Together, the two exchange-correlation functionals that was used in the SCF step, (FNL_{SCF}), and that was used in the time-dependent DFRT step, (FNL_{TDDFRT}), are described by the notation FNL_{SCF}/FNL_{TDDFRT}. Certain internally consistent combinations corresponding to the analytical derivative equivalent of finite field (FF) calculations are

Table II. Combinations of exchange-correlation functionals which should give the same static polarizability in the FF and TDDFRT.

FF	TDDFRT
Core	Core/IPA
Hartree	Hartree/RPA
LSDx	LSDx/TDLSDx
LSDxc	LSDxc/TDLSDxc

given in Table II. These are useful for debugging purposes because the DFRT and the FF approaches should yield the same polarizabilities (see Table III). Other combinations are also useful because they either result in a justifiable overall improvement of the results (LB94xc/TDLSDxc,etc.) or are useful when computational efficiency is paramount and some tolerance in the quality of results is permissible (LSDxc/RPA).

Time-dependent DFRT has been implemented in *deMon-DynaRho* at different levels of approximation, varying according to the level of approximation used for the treatment of the response of the SCF field. If only the response of the core Hamiltonian is considered, neglecting electron-electron interactions, the result is the independent particle approximation (IPA). If the response of both the core Hamiltonian and the electron-electron Coulomb interactions is considered, the result is the random phase approximation (RPA). If the response of the core Hamiltonian, the electron-electron Coulomb interactions, and the electron exchange potential with the local density approximation is considered, the result is the time-dependent exchange-only local density approximation (TDLDAx). If electron correlation effects are also included, the result is the time-dependent local density approximation (TDLDAxc). These four levels of approximation are summarized in Table I.

The present study extends the time-dependent DFRT to open-shell systems and implements time-dependent unrestricted DFRT at these four levels of approximation. Each level of approximation programmed for open-shell systems was tested by the comparison of the calculated static mean polarizability for the sodium trimer with the same quantity calculated using the finite field method [333, 327]. The two methods should give the same results under appropriate circumstances (Table II). The testing was performed at both MCP and all-electron levels, using different quality of grids. The MCP calculations were done with the orbital basis set (311/2) and the all-electron calculations were carried out with the Sadlej orbital basis set [334], (6311111/61111/22). Results are given in Table III which shows that the static mean polarizability of the sodium trimer is consistent with the two methods used. In the MCP calculations, the biggest error is 1.48% at the LSDxc/TDLSDxc level. In the all–electron Core/IPA calculation, the finite difference polarizability is almost 50% smaller than the corresponding time-dependent LSDxc value. This error was found to be due to the field strength used in the *deMon–KS* program which was fixed at 0.0005 a.u. Since the polarizability of the sodium trimer is very large at the IPA level, if the electric field used is too large, it will lead to a big error. This is found to be exactly the case. If the finite field calculation is redone with a smaller electric field 0.000008 a.u. by the least squares fitting procedure [327], the mean polarizability of sodium trimer is exactly the same for the two procedures, the finite field method (least square fitting procedure) and the time-dependent DFRT calculation.

There is a big difference in the calculation of the mean polarizability of the sodium trimer at the MCP level and all-electron level with the Core/IPA functional. This is due to the core electron-electron interactions which is neglected in the all-electron calculation, since the MCP calculations even at the Core/IPA level still include the core electron-electron interactions in the sense that these interactions are already built into the MCP. But for the all-electron calculations at the Core/IPA level, the core electron-electron interactions are completely neglected.

This is also true with the other functionals (Hartree/RPA, LSDx/TDLSDx). In fact, the difference between MCP and all-electron calculations of the mean polarizability of the sodium trimer is only 4% with the LSDxc/TDLSDxc functional. This deviation is believed to arise from the MCP, since the MCP may not be flexible enough to be well polarized.

The implementation of the IPA functional was also tested by comparison of the vertical excitation energies (E_T) with the orbital energy differences ($\epsilon_i - \epsilon_a$). Since at the Core/IPA level, excitation energies are the same as the corresponding transition orbital energy difference. This can be used to debug the program. Tables IV shows that the excitation energy and the orbital energy differences of the sodium trimer are consistent both for the MCP and all-electron calculations. However, there is a 0.001 eV difference between the excitation energy and the orbital energy difference for the 2^2B_2 symmetry in the MCP calculation and 0.01 eV for the 2^2A_2 symmetry in all-electron calculation. This 0.001 eV (or 0.01 eV in the all-electron case) deviation is from round off error, since $Dyna - SCF$ cuts off orbital energies at the fifth digit. If the sixth number is larger than 5, there will be 0.001 eV difference (if there is only one digit integer) or 0.01 eV difference (if there is two digit integer) between the excitation energy and the orbital energy difference (since excitation energies are cut off at the sixth decimal places). Please note that there are large differences between the excitation energies calculated by the MCP and by all-electron approach at the IPA level in Table IV, this is due to the core electron-electron interactions which are included in the MCP calculations, but they are not included in the all-electron calculations. It is the same as the explanation for the mean polarizabilities at the previous paragraph.

The present implementation also gives the option to force the alpha and the beta coefficients to be the same in the calculations by using the keyword "RKSTDRT" (for restricted Kohn-Sham time-dependent response theory) in the SCF input file.

It is worth mentioning that time-dependent unrestricted DFT method is used in the present studies, hence, spin contamination arises for a Kohn-Sham orbital determinant. This spin contamination was discussed a few years ago by Pople, Gill, and Handy [335], they argued that this "contamination" is allowed due to the determinant is not the correct wave function for the system and found that the spin contamination in the unrestricted DFT is very small. However, the spin contamination in the time-dependent unrestricted DFT can be evaluated by the expectation value of the total spin-squared operator. Similar calculations were also done by the unrestricted single-excitation configuration interaction (UCIS) method [336]. Spin-squared operator is defined as

$$\begin{aligned} \hat{S}^2 &= \hat{S}_-\hat{S}_+ + \hat{S}_z(\hat{S}_z+1) \\ &= \hat{S}_-\hat{S}_+ + \hat{S}_z^2 + \hat{S}_z\,, \end{aligned} \tag{3.10}$$

where $\hat{S}_+$ is the raising operator which is given by

$$\hat{S}_+ = \hat{S}_x + i\hat{S}_y\,, \tag{3.11}$$

and $\hat{S}_-$ is the lowering operator which is given by

$$\hat{S}_- = \hat{S}_x - i\hat{S}_y\,. \tag{3.12}$$

If the determinant, D, with n_α columns of α spin and with n_β columns of β spin, the spin-squared operator become

$$\begin{aligned} \hat{S}^2 D &= [\sum_{\mathcal{P}} \mathcal{P}_{\alpha\beta} + n_\beta + \hat{S}_z(\hat{S}_z+1)]D \\ &= \{\sum_{\mathcal{P}} \mathcal{P}_{\alpha\beta} + n_\beta + \frac{1}{4}[(n_\alpha - n_\beta)^2 + 2(n_\alpha - n_\beta)]\}D \\ &= \{\sum_{\mathcal{P}} \mathcal{P}_{\alpha\beta} + \frac{1}{4}[(n_\alpha - n_\beta)^2 + 2n_\alpha + 2n_\beta]\}D\,. \end{aligned} \tag{3.13}$$

where $\mathcal{P}_{\alpha\beta}$ is an operator which exchanges α and β spin functions in the original determinant and the sum is over all possible interchanges of α and β. The expectation value of spin-squared operator is

$$\langle \hat{S}^2 \rangle = \langle \Psi_I | \hat{S}^2 | \Psi_I \rangle$$

$$
\begin{aligned}
= \; & \langle\Phi|\hat{S}^2|\Phi\rangle - \sum_{rs}(\sum_{p} C^{I*}_{pr\uparrow}C^{I}_{ps\uparrow})(\sum_{\bar{l}} \Delta_{r\bar{l}}\Delta_{\bar{l}s}) \\
& + \sum_{pq}(\sum_{r} C^{I*}_{pr\uparrow}C^{I}_{qr\uparrow})(\sum_{\bar{l}} \Delta_{q\bar{l}}\Delta_{\bar{l}p}) - \sum_{\bar{r}\bar{s}}(\sum_{\bar{p}} C^{I*}_{\bar{p}\bar{r}\downarrow}C^{I}_{\bar{p}\bar{s}\downarrow})(\sum_{l} \Delta_{\bar{r}l}\Delta_{l\bar{s}}) \\
& + \sum_{\bar{p}\bar{q}}(\sum_{\bar{r}} C^{I*}_{\bar{p}\bar{r}\downarrow}C^{I}_{\bar{q}\bar{r}\downarrow})(\sum_{l} \Delta_{\bar{q}l}\Delta_{l\bar{p}}) - \sum_{pr\bar{q}\bar{s}} C^{I*}_{pr\uparrow}C^{I}_{\bar{q}\bar{s}\downarrow}\Delta_{r\bar{s}}\Delta_{\bar{q}p} \\
& - \sum_{\bar{p}\bar{r}qs} C^{I*}_{\bar{p}\bar{r}\uparrow}C^{I}_{qs\downarrow}\Delta_{\bar{r}s}\Delta_{q\bar{p}}\,, \qquad (3.14)
\end{aligned}
$$

where orbitals with superior-bar are β electron orbitals, Δ_{ij} is the molecular orbital $(\alpha - \beta)$ overlap, specifically,

$$\Delta_{r\bar{s}} = \langle r|\bar{s}\rangle\,, \qquad (3.15)$$

$$\Delta_{\bar{q}p} = \langle \bar{q}|p\rangle\,, \qquad (3.16)$$

and $C_{ij\sigma}$ is the expansion coefficients of the single excited configurations in the following equation,

$$\Psi_I = \sum_{pq\sigma}^{n_{p\sigma}-n_{q\sigma}>0} C^{I}_{pq\sigma}\Phi^{q\sigma}_{p\sigma}\,, \qquad (3.17)$$

in which Φ is the determinant of occupied Kohn-Sham orbitals, and

$$C^{I}_{pq\sigma} = \sqrt{\frac{\epsilon_{q\sigma} - \epsilon_{p\sigma}}{\omega_I}}F^{I}_{pq\sigma}\,. \qquad (3.18)$$

Since the spin contamination in the unrestricted DFT is very small [335], the present studies assign the spin multiplicities consulting the restricted case and with help of the transition intensities.

The time-dependent DFT method developed here can only treat single excitations in this stage, hence, doublet excited states were obtained in the present studies. To get quartet excited states, double excitations need to be considered, but the DynaRho program can not handle double excitations yet. However, it can be a project for the perspective work.

The bottleneck of the efficiency in the deMon–DynaRho calculations is diagonalization of the Ω matrix. The dimension of the Ω matrix depends on the number of occupied orbitals and virtual orbitals. If there are N electrons in the

system concerned, the number of occupied orbitals

$$n_{occ} = \frac{N}{2} \propto N\,, \tag{3.19}$$

this is for the closed-shell system, but for open-shell case, it is not exactly $\frac{N}{2}$, but it is also proportional to N, in any cases (closed-shell or open-shell), this will not affect the scale. The number of virtual orbitals depends on the basis set used, if a medium size basis (3N basis functions) is used, the number of virtual orbitals is

$$n_{unocc} = 3N - \frac{N}{2} \propto N\,. \tag{3.20}$$

Hence, the dimension of the Ω matrix is

$$n_{occ} \times n_{unocc} \propto N^2\,. \tag{3.21}$$

It is known that doing a full diagonalization of $N^2 \times N^2$ matrix (Ω matrix) needs $(N^2)^3$ operations [318]. Hence, the scale of deMon-DynaRho is approximately N^6. The CPU time used in the all-electron DynaRho calculations for sodium clusters is given in Table V.

Table III. Sodium trimer static mean polarizabilities (a.u.) calculated at the MCP and the all-electron (AE) levels.

MCP mean polarizabilities (a.u.).				
METHOD	Core/IPA	Hartree/RPA	LSDx/TDLSDx	LSDxc/TDLSDxc
FF(F,R)[a]	272.8	329.2	381.1	376.2
TDDFRT(F,R)	272.7	329.2	379.4	376.6
FF(XF,R)	272.8	329.2	381.8	376.6
TDDFRT(XF,R)	272.7	329.2	379.4	376.7
FF(XF,NR)[b]	272.8	329.2	381.8	376.6
TDDFRT(XF,NR)	272.7	329.2	379.3	371.1
AE mean polarizabilities (a.u.).				
METHOD	Core/IPA	Hartree/RPA	LSDx/TDLSDx	LSDxc/TDLSDxc
FF(XF,NR)[c]	2336.7	2816.6	446.0	392.9
TDDFRT(XF,NR)	4928.6	2731.2	445.7	392.8

[a] (F,R) indicates that FINE and Random grid is used.

[b] (XF,NR) indicates that EXTRA-FINE and NonRandom grid is used.

[c] At IPA level least square fitting gives the mean polarizability as 4928.6 which indicates that the electric field used for the Finite-Field (FF) calculation is not appropriate (see text).

Table IV. Comparison of vertical excitation energies (eV) and orbital energy differences (eV) of the sodium trimer calculated with the MCP and with the all-electron (AE) method at Core/IPA level (The ground state symmetry is 1^2B_2).

Symmetry	Transition	E_T	$\epsilon_i - \epsilon_a$
	MCP results.		
1^2A_1	$b_2^\alpha \rightarrow a_1^\alpha$	0.812	0.812
2^2A_1	$a_1^\beta \rightarrow b_2^\beta$	2.719	2.719
1^2A_2	$b_2^\alpha \rightarrow a_2^\alpha$	3.503	3.503
2^2A_2	$a_1^\alpha \rightarrow b_1^\alpha$	4.227	4.227
1^2B_1	$b_2^\alpha \rightarrow b_1^\alpha$	1.508	1.508
2^2B_1	$b_2^\alpha \rightarrow b_1^\alpha$	3.955	3.955
2^2B_2	$b_2^\alpha \rightarrow b_2^\alpha$	2.893	2.894
3^2B_2	$a_1^\alpha \rightarrow a_1^\alpha$	3.531	3.531
	All-electron results.		
1^2A_1	$b_2^\alpha \rightarrow a_1^\alpha$	0.058	0.058
2^2A_1	$b_2^\alpha \rightarrow a_1^\alpha$	1.655	1.655
1^2A_2	$b_2^\alpha \rightarrow a_2^\alpha$	3.705	3.705
2^2A_2	$b_2^\alpha \rightarrow a_2^\alpha$	14.70	14.69
1^2B_1	$b_2^\alpha \rightarrow b_1^\alpha$	2.877	2.877
2^2B_1	$b_2^\alpha \rightarrow b_1^\alpha$	14.71	14.71
2^2B_2	$b_2^\alpha \rightarrow b_2^\alpha$	1.421	1.421
3^2B_2	$a_1^\alpha \rightarrow a_1^\alpha$	12.32	12.32

Table V. The CPU time used (hour:minute:second) in the DynaRho all-electron calculations for the sodium clusters with the Sadlej basis, (6311111/61111/22) and by the LSDxc/TDLSDxc functional.

Clusters	CPU Time used
Na_2	21:45
Na_3	3:58:08
Na_4	26:39:29
Na_5	195:13:22
$Na_6(C_{5v})$	596:31:24
$Na_6(D_{3h})$	596:31:24

CHAPTER 4

SODIUM MODEL CORE POTENTIAL FOR DENSITY–FUNCTIONAL CALCULATIONS: COMPARISON OF CALCULATED SODIUM CLUSTER PROPERTIES WITH ALL–ELECTRON CALCULATIONS

4.1 INTRODUCTION

Metal clusters have been the subject of a number of recent books [337, 338] and reviews [339, 90]. Much of the interest focuses on how cluster properties vary with the number of atoms in the cluster. Alkali metal clusters, especially sodium clusters, have a privileged place in this domain for a number of reasons. On the one hand, alkali metal clusters are often thought of as the simplest type of metal clusters and so are a prototype for the understanding of more complex types of clusters. Calculations [340, 3, 341, 342, 343, 344] are facilitated by the presence of a single s-type valence electron. On the other hand, alkali metal clusters are now relatively easy to study experimentally [345, 346]. Even so, it is fair to say that the properties of large aggregates of alkali metal atoms are so far poorly understood. An important prerequisite to improved theoretical studies of larger sodium clusters is the implementation and characterization of efficient computational tools. It is the objective of the present chapter to present one such tool, namely a model core potential (MCP) for sodium suitable for use in density-functional calculations. This MCP is assessed by evaluating the

properties of homonuclear sodium clusters up through the hexamer and for the tridecamer against our own all-electron calculations.

An understanding of some of the factors governing the accurate calculation of sodium cluster properties can be obtained by considering previous theoretical studies reported in the literature. The simple shell model has successfully explained the mass spectra of molecular beams of sodium clusters [347, 346], and some other properties, but it cannot give detailed information about nuclear positions. The extended Hückel method does give qualitatively correct geometries [348, 349], but it is limited in property studies. *Ab initio* techniques, such as Hartree-Fock (HF), density-functional theory (DFT), and configuration interaction methods (CI), are both more accurate and more costly. They have also been used to study sodium cluster properties. In the HF studies, it has been shown that the sodium clusters are either weakly bound or even not bound with respect to atomization [3, 340]. The reason is that the binding and the correlation energies of the aggregates are of the same order of magnitude [350], so that theoretical study of the electronic properties of the sodium clusters must include an accurate treatment of electron correlation. Two commonly used approaches which include electron correlation are CI and DFT methods. Systematic CI calculations of sodium clusters have been carried out with effective core potentials (ECPs) [340, 3] and at the all-electron level [3, 351, 4] for up to nine atoms. On the other hand, the computational cost of the CI method increases rapidly and the attainable accuracy decreases as the number of electrons increases [4]. Hence the CI method is limited to smaller clusters. DFT calculations are much more efficient (nominal scaling of N^3 with the size of the basis set) in comparison with the CI method (nominal scaling of N^6 or worse), making DFT more suitable for the study of large clusters. Previous DFT studies of small sodium cluster properties used ECPs [341, 342, 343, 344]. All-electron DFT studies of sodium cluster properties have not been found in the literature, except for the recent paper of Guan *et al.* [122].

Although ECPs and MCPs are similar in philosophy, they differ in detail. Both ECPs [352, 353, 354] and MCPs [355, 356, 357, 358, 359] are based on the frozen core approximation. All the core electrons are replaced by a core potential and only valence electrons are treated explicitly. The ECPs and MCPs differ primarily in the character of the valence radial wave functions. In particular, in the MCP approach, the valence orbitals may retain approximately the same nodal structure as do the reference orbitals from all-electron calculations. In contrast, the valence orbitals in ECP calculations are nodeless in the core region, and hence provide a poorer description of the wave functions near the nuclei. The nodal structure of MCP orbitals requires more Gaussian primitives than are needed to describe the corresponding ECP orbitals, and therefore more integrals have to be evaluated for MCP calculations than for ECP calculations [360, 361]. In both cases, the reliability and efficiency of the core potential methods must be assessed by comparison against all-electron calculations.

The aim of the present work is to assess a new Huzinaga-type MCP [355] for sodium. To do so, we compare the properties for sodium clusters up to the hexamer calculated at the MCP level against those from our own all-electron DFT calculations. The comparison is also made with previous DFT ECP calculations [344, 362, 7, 8, 363], available experimental data, and with other theoretical studies. The assessment will focus on the geometric structures, vibrational frequency analysis, binding energies, ionization potentials from both all-electron calculations and the MCP calculations using the local density approximation (LDAxc) and gradient-corrected functionals (GCFs), namely the 1988 gradient-correction for exchange of Becke (B88x) [209], the 1986 gradient-correction for exchange of Perdew and Wang (PW86x) [211], and the 1986 gradient-correction for the correlation of Perdew (P86c) [210]. Polarizabilities of sodium clusters have also been calculated at the MCP level for comparison with our previous all-electron calculations [327, 122]. We have also calculated the properties of the sodium tridecamer in both high and low spin states. Our all-electron calculations

are interesting in their own right, given the dearth of all-electron DFT studies of the properties of sodium clusters.

4.2 METHODOLOGY

The MCP method was originally proposed by Bonifăcić and Huzinaga [355] for Hartree-Fock calculations. More detailed theoretical justifications of the method were later given by Höjer and Chung [364], and by Sakai and Huzinaga [365]. The MCP method has been adapted for spin-polarized local-spin-density calculations by Salahub and coworkers [358, 366]. Here, we give a brief description of the MCP used for DFT since this is the method used for the design and application of our sodium core potential.

The MCP method assumes that the core orbitals are well localized and environment-independent frozen atomic orbitals. With this assumption, the core orbitals, $\psi_c^\sigma(\mathbf{r})$, can be separated from valence orbitals, $\psi_v^\sigma(\mathbf{r})$, and a core potential can be defined (in hartree atomic units) as

$$v_c^\sigma(\mathbf{r}) = -\sum_I \frac{Z_I^c}{|\mathbf{r}-\mathbf{R_I}|} + \int \frac{n_c(\mathbf{r}')}{|\mathbf{r}-\mathbf{r}'|} d\mathbf{r}' + v_{xc}^\sigma[n_c^\uparrow, n_c^\downarrow](\mathbf{r}), \tag{4.1}$$

where $\mathbf{R_I}$ is the nuclear coordinate of atom I, with atomic number Z_I and core electrons Z_I^c ($Z_I^c = 10$ in the case of sodium), $n_c^\sigma = \sum |\psi_c^\sigma|^2$ is the spin σ charge density of the core electrons, n_c is the total core density, and the exchange-correlation potential, $v_{xc}^\sigma = \delta E_{xc}/\delta n_\sigma$, is the usual derivative of the DFT exchange-correlation energy with respect to the total spin σ charge density. The valence energy is written as

$$\begin{aligned} E_v &= \sum_{v\sigma} < \psi_v^\sigma | -\frac{1}{2}\nabla^2 - \sum_I \frac{Z_I^v}{|\mathbf{r}-\mathbf{R_I}|} + v_{appl} + v_c^\sigma | \psi_v^\sigma > \\ &\quad + \frac{1}{2}\int\int \frac{n_v(\mathbf{r}) n_v(\mathbf{r}')}{|\mathbf{r}-\mathbf{r}'|} d\mathbf{r} d\mathbf{r}' + E_{xc}[n_v^\uparrow, n_v^\downarrow], \end{aligned} \tag{4.2}$$

where $Z_I^v = Z_I - Z_I^c$, $n_v^\sigma = n^\sigma - n_c^\sigma, n_v = n_v^\uparrow + n_v^\downarrow$, and v_{appl} is the potential

corresponding to any applied electrical field whose effect on the core electrons is neglected.

Minimizing the valence energy with respect to the valence orbitals leads to the orbital equation,

$$\hat{F}_v^\sigma \psi_v^\sigma(\mathbf{r}) = \epsilon_v^\sigma \psi_v^\sigma(\mathbf{r}) \,, \tag{4.3}$$

where the spin(σ)–dependent Kohn-Sham (KS) operator

$$\hat{F}_v^\sigma = -\frac{1}{2}\nabla^2 - \sum_I \frac{Z_I^v}{|\mathbf{r} - \mathbf{R_I}|} + v_{appl}(\mathbf{r}) + v_c^\sigma(\mathbf{r}) \,. \tag{4.4}$$

Since the core orbitals are also solutions of Eq. (4.3), they must be moved out of the way before we have a truly valence-only variational method. This is done by introducing the "projector",

$$\hat{P}^\sigma = 2\sum_{\sigma,c} \epsilon_c^\sigma |\psi_c^\sigma >< \psi_c^\sigma| \,, \tag{4.5}$$

and this leads to

$$(\hat{F}_v^\sigma - \hat{P}^\sigma)\psi_v^\sigma(\mathbf{r}) = \epsilon_v^\sigma \psi_v^\sigma(\mathbf{r}) \,. \tag{4.6}$$

The projector for sodium is given in Table VI in terms of the core orbital energies from an atomic numerical LDAxc calculation and the coefficients and exponents of a Gaussian-type orbital fit to the core orbitals from the same numerical calculation.

The core potential, v_c^σ, is taken as a linear combination of atomic potentials (i.e. the MCP), rather than using Eq (4.1) directly,

$$v_{MCP}(\mathbf{r}) = -\frac{[Z_c + \sum_k A_k (\frac{\pi}{\alpha_k})^{3/2} \exp(-\alpha_k \mathbf{r}^2)]}{\mathbf{r}} \,. \tag{4.7}$$

and the exponents, α_k and A_k are varied, subject to the charge conservation constraint

$$\sum_k A_k = -Z_c \,, \tag{4.8}$$

until atomic MCP calculations using a finite orbital basis set give valence orbitals and orbital energies in good agreement with those from the reference numerical

atomic LDAxc calculation. The exponents and contraction coefficients for the Gaussian-type orbital basis set used to construct our sodium MCP are given in Table VII. The MCP itself is given in Table VIII. The auxiliary basis sets used to fit the charge density and exchange-correlation energy density and potential during the deMon-KS calculations are given in Table IX.

4.3 COMPUTATIONAL DETAILS

Both MCP and all-electron DFT calculations were carried out with the program *deMon-KS* (**de**nsité de **Mon**tréal– Kohn-Sham module) [367]. This program uses Gaussian-type orbitals (GTOs) as basis functions to expand the KS orbitals. GTO auxiliary basis sets are used to fit the charge density and exchange-correlation potentials and energy density. The fitting of the exchange-correlation terms involves the use of a molecular grid.

Geometries were optimized for sodium clusters containing six or fewer atoms. Singlet or doublet spin states were considered depending upon whether the number of atoms was even or odd. The tridecamer geometry was optimized with both doublet and sextuplet spin-multiplicity. Minima were confirmed by harmonic frequency analysis which involves two-point numerical differentiation of analytic gradients. These clusters have very flat potential energy surfaces, in some directions, making high quality numerics indispensable. Even so, numerical constraints limit the accuracy of frequencies to about ± 50 cm^{-1}. The numerical precision of the dimer bond length has been estimated at ± 0.035 bohr in all-electron calculations with the fine grid [327, 122].

All property calculations were carried out with the LDAxc and the gradient-corrected functionals, B88x+P86c and PW86x+P86c. To aid in assessing the MCP against the all-electron calculations, the same tight convergence criteria were used for both calculations. Specifically, an energy difference of less than

10^{-8} hartree and a change in charge density fitting coefficients of less than 10^{-7} a.u. between successive iterations was required. A FINE Random grid which is an angular grid ranging from 50 points to 194 points depending upon the radial distance (the final grid used for the total energy calculation consisted of 32 radial grid points and 26 angular grid points for a total of 832 grid points per atom) was used for the present calculations, except in the case of the tetramer which has a very soft in-plane lowest vibrational mode (*vide infra*). The final geometry of the tetramer was obtained with a user-defined grid [327] using 128 radial grid points and 194 angular grid points for a total of 24,832 grid points per atom. Polarizability calculations were carried out using the finite field method in which the derivative of the induced dipole moment is obtained by a 3 point finite difference formula [333] and *deMon-KS*'s default electric field strength of 0.0005 a.u.

All-electron geometry and property calculations (except the all-electron polarizability calculations given in Refs. [327, 122]) employed the valence double-zeta plus polarization function (DZVP) quality orbital basis set and the (5,4;5,4) auxiliary basis set in the *deMon-KS* basis set library. Three orbital bases used in the MCP calculations are basis A, (311/2); basis B, (311/11); and basis C, (311/111) which differ in the choice of p functions. The fitting procedure used to obtain the exponents and coefficients of s functions does not generalize in the present case to find the exponents and coefficients of p functions, since sodium has no occupied valence p orbital to fit. Instead, p functions in basis B were simply borrowed from the outermost two p functions in the all-electron DZVP basis to replace the p function in the basis A, (311/2). This basis B is the choice for comparing with all-electron calculations. However, MCP polarizability calculations used basis C, (311/111), which is supplemented with a field-induced polarization function borrowed from the all-electron basis set which was used in the all-electron polarizability calculations. These three orbital bases are given in Table VII(please note that the Tables and Figs. are given at the end of the

chapter). Auxiliary basis set (5,1;5,1) and model core potential (5:6,4) are given in Table IX and Table VIII, respectively.

4.4 RESULTS AND DISCUSSION

The MCP calculations are much faster than the all-electron calculations which make the MCP an important tool for the study of still larger clusters. The quality of the MCP was evaluated against all-electron calculations for geometry optimizations and electronic property calculations of sodium clusters up through the hexamer. Then the MCP is applied to the tridecamer. Many of the all-electron DFT calculations of sodium cluster properties reported here are the first in the literature. The total self-consistent field (SCF) cycles used for each calculation of the MCP and the all-electron (MCP/AE) are 47/47, 49/54, 64/62, 54/56, 57/137, and 54/56 for the atom, dimer, trimer, tetramer, pentamer, and the hexamer, respectively. This comparison shows that the total cycles used for the MCP and the all-electron calculations are basically the same, except for the pentamer (the total cycles used in the all-electron calculation is about twice that for the MCP calculation). Therefore, the time used per cycle can indicate the efficiency of the MCP calculations. This is demonstrated in Fig. 4(please note that Figs. and Tables are given at the end of the chapter) in terms of the central processing unit (CPU) time used per SCF cycle in comparison with the all-electron results.

4.4.1 OPTIMIZED GEOMETRIES

Structural parameters may be regarded as the most basic cluster properties, prerequisite to the detailed understanding of other properties. The all-electron LDAxc optimized geometries are with shorter bond lengths and larger bond angles compared with available experiment. In contrast, Hartree-Fock (HF) optimized

geometries are with longer bond lengths and even larger bond angles in comparison with the experiments. Tables X and XI show that the all-electron LDAxc dimer bond length is 0.1 bohr too short, while the HF bond length of Ref. [3] is 0.28 bohr too long, in comparison with the experimental results. For the trimer, the isosceles sides of the triangle are too short in comparison with the experiment by 0.17 bohr at the LDAxc level and too long by 0.33 bohr in the HF calculations of Ref. [3]. The trimer bond angle between the two isosceles sides of the triangle is too large compared to the experiment by 5.78° in the LDAxc calculations and too large by 9.23° in the HF calculations of Ref. [3].

The DFT gradient-corrected P86x+P86c and B88x+P96c functionals lead to longer bond lengths than those at the LDAxc level, while the CI leads to shorter bond lengths than those at the HF level [368]. However, both leading to better agreement with the experiment. Judging from the trimer results, the B88x+P96c functional is better than the P86x+P86c functional for the optimized geometries of sodium clusters.

The MCP optimized geometries, no matter whether the bond lengths are longer or shorter than the all-electron geometries, are in better agreement with the experiments. The comparison between the MCP (MCP/LDAxc, MCP/P86x+P86c and MCP/B88x+P86c) and the all-electron geometries is given in Tables X and XI. In the dimer case, the bond length obtained by the MCP/LDAxc and the MCP/PW86x+P86c functionals is longer than the all-electron geometry by 0.16 bohr and 0.09 bohr, respectively. In contrast, the MCP/B88x+P86c functional gives a bond length shorter than that of the all-electron B88x+P86c result by 0.04 bohr. In the trimer case, the bond lengths of the isosceles sides of the triangle are become shorter and the bond angle between the two isosceles sides of the triangle are decreased at all levels of the MCP/LDAxc (0.23 bohr, 1.2°), the MCP/B88x+P86c (0.02 bohr, 3.9°), and the MCP/PW86x+P86c (0.13 bohr, 8.4°) calculations compared to the all-electron values. It is worth mentioning that

the MCP tetramer geometry optimized with basis A is a nonrhomboid parallelogram, but basis B with the LDAxc functional yields a rhombus structure, which is the same as the all-electron result. The optimized geometry obtained with gradient-corrected functionals and basis B is closer to that optimized at the all-electron level than that with basis A, although it is not a rhombus yet. However, the MCP/B88x+P86c functional gives the best mimic to the all-electron optimized geometries and both the all-electron and the MCP geometries calculated with this functional are in better agreement with the experiment.

The all-electron and the MCP/LDAxc optimized geometries are also compared with the results obtained with Bachelet, Hamann, and Schlüter (BHS) [369] *ab initio* ECP and Bardsley (BRD) [370] semiempirical ECP taken from the literature [362, 7, 8, 363]. Tables X and XI show that the BHS ECP bond lengths are too short, while the BRD ECP bond lengths are a little bit too long, in comparison with the present all-electron results, but the bond lengths with both BHS and BRD ECP are shorter than the MCP results. However, the MCP and the BRD ECP optimized geometries agree well with the experiments, the difference is that the MCP yields positive errors, in contrast, BRD ECP gives negative errors.

The assessed MCP is applied to predict the tridecamer equilibrium geometry. The intent here is not to make a full exploration of the potential energy surface of Na_{13}, but rather to illustrate how the MCP might be used in treating larger clusters than would normally be treated at the all-electron level. Thus the present work focuses on the two likely structures, one for the doublet spin-multiplicity and the other for the sextuplet spin-multiplicity. According to the shell model [347, 346], the lowest energy sextuplet structure should have a compact spherical shape with a five-fold degenerate HOMO (highest occupied molecular orbital). Indeed the lowest energy structure for Li_{13} is believed to be icosahedral with sextuplet spin multiplicity [371]. But this is not the lowest energy structure for Na_{13} from the calculations by Röthlisberger and Andreoni [345, 372] or Spiegelmann and

Poteau [349] as well as our own calculations. The icosahedral structure is excluded by the Jahn–Teller effect from being a minimum on the doublet potential energy surface. According to the shell model, the lowest energy doublet structure is an ellipsoid with principle axis lengths in the ratio [346] of 1.25:1.08:0.73. In fact, Spiegelmann and Poteau, in their distance-dependent tight binding model study of sodium cluster geometries [349], found the minimum energy doublet structure to be roughly ellipsoidal with principle axis lengths in the ratio of 1.34:1.08:0.69. A qualitatively similar result was also found in the Car–Parrinello study by Röthlisberger and Andreoni [345, 372]. Although these are some of the most complete studies of the structure of the sodium tridecamer, very few properties were actually calculated for the structures found.

The tridecamer geometry optimizations are presently carried out without any symmetry constraints for both the sextuplet and doublet spin multiplicities beginning in each case with both an icosahedral starting geometry and the minimum energy doublet geometry of Spiegelmann and Poteau. The result of the doublet geometry beginning with the Spiegelmann and Poteau structure led to a minimum geometry with energy of 0.245 eV below that of the minimized icosahedral sextuplet structure (whose mean coordination number given in Table XX), confirming that the true minimum of the tridecamer is not the same as Li_{13} with an icosahedral structure, but an asymmetric structure with doublet multiplicity whose coordinates and nearest–neighbor distance are given in Table XVIII and XIX. The present MCP found the minimum geometry of the tridecamer to be the same as that found by Röthlisberger and Andreoni [345, 372] and by Spiegelmann and Poteau [349].

4.4.2 VIBRATIONAL FREQUENCIES

Vibrational analysis is necessary in order to confirm that stationary points obtained during geometry optimizations are indeed minima. Vibrational frequen-

cies are also of spectroscopic interest and may be used to judge the shape of the potential energy surface. The sodium cluster vibrational frequencies reported here are harmonic frequencies calculated by finite difference of the analytic gradients [280, 249]. These calculations have been made at the all-electron and the MCP levels using both local and gradient-corrected functionals for the clusters up through the hexamer and at the MCP level using the LDAxc functional for the tridecamer. The present calculated frequencies are compared with available experiment and other theoretical results in Table XII, and Table XIII. The symmetry of the normal modes have been assigned for the all-electron calculations (a few differences in the ordering of modes between the all-electron and the MCP calculations are observed for quasidegenerate modes). Neither experimental nor calculated frequencies are available to our knowledge beyond the trimer, with the exception of the spherically-averaged pseudopotential (SAPS) calculations of Aguilar *et al.* [2]. However, the SAPS model leads to overly symmetric optimized structures which make vibrational modes be too degenerate (see Tables XII, XIII and XX). Given this fact and the quality of our results for the dimer and trimer, the present results may be regarded as the first semiquantitative prediction of sodium cluster frequencies for the tetramer and above.

Tables XII and XIII show that all the frequencies obtained at the all-electron level are real, confirming that the optimized equilibrium geometries are minima on the potential energy surface. Table XII shows that the present calculated frequencies agree well with the experiment and other theories for the dimer and trimer. In the dimer case, the all-electron LDAxc vibrational frequency is in the best agreement with the experimental result, being larger by only 0.8%, while the PW86x+P86c yields larger frequencies by 3.8% and the B88x+P86c gives smaller vibrational frequencies by 5.6% in comparison with experiment. In comparison, a multiconfigurational self-consistent field (MCSCF) calculated frequency of the dimer [373] is 1.9% too small compared with the experiment, and a full CI molecular dynamics calculation gives the anharmonic frequency of

the dimer differing from the experiment by 14% [374]. In the trimer case, the present all-electron calculations of the three frequencies (sym., asym., and bending) at the LDAxc level differ from the experiment by 1.8%, 28.3%, and 18.7%, respectively. The differences increase at the gradient-corrected functional level (PW86x+P86c and B88x+P86c). In comparison, full CI molecular dynamics calculated anharmonic frequencies [374] differ from the experiment by 1.5%, 4.0%, and 27.3%, respectively. The differences between the present calculations and the experiment may not come from the comparison of theoretical harmonic frequencies with experimental anharmonic frequencies. Since the effect of anharmonicity has been estimated by the present work for the dimer, the anharmonic correction is only about one percent of the harmonic frequency.

The frequencies calculated by the MCP (Table XII) are in better agreement with the experiment. Although there are deviations between the MCP and the all-electron calculations, at the LDAxc level, the deviations are no larger than 7% for the dimer and the trimer. But the gradient-corrected functionals (PW86x+P86c and B88x+P86c) yield larger differences (9% and 33%).

Table XII and Table XIII show that the MCP frequencies are all positive, which indicates that the MCP optimized geometries are indeed minima. With the exceptions of one mode in the trimer and two modes in the hexamer, the MCP vibrational frequencies are lower than the corresponding all-electron calculations at the LDAxc level, typically by $2 - 10$ cm^{-1}. Thus the MCP potential energy surface around the minima is slightly flatter than that of the all-electron calculations.

In order to judge the nature of sodium tridecamer stationary points, a vibrational analysis (with basis A) was carried out for the optimized geometries. The vibrational analysis revealed the asymmetric structure optimized starting from the Spiegelmann and Poteau structure with doublet spin multiplicity and the icosahedral geometry with sextuplet multiplicity to be the minimum structures

among our four optimized geometries. The vibrational frequencies for these two minima are given in Table XX.

4.4.3 BINDING ENERGY PER ATOM

Binding energy per atom (BEPA) is an important indicator of the relative thermodynamic stability of clusters. It should approach the bulk cohesive energy in the limit of a large enough cluster. However, the shell model [347, 346] predicts that an odd-even alternation should be superimposed upon this trend due to the relative instability of half-closed shells in comparison with closed shells. These trends have been observed in the calculations at a variety of levels [5, 3]. Here we are interested in how the detailed features of calculated BEPAs depend on the choice of functional and the use of an MCP rather than all-electron calculations.

The BEPA were calculated according to the following atomization reaction,

$$\mathrm{Na}_n \rightarrow n\mathrm{Na} \tag{4.9}$$

and the formula,

$$E_b(n) = E(1) - E(n)/n\,, \tag{4.10}$$

where $E(n)$ is the energy of a cluster with n atoms. The BEPA measures the average binding energy in the cluster and becomes equal to the cohesive energy of the bulk crystal when n is sufficiently large.

Since basis set borrowing may lead to a better description of the cluster than the atom, corrections for basis set superposition error (BSSE) are in principle necessary when calculating the BEPA. These were estimated for the dimer using the counterpoise method. The calculations show that the BSSE for the dimer is 0.003 eV or less at both all-electron and MCP levels for the local (LDAxc) and the gradient-corrected functionals (PW86x+P86c, B88x+P86c). It is therefore reasonable to neglect the BSSE correction to the BEPAs reported here.

The BEPAs of the sodium clusters were calculated with the LDAxc, the B88x+P86c, and the PW86x+P86c functionals at both all-electron and MCP levels. The comparison with available experiments and traditional *ab initio* CI [3, 4] and fourth-order Møller-Plesset perturbation theory (MP4) [5] are given in Table XIV. The present all-electron calculations show that the BEPAs are overestimated at the LDAxc level and at the PW86x+P86c level. In contrast, the BEPAs are underestimated by the B88x+P86c functional and by traditional *ab initio* methods (CI and MP4). For example, in the trimer case, the LDAxc and the PW86x+P86c functionals yield BEPA larger than the experiment by 0.07 eV and 0.03 eV, respectively. In contrast, the B88x+P86c functional, CI, and MP4 give the BEPA lower than the experiment by 0.05 eV, 0.1 eV, and 0.17 eV, respectively. However, the BEPAs calculated by the gradient-corrected functionals are in better agreement with the experiment.

Fig. 7 shows that the distinct odd-even alternation is observed as the number of atoms in the clusters increases for the PW86x+P86c functional, which is the same as previously observed at the MP4 level [5]. The LDAxc and the B88x+P86c results obey similar trends to the CI results [4, 3] in that the BEPAs increase with cluster size and the odd-even alternation behavior is less pronounced.

The MCP BEPAs nicely reproduce the all-electron results. Table XIV shows that the differences between BEPAs calculated by the MCP and by the all-electron approach increase when the cluster size increases at the LDAxc level, while this difference decreases as the cluster size increases at the level of the gradient-corrected functionals (PW86x+P86c and B88x+P86c). However, the MCP/LDAxc and the MCP/PW86x+P86c results are lower than the corresponding all-electron calculations by less than 0.04 eV and 0.06 eV, respectively. In contrast, the gradient-corrected MCP/B88x+P86c functional gives a BEPA about 0.04 eV larger than the all-electron results.

Fig. 8 shows that the present MCP BEPAs calculated with the LDAxc and

B88x+P86c functional obey similar trends to the all-electron results. But the PW86x+P86c BEPAs are different from the all-electron calculations, in which the distinct odd-even alternation behavior observed at the all-electron level becomes simply increasing with cluster size. Hence the three functionals at the MCP level yield very similar trends for the BEPAs.

The sodium tridecamer BEPA is presented for the asymmetric structure with doublet spin multiplicity and for the icosahedral geometry with sextuplet multiplicity at the LDAxc level (with basis A) in Table XXI. The BEPAs of the asymmetric structure (0.74 eV) is larger than that of the icosahedral geometry (0.72 eV), this coincides with the geometry optimizations which asymmetric structure has lower energy than the icosahedral geometry. However, the present calculated BEPAs with the two structures (asymmetric structure and icosahedral geometry) are smaller than other theoretical results. A Car-Parrinello calculation yielded 0.80 eV on a structure with five-fold symmetry and doublet spin multiplicity [345], and a self-consistent pseudopotential local spin density calculation gave 0.86 eV for the BEPA [344] with a different symmetry (i.e. a distorted cubo-octahedron). We believe this difference to be due to different structures being used in the different calculations. Although the BEPA of the tridecamer is still far away (by about 0.37 eV) from the bulk value, sodium cluster BEPAs do eventually converge smoothly to the bulk value (1.11) [375].

4.4.4 IONIZATION POTENTIALS

Cluster ionization potentials (IPs) are one of the interesting cluster properties serving as an indicator of cluster reactivity. Sodium cluster IPs have been well studied both experimentally [6, 376] and theoretically [344, 3, 5]. The global trend in vertical IPs as a function of size has been described by multireference double configuration interaction (MRD-CI) [3], and fourth-order Møller-Plesset perturbation theory (MP4) [5] and in adiabatic IPs by LDAxc ECP calculations [344]

and with the liquid droplet model [6]. The IPs for small clusters show oscillations which are described by the shell model [347, 346]. Particularly notable are the even-odd alternations as orbitals are successively filled and half-filled. The MCP vertical IPs reported here will be judged in part by their ability to reproduce both qualitatively and quantitatively the trend for IPs calculated at the all-electron level.

The results of the MCP and the all-electron calculations of IPs are given in Table XV. The energies of the cationic sodium clusters are calculated at the same geometries as for the neutral clusters. Hence the IPs reported here are vertical. Note that the experimental IPs given in Table XV are probably best interpreted as adiabatic IPs. Nevertheless they still serve as useful points of reference, especially where structural relaxation effects are expected to be small.

Fig. 10 shows that the MCP IPs carried out with the LDAxc, the PW86x+P86c, and the B88x+P86c functionals have a similar trend versus the cluster size to the experiment which has mild odd-even alternation. This is similar to the all-electron results (see Fig. 9). In contrast, traditional *ab initio* MRD-CI [3] and MP4 [5] produced distinct odd-even alternation. The MCP IPs calculated with the local and the gradient–corrected functionals differ very little from one another so that no particular functional appears to be better than any other for this property.

The MCP in the application (with LDAxc and basis A) to calculate the vertical IP for the doublet asymmetric geometry and for the sextuplet icosahedral tridecamer structure is compared, in Table XXI, with IPs from other models and with experiment. The IP with the asymmetric structure agrees well with previous ECP DFT calculations with a distorted cubo-octahedral structure and both are larger than the experiment. At first glance, the spherical droplet model would seem to be ideally suited for estimating the IP of such a "spherical" structure as an icosahedron. However, the spherical droplet IP, which compares quite favorably against the experimental IP, overestimates the present calculated IP

(with icosahedral structure) by 0.44 eV. This, of course, is less surprising when it is taken into account that the spherical droplet model is parameterized using the work function of the essentially closed-shell bulk and that the open-shell sextuplet should be destabilized with respect to similar closed-shell structures.

4.4.5 POLARIZABILITIES

Polarizabilities of metal clusters are an interesting property which may provide helpful information on both cluster structure and cluster electronic structure [7, 362, 8, 363]. The simplest model for describing cluster polarizabilities is that of a classical metal sphere. This is the so-called "spill-out" model and predicts that the static polarizability is proportional to the volume of the cluster. However, real clusters are not spherical and accurate calculations are necessary to obtain quantitative agreement with experiment. MCPs offer a way to extend previous all-electron DFT calculations of polarizabilities [327, 122] to larger clusters.

Calculations of the mean polarizabilities and polarizability anisotropies of the sodium clusters up through the hexamer have been carried out at the all-electron and the MCP levels using both local (LDAxc) and gradient-corrected functionals (PW86x+P86c and B88x+P86c). The all-electron results have been reported previously [327, 122]. Here the main focus is on the discussion of the MCP polarizabilities and comparing them with the previously published all-electron results. The MCP was also applied to calculate polarizabilities of the tridecamer.

The MCP mean polarizabilities and polarizability anisotropies as well as the all-electron results, previously reported effective core potential calculations of Moullet *et al.* [7, 362, 8, 363], and experimental results are presented in Table XVI and Table XVII. Table XVI shows that the mean polarizabilities calcu-

lated at the MCP level are in reasonable agreement with the all-electron mean polarizabilities. The largest error between the all-electron and the MCP mean polarizabilities is always for the atom regardless of the functional used. However, the difference between the MCP mean polarizabilities and the all-electron mean polarizabilities decreases when the cluster size increases, regardless of whether a local or gradient–corrected functional is used. This trend can be clearly seen in Fig. 11. This phenomenon is believed to be due to basis set borrowing. The differences between the MCP and the all-electron mean polarizabilities calculated at the LDAxc level using geometries optimized at the same level are in the range of 16% except for the atom (50%) and dimer (25%). The MCP/B88x+P86c mean polarizabilities are in best agreement with the all-electron results (it is 36% for the atom and 15% for the dimer larger than the all-electron results, for larger clusters it is about 8% larger than the all-electron result). This is obvious in Fig. 11 on which the ratio of the MCP mean polarizabilities and the all-electron mean polarizabilities with the B88x+P86c functional is closer to 1 than that with the LDAxc and the PW86x+P86c functionals. In comparison with the experiment, the MCP overestimates mean polarizabilities for atom (31%) and the dimer (9%), in contrast, it underestimates those for larger clusters (9% for the trimer, 5% for the tetramer, 13% for the pentamer, and 19% for the hexamer).

The ECP LDAxc mean polarizabilities reported previously using the *ab initio* BHS ECP given in Table XVI are in better agreement with the all-electron LDAxc mean polarizabilities than are the BRD ECP ones. The discrepancies between the ECP BHS mean polarizabilities and the all-electron mean polarizabilities are in the range from about 1% for the atom to 5% for the pentamer. However the semiempirical BRD ECP mean polarizabilities are in better agreement with experiment. The MCP/LDAxc mean polarizabilities are similar to BRD ECP mean polarizabilities for the larger sodium clusters (e.g. the pentamer and the hexamer).

The MCP polarizability anisotropies (a sensitive property) agree roughly with the all-electron calculations. Similar to the mean polarizabilities, the largest deviation between the MCP and the all-electron calculations occurs for the dimer regardless of the functional used. The MCP/LDAxc and the MCP/PW86x+P86c overestimate polarizability anisotropies by about 2% and 10%, respectively, in comparison with the all-electron results, except for the dimer (25% and 20%, respectively). In contrast, the B88x+P86c functional underestimates polarizability anisotropies by about 3%, except for the dimer (27%). The percent difference between the all-electron LDAxc polarizability anisotropies and BHS polarizability anisotropies is also large, ranging from 5% to 16%, but there are no experimental results available to judge which one is better.

The mean polarizability of the doublet asymmetric and the sextuplet icosahedral tridecamer, as well as the experimental polarizability, is given in Table XXI. The close agreement between the present MCP calculated polarizability and that given by the spill-out model is interesting since an icosahedron is nearly spherical, though we would have expected the polarizability of the sextuplet to be a bit larger than that of the spill-out model which is parametrized using the Wigner-Seitz radius of the bulk (closed shell) and the polarizability of the atom (doublet). It is interesting that the polarizability of the doublet asymmetric structure is larger than that of the sextuplet icosahedron and that of the spill-out model. Moreover, the available experimental polarizabilities for the trimer and larger clusters are consistently larger than the most rigorous DFT values [122]. Hence the roughly 15% difference between the experimental value and the present MCP value for the tridecamer is not surprising.

4.5 CONCLUSION

A model core potential for sodium has been presented in this chapter. Its efficiency and accuracy were assessed by performing geometry optimizations

and calculations of vibrational frequencies, binding energies, ionization potentials, and polarizabilities against corresponding all-electron calculations for clusters up through the hexamer using both local and gradient–corrected exchange–correlation functionals. Such calculations are a useful calibration prior to use of the MCP in the application to the tridecamer property calculations and future studies. However, many of the all-electron density functional calculations presented here are the first all-electron results for those properties. In the particular case of vibrational frequencies, neither quantitative MCP nor all-electron results have been reported previously.

The accuracy of the MCP was found to vary according to the property considered and the exchange-correlation functional used. In most cases, the MCP properties calculated from the B88x+P86c functional are in the best agreement with those from the all-electron calculations, and are in better agreement with available experiment and correlated *ab initio* results. In particular, optimized geometry bond lengths differ by only about 1% from corresponding distances calculated at the all-electron level, and polarizabilities differ by only 8%. The MCP structures optimized with the B88x+P86c functional are also in significantly better agreement with the all-electron calculations than are the structures obtained in the previous ECP LDAxc calculations [350]. For the binding energy per atom, there is a larger but still small discrepancy between the MCP and the all-electron calculations. For example, the discrepancy is about 12% (or 0.04 eV) for the binding energy per atom for the dimer and the trimer with the B88x+P86c functional. For the ionization potential and vibrational analysis, the MCP/LDAxc functional gives the best mimic to the all-electron calculations. Based on the all-electron calculations, the best exchange-correlation functional to use depends to some extent on the property being calculated. The B88x+P86c functional is the best for geometry optimizations and polarizability calculations, while the LDAxc functional gives the best agreement between the calculated harmonic frequencies and experimentally observed vibrational frequencies.

The geometry optimizations and electronic properties of Na_{13} were carried out without the use of symmetry as an illustrative application of the MCP to a system which would not normally be treated at the all-electron level. We are encouraged by the efficiency of this MCP which was used to calculate vibrational frequencies for a number of stationary points on the potential energy surface. The found minimum geometry agrees with that previously reported by Röthlisberger and Andreoni [345, 372] and by Spiegelmann and Poteau [349].

Table VI. Projector used in MCP calculations.

Core orbitals in the projector		
Exponent	Contraction coefficients	Orbital energies (hartree)
1s		
0.0110207926	0.0110207926	-37.7147636414
-0.0201002043	-0.0201002043	
0.3847575486	0.3847575486	
0.5465959907	0.5465959907	
0.1737338752	0.1737338752	
0.0556630157	0.0556630157	
2s		
0.0110207926	-0.6633609533	-2.0584678650
-0.0201002043	-0.5141829252	
0.3847575486	0.2081092298	
0.5465959907	0.1834869534	
0.1737338752	0.0456662029	
0.0556630157	0.0141356653	
2p		
0.5065137	0.3667361438	-1.0556892157
1.9797206	0.5607790351	
7.7377839	0.2682032287	
30.2433071	0.0574445985	

Table VII. Orbital basis sets used in MCP calculations. Note that basis sets A, B, and C differ by the *p*-functions added to the substrate basis set.

Orbital basis	
Exponent	Contraction coefficients
Substrate basis	
1s	
205.06946	-0.00554574
29.673375	-0.03273471
1.0632752	0.24903133
2s	
0.0840500	1.00000000
3s	
0.0323178	1.00000000
p-functions for basis A	
1p	
0.067700500	0.52450640
0.030000000	0.52450640
p-functions for basis B	
1p	
0.4702690000	1.00000000
2p	
0.0647000000	1.00000000
p-functions for basis C	
1p	
0.4702690000	1.00000000
2p	
0.0647000000	1.00000000
3p	
0.0280000000	1.00000000

Table VIII. Model core potential used in MCP calculations.

Model core potential	
Exponent	Contraction coefficients
541.2974243	-1.6272639
53.5501099	-2.8618634
5.2941766	-3.3278172
0.6764935	-2.0552888
0.1380625	-0.1277668

Table IX. Auxiliary basis set used for fitting charge density (CD) and exchange-correlation (XC) potential in MCP calculations.

Exponents used for fitting CD and XC		
GTO	Charge density	Exchange correlation
s	410.1300000	136.7100000
s	59.3470000	19.7823333
s	2.1260000	0.70866670
s	0.1681000	0.05603333
s	0.0646000	0.02153333
spd	0.1354010	0.0451337

Table X. Comparison of all-electron (AE) and MCP DFT optimized geometries of sodium dimer, trimer, and tetramer with previous effective-core potential (ECP) DFT, Hartree–Fock (HF), and configuration interaction (CI) calculations, with previous AE HF calculations and with experiment. Geometrical variables are defined in Fig. 5. Bond lengths are in bohr, bond angles are in degrees.

		DFT			Other		
		LDAxc	PW86x+P86c	B88x+P86c	HF	CI	EXPT
			Dimer				
R	ECP	5.47[a] (5.78[b])					
	MCP (Basis A)	5.89	5.85	5.83			
	MCP (Basis B)	5.87	5.85	5.82			
	AE	5.71	5.76	5.86	6.10[c]	5.815[d]	
							5.818[e]
			Trimer				
r	ECP	5.68[a] (6.05[b])			6.43[f]	6.43[g]	
	MCP (Basis A)	6.25	6.24	6.20			
	MCP (Basis B)	6.19	6.16	6.14			
	AE	5.96	6.03	6.12	6.46[c]	6.26[h]	
							6.13[i]
Θ	ECP	78.01[a] (83.03[b])			87.2[f]	84.9[g]	
	MCP (Basis A)	88.98	88.14	91.47			
	MCP (Basis B)	84.26	83.83	84.04			
	AE	85.48	92.20	87.97	88.9[c]	73.2[h]	
							79.70[i]
			Tetramer				
r	ECP	6.18[a] (6.57[b])			6.99[f]	6.88[g]	
	MCP (Basis A)	8.02/6.20[j]	8.83/6.04[j]	8.21/6.12[j]			
	MCP (Basis B)	6.73	7.57/6.24[j]	6.80/6.57[j]			
	AE	6.48			7.07[c]		
R	ECP	5.42[a] (5.80[b])			6.10[f]	6.24[g]	
	MCP (Basis A)	6.29	6.44	6.32			
	MCP (Basis B)	5.93	5.99	5.87			
	AE	5.68			6.14[c]		

[a] *Ab initio* Bachelet, Hamann, and Schlüter ECP calculations taken from Ref. [8].

[b] Semi-empirical Bardsley ECP calculations taken from Ref. [8].

[c] All-electron Hartree-Fock calculations taken from Ref. [3].

[d] All-electron multireference singles and doubles configuration interaction calculations taken from Ref. [351].

[e] From Ref. [377].

[f] Effective core potential Hartree-Fock calculations taken from Ref. [3].

[g] Effective core potential configuration interaction calculations taken from Ref. [3].

[h] All-electron multireference singles and doubles configuration interaction calculations taken from Ref. [368].

[i] From Ref. [378].

[j] Only a nonrhomboid parallelogram structure was found, with side lengths given here.

Table XI. Comparison of all-electron (AE) and MCP DFT optimized geometries of soidum pentamer and hexamer with previous effective-core potential (ECP) DFT, Hartree–Fock (HF), and configuration interaction (CI) calculations, and with previous AE HF calculations. Geometrical variables are defined in Fig. 5. Bond lengths are in bohr, bond angles are in degrees.

		DFT			Other	
		LDAxc	PW86x+P86c	B88x+P86c	HF	CI
		Pentamer				
R_1	ECP	6.36[a] (6.55[b])			6.92[c]	
	MCP (Basis A)	6.85	6.94	6.83		
	MCP (Basis B)	6.74	6.79	6.71		
	AE	6.49			6.97[d]	
R_2	ECP	6.01[a] (6.42[b])			7.09[c]	
	MCP (Basis A)	6.94	6.84	6.88		
	MCP (Basis B)	6.71	6.61	6.64		
	AE	6.43			7.12[d]	
R_3	ECP	6.04[a] (6.37[b])			6.82[c]	
	MCP (Basis A)	6.54	6.51	6.54		
	MCP (Basis B)	6.49	6.48	6.45		
	AE	6.23			6.94[d]	
R_4	ECP	6.03[a] (6.30[b])			6.88[c]	
	MCP (Basis A)	6.59	6.61	6.56		
	MCP (Basis B)	6.50	6.53	6.48		
	AE	6.20			6.95[d]	
		Hexamer				
r	ECP	6.27[a] (6.62[b])			7.28[c]	7.26[e]
	MCP (Basis A)	6.82	6.89	6.81		
	MCP (Basis B)	6.77	6.85	6.76		
	AE	6.58			7.52[d]	
R	ECP	5.89[a] (6.30[b])			7.24[c]	6.67[e]
	MCP (Basis A)	6.63	6.54	6.56		
	MCP (Basis B)	6.46	6.40	6.41		
	AE	6.19			6.58[d]	

[a] *Ab initio* Bachelet, Hamann, and Schlüter ECP calculations taken from Ref. [8].

[b] Semi-empirical Bardsley ECP calculations taken from Ref. [8].

[c] Effective core potential Hartree-Fock calculations taken from Ref. [3].

[d] All-electron Hartree-Fock calculations taken from Ref. [3].

[e] Effective core potential configuration interaction calculations taken from Ref. [3].

Table XII. Sodium dimer and trimer harmonic vibrational frequencies calculated at the all-electron (AE) and MCP levels with various functionals. All calculations have been carried out at the optimized geometry for that level and functional. Frequencies from the spherically–averaged pseudopotential (SAPS) calculations of Ref. [2] are also listed. Note that the SAPS structures are too symmetric compared to the present calculations, leading to too few distinct frequencies.

Assignment[a]		Na_n harmonic frequencies (cm^{-1})			
		Density-functional theory			Other
		LDAxc	PW86x+P86c	B88x+P86c	
		Dimer ($D_{\infty h}$)			
Σ_g^+	MCP (Basis A)	150	151	154	
	MCP (Basis B)	155	159	159	
	AE	160	165	153	
	MCSCF[b]				156
	EXPT[c]				159
		SAPS: 189			
		Trimer (C_{2v})			
A_1	MCP (Basis A)	37.1	39.6	33.4	
	MCP (Basis B)	43.1	42.7	42.4	
	AE	40.3	23.6	36.5	
	CI[d]				63.
	EXPT[e]				49.
B_2	MCP (Basis A)	98.6	93.9	108	
	MCP (Basis B)	102	95.3	104	
	AE	112	117	99.6	
	CI[d]				83.5
	EXPT[e]				87.
A_1	MCP (Basis A)	127	123	124	
	MCP (Basis B)	136	135	138	
	AE	142	134	128	
	CI[d]				141
	EXPT[e]				139
		SAPS: 137, 165			

[a] Based on present AE/LDAxc calculations.

[b] Harmonic frequency from the multiconfiguration self-consistent field calculation of Ref. [373].

[c] From Ref. [379].

[d] Frequency from the configuration-interaction molecular dynamics power spectrum calculated in Ref. [374].

[e] Taken from Refs. [380, 57].

Table XIII. Sodium tetramer, pentamer, and hexamer harmonic vibrational frequencies calculated at the all-electron (AE) and MCP levels with various functionals. All calculations have been carried out at the optimized geometry for that level and functional. Frequencies from the spherically–averaged pseudopotential (SAPS) calculations of Ref. [2] are also listed. Note that the SAPS structures are too symmetric compared to the present calculations, leading to too few distinct frequencies. With the exception of the results in parentheses, which were calculated with basis B, all MCP DFT calculations have been performed with basis A.

Na_n harmonic frequencies (cm^{-1})				
MCP			AE	Assignment[a]
LDAxc	PW86x+P86c	B88x+P86c	LDAxc	
Tetramer (D_{2h})				
29.5 (17.8)	25.7 (22.5)	29.0 (24.8)	24.7	B_{2g}
36.2 (40.1)	28.5 (37.4)	37.9 (40.3)	42.4	B_{2u}
46.1 (73.8)	31.9 (55.3)	43.2 (73.4)	75.7	B_{1u}
98.6 (96.1)	97.4 (106)	103 (98.8)	99.4	A_g
136 (136)	134 (141)	137 (139)	140	B_{3u}
138 (156)	140 (149)	139 (159)	164	A_g
SAPS: 113, 131, 151				
Pentamer (C_{2v})				
22.2 (26.1)	25.7 (28.9)	24.4 (28.9)	26.1	B_2[b]
23.5 (26.6)	28.8 (30.9)	27.0 (29.3)	27.9	A_2
54.8 (58.5)	53.9 (58.8)	56.7 (59.8)	61.0	A_1
58.9 (67.0)	60.8 (72.7)	60.7 (69.6)	68.2	B_1
77.5 (82.2)	75.5 (77.9)	78.1 (82.3)	87.5	A_1
86.1 (93.3)	79.3 (89.0)	86.4 (93.1)	101	B_1
103 (114)	96.6 (110)	104 (117)	120	A_1
120 (126)	119 (126)	119 (129)	134	A_1
136 (146)	134 (144)	136 (148)	155	B_1
SAPS: 58, 80, 133, 143, 149, 158				
Hexamer (C_{5v})				
16.1 (22.3)	16.8 (23.5)	18.7 (25.4)	33.0	E_2
60.6 (57.2)	53.4 (49.3)	57.6 (54.6)	56.0	A_1
64.5 (71.7)	60.2 (68.4)	63.9 (71.3)	72.9	E_1
79.9 (85.5)	82.7 (88.1)	81.8 (87.6)	90.1	E_2
94.4 (98.4)	83.8 (90.1)	91.3 (95.3)	98.1	E_2
120 (124)	117 (122)	121 (126)	129	A_1
126 (137)	127 (140)	127 (140)	145	E_1
SAPS: 81, 96, 139, 145, 152				

[a] Based on present AE/LDAxc calculations.

[b] Due to numerical imprecision, this mode is significantly mixed in our calculations with the quasidegenerate A_2 mode.

Table XIV. Binding energy per atom (eV) of sodium clusters Na_n ($n = 2 - 6$) calculated with local and gradient-corrected functionals. Note that BEPA calculations at the all-electron level with the B88x+P86c and the PW86x+P86c functionals used the LDAxc optimized geometries. All other BEPAs were calculated for the geometries optimized at the same level. MCP results in parentheses were calculated using basis B.

	Binding energy per atom (eV)				
Methods	Na_2	Na_3	Na_4	Na_5	Na_6
	All-electron calculations				
LDAxc	0.43	0.43	0.55	0.60	0.69
B88x+P86c	0.33	0.31	0.42	0.45	0.52
PW86x+P86c	0.42	0.39	0.49	0.42	0.60
	Model core potential calculations				
LDAxc	0.40 (0.42)	0.38 (0.40)	0.49 (0.52)	0.53 (0.56)	0.61 (0.65)
B88x+P86c	0.36 (0.37)	0.33 (0.35)	0.40 (0.45)	0.45 (0.49)	0.51 (0.55)
PW86x+P86c	0.35 (0.36)	0.33 (0.35)	0.41 (0.43)	0.44 (0.48)	0.50 (0.55)
	Experimental results				
EXPT.[a]	0.37	0.36			
	All-electron conventional *ab initio* calculations				
MP4[b]	0.27	0.19	0.35	0.29	0.45
MRD-CI[c]	0.29	0.26	0.39	0.44	0.49
	Effective core potential calculations				
CI[d]	0.29	0.25	0.34	0.36	0.41
LSDxc[e]	0.45	0.43	0.61	0.64	0.73

[a] Taken from Ref. [377, 381].

[b] Fourth-order Møller-Plesset perturbation theory taken from Ref. [5].

[c] Multireference double configuration interaction calculations taken from Ref. [4, 3].

[d] Configuration interaction calculations taken from Ref. [4, 3].

[e] Local spin density calculations taken from Ref. [344].

Table XV. Sodium cluster ionization potentials calculated at the all-electron and MCP levels, compared with the experiment and other theoretical results. Note that the theoretical ionization potentials are vertical, while the experimental ionization potentials are probably best described as being adiabatic. Both the all-electron and MCP calculations were carried out at the geometries optimized with the same functional. MCP results in parentheses were calculated using basis B.

	Ionization potentials (eV)					
Functional	Na	Na_2	Na_3	Na_4	Na_5	Na_6
	All-electron calculations					
LDAxc	5.37	5.29	4.31	4.41	4.34	4.64
PW86x+P86c	5.53	5.45	4.54			
B88x+P86c	5.34	5.16	4.34			
	Model core potential calculations					
LDAxc	5.12 (5.12)	5.22 (5.19)	4.27 (4.22)	4.41 (4.35)	4.26 (4.26)	4.60 (4.61)
PW86x+P86c	5.37 (5.37)	5.35 (5.30)	4.46 (4.40)	4.53 (4.44)	4.38 (4.38)	4.76 (4.64)
B88x+P86c	5.40 (5.40)	5.38 (5.34)	4.50 (4.41)	4.48 (4.42)	4.49 (4.41)	4.65 (4.65)
	Other theoretical calculations					
MRD-CI[a]		4.6	3.6	4.2	3.8	4.0
MP4[b]		4.6	3.8	5.6	3.2	4.5
	Experimental results[c]					
EXPT[d]	5.14	4.93	3.97	4.27	4.05	4.12
EXPT[e]	5.14	4.91	3.98	4.28	3.95	3.97

[a] Multireference double configuration calculation taken from Ref. [3].

[b] Fourth-order Møller-Plesset perturbation theory calculation taken from Ref. [5].

[c] Best described as adiabatic. Note that adiabatic IPs are reduced in comparison with vertical IPs by the inclusion of the structural relaxation energy in the daughter ion.

[d] Taken from Ref. [6].

[e] Taken from Ref. [376].

Table XVI. Sodium cluster mean polarizabilities calculated with different functionals at the all-electron and MCP levels, experiment and previous ECP DFT results are also given for comparison. Note that the calculations at the all-electron level with the B88x+P86c and the PW86x+P86c functionals were done using the LDAxc optimized geometries. All other calculations were done using structures optimized at the same level.

	Mean polarizability $\bar{\alpha}$ (bohr^3)					
Functional	Na	Na_2	Na_3	Na_4	Na_5	Na_6
	All-electron calculations[a]					
LDAxc	140.1	226.2	371.3	459.2	560.0	611.6
PW86x+P86c	135.4	221.4	360.8	447.8	548.3	603.4
B88x+P86c	153.8	242.3	394.5	481.5	584.5	639.5
	Model core potential calculations[b]					
LDAxc						
Basis A	163.6	242.2	387.4	504.7	610.1	654.9
Basis B	102.5	203.5	333.9	440.0	555.0	604.3
Basis C	210.0	282.3	432.1	532.3	648.3	676.0
PW86x+P86c						
Basis A	153.5	235.3	370.1	510.6	600.6	639.5
Basis B	105.2	202.1	331.2	451.2	560.4	615.1
Basis C	196.1	275.1	415.4	541.6	648.4	687.2
B88x+P86c						
Basis A	168.2	237.9	391.1	489.5	617.0	651.0
Basis B	105.2	200.5	334.3	434.3	550.2	598.1
Basis C	208.9	277.7	427.2	521.6	634.9	664.4
	Effective core potentials DFT calculations[c]					
BHS LDAxc	141.7	223.3	363.0	452.8	587.7	603.2
BRD LDAxc	148.4	251.0	408.2	515.5	649.8	677.5
	Experimental results[d]					
EXPT	159.27±3.37	255.78±8.10	471.06±16.20	545.97±20.25	726.16±29.02	823.89±30.36

[a] All-electron results taken from our previous publications [327, 122].

[b] Present work

[c] ECP results from Ref. [362].

[d] Calculated from the measurements of relative polarizabilities of Knight *et al.* from Ref. [46] and the absolute measurement of the atomic polarizability by Molof *al.* from Ref. [382].

Table XVII. Sodium cluster polarizability anisotropies calculated with different functionals at the all-electron and the MCP levels. Note that the calculations at the all-electron level with the B88x+P86c and the PW86x+P86c functionals were done using the LDAxc optimized geometries. All other calculations were done using structures optimized at the same level.

	Polarizability anisotropy $\Delta\alpha$ (bohr^3)				
Functional	Na_2	Na_3	Na_4	Na_5	Na_6
All-electron calculations[a]					
LDAxc	135.8	284.6	446.4	430.9	377.6
PW86x+P86c	139.8	272.4	444.2	424.4	379.9
B88x+P86c	139.0	301.1	461.8	440.5	391.6
Model core potential calculations[b]					
LDAxc					
Basis A	141.5	307.3	523.3	494.1	420.8
Basis B	203.5	314.3	557.6	556.7	460.2
Basis C	101.9	268.4	453.9	434.0	379.9
PW86x+P86c					
Basis A	158.2	287.8	565.1	512.0	421.2
Basis B	196.5	318.2	594.4	575.1	480.1
Basis C	111.3	278.2	513.3	469.6	414.1
B88x+P86c					
Basis A	129.8	324.3	510.5	508.7	416.9
Basis B	195.8	322.4	552.9	551.6	457.4
Basis C	101.4	276.9	455.8	428.6	378.9
Effective core potentials DFT calculations[c]					
BHS LDAxc	142.4	260.5	382.1	339.4	318.88

[a] Taken from our previous publications [327, 122].

[b] Present work

[c] ECP results from Ref. [362].

Table XVIII. MCP LDAxc optimized sodium tridecamer doublet asymmetric geometry coordinates. Atom numbers as in Fig. 6.

Coordinates (bohr) for Doublet Na_{13}			
Center	x	y	z
1	-9.1351	-4.2501	1.8236
2	-1.9162	-4.8605	2.2261
3	-5.4179	1.0961	3.7946
4	-6.4913	-9.7077	4.5260
5	-5.5521	-0.8277	-2.7326
6	0.4025	-4.3956	-4.1575
7	-5.5389	-4.1008	8.2772
8	0.4157	-0.5386	7.0148
9	-5.1420	-8.0712	-2.7326
10	-4.5146	-4.1065	-8.9386
11	-10.3616	-5.1194	-5.5861
12	0.5650	1.3436	0.0019
13	-0.8920	1.6611	-7.1074

Table XIX. Interatomic distances for the sodium tridecamer doublet asymmetric structure. Atom numbers as in Fig. 6.

Nearest-neighbor distances (bohr)		
Pair	Ref. [349][a]	Present work[b]
(2, 1)	6.35	7.26
(3, 1)	6.12	6.80
(3, 2)	6.23	7.09
(4, 1)	6.11	6.64
(4, 2)	6.08	7.05
(5, 1)	6.05	6.73
(5, 2)	6.32	7.35
(5, 3)	6.04	6.81
(6, 2)	6.07	6.81
(6, 5)	6.22	7.09
(7, 1)	6.38	7.39
(7, 2)	6.11	7.09
(7, 3)	6.20	6.86
(7, 4)	6.26	6.81
(8, 2)	6.09	6.86
(8, 3)	6.22	6.86
(8, 7)	6.36	7.05
(9, 1)	6.27	7.16
(9, 2)	6.05	6.73
(9, 4)	6.31	7.56
(9, 5)	6.31	7.26
(9, 6)	6.12	6.80
(10, 5)	6.10	7.10
(10, 6)	6.21	6.86
(10, 9)	6.38	7.39
(11, 1)	6.30	7.56
(11, 5)	6.08	7.05
(11, 9)	6.12	6.64
(11, 10)	6.26	6.82
(12, 2)	6.08	7.04
(12, 3)	6.25	7.09
(12, 5)	6.07	7.04
(12, 6)	6.24	7.09
(12, 8)	6.50	7.26
(13, 5)	6.12	6.86
(13, 6)	6.23	6.86
(13, 10)	6.36	7.05
(13, 12)	6.51	7.26

[a] Taken from Ref. [349].

[b] MCP LDAxc calculations. See text.

Table XX. Na_{13} doublet asymmetric (asy) and sextuplet icosahedral (ico) mean nearest-neighbor distance and vibrational frequencies calculated at the MCP LDAxc level compared with other theoretical results.

Tridecamer properties	
Mean coordination number	
ico	6.46
asy	5.85
bulk	12.00
Mean nearest-neighbor distance	
Present work: ico	7.11
Present work: asy	7.03
TB[a]: cpb	5.85
CP[b]: cpb	6.66
Bulk[c] : bcc	7.01
Vibrational frequencies (cm^{-1})	
Present work: ico[d]	50.7(H), 54.0(H), 69.2(T), 75.2(G), 82.2(T), 91.5(G), 107.(A), 112.(H), 135.(T)
Present work: asy	30.55, 35.42, 35.45, 43.58, 44.82, 49.10, 53.64, 55.66, 56.04, 58.14, 62.24, 63.09, 67.22, 67.31, 68.29, 69.53, 72.92, 73.84, 78.09, 82.26, 85.33, 89.28, 89.40, 98.76, 109.40, 110.70, 111.85, 115.79, 118.31, 125.76, 126.76, 134.04, 135.72
SAPS model[e]	58.4, 70.6, 89.7, 103., 114., 155., 162., 197.

[a] Distance-dependent tight-binding method from Ref.[349].

[b] LDAxc Car-Parrinello taken from Ref. [345, 372].

[c] Ref.[375] page 29. The bulk crystal structure is body-centered cubic (bcc).

[d] Letters in parentheses indicate the degeneracy of the mode.

[e] Spherically averaged pseudopotential results taken from Ref. [2].

Table XXI. Na_{13} doublet asymmetric and sextuplet icosahedral binding energy per atom, ionization potential, mean polarizability, and polarizability anisotropy obtained at the MCP LDAxc level compared with experiments and other theoretical results.

Tridecamer properties	
	Binding energy per atom (eV)
Present work: ico	0.72
Present work: asy	0.74
CP[a]: cpb	0.80
ECP LDAxc[b] : cubo	0.86
Bulk cohesive energy[c] : bcc	1.11
	Ionization potential (eV)
Present work (vertical IP) : ico	3.16
Present work (vertical IP) : asy	3.86
ECP LDAxc[b]: cubo	3.89
Experiment[d]	3.6
Spherical droplet model[e]	3.6
Bulk work function[f]	2.3
	Mean polarizability ($bohr^3$)
Present work: ico	1192.7
Present work: asy	1309.1
Experiment[g]	1523.5
Spill-out model[h]	1263.8
	Polarizability anisotropy ($bohr^3$)
Present work: ico	0.[i]
Present work: asy	708.

[a] LDAxc Car-Parrinello taken from Ref. [345, 372].

[b] ECP LDAxc calculation for a doublet distorted cuboctahedron taken from Ref. [344].

[c] Taken from Ref. [375].

[d] From Ref. [6].

[e] See Ref. [6] for a further discussion of the spherical droplet model.

[f] From Ref. [383] page E-81.

[g] Beam deflection measurement from Ref. [46].

[h] As parameterized in Ref. [122]. A brief review of this model may also be found in this reference.

[i] By symmetry.

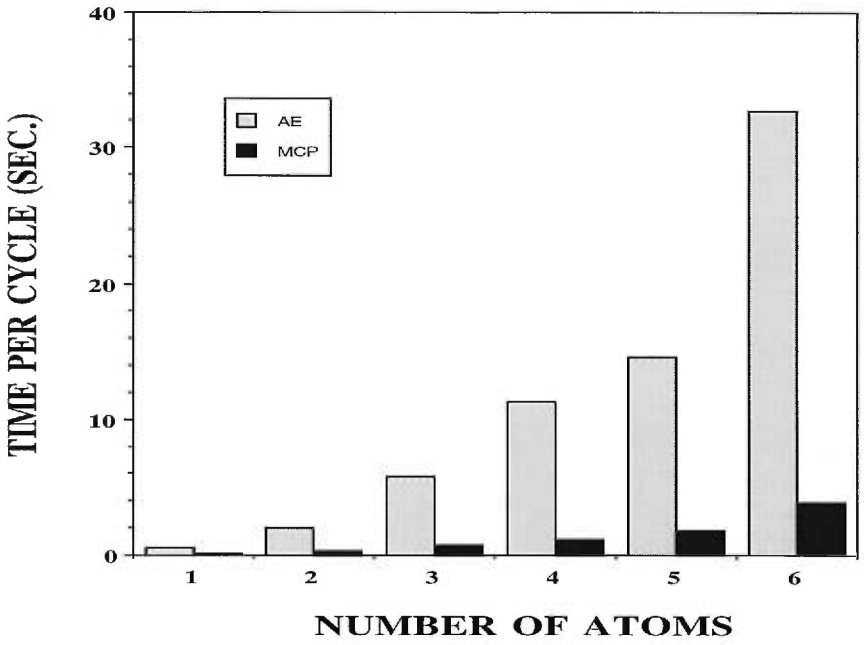

Figure 4. Comparison of the central processing unit time used per self-consistent field cycle in energy calculations of Na_n ($n \leq 6$) at the MCP and all-electron (AE) levels. All calculations were performed on a Silicon Graphics Challenge computer with R4000 processors.

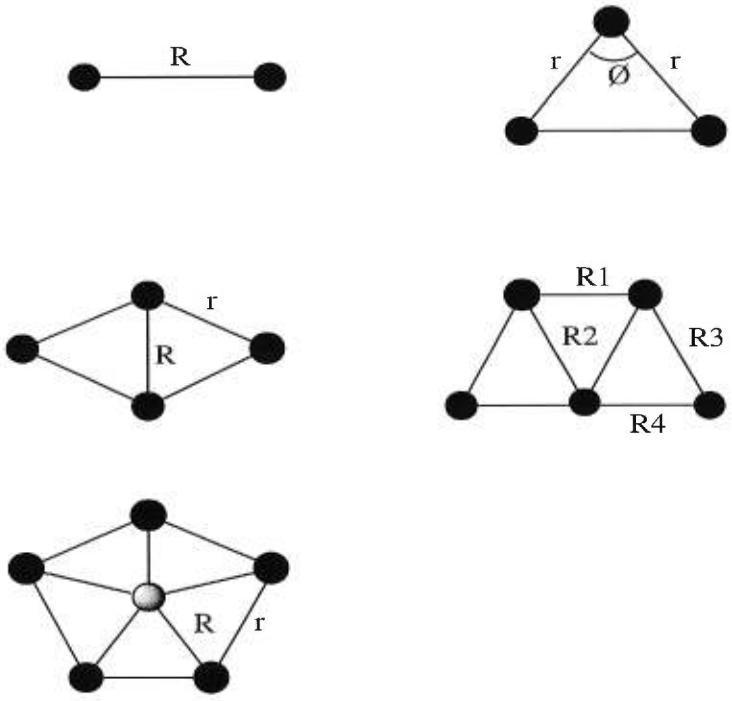

Figure 5. Structure parameters of the sodium clusters are defined here. The specific geometrical parameters are given in Table X and XI .

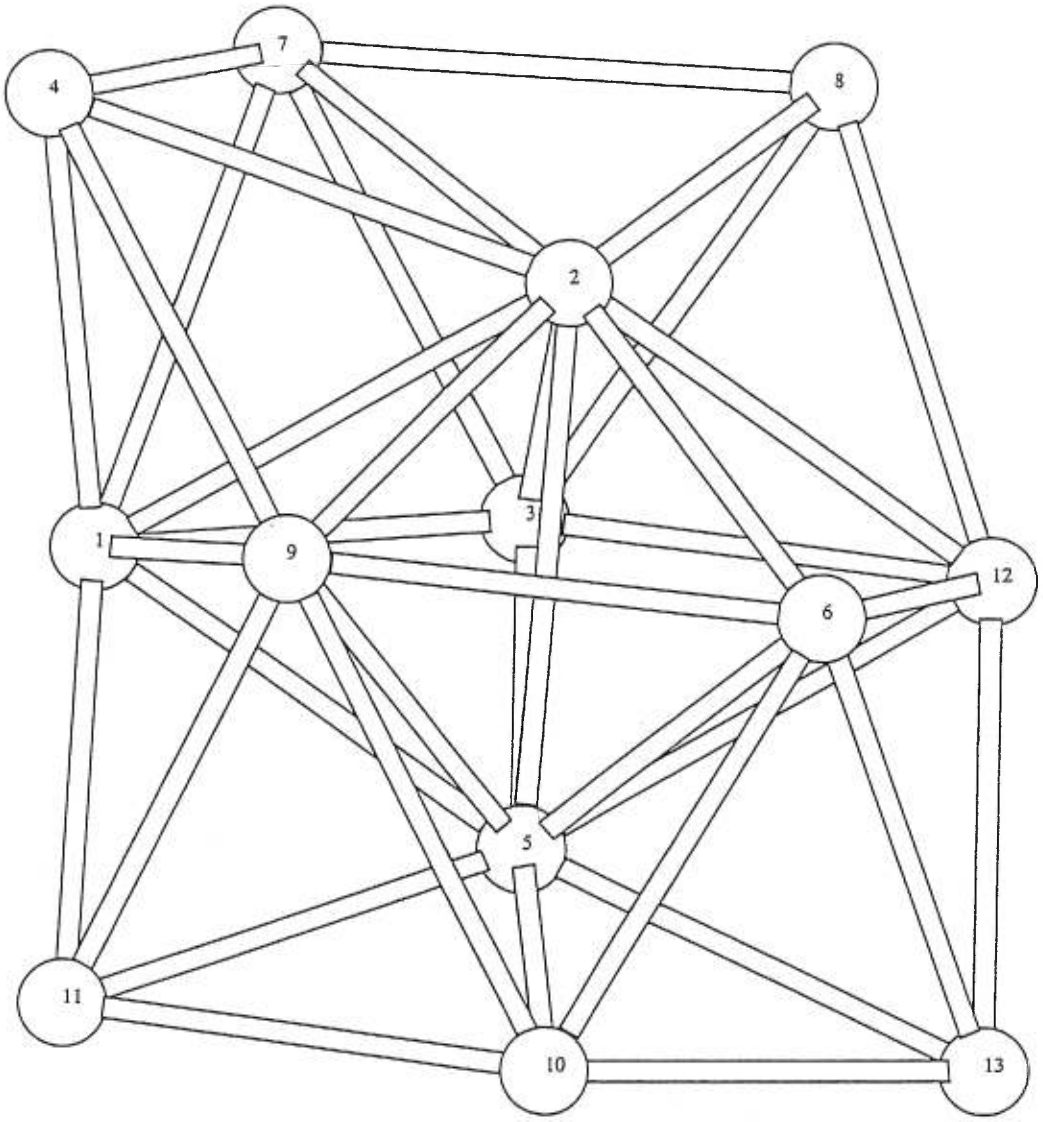

Figure 6. Optimized sodium tridecamer doublet geometry obtained at the MCP LDAxc level in the present work. Lines connect nearest neighbors. The geometric coordinates and nearest-neighbor distances are given in Table XVII and XVIII.

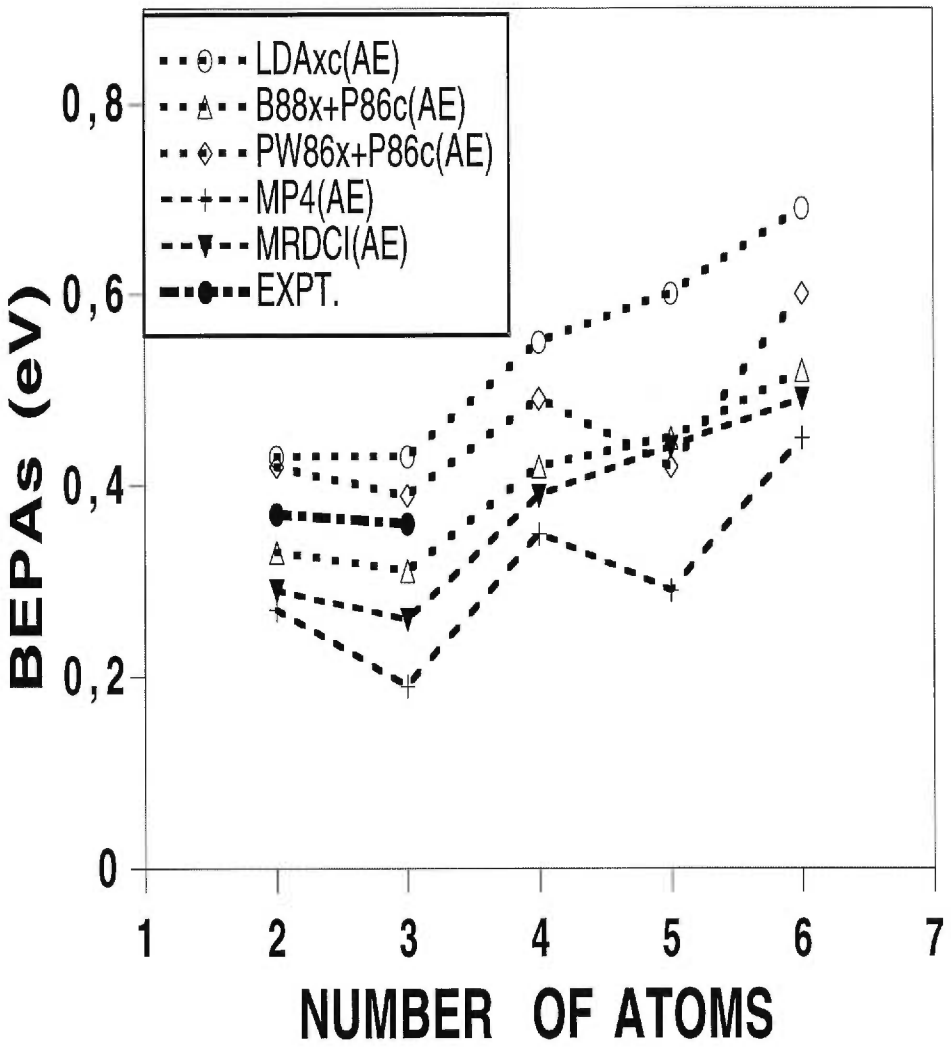

Figure 7. Comparison of the all-electron binding energy per atom carried out by the LDAxc, the PW86x+P86c, and the B88x+P86c functionals with experimental values and the results of all-electron (AE) multireference double configuration interaction (CI) [3, 4] and fourth order Møller-Plesset perturbation theory (MP4) [5].

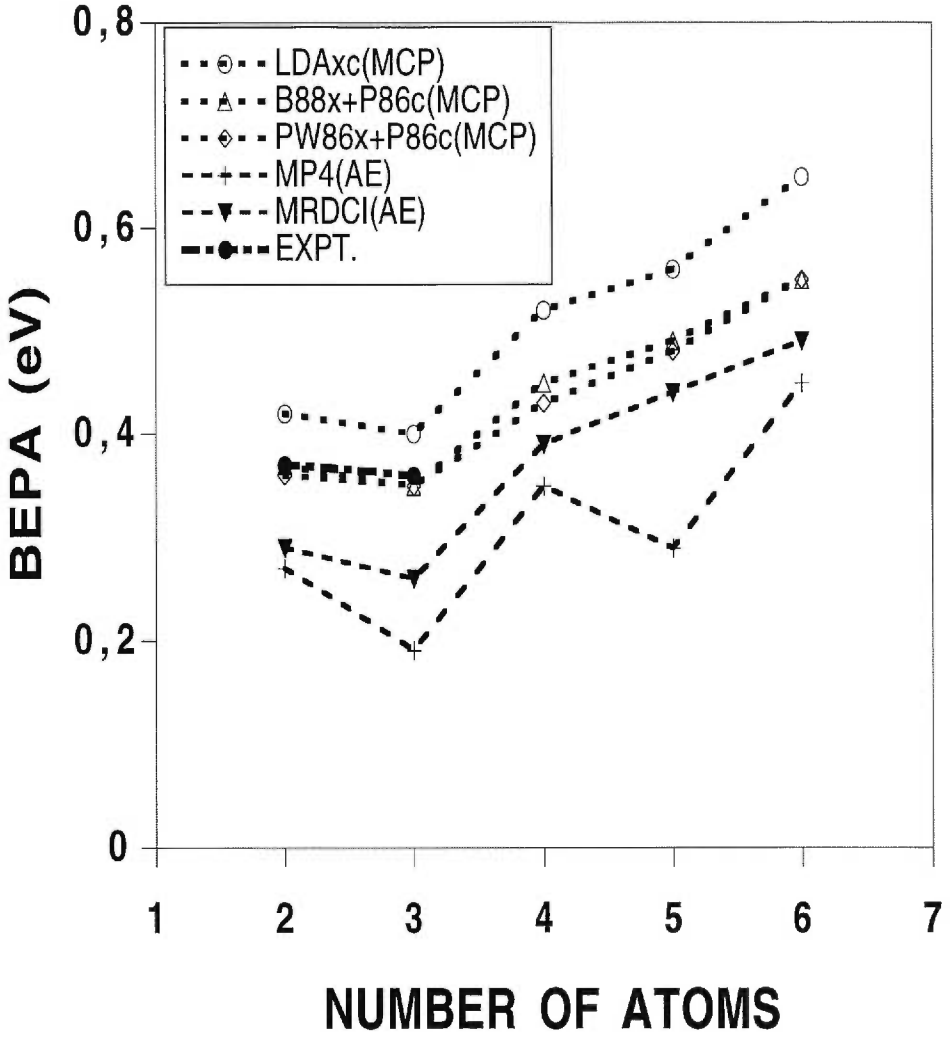

Figure 8. Comparison of the MCP binding energy per atom carried out by the LDAxc, the PW86x+P86c, and the B88x+P86c functionals with experimental values and the results of all-electron (AE) multireference double configuration interaction (CI) [3, 4] and fourth order Møller-Plesset perturbation theory (MP4) [5].

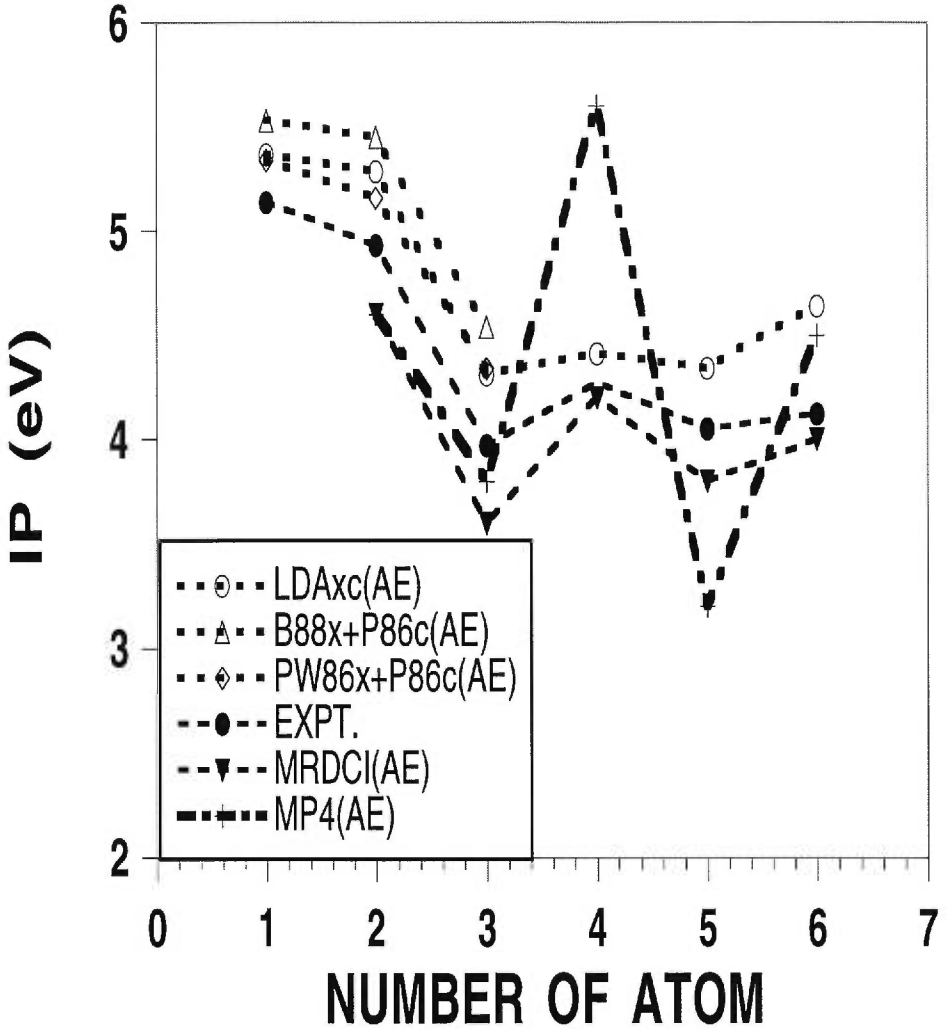

Figure 9. Comparison of the all-electron vertical ionization potentials (IPs) calculated by the LDAxc, the PW86x+P86c, and the B88x+P86c functionals with all-electron (AE) multireference double configuration interaction vertical IPs from Ref. [3], fourth-order Møller-Plesset perturbation theory vertical IPs from Ref. [5], as well as experimental (adiabatic) IPs from Ref. [6].

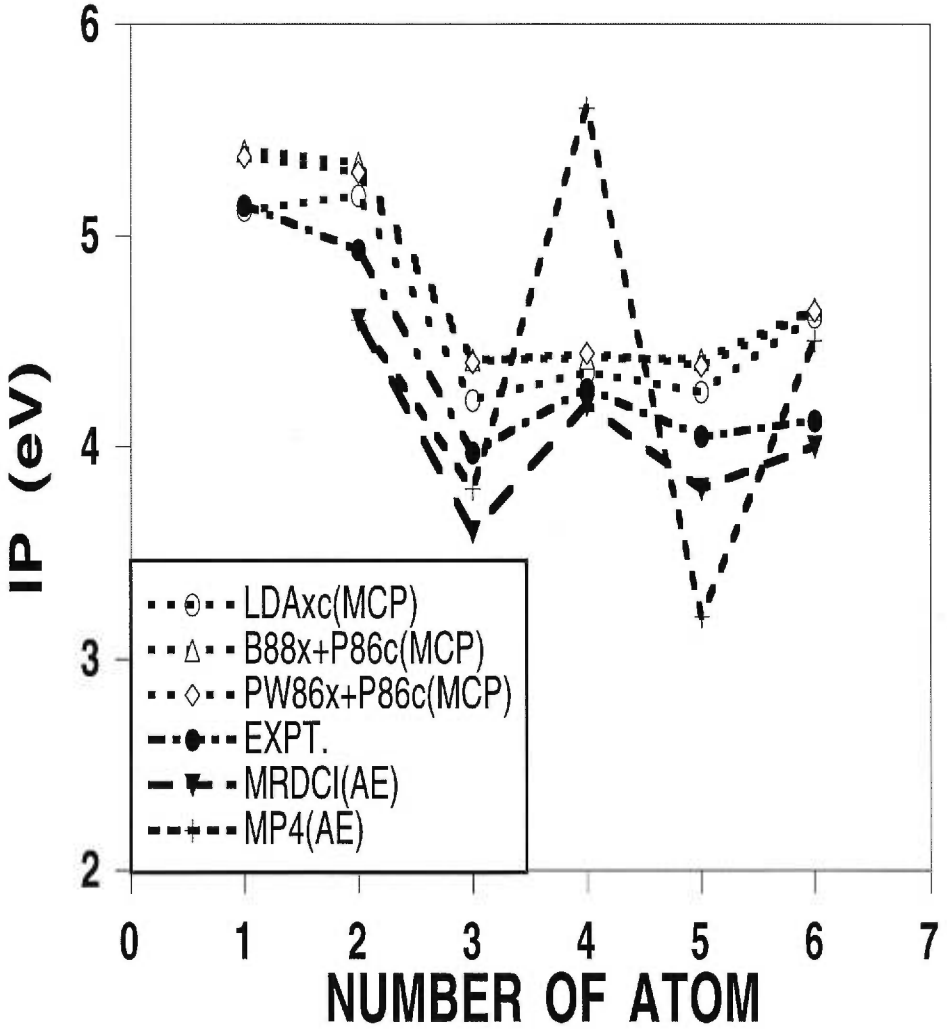

Figure 10. Comparison of the MCP vertical ionization potentials (IPs) calculated by the LDAxc, the PW86x+P86c, and the B88x+P86c functionals with all-electron (AE) multireference double configuration interaction vertical IPs from Ref. [3], fourth-order Møller-Plesset perturbation theory vertical IPs from Ref. [5], as well as experimental (adiabatic) IPs from Ref. [6].

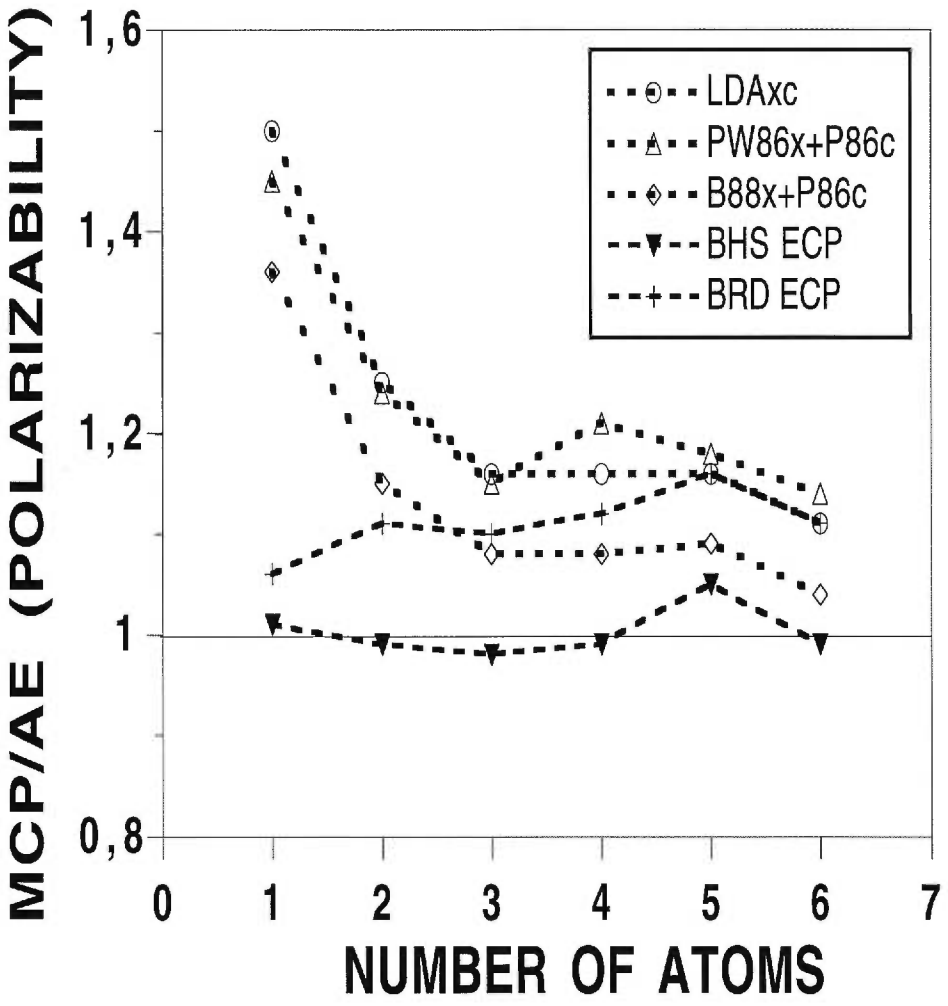

Figure 11. MCP polarizabilities calculated with the LDAxc, the PW86x+P86c, and the B88x+P86c functionals and the previously reported ECP [7, 8] mean polarizabilities divided by the all-electron (AE) mean polarizabilities calculated using corresponding functional versus size of sodium clusters.

CHAPTER 5

TIME–DEPENDENT DENSITY–FUNCTIONAL THEORY INVESTIGATION OF EXCITATION SPECTRA OF OPEN–SHELL MOLECULES

5.1 INTRODUCTION

Time-dependent density-functional response theory (DFRT) is a prototype of the successful implementation of time-dependent density-functional theory (DFT) [138, 139, 156, 167, 168, 169]. It plays an important role in the study of dynamic response properties, such as electronic excitation spectra, dynamic polarizabilities and hyperpolarizabilities, and van der Waals coefficients. The applications of time-dependent DFRT have been impressive for atoms [20, 21, 139, 160, 173, 174, 384, 385], the solid state [176, 386], metal clusters with a jellium sphere model [194, 195, 196, 197, 198] and the spherical average pseudopotential model [186, 199, 200], as well as closed-shell molecules [22, 33, 34, 36, 37, 173, 182, 183, 184]. The calculation of photoabsorption cross-sections for rare gas atoms was first performed by Zangwill and Soven [160]. Nuroh, Stott, and Zaremba [384] calculated photoabsorption spectra for barium and its ions. The C_6 van der Waals coefficients between all pairs of fourteen different ions have been studied with time-dependent DFRT by Mahan [385]. Time-dependent DFRT calculations of frequency-dependent dielectric constants of the solid state were made by Baroni, Giannozzi, and Testa [386], and by Levin and Allan [176].

These atomic calculations and solid state studies are well established, but the algorithm is difficult to extend to molecules because spherical symmetry is lost in molecules. However, Levine and Soven [173, 182] have tried to keep the advantages of the atomic-like algorithm and used single-center expansions to calculate time-dependent response properties for small molecules. This single-center expansion algorithm is unsuitable for general molecular applications. An algorithm suitable for general molecules has been recently proposed in a few groups, in the Salahub group [29, 30, 183, 387], the Baerends group [31, 184, 201, 202, 388], the Ahlrichs group [22, 33], and the Handy group [32, 35], etc. This algorithm has been used to study time-dependent molecular properties, such as frequency-dependent polarizabilities and hyperpolarizabilities [31, 184, 201, 202, 389], van der Waals dispersion coefficients [31, 390], Raman scattering [388], and excitation energies [22, 29, 33, 36, 37, 183, 387]. All these molecular calculations have been for closed-shell molecules. The time-dependent DFRT treatment of open-shell molecular excitations has been an open question. Recently Hirata and Head–Gordon [1] reported calculations of the lowest two excitation energies for open-shell molecules, such as diatomic radicals, CN, CO^+, BeH and BeF, as well as some organic radicals by time-dependent DFT. But only for the first two excitation energies, no higher excitations and no oscillator strengths were given. The present study provides a unique time-dependent DFRT study of excitation energies and oscillator strengths of such open-shell molecules.

Open-shell molecules play an important role in chemistry and astrophysics. The CN radical is an essential intermediate in flame chemistry as well as being of considerable astrophysical significance [391]. The spectral properties of the CN radical can provide information about the photochemical history of molecules in comets, it can also be used as an indication of the atomic nitrogen abundance in red giant stars [392]. CO^+ is a prominent component of the spectra of comets. on the other hand, the first-row diatomic hydrides are also the simplest heteronuclear diatomic molecules, since they only have a few electrons (e.g. BeH).

The excitation spectra of these free radicals have been studied by traditional *ab initio* methods. For the simplest heteronuclear molecule, BeH, a few low-lying transitions were calculated by the configuration interaction (CI) method [393, 394, 395], the adiabatic and quasiadiabatic first five $^2\Sigma^+$ states of BeH were studied by Petsalakis, *et al.* [396]. There are few theoretical calculations of transition energies of BeF; however, some spectroscopic constants and potential energy curves have been studied at the post-Hartree-Fock level by many authors [397, 398, 399, 400, 401, 402, 403, 404, 405, 406]. The CN radical has been extensively studied. Washida, Kley, Becker, and Groth [407] have observed potential energy curves for $X^2\Sigma, A^2\Pi, B^2\Sigma, D^2\Pi$ and for $J^2\Delta$ states. The quartet states have been studied by Coxon, Ramsay, and Setser [408] and by Miller, Freund, and Field [391]. The theoretical studies of low-lying doublet states have been computed by the multiconfiguration self-consistent field (MCSCF) approach [409], by the singles and doubles excitations configuration interaction (SDCI) method [410], by a full valence configuration interaction (FVCI) procedure [411, 412] and by the singles and doubles coupled cluster method [413]. The quartet states have also been undertaken by the configuration interaction (CI) method [414], by the MCSCF method [415], and by the multireference (single) and double-excitation configuration interaction (MRD-CI) approach [416]. A detailed review of the CN radical has appeared in the literature [417]. The electronic structure and excitation energies of CO^+ have been the subject of renewed interest in recent years [418, 419, 420, 421, 422, 423, 424, 425, 426, 1]. Four states, $1^2\Sigma^+(X^2\Sigma^+), 1^2\Pi(A^2\Pi), 2^2\Sigma^+(B^2\Sigma^+)$, and the $1^2\Delta(C^2\Delta)$ state, were unambiguously identified by emission spectroscopy [379]. The other two states, $2^2\Pi(D^2\Pi)$ and $3^2\Sigma^+(G^2\Sigma^+)$ states, were determined by photoelectron spectroscopy [427]. Honjou and Sasaki [419] calculated excitation energies using SCF–full valence CI approach and with a minimal STO basis set agrees reasonably with experiment. Lavendy *et al* [424] with MCSCF–CI method and with an extended GTO basis set underestimated excitation energies. Honjou and Miyoshi [426] have

recently reported that the lowest Rydberg states are $4^2\Sigma^+$ and $5^2\Sigma^+$ states at about 18 eV above the ground state of CO^+. N_2^+ [428, 429, 430, 431] has also been the subject of experimental and theoretical investigations. Five valence states, $1^2\Sigma_g^+(X^2\Sigma_g^+)$, $1^2\Pi_u(A^2\Pi_u)$, $1^2\Sigma_u^+(B^2\Sigma_u^+)$, $1^2\Pi_g(D^2\Pi_g)$, and $2^2\Sigma_u^+(C^2\Sigma_u^+)$, were identified unambiguously [379]. The four lowest $^2\Sigma_g^+$ states, the three lowest $^2\Sigma_u^+$ states, and the three lowest $^2\Pi_u$ states of N_2^+ have been studied by the CI approach [432, 433, 434, 431] and by the multiconfigurational electron propagator (MCEP) method [435]. There are only a few studies [336, 436, 437] of all these radicals simultaneously. Unrestricted CI singles (UCIS) and restricted open-shell CIS (ROCIS) have been used to study these open-shell radicals [336] and overestimated the first two excitation energies by 2.5 eV – 5.5 eV. It is believed that this deviation may be caused by the lack of double excitations in the UCIS and ROCIS [336, 438, 437] methods. Since extended CIS (XCIS), which includes doubly excited configurations, improved the results, but it still overestimated the lowest two excitation energies by 1.0 eV – 2.5 eV, it seems that more highly excited configurations are needed. The simpler and more efficient time-dependent DFT calculations of these first two excitation energies have been reported recently by Hirata and Head-Gordon [1] and have given encouraging results. Nevertheless, they only gave the first two excitation energies. Moreover, there is no time-dependent DFT study of oscillator strengths of such open-shell molecules reported in the literature. This work provides the first simultaneous time-dependent DFRT study of excitation spectra (excitation energies and oscillator strengths) of all these open-shell radicals.

5.2 COMPUTATIONAL DETAILS

The excitation energies and oscillator strengths are computed using version 2pX of the time-dependent DFT program *deMon–DynaRho* [208]. The version 2pX permits to calculate excited state properties for open–shell systems, this

differs from previous version 1 or version 2p0 which only treat the closed–shell systems.

The experimental geometries [379] of the six chosen small molecules have been used in the present calculations. For CO^+ and N_2^+, both the cation geometries and the neutral minimum geometries of CO and N_2 are used. Whereas only neutral minimum geometry of H_2CO is used for the H_2CO^+ calculations. Table XXII(please note that Tables and Figs. are given at the end of the chapter) gives the geometrical parameters for these chosen molecules.

All of the calculations used Gaussian-type orbital basis sets, specifically Sadlej and Urban orbital basis sets [439, 334] (referred to as Sadlej bases). In order to test the quality of the Sadlej bases for excitation energy calculations for the chosen molecules, more diffuse functions [387] have been added for H, C, N, and O. These new bases are referred to as the extended Sadlej bases (XB). The auxiliary basis sets are taken from the *deMon–KS* basis library, in particular, the auxiliary basis (4,2;4,2) is used for H, (4,3;4,3) for Be, and (4,4;4,4) for C, N, O, and F.

The grid used in the present calculations is EXTRA-FINE (with 32 radial grid points and 194 angular grid points at each radial sphere) with the Non-Random option, since the Random grid may cause symmetry breaking in the post-SCF calculations. This was tested in the sodium trimer excitation calculations (see Chapter 7 of this thesis). The SCF calculations were performed using version 1.2 of the program *deMon–KS* [367]. The convergence criteria used for the SCF calculations correspond to a change in the total energy of less than 10^{-8} hartree and a change in the charge density fitting coefficients of less than 10^{-7} a.u., since the charge density convergence is much more difficult to achieve than the total energy.

The exchange-correlation functionals used in the program *deMon-DynaRho*

can be different at the SCF step and at the post-SCF step, which is used to construct the coupling matrix. In the present calculations the local spin density approximation (LSDxc) is used at the SCF step and the time-dependent LSDxc (TDLSDxc) is used at the post-SCF step. This is denoted as LSDxc/TDLSDxc. Alternatively, van Leeuwen and Baerends proposed an exchange-correlation functional in 1994 (LB94xc) [212] which is also used in the SCF step along with the time-dependent LSDxc used at the post-SCF step (LB94xc/TDLSDxc).

5.3 RESULTS AND DISCUSSION

Six small well studied open-shell molecules, three neutral molecules (BeH, BeF, CN) and three positive ions (CO^+, N_2^+, CH_2O^+), have been chosen to evaluate the quality of the time-dependent DFT for the calculation of excitation spectra of open-shell molecules. With the exception of the lowest two excitation energies (without oscillator strengths) of a few open–shell molecules (BeH, BeF, CN, and CO^+) calculated by the time-dependent DFT which recently appeared in the literature [1], the present calculations of excitation spectra (excitation energies and oscillator strengths) of open–shell molecules are the first time-dependent DFT study reported in the literature. However, these small molecules (BeF, CN, CO^+, and N_2^+ belong to the diatomic 13–electron sequence) have been well studied by conventional *ab initio* methods. The present calculations of excitation spectra for the six chosen small open-shell molecules with the LSDxc/TDLSDxc and the LB94xc/TDLSDxc functionals are shown in Fig. 12, 13 14, 15, 17, 18, 20, 21, 23, 24, 26, and 27 (please note that Figs. and Tables are given at the end of the chapter). The present calculated excitation energies compared with conventional *ab initio* results and with available experiments are given in Tables XXIV, XXVI, XXVIII, XXX, XXXII, and XXXIV. Some occupied and virtual orbital energies for both α and β spins of each molecule with symmetry assignments are listed in Tables XXV, XXVII, XXIX, XXXI, XXXIII, and XXXV.

The potential energy curve for CH_2O^+ is shown in Fig. 29. The ground state configurations of the six chosen molecules obtained from the present DFT SCF calculations with both LSDxc and LB94xc functionals are shown in Table XXIII. The LSDxc and the LB94xc functional give the same ground state configurations. The BeH, CN, CO^+, and N_2^+ configurations are the same as those known experimentally [440], while the CO^+ configuration differs from that calculated from the full valence configuration interaction [419] (FVCI) method with a minimum STO basis set by changing the order of the 5σ and the 1π orbital. The BeF has the 4σ orbital above the 1π orbital, leading to a configuration different from its sequence partners (CN and CO^+), which are supposed to have the same configuration as CN and CO^+ by experiment [440].

Occupied orbital energies and bound virtual orbital energies of the six small molecules are well converged with the Sadlej basis set in comparison with those of the extended Sadlej basis. The deviations of the orbital energies for the Sadlej basis and the extended Sadlej basis are generally less than 0.05 eV. However, bigger differences occur for higher unbound virtual orbitals. This indicates that unbound virtual orbitals are sensitive to the diffuse basis functions, hence these unbound virtual orbitals are related to the long–range part of the potential. This has been illustrated for the CN molecule (see Table XXIX). Moreover, the orbital energies are much more sensitive to the exchange–correlation functional used. The orbital energy difference between the LSDxc and the LB94xc functionals can be as large as 28 eV for the lowest occupied orbitals. For the valence orbitals, this deviation is about 5 eV. However, adjacent orbital energy differences are very similar (in most cases the deviation is less than 0.5 eV) for the LSDxc and the LB94xc functionals. Nevertheless, the HOMO (highest occupied molecular orbital) energy from the LSDxc functional is too high (ionization energy, $-\epsilon_{HOMO}^{LSDxc}$, is too small) in comparison with the experimental ionization potential. This difference can be as large as 5 eV (see orbital energy tables for the chosen molecules). It is believed that this error is associated with the incorrect long–range behavior

of the LSDxc functional. In contrast, a functional with the correct asymptotic behavior, such as the LB94xc functional, does correct this error and leads to an approximately correct ionization potential. The $-\epsilon_{HOMO}^{LB94xc}$ differs from the experimental ionization potential by about 0.5 eV (see Table XXV, XXIX, and XXXI), except for N_2^+ for which it differs by 1.6 eV. It can be seen that the asymptotic behavior of exchange–correlation functionals also affects the number of bound virtual orbitals. The LSDxc functional, with an incorrect long–range behavior, gives only 2 to 3 bound virtual orbitals (orbital degeneracies are counted) for the chosen molecules (BeH, BeF, CN), while the LB94xc functional, with correct asymptotic behavior, produces many more bound virtual orbitals. It yields 11 to 15 bound unoccupied molecular orbitals. For the positive ions (CO^+, N_2^+, CH_2O^+) the LSDxc functional supports 11 to 16 bound virtual orbitals, while the LB94xc functional gives 18 to 23. This indicates that the LSDxc potential is more shallow than that of LB94xc.

The lowest eight vertical excitation energies for CN, CO^+, and N_2^+ as well as the fifteen vertical excitation energies for CH_2O^+ calculated with the Sadlej basis and with the extended Sadlej basis set show that the Sadlej basis set is flexible enough (within the limit of s-, p-, and d-type basis functions) to describe the low excitations of CN, CO^+, N_2^+, and CH_2O^+. The excitation energies calculated with the Sadlej basis and the extended Sadlej basis for all eight excited states (fifteen for CH_2O^+) differs by 0.005 eV at most, except for the $4^2\Pi$ state of CN (0.3 eV) and for the 4^2A_2 state of CH_2O^+ (0.22 eV). However, it is necessary to use the more diffuse basis functions for the higher excitations, since the excitation energies can change by 0.8 eV for the $5^2\Sigma^+$ state of N_2^+ when the diffuse basis functions are added.

Fig. 19 and 20, Fig. 22 and 23, Fig. 26 and 25 show that the Sadlej basis and the extended Sadlej basis give the same pattern for the excitation spectra of the chosen positive ions (CO^+, N_2^+, and CH_2O^+). The difference for the

oscillator strength caused by the diffuse function in the extended Sadlej basis is less than 0.008. However, the diffuse basis functions in the extended Sadlej basis do have a large effect on the CN excitation spectra, as can be seen from Fig. 17 and 18. The oscillator strengths differ by as much as 0.1 for the $5^2\Sigma^+$ state and the pattern of the spectra also changed dramatically.

The vertical excitation energies for the first eight excited states of CO^+ and N_2^+ with the cation geometry and the corresponding neutral geometry of CO and N_2 are shown in Table XXX and XXXII. The bond length difference between the neutral and the cation geometries is 0.013 $\mathring{A}$ and 0.019 $\mathring{A}$ for CO^+ and the N_2^+, respectively. This bond length difference affects the excitation energies by no more than 0.3 eV in both calculations for CO^+ and N_2^+, regardless of the functional used in the calculations. It is interesting to note that the excitation energies of CO^+ with the cation geometry are larger than those with the neutral geometry by 0.16 eV. In contrast, the calculation with the N_2^+ cation geometry underestimates the excitation energies by 0.2 eV in comparison with the neutral geometry calculation.

The LSDxc/TDLSDxc functional gives good excitation energies, when they are below the ionization threshold, $-\epsilon_{HOMO}^{LSDxc}$. The average error between calculated excitation energies and experimental results is less than 0.8 eV for BeH, BeF, CN and CO^+ molecules. However, some excitation energies are underestimated by about 1.3 eV if the transition arrives at π type virtual orbitals, for example, the $2^2\Pi$ ($3\sigma^+ \longrightarrow 2\pi$) state for BeH, and $3^2\Sigma^+$ ($1\pi \longrightarrow 2\pi$), $1^2\Delta$ ($1\pi \longrightarrow 2\pi$), $2^2\Pi$ ($5\sigma^+ \longrightarrow 2\pi$), and $2^2\Delta$ ($1\pi \longrightarrow 2\pi$) states for CN. All these states arrive at π type orbitals and all these transitions have errors larger than 1.0 eV. The difference between the experiment and calculations is not due to the comparison of the adiabatic (experiment) and the vertical (calculations) transitions, since the experimental adiabatic excitation energies are converted to vertical excitation energies here according to Morse potential.

There is an ordering change with the LSDxc/TDLSDxc functional after the fourth transition in most cases in comparison with those of the LB94xc/TDLSDxc functional. The $2^2\Pi$ state has fallen below the $4^2\Sigma^+$ state, and $3^2\Pi$ state moves above $5^2\Sigma^+$ state in BeH. The $4^2\Sigma^+$ state and $1^2\Delta$, $3^2\Pi$ and $5^2\Sigma^+$ states change order in BeF. This ordering change also occurred for CO^+ and CH_2O^+. (See Tables XXIV, XXVI, XXVIII, XXX, XXXII, and XXXIV). However, both the LSDxc/TDLSDxc and the LB94xc/TDLSDxc functionals give the order of the $3^2\Sigma_u^+$ and the $2^2\Sigma_g^+$ states of N_2^+ different from experiment [441] and *ab initio* CI [432, 433, 442, 431] and MECP [435] (Multiconfigurational electron propagator) results.

The LB94xc/TDLSDxc functional gives better excitation energies for higher transitions. Especially when the excitation energies are larger than the LSDxc ionization potential threshold ($-\epsilon_{HOMO}^{LSDxc}$), the LB94xc/TDLSDxc functional leads to excitation energies in better agreement with available experiment. It can be seen for BeH (Tables XXIV) that for excitation energy under $-\epsilon_{HOMO}^{LSDxc}$, the LB94xc/TDLSDxc functional gives a larger error (0.33 eV for $1^2\Pi$) than does the LSDxc/TDLSDxc functional (0.09 eV for $1^2\Pi$). In contrast, for excitation energies above $-\epsilon_{HOMO}^{LSDxc}$, the LB94xc/TDLSDxc functional leads to smaller errors (0.5 eV for $2^2\Pi$, 1.0 eV for $4^2\Pi$) in comparison with the LSDxc/TDLSDxc functional (1.5 eV for $2^2\Pi$, 1.7 eV for $4^2\Pi$).

Fig. 12, 13 14, 15, 17, 18, 20, 21, 23, 24, 26, and 27 show that oscillator strengths are sensitive to the exchange-correlation functional used for the neutral molecules (BeH, BeF, and CN). In contrast, the functional has little effect on the oscillator strengths for the positive ions (CO^+, N_2^+, and CH_2O^+). For example, the $4^2\Sigma^+$ state of BeH is a small peak in the LSDxc/TDLSDxc case, but it becomes a large peak if the LB94xc/TDLSDxc functional is used. The $4^2\Pi$ state of CN shows a similar change.

Excitation energies of CO^+ with the neutral geometry of CO and the LS-

Dxc/TDLSDxc functional are underestimated by 0.27 eV for the $1^2\Pi$ state, 0.8 eV for the $2^2\Sigma^+$ state, and by 0.5 eV for the $1^2\Delta$ state. The LB94xc/TDLSDxc functional gives excitation energies with errors that are twice as large for these excited states. However, if the cation geometry is used and with the LSDxc/TDLSDxc functional, the excitation energies differ from the experiment by 0.1 eV for the $1^2\Pi$ state, and 0.2 eV for the $1^2\Delta$ state. However, the excitation energy seems to yield no improvement for the $2^2\Sigma^+$ state. This deviation or even larger errors can also be observed for traditional *ab initio* calculations. The UCIS (unrestricted configuration interaction singles) and ROCIS (restricted open–shell CIS) calculations [336] overestimated the first two excitation energies ($1^2\Pi$ and $2^2\Sigma^+$ states) by 2.5 eV – 5.5 eV. Even the XCIS (extended CIS) method [437] which considers doubly excited configurations still overestimated excitation energies by 1.0 eV – 2.5 eV. Full CI [443] and symmetry-adapted-cluster CI (SACCI) [443] gave the first two excitation energies ($1^2\Pi$ and $2^2\Sigma^+$ states) close to experiment with the error being 0.1–0.2 eV. But for the $1^2\Delta$ state, the error is about 2.0 eV.

Excitation energies of N_2^+ show the largest deviation from experiment. The LSDxc/TDLSDxc calculation with neutral geometry shows that the first three $^2\Pi_u$ excitation energies differ from experiment by 0.2 – 3.5 eV (3.5 eV for the $2^2\Pi_u$ state) and the lowest three $^2\Sigma_u^+$ transitions have errors of 0.1 – 1.7 eV (1.7 eV for the $2^2\Sigma_u^+$ state). The biggest error is 4.6 eV for the $2^2\Sigma_g^+$ state. The LB94xc/TDLSDxc functional gives very similar results as the LSDxc/TDLSDxc functional. These states seem also to be hard to calculate with conventional *ab initio* methods. CI [442] with Gaussian basis functions gave an error of 1.2 eV for the $2^2\Pi_u$ state, 1.9 eV for the $2^2\Sigma_u^+$ state, 1.3 eV for the $2^2\Sigma_g^+$ state, and 3.1 eV for the $3^2\Sigma_u^+$ state (the LSDxc/TDLSDxc got this state right with the error being 0.1 eV, while MCEP gave an error of 5.4 eV). However, CI [431] with STO basis functions and f–type basis functions reduced the error to less than 1 eV. This seems to suggest that higher polarization functions are needed, such as f–type functions, for this calculation.

Table XXXIV shows that fifteen excitation energies of CH_2O^+ calculated with the LSDxc/TDLSDxc functional are underestimated by about 1 eV (2.5 eV for 4^2B_1 state) in comparison with available MRD-CI results [9]. This is not so surprising, since CI overestimates excitation energies for the other molecules (CO^+, N_2^+, CN, BeF, and BeH) in comparison with experiments. However, the excited states arise from the same excitation between the present work and the MRD-CI calculations [9]. $^2B_2$ states arise from the excitation $b_2 \longrightarrow b_2$ or $b_1 \longrightarrow b_1$. $^2B_1$ states are from the excitation $b_1 \longrightarrow b_2$ or $b_2 \longrightarrow b_1$. $^2A_1$ states are from transition $a_1 \longrightarrow b_2$ or $b_2 \longrightarrow a_1$. $^2A_2$ states arise from the excitation $a_1 \longrightarrow b_1$ or $b_1 \longrightarrow a_1$. The LB94xc/TDLSDxc calculations yields the lowest fifteen excitation energies smaller than those of the LSDxc/TDLSDxc, this observation is the same as for other molecules discussed above, since these fifteen excitation energies are below $-\varepsilon_{HOMO}^{LSDxc}$.

Excitation spectra of CH_2O^+ (Fig. 26, and 27) show that the LSDxc/TDLSDxc and the LB94xc/TDLSDxc functionals give similar spectroscopic patterns for CH_2O^+. The first two medium peaks are assigned to 2^2B_2 and 2^2A_1 states, the strongest peak is the 4^2B_2 state and followed by the 5^2B_2 state with the LSDxc/TDLSDxc functional. However, the 4^2B_2 and 5^2B_2 states derived from the LB94xc/LSDxc functional have similar height (similar oscillator strengths) and the 5^2B_2 peak is a little larger than the 4^2B_2 band. MRD-CI calculations by Bruna, Hachey, and Grein [9] yield a spectrum (Fig. 28) similar as the present calculations. They produced the 4^2B_2 state as the largest peak; however, the 5^2B_2 state does not appear in the MRD-CI spectrum.

The potential energy curve of CH_2O^+, Fig. 29, shows that there is an avoided crossing between the 2^2B_2 and the 3^2B_2 states at about the bond length of the minimum geometry ($R_{CO} = 1.2078\mathring{A}$). This observation is the same as that found by the MRD-CI method [9]. Moreover, the 2^2B_2 state curve calculated by the present work does not have a flat tail in the given energy range, this behavior is

different from the MRD-CI calculations [9] which show a large flat tail for the 2^2B_2 state (see Fig. 30). The present work also found that the 2^2B_1 and the 1^2A_1 states have a minimum around the equilibrium geometry, the 1^2B_1, the 3^2B_2, and the 1^2A_2 states have a minimum at about $R_{CO} = 1.3\mathring{A}$, while the 2^2B_2 and the 3^2B_1 states have a minimum around $R_{CO} = 1.4\mathring{A}$.

5.4 CONCLUSION

The present work has implemented time-dependent DFT for open-shell systems in the program *deMon-DynaRho*, version 2pX. This implementation provides a unique practical molecular time-dependent DFT code capable of treating excited state properties for open–shell molecules or clusters. As a case study, excitation spectra of the six small open–shell molecules (three neutral molecules, BeH, BeF, and CN and three positive ions, CO^+, N_2^+, and CH_2O^+) have been carried out by the present calculations with the new modified code. The results show that time-dependent DFT can treat open–shell systems fairly well. The excitation spectra calculated with both the LSDxc/TDLSDxc and the LB94xc/TDLSDxc functionals are comparable with traditional *ab initio* methods. The time-dependent DFT with the LSDxc/TDLSDxc and the LB94xc/TDLSDxc functionals underestimate excitation energies by about 1.0 eV compared to the available experimental results for the low lying transitions of the six chosen small open–shell molecules. In contrast, conventional *ab initio* calculations, such as MRCI [411, 432, 419, 433, 434, 421, 146, 431] and MCEP [435] overestimate the excitation energies by about 0.5 eV for the molecules studied here. While CIS calculations of excitation energies are much larger than experiment [336, 437], especially for CN and CO^+ radicals, the CIS results are about 3 – 5 eV larger than the measurements, even when double excitations are considered, the extended CIS (XCIS) [437], excitation energies are still overestimated by around 1.5 eV.

The LSDxc/TDLSDxc functional does fairly well for the low lying excitation

energies, especially when the excitation energies are below $-\varepsilon_{HOMO}^{LSDxc}$. At above $-\varepsilon_{HOMO}^{LSDxc}$, excitation energies collapse with the LSDxc/TDLSDxc functional, this arise from the incorrect long-range behavior of the LSDxc functional. In contrast, the LB94xc/TDLSDxc functional, with correct asymptotic behavior, does correct this problem and gives better results for the higher transitions. But the LB94xc/TDLSDxc functional yields too small excitation energies for the low excitations.

The medium size Sadlej basis is flexible enough to describe the low–lying excitation energies for the six chosen small molecules. However, for higher transitions, such as Rydberg state calculations, more diffuse basis functions must be included.

Table XXII. Experimental geometries[a] of the six chosen small molecules used in present calculations.

Molecules	Symmetry	bond length[b] (Å)	Bond angle[b](degree)
BeH	$C_{\infty v}$	R_e (BeH) = 1.3426	
BeF	$C_{\infty v}$	R_e (BeF) = 0.9697	
CN	$C_{\infty v}$	R_e (CN) = 1.1718	
CO^+	$C_{\infty v}$	R_e (CO) = 1.1151 (1.1283)	
N_2^+	$D_{\infty h}$	R_e (NN) = 1.1164 (1.0977)	
CH_2O^+	C_{2v}	R_e (CO) = (1.2078)	$\angle$(HCH) = (116.57)
		R_e (CH) = (1.1161)	

[a] Taken from Ref. [379].

[b] The number in parentheses is the corresponding neutral geometry structure parameter.

Table XXIII. Ground state configurations for the six chosen molecules from the present DFT SCF calculations.

Molecule	Lowest electron configuration	Ground state symmetry
BeH	$(1\sigma)^2(2\sigma)^2(3\sigma)^1$	$X^2\Sigma^+(1^2\Sigma^+)$
BeF	$(1\sigma)^2(2\sigma)^2(3\sigma)^2(1\pi)^4(4\sigma)^2(5\sigma)^1$	$X^2\Sigma^+(1^2\Sigma^+)$
CN,CO^+	$(1\sigma)^2(2\sigma)^2(3\sigma)^2(4\sigma)^2(1\pi)^4(5\sigma)^1$	$X^2\Sigma^+(1^2\Sigma^+)$
N_2^+	$(1\sigma_g)^2(1\sigma_u)^2(2\sigma_g)^2(2\sigma_u)^2(1\pi_u)^4(3\sigma_g)^1$	$X^2\Sigma_g^+(1^2\Sigma_g^+)$
CH_2O^+	$(1a_1)^2(2a_1)^2(3a_1)^2(4a_1)^2(1b_2)^2(5a_1)^2(1b_1)^2(2b_2)^1$	$X^2B_2(1^2B_2)$

Table XXIV. BeH vertical excitation energies (eV) calculated with the LSDxc/TDLSDxc and the LB94xc/TDLSDxc functionals using the Sadlej basis set[a].

	Vertical excitation energies (eV).								
State	$1^2\Sigma^+$	$1^2\Pi$	$2^2\Sigma^+$	$3^2\Sigma^+$	$2^2\Pi$	$4^2\Sigma^+$	$5^2\Sigma^+$	$3^2\Pi$	$4^2\Pi$
LSDxc/ TDLSDxc	0.000	2.391	4.593	4.771	4.858	5.129	5.418	5.671	5.732
LB94xc/ TDLSDxc	0.000	2.154	4.825	5.236	5.867	5.692	6.459	6.235	6.417
EXPT[b]	0.000	2.484			6.317				7.460[c]
PTN[d]	0.000	2.56	5.51	5.61	6.31	6.12	6.71	6.74	7.27
UCIS[e]	0.000	2.752			6.525				
ROCIS[e]	0.000	2.715			6.544				
XCIS[f]	0.000	2.661			6.468				
TDDFT[g]	0.000	2.345			4.862				

[a] (411/22) for hydrogen taken from Ref. [444] and (52111/411/11) for beryllium taken from Ref. [334].

[b] Converted from Ref [379].

[c] Converted from Ref. [445].

[d] Taken from Ref. [396].

[e] Unrestricted (non-spin-adapted) CIS (UCIS) and restricted open-shell (spin-adapted) CIS (ROCIS) taken from Ref. [336].

[f] Extended CIS (XCIS) taken from Ref. [437].

[g] Time-dependent density-functional theory (TDDFT) calculations taken from Ref. [1].

Table XXV. BeH orbital energies (eV) calculated with the LSDxc and the LB94xc functionals using the Sadlej basis.

Orbital	LSDxc[a]	LB94xc
α unoccupied orbitals energies (eV).		
$6\sigma^+$	0.86	-1.61
2π	0.29	-1.56
$5\sigma^+$	0.21	-2.12
$4\sigma^+$	0.05	-2.61
1π	-2.32	-5.87
α occupied orbitals energies (eV).		
$3\sigma^+$	-4.60(8.21)	-7.91
$2\sigma^+$	-8.37	-12.52
$1\sigma^+$	-104.32	-120.33
β unoccupied orbitals energies (eV).		
$6\sigma^+$	0.89	-1.53
2π	0.33	-1.96
$5\sigma^+$	0.25	-1.84
$4\sigma^+$	0.15	-2.85
1π	-1.59	-5.78
$3\sigma^+$	-2.90	-7.41
β occupied orbitals energies (eV).		
$2\sigma^+$	-7.99	-12.19
$1\sigma^+$	-104.06	-120.42

[a] Number in the parenthesis is ionization potential taken from Ref. [379].

Table XXVI. BeF vertical excitation energies (eV) calculated with the LSDxc/TDLSDxc and the LB94xc/TDLSDxc functionals using the Sadlej basis set[a].

	Vertical excitation energies (eV).								
State	$1^2\Sigma^+$	$1^2\Pi$	$2^2\Sigma^+$	$3^2\Sigma^+$	$2^2\Pi$	$4^2\Sigma^+$	$1^2\Delta$	$5^2\Sigma^+$	$3^2\Pi$
LSDxc/ TDLSDxc	0.000	4.366	4.770	4.929	5.274	5.574	5.951	6.013	6.114
LB94xc/ TDLSDxc	0.000	4.508	5.116	6.064	6.933	7.039	6.995	8.184	7.293
EXPT[b]	0.000	4.137	6.158	6.272					
UCIS[c]	0.000	4.268	6.356	6.600					
ROCIS[c]	0.000	4.260	6.349	6.600					
XCIS[d]	0.000	4.249	6.345	6.587					
TDDFT[e]	0.000	4.030	5.321	5.346					

[a] (411/22) for hydrogen taken from Ref. [444]. And (52111/411/11) for beryllium, taken from Ref. [334].

[b] Converted from Ref. [379].

[c] unrestricted (non-spin-adapted) CIS (UCIS) and restricted open-shell (spin-adapted) CIS (ROCIS) taken from Ref. [336].

[d] Extended CIS (XCIS) from Ref. [437].

[e] Time-dependent density-functional theory (TDDFT) calculation taken from Ref. [1].

Table XXVII. BeF orbital energies (eV) calculated with the LSDxc and the LB94xc functionals using the Sadlej basis.

Orbital	LSDxc	LB94xc
α unoccupied orbitals energies (eV).		
$8\sigma^+$	0.79	-1.01
3π	0.42	-1.15
$7\sigma^+$	0.16	-2.08
$6\sigma^+$	-0.04	-3.08
2π	-0.58	-3.91
α occupied orbitals energies (eV).		
$5\sigma^+$	-4.81	-8.16
$4\sigma^+$	-12.58	-18.93
1π	-13.18	-19.32
$3\sigma^+$	-31.22	-37.49
$2\sigma^+$	-103.88	-119.12
$1\sigma^+$	-656.38	-689.37
β unoccupied orbitals energies (eV).		
$8\sigma^+$	0.96	-0.89
3π	0.62	-1.72
$7\sigma^+$	0.24	-1.81
$6\sigma^+$	0.09	-3.58
2π	-0.08	-4.36
$5\sigma^+$	-3.12	-8.72
β occupied orbitals energies (eV).		
$4\sigma^+$	-12.55	-19.00
1π	-13.11	-19.38
$3\sigma^+$	-31.21	-37.46
$2\sigma^+$	-103.61	-119.06
$1\sigma^+$	-656.40	-689.37

Table XXVIII. CN vertical excitation energies (eV) calculated with the LSDxc/TDLSDxc and the LB94xc/TDLSDxc functionals using the Sadlej basis set[a].

	Vertical excitation energies (eV).								
Methods	$1^2\Sigma^+$	$1^2\Pi$	$2^2\Sigma^+$	$3^2\Sigma^+$	$1^2\Delta$	$2^2\Pi$	$2^2\Delta$	$3^2\Pi$	$4^2\Pi$
LSDxc/ TDLSDxc	0.000	1.340	3.227	6.629	7.434	8.061	8.626	9.240	9.786
LB94xc/ TDLSDxc	0.000	1.296	3.379	6.400	7.271	7.743	8.554	9.152	11.500
LSDxc(XB)/[b] TDLSDxc	0.000	1.343	3.225	6.632	7.438	8.062	8.628	9.232	9.471
EXPT[c]	0.000	1.316	3.218	8.274	8.626	9.159	9.685		
CI[d]	0.000	2.187	3.769	8.761	9.554	9.479	9.988	10.036	13.456
UCIS[e]	0.000	4.070	6.546						
ROCIS[e]	0.000	2.185	6.378						
XCIS[f]	0.000	1.150	4.802						
TDDFT[g]	0.000	1.637	3.023						

[a] (52111/411/22) for carbon and nitrogen taken from Ref. [444].

[b] Calculation is done with the extended Sadlej basis.

[c] Converted from Ref. [379].

[d] Converted from Ref. [411].

[e] Unrestricted (non-spin-adapted) CIS (UCIS) and restricted open-shell (spin-adapted) CIS (ROCIS) taken from Ref. [336].

[f] Extended CIS (XCIS) from Ref. [437].

[g] Time-dependent density-functional theory (TDDFT) calculations from Ref. [1].

Table XXIX. CN orbital energies (eV) calculated with the LSDxc and the LB94xc functionals using the Sadlej basis and the extended Sadlej basis (XB).

Orbital	LSDxc[a]	LB94xc[a]	LSDxc(XB)[b]
α unoccupied orbitals energies (eV).			
$8\sigma^+$	2.61	-1.26	0.32
3π	1.30	-2.09	0.43
$7\sigma^+$	1.06	-2.88	0.24
$6\sigma^+$	0.21	-3.42	-0.07
2π	-1.82	-7.12	-1.82
α occupied orbitals energies (eV).			
$5\sigma^+$	-9.73(14.17)	-14.70	-9.73
1π	-9.85	-15.09	-9.85
$4\sigma^+$	-12.09	-17.29	-12.09
$3\sigma^+$	-23.94	-28.66	-23.94
$2\sigma^+$	-270.19	-294.34	-270.21
$1\sigma^+$	-379.84	-407.05	-379.83
β unoccupied orbitals energies (eV).			
$8\sigma^+$	2.72	-1.03	0.35
3π	1.36	-2.08	0.45
$7\sigma^+$	1.15	-2.44	0.25
$6\sigma^+$	0.34	-3.16	-0.01
2π	-1.17	-6.64	-1.18
$5\sigma^+$	-8.09	-13.41	-8.09
β occupied orbitals energies (eV).			
1π	-9.48	-14.77	-9.49
$4\sigma^+$	-10.98	-16.41	-10.98
$3\sigma^+$	-23.47	-27.81	-23.48
$2\sigma^+$	-269.79	-294.57	-269.80
$1\sigma^+$	-379.69	-407.21	-379.68

[a] Calculations are with the Sadlej basis. Number in parentheses is the experimental ionization potential taken from Ref. [379].

[b] Calculations are with extended Sadlej basis.

Table XXX. Carbon monoxide positive ion vertical excitation energies (eV) calculated with the LSDxc/TDLSDxc and the LB94xc/TDLSDxc functionals and with the cation and the neutral CO molecular geometries using Sadlej basis set[a].

	Vertical excitation energies (eV).								
Methods	$1^2\Sigma^+$	$1^2\Pi$	$2^2\Sigma^+$	$3^2\Sigma^+$	$1^2\Delta$	$2^2\Pi$	$1^2\Sigma^-$	$3^2\Pi$	$4^2\Pi$
LSDxc(+)/ TDLSDxc[b]	0.000	3.140	4.990	8.065	8.895	8.992	9.866	10.971	13.223
LB94xc(+)/ TDLSDxc	0.000	2.419	4.347	7.769	8.745	8.534	9.634	10.658	12.998
LSDxc/ TDLSDxc	0.000	2.998	4.982	7.812	8.630	8.832	9.600	10.866	13.134
LB94xc/ TDLSDxc	0.000	2.302	4.365	7.514	8.481	8.380	9.271	10.545	12.909
LSDxc(XB)/ TDLSDxc	0.000	2.996	4.978	7.811	8.630	8.832	9.600	10.863	13.131
EXPT[c]	0.000	3.264	5.819		9.116				
FCI[d]	0.000	3.137	5.965		10.952	11.091	10.902		
SACCI[d]	0.000	3.099	5.940		11.013	11.105	10.982		
FOCI[e]	0.000	2.960	5.844	10.150		9.421		13.719	
MCSCF[e]	0.000	3.528	6.704	11.306		10.268		14.996	
VCI[f]	0.00	3.14	5.89	10.01		8.82		12.46	14.04
UCIS[g]	0.000	7.504	11.315						
ROCIS[g]	0.000	5.656	10.403						
XCIS[h]	0.000	4.267	8.192						
TDDFT[i]	0.000	3.620	5.025						

[a] (52111/411/22) for carbon and oxygen taken from Ref. [334].

[b] + indicates the geometry used is molecular cation geometry. Without "+" indicates that the geometry used in the calculations is neutral molecular geometry.

[c] Converted from Ref. [379].

[d] Full-CI and symmetry-adapted-cluster CI (SACCI). Converted from Ref. [443].

[e] First-order CI. Converted from Ref. [421].

[f] Full valence CI taken from Ref. [419].

[g] Unrestricted (non-spin-adapted) CIS (UCIS) and restricted open-shell (spin-adapted) CIS (ROCIS) taken from Ref. [336].

[h] Taken from Ref. [437].

[i] Taken from Ref. [1].

Table XXXI. CO^+ orbital energies (eV) calculated with the LSDxc and the LB94xc functionals using the Sadlej basis and the extended Sadlej basis (XB).

Orbital	LSDxc(+)[a]	LB94xc(+)[a]	LSDxc[b]	LB94xc[b]	LSDxc(XB)[c]
		α unoccupied orbitals energies (eV).			
$8\sigma^+$	-2.14	-6.48	-2.15	-6.50	-2.36
3π	-3.52	-8.10	-3.51	-8.07	-3.56
$7\sigma^+$	-3.93	-8.92	-3.96	-8.95	-3.97
$6\sigma^+$	-5.12	-10.10	-5.14	-10.12	-5.15
2π	-13.10	-19.30	-13.23	-19.43	-13.23
		α occupied orbitals energies (eV).			
$5\sigma^+$	-21.79(26.8)	-27.51	-21.77	-27.49	-21.77
1π	-22.52	-28.78	-22.38	-28.64	-22.38
$4\sigma^+$	-24.48	-30.74	-24.53	-30.77	-24.53
$3\sigma^+$	-40.24	-45.92	-40.03	-45.70	-40.04
$2\sigma^+$	-283.63	-308.33	-283.69	-308.42	-283.70
$1\sigma^+$	-521.28	-552.30	-521.31	-552.29	-521.29
		β unoccupied orbitals energies (eV).			
$8\sigma^+$	-1.96	-6.34	-1.96	-6.35	-2.23
3π	-3.40	-7.84	-3.40	-7.82	-3.46
$7\sigma^+$	-3.64	-7.76	-3.66	-7.78	-3.68
$6\sigma^+$	-4.80	-9.84	-4.81	-9.85	-4.82
2π	-11.91	-18.83	-12.04	-18.94	-12.04
$5\sigma^+$	-18.93	-26.05	-18.95	-26.02	-18.95
		β occupied orbitals energies (eV).			
1π	-22.22	-28.62	-22.09	-28.47	-22.09
$4\sigma^+$	-23.86	-30.20	-23.88	-30.20	-23.88
$3\sigma^+$	-40.03	-45.42	-39.82	-45.20	-39.82
$2\sigma^+$	-282.99	-308.46	-283.06	-308.55	-283.06
$1\sigma^+$	-521.28	-552.39	-521.31	-552.39	-521.29

[a] Calculations are with cation geometry and with the Sadlej basis. Number in the parentheses is experimental ionization potential taken from Ref. [379].

[b] Calculations are with neutral CO geometry and Sadlej basis.

[c] Calculations are with neutral CO geometry and with extended Sadlej basis.

Table XXXII. N_2^+ vertical excitation energies (eV) calculated with the LSDxc/TDLSDxc and the LB94xc/TDLSDxc functionals and with the cation and the neutral N_2 molecular geometries using Sadlej basis set[a].

	Vertical excitation energies (eV).								
Methods	$1^2\Sigma_g^+$	$1^2\Pi_u$	$1^2\Sigma_u^+$	$2^2\Sigma_u^+$	$2^2\Pi_u$	$3^2\Pi_u$	$3^2\Sigma_u^+$	$2^2\Sigma_g^+$	$3^2\Sigma_g^+$
LSDxc(+)[b]/ TDLSDxc	0.000	1.445	3.724	7.325	10.513	13.783	16.102	17.718	18.753
LB94xc(+)/ TDLSDxc	0.000	1.201	3.784	6.776	10.250	13.517	15.942	17.534	18.858
LSDxc/ TDLSDxc	0.000	1.598	3.632	7.729	10.620	13.888	16.441	17.775	19.009
LB94xc/ TDLSDxc	0.000	1.351	3.702	7.158	10.344	13.610	16.309	17.826	18.926
LSDxc(XB)[c]/ TDLSDxc	0.000	1.598	3.633	7.730	10.620	13.887	16.440	17.708	18.920
EXPT/XPS[d]	0.000	1.4	3.2	9.4	14.07		16.3	13.2	17.5
EXPT/UPS[e]	0.000	1.346	3.171	9.934	14			13.2	
CI[f]	0.000	1.83	3.27	10.78	13.66	18.17	19.28	14.60	20.21
CI[g]	0.000	1.83	3.27	9.94	13.50	18.11	18.55	13.92	19.76
CI[h]	0.000	1.48	3.40	11.27	15.30	18.79	19.39	14.53	19.72
CI[i]	0.000		3.27	9.82			17.24	13.47	17.95
MCEP[j]	0.000	1.72	3.04	10.79	14.07	18.61	21.65	14.26	19.72
GF[k]	0.000	1.15	3.26	9.43	12.93	19.87	19.64	13.50	21.73

[a] (52111/411/22) for nitrogen taken from Ref. [444].

[b] + in the parenthesis indicates that the cation geometry used in the calculations. Without + indicates that the calculations are done with neutral geometry.

[c] Calculations are with extended Sadlej basis set, see text for details.

[d] X-ray photoelectron spectroscopy taken from Ref. [441].

[e] Ultraviolet photoelectron spectroscopy taken from Ref. [446].

[f] CI with double-zeta basis and polarization functions taken from Ref. [432].

[g] CI with extended basis taken from Ref. [433].

[h] CI with extended basis containing diffuse functions taken from Ref. [442].

[i] Multireference CI with extended basis including diffuse functions taken from Ref. [431].

[j] Multiconfigurational electron propagator with extended basis taken from Ref. [435].

[k] Extended two-particle-hole Tamm-Dancoff approximation with extended basis taken from Ref. [447].

Table XXXIII. N_2^+ orbital energies (eV) calculated with the cation geometry and the neutral molecular geometry and with the LSDxc and the LB94xc functionals using the Sadlej basis and the extended Sadlej basis (XB).

Orbital	LSDxc(+)[a]	LB94xc(+)[a]	LSDxc[b]	LB94xc[b]	LSDxc(XB)[c]
			α unoccupied orbitals energies (eV).		
$5\sigma_g^+$	-2.14	-6.96	-2.14	-7.00	-2.42
$2\pi_u$	-3.39	-8.16	-3.51	-8.18	-3.66
$3\sigma_u^+$	-3.55	-8.29	-3.53	-8.25	-3.61
$4\sigma_g^+$	-5.01	-9.96	-5.01	-9.96	-5.07
$1\pi_g$	-13.65	-20.17	-13.45	-20.00	-13.45
			α occupied orbitals energies (eV).		
$3\sigma_g^+$	-22.70(27.1)	-28.72	-22.74	-28.77	-22.74
$1\pi_u$	-22.91	-29.00	-23.11	-29.20	-23.11
$2\sigma_u^+$	-25.59	-31.71	-25.50	-31.63	-25.50
$2\sigma_g^+$	-39.95	-45.48	-40.28	-45.85	-40.28
$1\sigma_u^+$	-393.99	-422.16	-393.94	-422.13	-393.97
$1\sigma_g^+$	-394.01	-422.19	-393.97	-422.16	-394.01
			β unoccupied orbitals energies (eV).		
$5\sigma_g^+$	-2.02	-6.43	-2.02	-6.48	-2.35
$3\sigma_u^+$	-3.42	-7.87	-3.39	-7.82	-3.49
$2\pi_u$	-3.43	-8.01	-3.45	-8.02	-3.62
$4\sigma_g^+$	-4.84	-9.76	-4.83	-9.75	-4.91
$1\pi_g$	-12.95	-19.65	-12.74	-19.47	-12.74
$3\sigma_g^+$	-20.94	-27.35	-20.99	-27.40	-20.99
			β occupied orbitals energies (eV).		
$1\pi_u$	-22.44	-28.60	-22.63	-28.81	-22.63
$2\sigma_u^+$	-24.15	-30.68	-24.05	-30.59	-24.05
$2\sigma_g^+$	-39.38	-44.47	-39.72	-44.83	-39.72
$1\sigma_u^+$	-393.65	-422.35	-393.60	-422.32	-393.63
$1\sigma_g^+$	-393.67	-422.38	-393.63	-422.35	-393.66

[a] + in the parenthesis indicates that the calculation is done with cation geometry. Number in parentheses is experimental ionization potential taken from Ref. [379].

[b] Calculations are done with neutral N_2 molecular geometry.

[c] XB in parentheses indicates that the calculation is done with the extended Sadlej basis.

Table XXXIV. $CH2O^+$ vertical excitation energies (eV) calculated with the LSDxc/TDLSDxc and the LB94xc/TDLSDxc functionals using the Sadlej basis set[a] and the extended Sadlej basis (XB)[b].

	Vertical excitation energies (eV).				
State	LSDxc[c]/ TDLSDxc	LB94xc[c]/ TDLSDxc	LSDxc(XB)[d]/ TDLSDxc	MRD-CI[e]	MRCI[f]
1^2B_2	0.000	0.000	0.000	0.000	0.000
1^2B_1	4.062	3.908	4.061	3.86	3.84
2^2B_1	5.089	4.626	5.090	5.78	6.46
1^2A_1	5.266	4.926	5.263	5.30	5.46
2^2B_2	6.299	5.872	6.302	6.37	6.45
3^2B_2	6.768	6.475	6.770	8.07	8.69
1^2A_2	8.462	7.976	8.461	9.89	
3^2B_1	9.318	8.764	9.324	10.18	10.79
2^2A_1	9.554	9.108	9.552	10.40	10.90
2^2A_2	9.603	9.037	9.601	10.97	
4^2B_1	10.331	9.753	10.337	12.85	14.05
3^2A_1	11.074	11.187	11.070	11.97	14.65
4^2B_2	11.086	10.859	11.082	11.30	12.75
4^2A_1	12.053	12.541	12.041	13.88	15.17
3^2A_2	12.058	11.457	12.056	13.71	
4^2A_2	13.788	13.742	14.011	15.27	

[a] (411/22) for hydrogen taken from Ref. [444] and (52111/411/22) for carbon and oxygen taken from Ref. [334].

[b] Extended Sadlej basis is (41111/221) for hydrogen, (5211111/4111/221) for carbon and oxygen. See text.

[c] Calculations are done with Sadlej basis.

[d] Calculations are done with extended basis.

[e] Taken from Ref. [9].

[f] Taken from Ref. [448].

Table XXXV. CH_2O^+ orbital energies (eV) calculated with the LSDxc and the LB94xc functionals using the Sadlej basis and the extended Sadlej basis.

Orbital	LSDxc[a]	LB94xc[a]	LSDxc(XB)[b]
α unoccupied orbitals energies (eV).			
$8a_1$	-3.65	-8.23	-3.66
$3b_2$	-4.80	-10.37	-4.80
$7a_1$	-5.15	-10.32	-5.16
$6a_1$	-6.18	-11.78	-6.18
$2b_1$	-12.22	-18.37	-12.22
α occupied orbitals energies (eV).			
$2b_2$	-17.24	-22.91	-17.24
$1b_1$	-20.30	-26.12	-20.30
$5a_1$	-21.36	-26.91	-21.36
$1b_2$	-22.41	-27.97	-22.41
$4a_1$	-25.26	-30.84	-25.26
$3a_1$	-37.58	-42.71	-37.57
$2a_1$	-279.21	-304.22	-279.19
$1a_1$	-519.76	-549.54	-519.74
β unoccupied orbitals energies (eV).			
$8a_1$	-3.51	-8.04	-3.52
$3b_2$	-4.55	-9.95	-4.56
$7a_1$	-4.96	-10.05	-4.97
$6a_1$	-5.91	-11.33	-5.92
$2b_1$	-11.96	-18.09	-11.95
$2b_2$	-15.64	-21.69	-15.64
β occupied orbitals energies (eV).			
$1b_1$	-19.80	-25.71	-19.80
$5a_1$	-20.72	-26.43	-20.71
$1b_2$	-21.47	-27.07	-21.48
$4a_1$	-24.73	-30.28	-24.73
$3a_1$	-36.73	-41.98	-36.73
$2a_1$	-279.22	-304.25	-279.20
$1a_1$	-519.19	-549.90	-519.17

[a] Calculations are with neutral CH_2O geometry and Sadlej basis.

[b] Calculations are with neutral CH_2O geometry and with extended Sadlej basis.

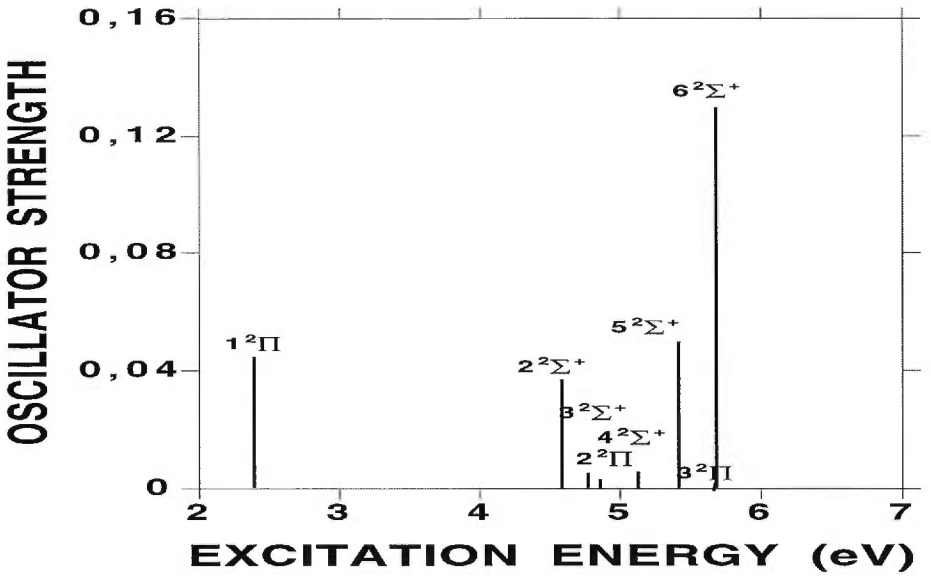

Figure 12. Excitation spectrum of BeH with the LSDxc/TDLSDxc functional and the Sadlej basis.

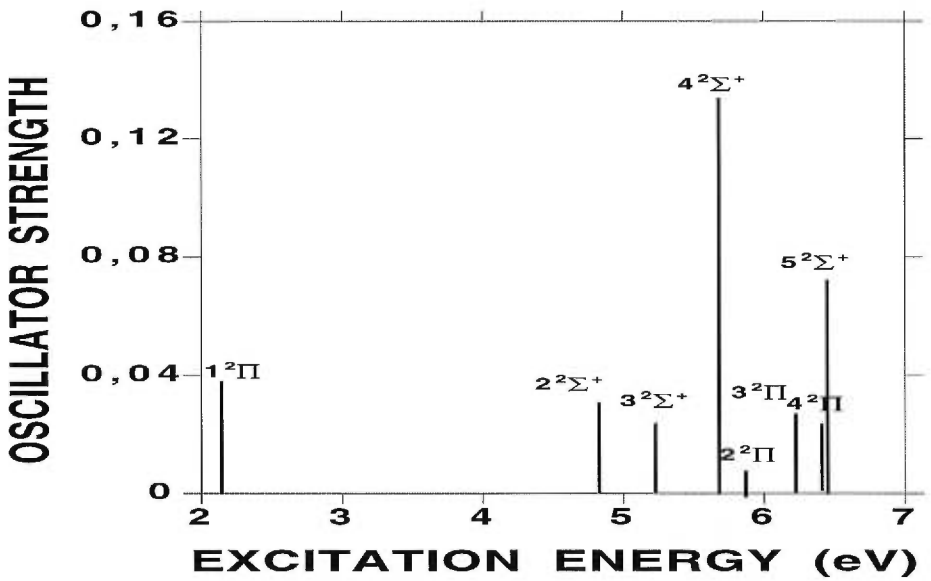

Figure 13. Excitation spectrum of BeH with the LB94xc/TDLSDxc functional and the Sadlej basis.

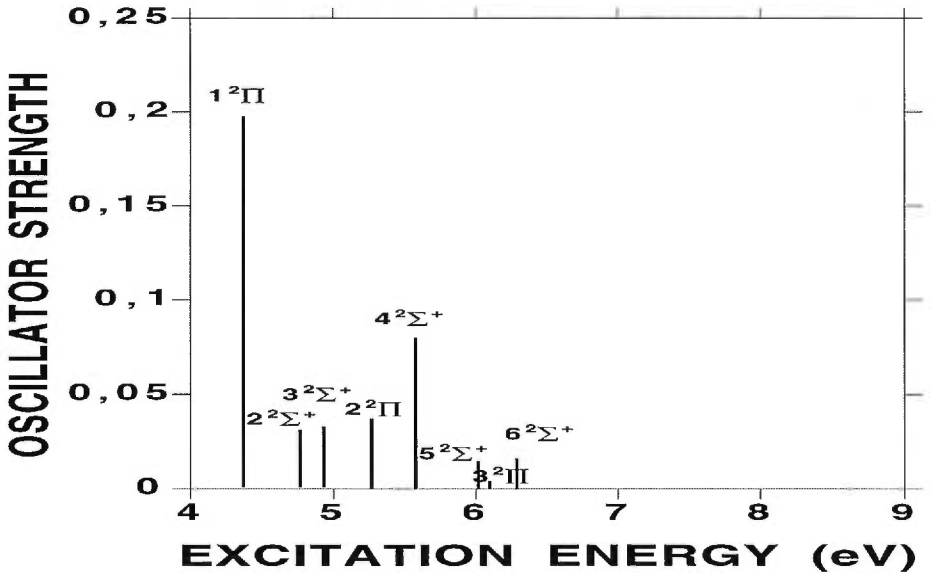

Figure 14. Excitation spectrum of BeF with the LSDxc/TDLSDxc functional and the Sadlej basis.

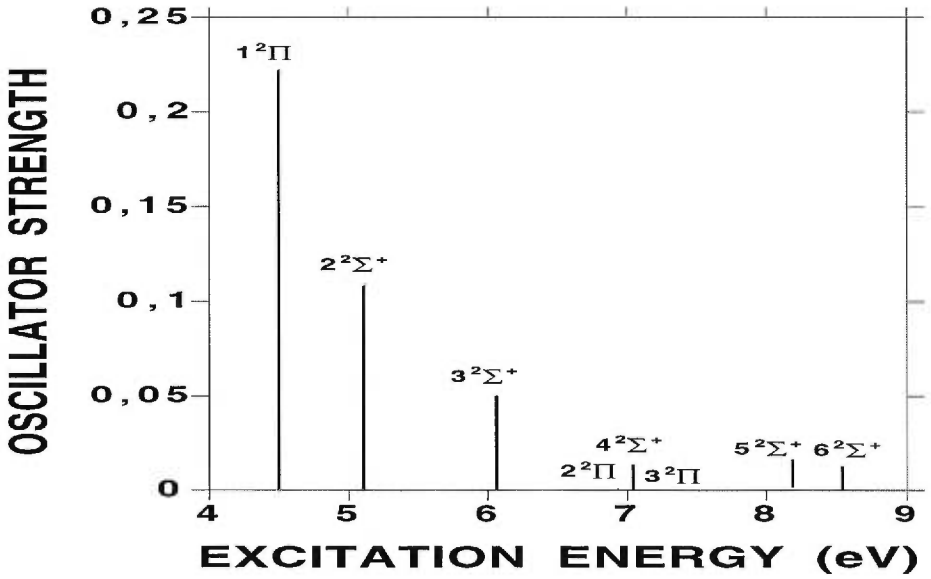

Figure 15. Excitation spectrum of BeF with the LB94xc/TDLSDxc functional and the Sadlej basis.

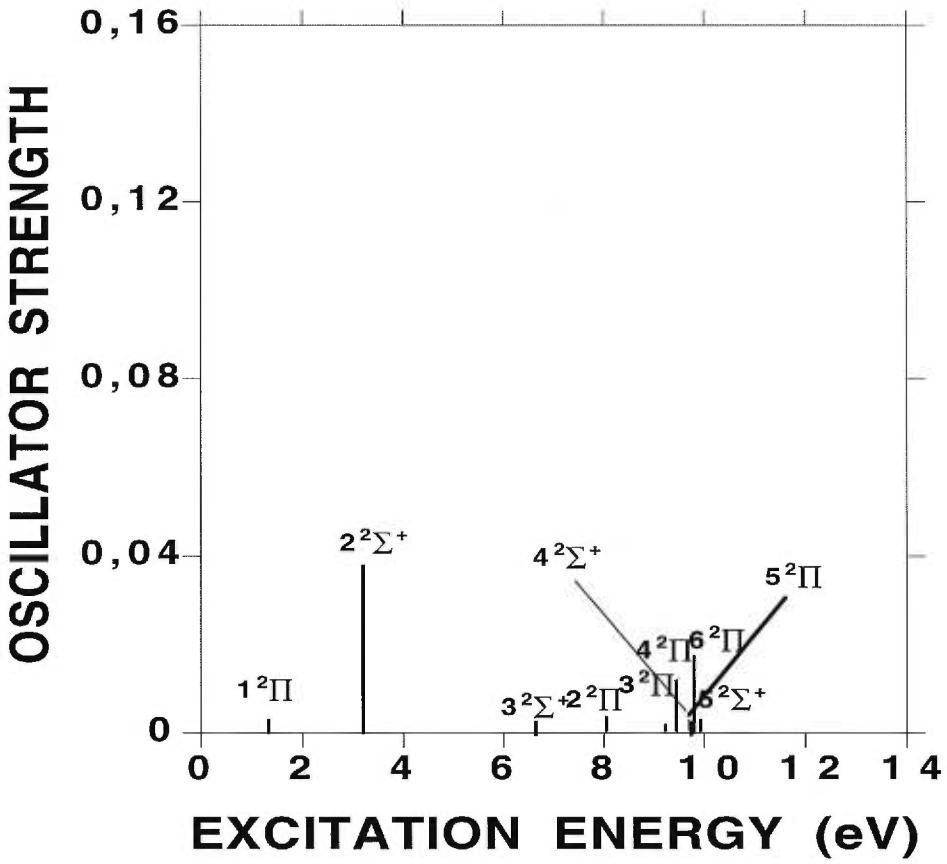

Figure 16. Excitation spectrum of CN with the LSDxc/TDLSDxc functional and the extended Sadlej basis.

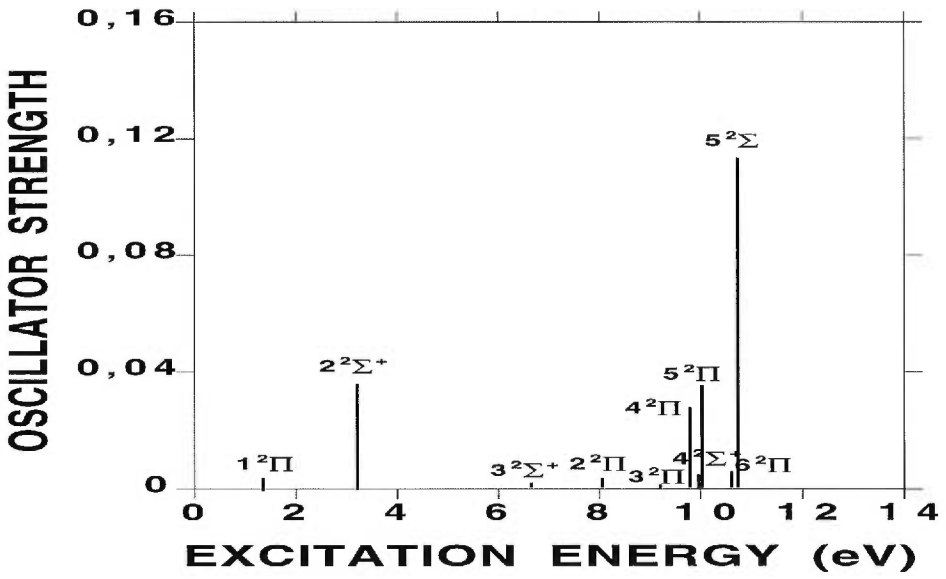

Figure 17. Excitation spectrum of CN with the LSDxc/TDLSDxc functional and the Sadlej basis.

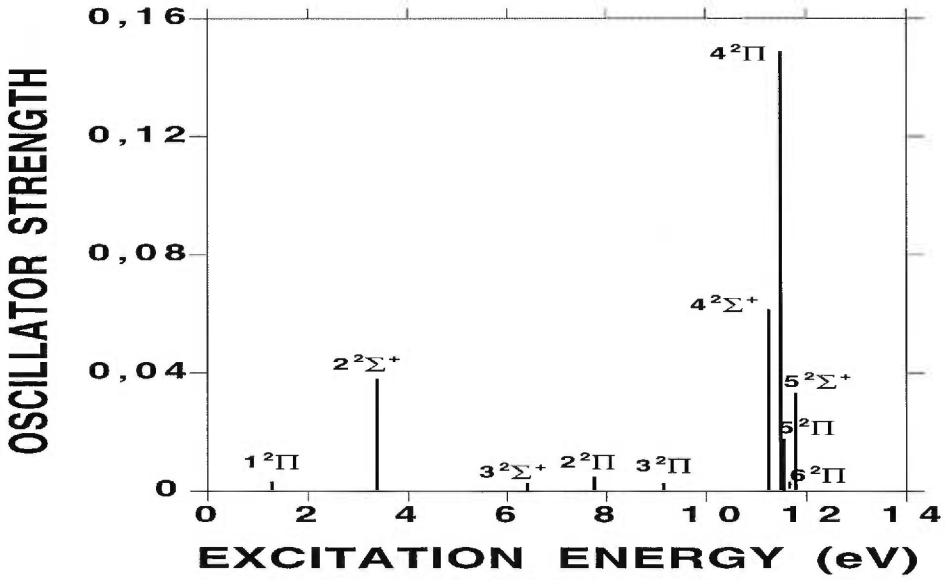

Figure 18. Excitation spectrum of CN with the LB94xc/TDLSDxc functional and the Sadlej basis.

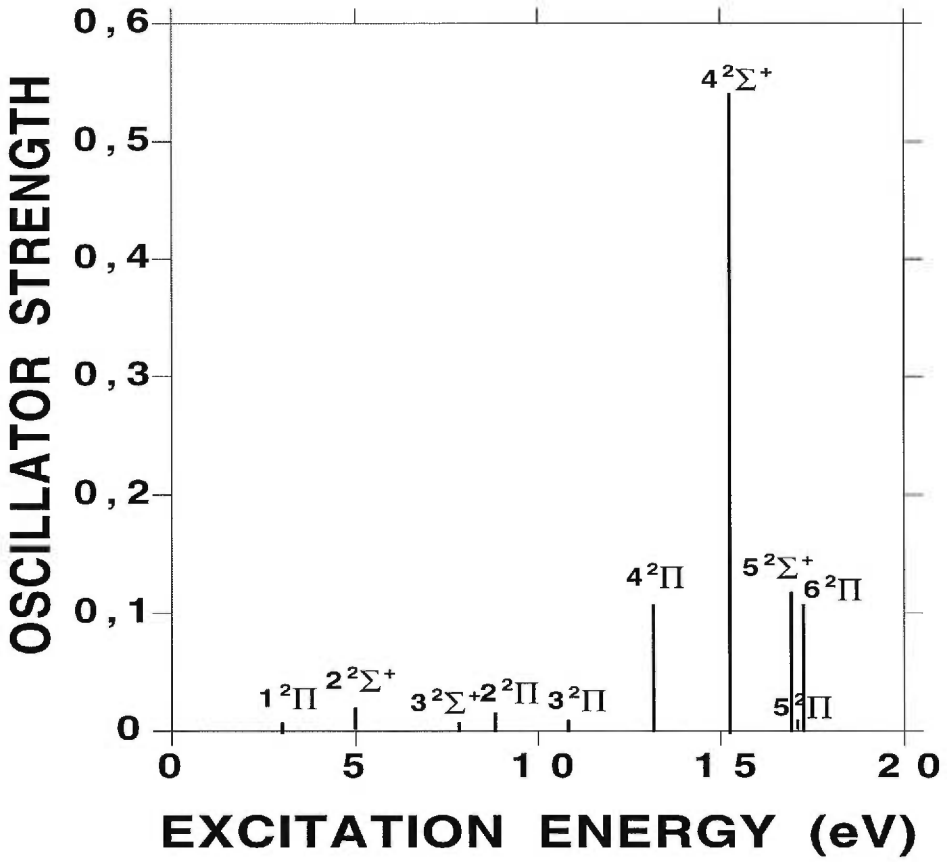

Figure 19. Excitation spectrum of CO^+ with the LSDxc/TDLSDxc functional and the extended Sadlej basis.

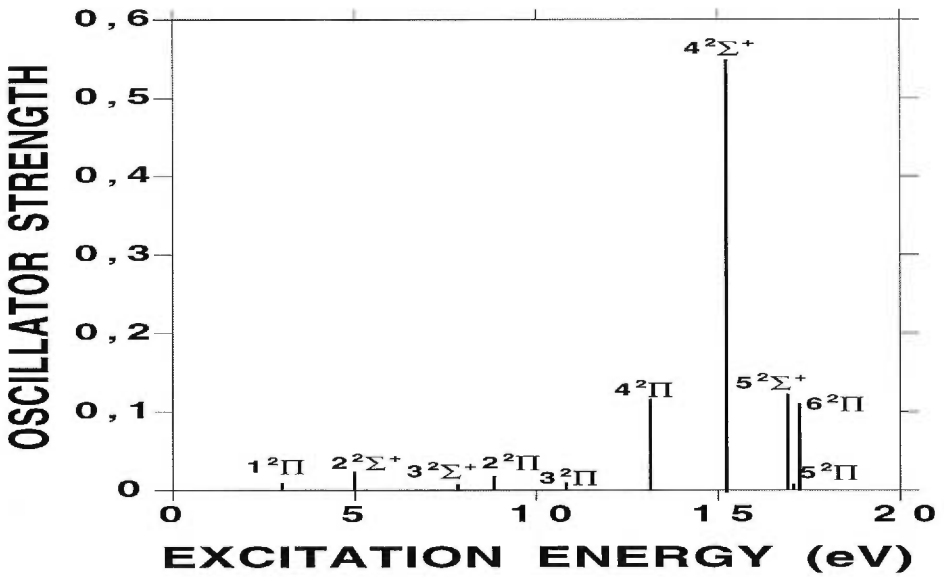

Figure 20. Excitation spectrum of CO^+ with the LSDxc/TDLSDxc functional and the Sadlej basis.

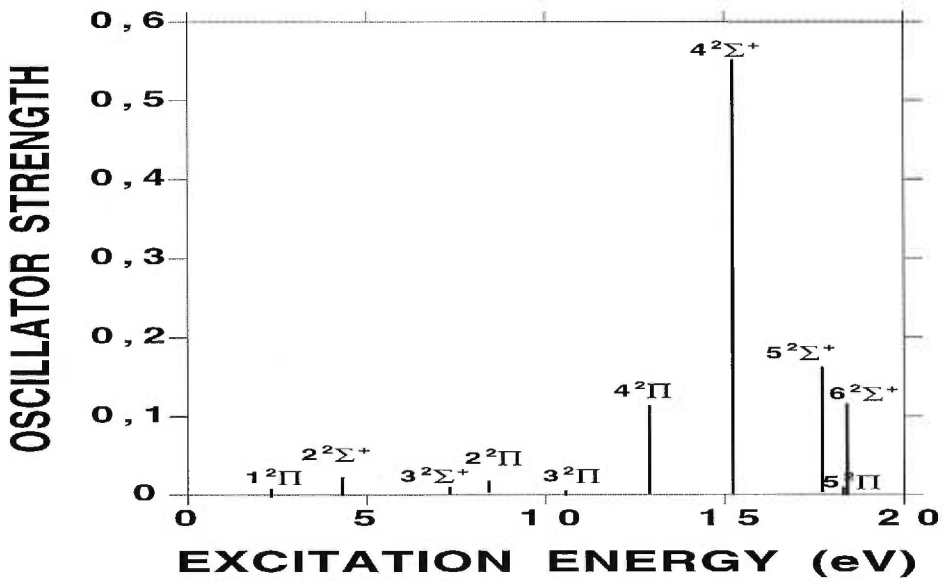

Figure 21. Excitation spectrum of CO^+ with the LB94xc/TDLSDxc functional and the Sadlej basis.

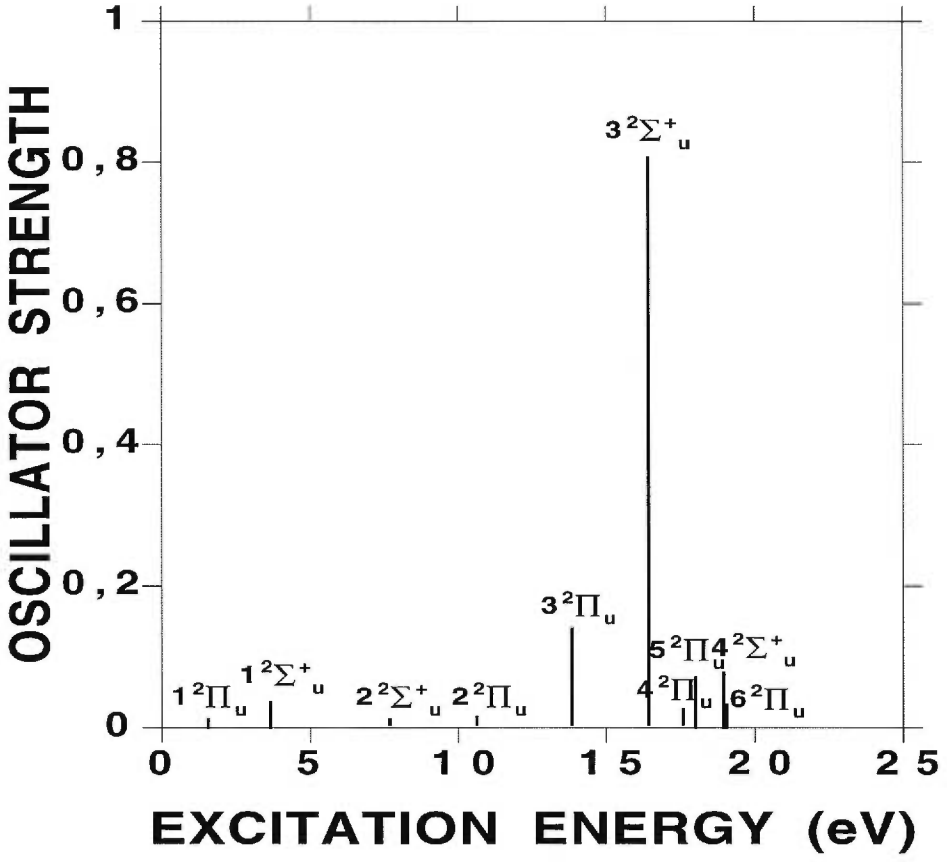

Figure 22. Excitation spectrum of N_2^+ with the LSDxc/TDLSDxc functional and the extended Sadlej basis.

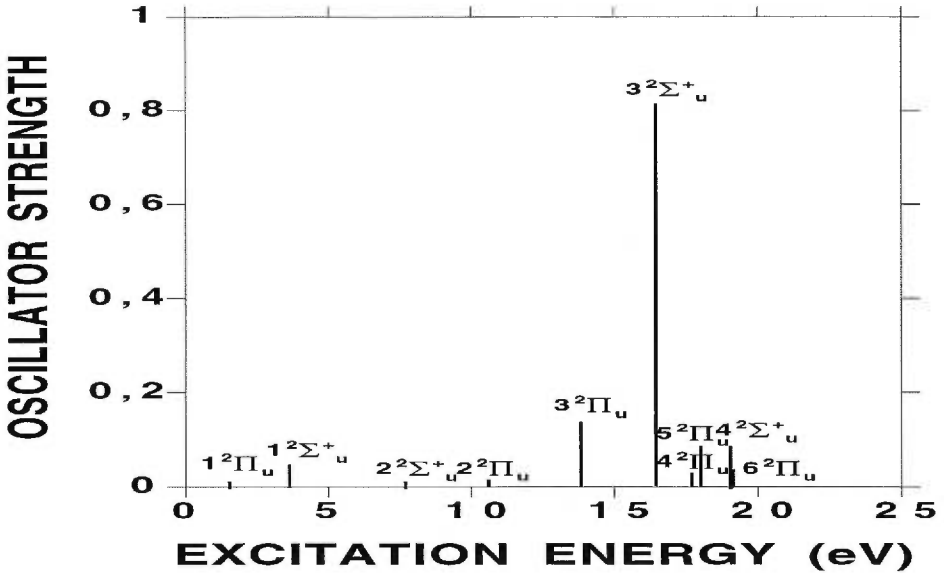

Figure 23. Excitation spectrum of N_2^+ with the LSDxc/TDLSDxc functional and the Sadlej basis.

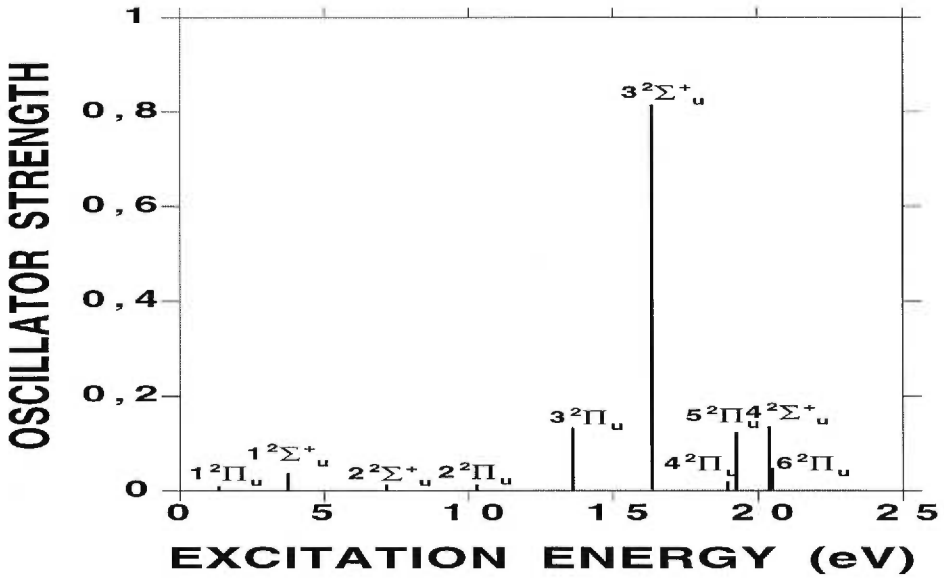

Figure 24. Excitation spectrum of N_2^+ with the LB94xc/TDLSDxc functional and the Sadlej basis.

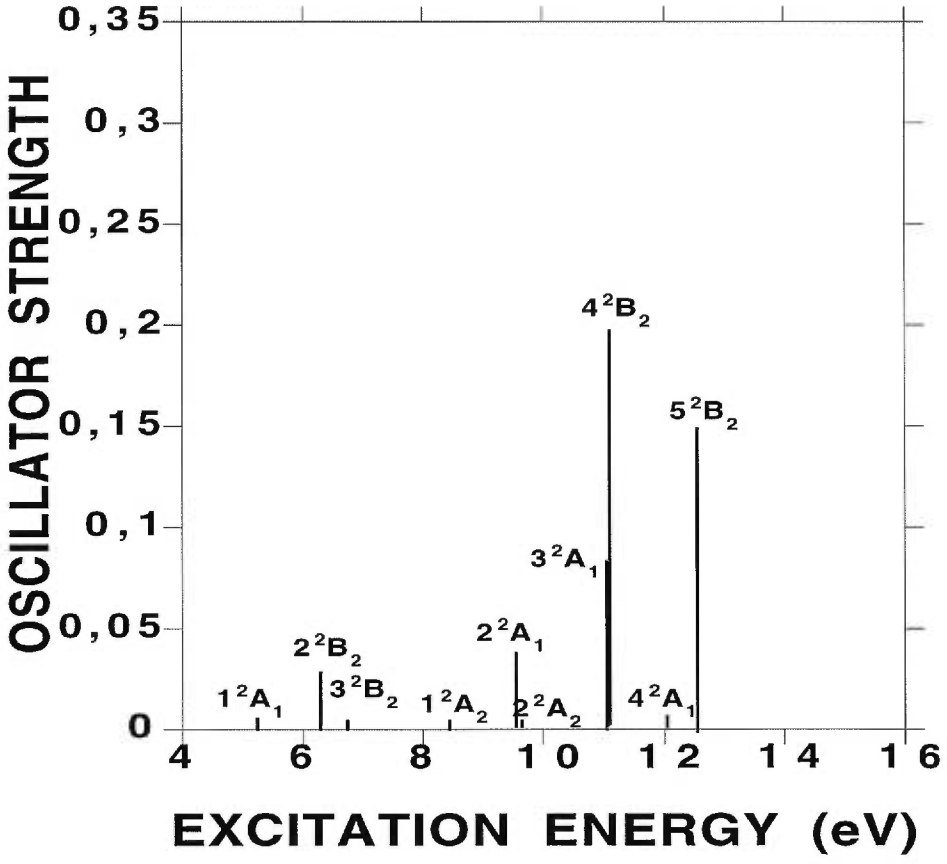

Figure 25. Excitation spectrum of CH_2O^+ with the LSDxc/TDLSDxc functional and the extended Sadlej basis.

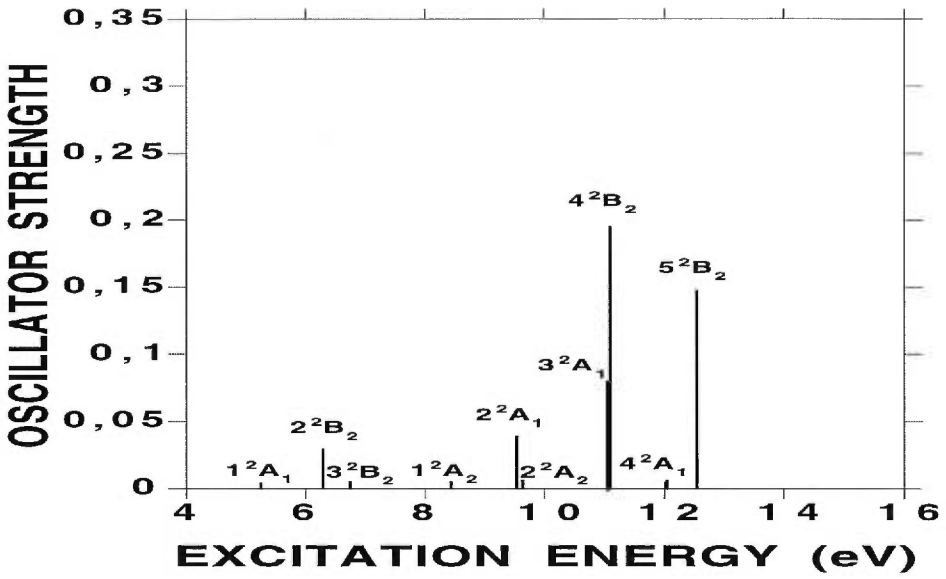

Figure 26. Excitation spectrum of CH_2O^+ with the LSDxc/TDLSDxc functional and the Sadlej basis.

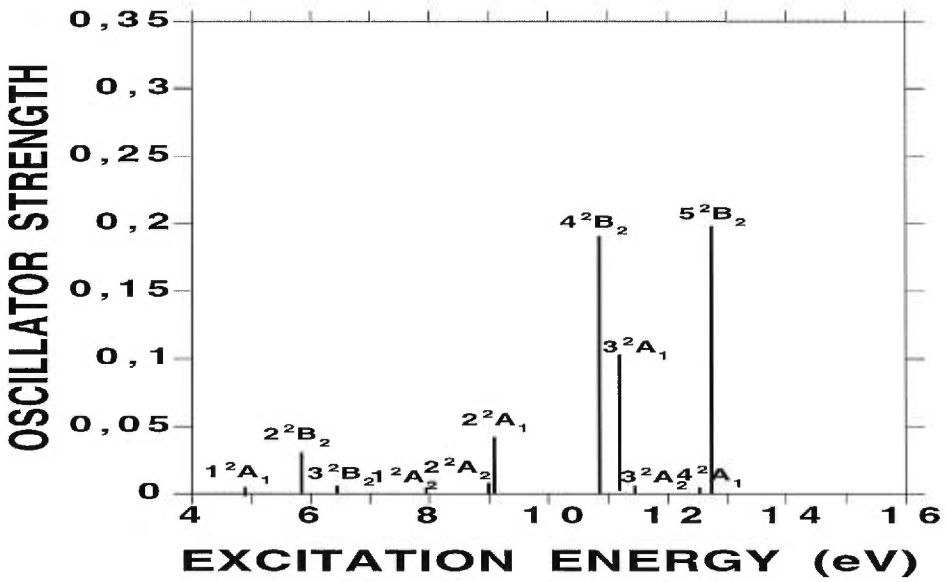

Figure 27. Excitation spectrum of CH_2O^+ with the LB94xc/TDLSDxc functional and the Sadlej basis.

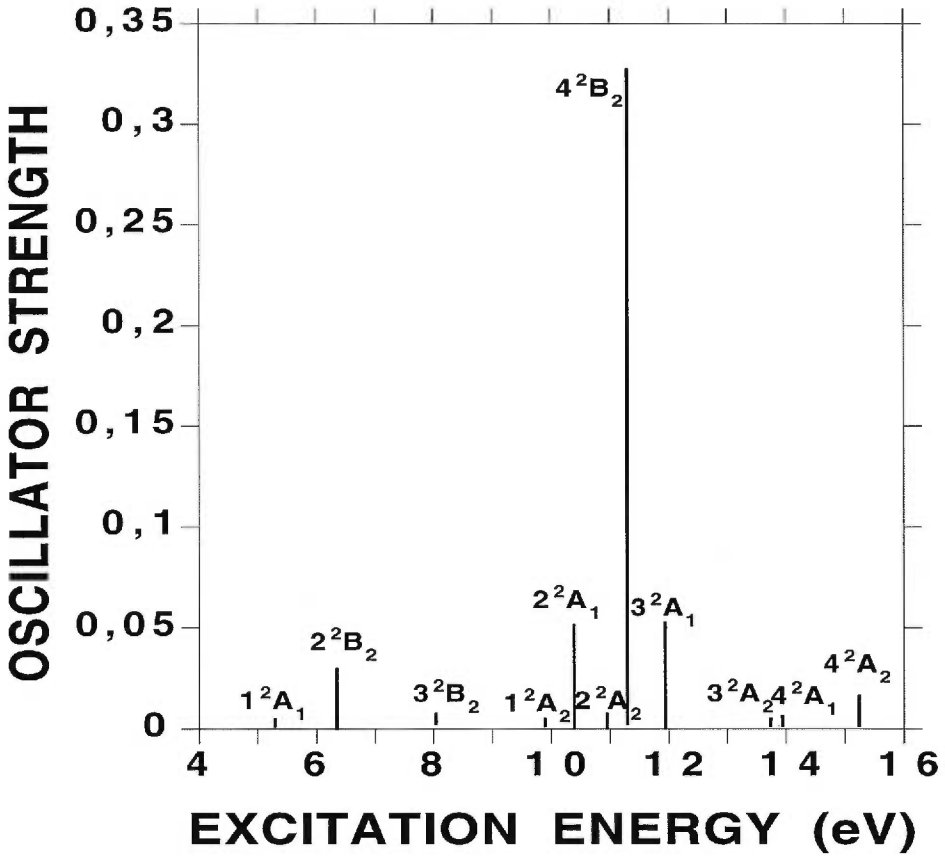

Figure 28. Excitation spectrum of CH_2O^+ with the MRD-CI method taken from Ref. [9].

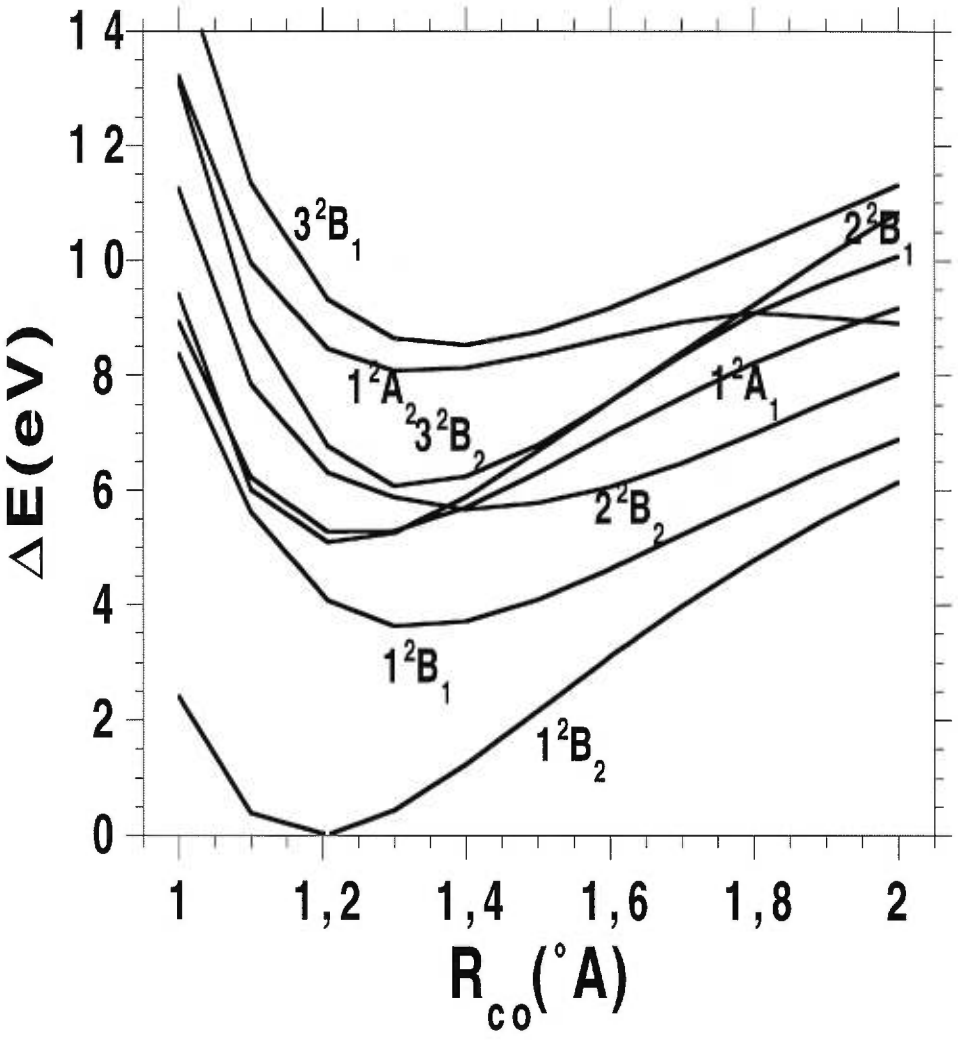

Figure 29. Potential energy curves of CH_2O^+ for low lying doublet states with the LSDxc/TDLSDxc functional and the Sadlej basis.

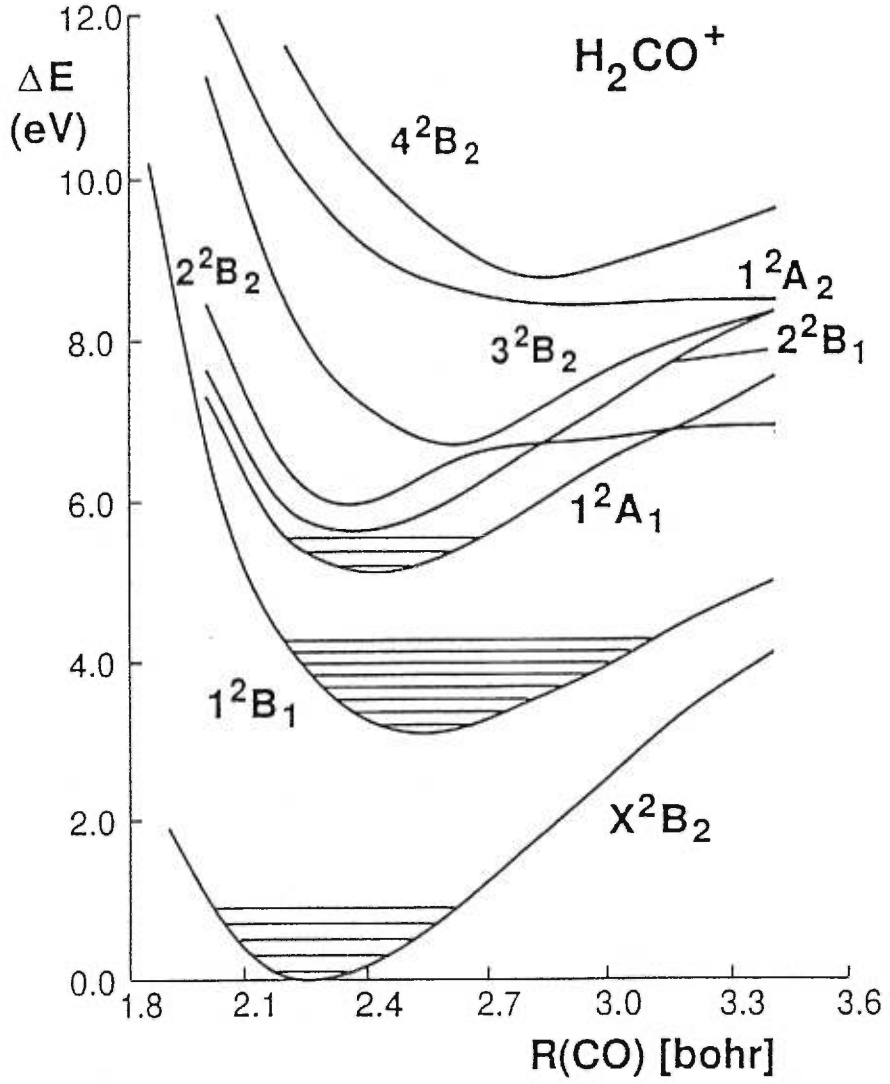

Figure 30. Potential energy curves of CH_2O^+ for low lying doublet states calculated by the MRD-CI, taken from Ref. [9].

CHAPTER 6

PREDICTION AND INTERPRETATION OF ABSORPTION SPECTRA OF SMALL LITHIUM CLUSTERS BY TIME–DEPENDENT DENSITY–FUNCTIONAL THEORY

6.1 INTRODUCTION

Lithium clusters are the simplest metal clusters with only three s electrons for each atom, and this advantage has been used for observations of lithium cluster ground and excited state properties (e.g. electronic spectroscopy [449]). Experimental observations and traditional *ab initio* calculations of electronic spectra of the lithium clusters have been reported in the literature. Time-dependent density–functional study of excitation spectra of the lithium clusters lag behind, only a few publications have appeared recently. Pacheco and Martins [450] calculated photoabsorption spectra of Li_8 and Li_{20} with time-dependent density-functional theory (DFT) and with pseudopotentials. Rubio and co-workers [451] used the time-dependent local density approximation with the jellium model to describe the photoabsorption cross section for Li_8. However, an all-electron time-dependent DFT study of the electronic spectra of lithium clusters with quantum molecular models considering the molecular nature of the clusters has not yet appeared. The present work provides the first study of excitation energies and oscillator strengths of lithium clusters by time-dependent DFT at the all-electron level.

Excited states of the lithium dimer were experimentally investigated [452] and its absorption bands were measured [453] in the early thirties. Though the first spectra of metal cluster trimers (Na_3) were already recorded with two-photon ionization in 1979 [454], the first observation of excited states of the lithium trimer in a gas-phase absorption experiment by laser-induced fluorescence was only performed in 1989 [58]. Due to the predissociation processes in the larger metal clusters, this technique has not been used in applications to metal clusters larger than the trimer. The photodissociation technique [64, 455, 67, 23, 66, 68] provides a useful tool for the study of larger clusters. This technique has been used to observe the lithium tetramer spectroscopy [68] as well as the vibronic structure of several electronic transitions. The high–resolution spectra of the lithium clusters up to eight atoms were also reported in the literature [68, 456, 12, 69]. These experimental recordings provide the opportunity for theoretical interpretations.

Theoretical investigations of the excited states of the lithium clusters have made considerable progress. For the dimer, there was a burst of interest for the study of ground state properties [457] and those of excited states [458, 459] seven decades ago. Lithium trimer has been extensively studied for its ground state by semiempirical [460, 461] and *ab initio* methods [462, 463, 464, 465]. The study of ground states and excited state energy surfaces of the lithium trimer was carried out two decades ago [464]. But interpretations of absorption spectra of the trimer are surprisingly rare, only one traditional density–functional theory "multiplet" approach calculation of the electronic spectra of the lithium trimer is found in the literature [10] and one CI study of the first few excitation energies of the lithium trimer [466]. The first attempt at calculating excited states and interpreting the absorption spectra of the lithium tetramer was achieved by Bonačić–Koutecký *et al.* [78] using the configuration interaction (CI) method. The interpretation of depletion spectra of the tetramer was also performed later using multiconfigurational linear response (MCLR) theory [11]. Bonačić–Koutecký and co-workers,

using this high precision CI technique, tried to interpret absorption spectra of the lithium hexamer [467, 12, 468, 69], heptamer [69], and octamer [69]. However, there are no theoretical calculations on the lithium pentamer in the literature. Recently, *ab initio* Hartree–Fock self–consistent–field study dynamics of Li_8, Li_9^+, Li_{10}, and Li_{11}^+ [469, 470] and *ab initio* gradient–corrected density–functional study dynamics of Li_8 [471] have also been reported by Bonačić–Koutecký *et al.*. Nevertheless, the study of open-shell lithium clusters, especially clusters larger than the trimer, has lagged far behind.

The present work calculates excitation spectra of the lithium clusters from the dimer to the hexamer by time-dependent DFT. This fills in the gap left by the absence of theoretical studies of the lithium pentamer electronic spectra. This also provides useful information on the time-dependent DFT treatment of alkali metal clusters including both closed-shell and open-shell cases. The present calculations were carried out by local spin density approximation and the exchange-correlation functional proposed by van Leeuwen and Baerends in 1994 [212] associated with the time-dependent local spin density approximation. A few orbital basis sets and several auxiliary basis sets were examined in the calculation of excitation energies. The grid used in fitting the exchange-correlation terms was treated properly to avoid symmetry breaking in the present calculations.

6.2 COMPUTATIONAL DETAILS

The excitation spectra of small lithium clusters (the symmetry of each cluster and its ground state configuration shown in Table XXXVII(please note that Tables and Figs. are given at the end of the chapter), Li_n ($n = 2 - 6$), were carried out with the time-dependent DFT program *deMon–DynaRho*, version 2pX [208]. Exchange-correlation functionals used in the present calculations were the local spin density approximation (LSDxc) and the functional proposed by van Leeuwen and Baerends in 1994 (LB94xc), respectively, in the SCF step, and the

time-dependent local spin density approximation (TDLSDxc) was used in the post-SCF step. These functionals used at the SCF step and the post-SCF step are referred to as LSDxc/TDLSDxc and LB94xc/TDLSDxc functionals. The *deMon-KS* EXTRA-FINE and NonRandom grid which consists 6208 grid points per atom were used in the present calculations. However, a user-defined grid [327] which contains 24832 grid points for each atom was used for the pentamer calculations with the LB94xc/TDLSDxc functional due to symmetry breaking in the assignments with the EXTRA-FINE grid. This kind of symmetry breaking with EXTRA-FINE and Random grid also occurred in the sodium trimer calculations (see Chapter 7 of this thesis). The SCF calculations were performed with a tolerance in the total energy of less than 10^{-8} hartree and a change in the charge density fitting coefficients of less than 10^{-7} a.u.. Geometries of the lithium clusters used in the present calculations, optimized by *deMon–KS* with the LSDxc functional, were taken from the literature [465], except for the hexamer with C_{2v} symmetry which used both the DFT optimized geometry taken from Ref. [465] and the CI optimized geometry taken from Ref. [472]. The orientation of the geometries in the present calculations follows the rules in Ref. [473]. Specifically, the dimer lies on the z-axis. The trimer, pentamer, and hexamer with D_{3h} symmetry lie in the yz–plane, since the hexamer, with D_{3h} symmetry, was also assigned under the C_{2v} subgroup. The tetramer lies in the xy–plane. The hexamer with C_{2v} symmetry has the two planes lying in the yz–plane and xz–plane.

Both orbital and auxiliary basis sets are Gaussian-type functions. Several orbital basis sets were examined in the present calculations. Specifically, the orbital bases are the double zeta valence plus polarization (DZVP) (621/1*/1+) and the Huzinaga (51111/111) bases taken from the *deMon-KS* basis sets library, the Beckmann, Koutecký, and Bonačić-Koutecký basis (3111111/111) taken from Ref. [351]. This basis was used in the lithium trimer and the tetramer excitation energy calculations with the MRD-CI method by Beckmann [466] and Beckmann, Koutecký, and Bonačić-Koutecký [351], respectively. This basis is referred to as

the BKK basis. Sadlej and Urban's orbital basis set (52111/411/22) is taken from the literature [334] (referred to as the Sadlej basis). The present calculations also used the fully decontracted Sadlej basis (1111111111/111111/1111) which is referred to as the Sadlej (FD). Since 6 cartesian d-type basis functions are used in *deMon-KS*, the total basis functions are 36, 42, 48, 78, 156 for the DZVP, the Huzinaga, the BKK, the Sadlej, and the Sadlej (FD) basis sets, respectively, in the trimer calculations. The auxiliary basis set (4,3;4,3) is taken from the *deMon–KS* basis library. In order to see the quality of the auxiliary basis in the calculation of the excitation energies, a few larger auxiliary basis sets are created by the present work based on the Sadlej orbital basis; typically, these auxiliary basis sets are (4,4;4,4), (5,3;5,3), (5,4;5,4) and (5,5;5,5).

6.3 RESULTS AND DISCUSSION

Excitation spectra of five small lithium clusters from the dimer up to the hexamer (three closed-shell clusters, Li_2, Li_4, and Li_6, two open-shell clusters, Li_3 and Li_5) are calculated by time-dependent DFT with LSDxc/TDLSDxc and LB94xc/TDLSDxc functionals. The present calculated excitation energies are compared with available experimental results and traditional *ab initio* calculations in Tables XXXVIII, XXXIX, XL, XLI, XLIII. and XLII (ionization threshold calculated with thw two functionals are given in Table XXXVI) . Excitation spectra are shown in Figs. 31, 32, 34, 35, 37, 38, 39, 40, 42, 43, 45, 46, 47 and 48 (please note that Tables and Fig s. are given at the end of the chapter).

Excitation energy calculations require a certain number of diffuse functions and polarization functions in the orbital basis set. The eighteen lowest vertical excitation energies of the trimer calculated with five different orbital bases are given in Table XLV. It shows that the polarization and diffuse basis functions are very important in the calculation of excitation energies. The Huzinaga and the BKK bases have the same number of primitive Gaussian functions (9s,3p),

the first s basis function is contracted with five s-type primitive Gaussians in the Huzinaga basis, while it is contracted with three s-type primitive Gaussians in the BKK basis set. The other s and p basis functions in the BKK basis are more diffuse than those in the Huzinaga basis. These diffuse functions improve the excitation energies remarkably. The listed excitation energies of three $^2A_2$ states and three $^2B_1$ states calculated with the Huzinaga basis have errors larger than 3 eV in comparison with those calculated with the fully decontracted Sadlej basis (see Table XLV). These excitation energies of the $^2A_2$ and the $^2B_1$ states carried out with the BKK basis reduce the error to less than 1 eV, some of them even less than 0.02 eV. For example, the 1^2B_1 state excitation energy has an error of 0.01 eV. The DZVP basis set has also nine s-type primitive Gaussians, but only one p-type and one polarization d-type Gaussian functions. The nine s-type primitive Gaussian functions were contracted to three s basis functions (621) with one p and one d functions comprising the DZVP basis. It has 36 basis functions which is the smallest basis set used for the trimer calculations. The one polarization function seems to be very important for the excitation energy calculations, which leads the excitation energy to differ from those with the fully decontracted Sadlej basis by no more than 1 eV, except for the 6^2A_1, the 7^2A_1, and the 3^2B_1 states, where the error is about 1.3 eV. The Sadlej basis has twenty primitive Gaussians functions (10s/6p/4d) which were contracted to five s, three p, and two d basis functions. It is larger than the above three basis sets, but it does give more accurate results, the deviations of excitation energies calculated with the Sadlej basis and with the fully decontracted Sadlej basis are no larger than 0.01 eV [except for the 6^2A_1 state (0.04 eV), and the 7^2A_1 state (0.05 eV)]. Hence the Sadlej basis set is chosen in the larger lithium cluster calculations.

Excitation energy calculations seem to be less demanding on the auxiliary basis set. Table XLIV lists the excitation energies of the lithium trimer which were carried out with five different auxiliary basis sets, namely, A(4,3;4,3), A(4,4;4,4), A(5,3;5,3), A(5,4;5,4), and A(5,5;5,5). Excitation energies calculated with the

smallest auxiliary basis, A(4,3;4,3), differ from those carried out with the largest auxiliary basis, A(5,5;5,5), by no more than 0.04 eV. The other three auxiliary bases yield no remarkable improvement in the calculation of the excitation energies. The smallest auxiliary basis, A(4,3;4,3), is therefore chosen in the present work.

The LSDxc/TDLSDxc functional provides quite accurate excitation energies for small lithium clusters in comparison with experiment. The deviations between the calculated excitation energies and the experimental results for all the clusters are less than 0.3 eV (except for the $1^1\Sigma_u^+$ state in the dimer, for which the excitation energy differs by 0.8 eV). This error is larger than that of the CI calculations. In the dimer and the tetramer cases, excitation energies calculated by the CI method [474, 69] have errors no larger than 0.1 eV in comparison with available experimental results. But CIS [69, 475] and RPA [69] give similar deviations as the present LSDxc/TDLSDxc calculations for the dimer and the tetramer. However, in the hexamer case, the present LSDxc/TDLSDxc calculations yield excitation energies with an absolute average error of 0.26 eV in comparison with the CI calculations [69] (0.16 eV if CI geometry was used) for the listed 26 excited states. But CIS [69] and RPA [69] give absolute average errors of 0.78 eV and 0.73 eV, respectively, in the excitation energies.

The LSDxc/TDLSDxc functional also gives reasonable oscillator strengths for the small lithium clusters. The calculated excitation spectra (see Figs. 34, and 37) show that the LSDxc/TDLSDxc functional yields the correct number of absorption bands in comparison with available experimental spectra. For example, the spectrum of the trimer performed by the LSDxc/TDLSDxc functional provides three strong peaks which are the same as the experimental spectrum cited in Ref. [10]. However, the present calculations give too large oscillator strengths for the two bands in the red–yellow region (5^2B_2 and 4^2A_1 states). It can also be seen clearly that the present calculated spectrum is much better than that cal-

culated by the traditional DFT method (multiplets approach) in Ref. [10], since the latter did not provide the correct number of peaks and the locations of the peaks are also not as good as the present calculations (see Figs. 33 and 34). In the tetramer spectrum, the LSDxc/TDLSDxc functional gives quite good absorption bands compared with experiment and conventional *ab initio* calculations. In the energy range from 0 to 3 eV, the present calculation gives one intense peak (1^1B_{3u}) in the near infrared region, two small peaks (2^1B_{3u} larger than 1^1B_{1u}) in the red–yellow region, and two strong bands (2^1B_{2u} and 2^1B_{1u}) in the blue and near UV (ultraviolet) region. This agrees well with the experimental spectrum in Refs [69, 10]. It can be seen from Figs. 36 and 37 that the present calculations give much improvement over the excitation spectra (excitation energies and oscillator strengths) calculated by the traditional DFT method ("multiplets" and Fritsche approaches) in Ref. [10]. The "multiplets" and Fritsche approaches provided almost all of the bands with the same value of oscillator strength (peaks with the same height). Moreover, the present calculated spectrum can also be compared with the CI calculations [69]. The present calculations in the energy region from 0 to 3 eV yields one more small peak (around 3 eV) than those of the CI calculations which show six bands (three strong bands and three small ones). Nevertheless, both the present calculations and the CI results agree well with the experiment and the time-dependent DFT assignments are the same as those of the traditional CI method.

Excitation energies calculated with the LB94xc/TDLSDxc functional have larger errors than those carried out with the LSDxc/TDLSDxc functional in the energy range listed in Tables XXXVIII, XXXIX, XL, XLI, XLIII, and XLII. This presumedly comes from the difference in the short–r behavior of the LSDxc and the LB94xc functionals. For example, in the dimer case, the calculated excitation energy of the $3^1\Sigma_g^+$ state with the LB94xc/TDLSDxc functional differs from the experiment by 0.74 eV, whereas, that with the LSDxc/TDLSDxc functional has an error of 0.36 eV. The $2^1\Pi_u$ state excitation energy performed

by the LB94xc/TDLSDxc functional gives an error of 0.6 eV in comparison with experiment, while the excitation energy of this state calculated with the LSDxc/TDLSDxc functional differs from the experiment by 0.04 eV. However, the difference between the excitation energies calculated by the LSDxc/TDLSDxc and the LB94xc/TDLSDxc functionals can be as large as 1 eV. For example, in the tetramer case, the largest difference between the excitation energies calculated with the LSDxc/TDLSDxc and LB94xc/TDLSDxc functionals is 0.9 eV for the 5^1B_{2u} state.

For low excitation energies, the LSDxc/TDLSDxc functional provides larger excitation energies than those carried out by the LB94xc/TDLSDxc functional. In contrast, for high excitations, the LSDxc/TDLSDxc functional gives excitation energies lower than those calculated by the LB94xc/TDLSDxc functional. This is assumed to be due to the short–r and asymptotic behavior of the two functionals. It seems that the potential energy curve of the LB94xc/TDLSDxc functional is very shallow and more flat than that of the LSDxc/TDLSDxc functional in the short–r region. But at large–r, the energy potential curve of the LB94xc/TDLSDxc functional has a much longer tail than that of the LSDxc/TDLSDxc functional.

There is a change in the ordering between the excited states calculated with the LSDxc/TDLSDxc and the LB94xc/TDLSDxc functionals in all cluster calculations. In the dimer case, the $1^3\Sigma_g^+$ state with the LB94xc/TDLSDxc functional rises above the $1^1\Pi_u$ and the $1^1\Sigma_u^+$ states. The $2^3\Pi_u$ state with the LB94xc/TDLSDxc functional falls below the $1^1\Pi_g$ state. However, the state ordering of the $1^1\Pi_u$ state being above the $1^1\Sigma_u^+$ state predicted by both the LSDxc/TDLSDxc and the LB94xc/TDLSDxc functionals is different from that of the experiment and the CCSD (coupled cluster single and double excitations) results [476], the CI calculation [474], and the CIS state ordering [475]. For the trimer, the 2^2B_2 state with the LB94xc/TDLSDxc functional comes up to the

2^2A_1 state, and the 3^2A_2 state excitation energy with the LB94xc/TDLSDxc functional is smaller than the 7^2A_1 and the 3^2B_1 states. This ordering change also occurred in the calculations of the tetramer and the pentamer.

Excitation spectra of the lithium clusters calculated by the LSDxc/TDLSDxc and the LB94xc/TDLSDxc functionals are very similar. The calculations with both the LSDxc/TDLSDxc and the LB94xc/TDLSDxc functionals give the same number of strong bands in the predicted excitation spectra. However, the oscillator strengths calculated with the LSDxc/TDLSDxc and the LB94xc/TDLSDxc functionals may be different. For example, in the trimer case, the excitation spectra predicted by both the LSDxc/TDLSDxc and the LB94xc/TDLSDxc functionals show three strong peaks, and the two functionals give the same assignments, the first strong peak is assigned to the 4^2A_1 state, the second band belongs to the 5^2B_2 state, and the third band is assigned to the 3^2A_2 state. However, the LSDxc/TDLSDxc functional predicts the 5^2B_2 state as the most intense peak, whereas, the LB94xc/TDLSDxc functional gives the 3^2A_2 state as the strongest band, in the trimer spectrum. In the tetramer case, there are also differences in the calculated oscillator strengths between the LSDxc/TDLSDxc and the LB94xc/TDLSDxc functionals. The LSDxc/TDLSDxc functional yields the first strong band as the 1^1B_{3u} state and a weaker peak with higher excitation energy is assigned to the 2^1B_{3u} state. In contrast, the LB94xc/TDLSDxc functional gives the first strong peak as the 2^1B_{3u} state, the weaker band with lower transition energy is assigned to the 1^1B_{3u} state.

The calculations of larger lithium clusters (the pentamer and the hexamer) with the LB94xc/TDLSDxc functional have a problem – symmetry breaking. The molecular orbital symmetries of the pentamer carried out by the LB94xc/TDLSDxc functional are difficult to be assigned due to symmetry breaking with the EXTRA-FINE grid (6208 grid points per atom), and the final results of the pentamer with the LB94xc/TDLSDxc functional had to be recalculated with the user-

defined grid (24832 grid points per atom). Unfortunately, there are no other *ab initio* calculations or experimental results available for comparison with the present calculations of the pentamer. Hence the excitation energies of the pentamer are only compared between the present LSDxc/TDLSDxc calculation and the LB94xc/TDLSDxc calculation which are given in Table XLI. The excitation energies calculated with the LSDxc/TDLSDxc functional are larger than those carried out by the LB94xc/TDLSDxc functional for the lowest twenty-seven excited states. Nevertheless, the difference is less than 0.2 eV. This may be due to the difference in the short–r behavior of the two functionals. However, the calculations with the two functionals provide very similar excitation spectra with two strong bands (the 6^2B_2 and the 10^2A_1 states) and thirty-three small peaks (thirty-two with the LB94xc/TDLSDxc). Moreover, the present calculations show that the excitation energies between two adjacent transitions are very close (e.g. the excitation energy difference between the 1^2A_2 and the 3^2A_1 states is 0.001 eV). This indicates that electronic states of the pentamer are very closely distributed. This may also be the reason why the pentamer is difficult to measure. In the hexamer case, symmetry breaking occurred in excitations performed with the D_{3h} geometry and the LB94xc/TDLSDxc functional, no matter what quality of grid was used (EXTRA-FINE, or different quality of user-defined grid with Random or even NonRandom options). This symmetry breaking also occurred in the calculations with the C_{2v} geometry (no matter whether the DFT optimized geometry in Ref [465] or the CI optimized geometry in Ref. [472] were used) by both the LSDxc/TDLSDxc and the LB94xc/TDLSDxc functionals. Moreover, the hexamer calculations yield imaginary excitation energies for a couple of the lowest excitations with both the LSDxc/TDLSDxc and the LB94xc/TDLSDxc functionals and the DFT C_{2v} geometry. This also occurred for the LB94xc/TDLSDxc functional calculation with the CI C_{2v} geometry. Nevertheless, the final calculations were done with the EXTRA–FINE and the NonRandom grid option and the excitation energies were assigned with

the largest transition coefficient which in general is one order of magnitude larger than the others. Tables XLIII and XLII show that excitation energies of the hexamer calculated with the LSDxc/TDLSDxc functional and the LB94xc/TDLSDxc functional are close to those calculated by the CI method [12] (note that the CI excitation energies are estimated from the CI calculated excitation spectrum). The deviations are no larger than 0.3 eV for the twenty-five optically allowed excitation energies, except for the 1^1B_1 and the 3^1B_1 states which differ by 0.39 eV and 0.46 eV, respectively for the LSDxc/TDLSDxc calculation, and by 0.5 eV for both states from the LB94xc/TDLSDxc calculation. The spectrum predicted by both the LSDxc/TDLSDxc and the LB94xc/TDLSDxc functionals is quite similar to that from the CI calculations with the D_{3h} geometry [12]. Both of the present calculations and the CI calculation [12] give two intense peaks in the red-yellow region (the 3^1B_2 and the 4^1A_1 states), and two weaker (medium) peaks around 3 eV (the 8^1B_2 and the 10^1A_1 states in the present calculations, the 10^1B_2 and the 11^1A_1 states in the CI calculation). However, this is different from the experimental spectrum which just exchanges the locations of the intense peaks and the weaker (medium) peaks. This may suggest that the D_{3h} geometry is not the equilibrium geometry. Excitation spectrum of the hexamer with the C_{2v} geometry predicted by the LSDxc/TDLSDxc functional and the LB94xc/TDLSDxc functional is different whether the calculation started with the DFT optimized geometry or the CI optimized geometry. The excitation spectrum predicted with the CI optimized C_{2v} geometry shows that both the LSDxc/TDLSDxc the LB94xc/TDLSDxc functionals yielding two strong bands around 2.4 eV and 3 eV, respectively, but the assignments are different between the two functionals. The LSDxc/TDLSDxc assigned two most intense bands to the 4^1B_2 and the 5^1B_1 states, the LB94xc/TDLSDxc functional assigned them to the 7^1A_1 and the 6^1B_1 states. However, the two functionals predicted a spectrum of the hexamer that is different from the experimental results due to the extra strong band at 3 eV. But the CI calculation with the same CI optimized C_{2v} ge-

ometry [12] did get very good agreement between the calculated spectrum and the experimental results (see Fig. 44). This may indicate that the CI minimum geometry might not be the minimum on the DFT energy surface, since the excitation spectrum predicted with the DFT optimized geometry did give some improvement compared with those predicted with the CI optimized geometry. Both the excitation spectrum predicted by the LSDxc/TDLSDxc and the LB94xc/TDLSDxc functionals shows two strong bands (the 7^1A_1 and the 7^1B_2 states) around 2.4 eV and a large number of small bands in the energy interval up to 3 eV. This coincides with the recorded spectrum. But the LSDxc/TDLSDxc calculations yield one more strong peak at 3 eV which leads to a different spectrum from the experimental results, whereas the spectrum predicted by the LB94xc/TDLSDxc functional agrees well with the experiment. This suggests that the equilibrium geometry has C_{2v} symmetry which is consistent with the DFT geometry optimization in which DFT predicted C_{2v} geometry for the most stable isomer [465]. This is also the same as the prediction of the CI method [472, 12]. Moreover, geometry is an important ingredient in the calculation of excitation spectra, since the DFT C_{2v} geometry and the CI C_{2v} geometry did yield quite a different excitation spectrum for the hexamer. The excitation spectrum with the CI C_{2v} geometry gives more peaks than that with the DFT C_{2v} geometry and the number of the strong bands are also different with the two geometries. It seems to suggest that the excitation spectra not only depend on the functional, but also depend on the geometry.

The excitation spectra of the lithium clusters (Figs. 31 – 48) show that the open–shell clusters (the trimer and the pentamer) yield more bands than the closed–shell clusters (the dimer, the tetramer, and the hexamer) in the given energy interval. This can be understood from the case of HOMO electron transitions, in the closed–shell clusters, HOMO electron transitions occur to singlets and triplets, but only singlet transitions are optically allowed; while in the open–shell clusters, HOMO electron transitions only occur to doublets which are opti-

cally allowed. Hence, in the certain energy range, open–shell clusters yield more bands.

6.4 CONCLUSION

Excitation spectra of small lithium clusters (from the dimer up to the hexamer) have been calculated by time-dependent DFT with the LSDxc/TDLSDxc and the LB94xc/TDLSDxc functionals. The present calculated excitation spectra agree well with the experimental results as well as with high quality CI calculations. But the simplicity and computational efficiency give the time-dependent DFT more advantages. The time-dependent DFT results get much more improvement over those of the traditional DFT "multiplets" and Fritsche approaches, especially for the oscillator strengths.

The present calculations show that the exchange-correlation functional is very important in the calculation of excitation energies. Different functionals can change excitation energies dramatically. The present calculations show that the difference of excitation energies calculated between the LSDxc/TDLSDxc and the LB94xc/TDLSDxc functionals can be as large as 1 eV. This suggests that a better functional may improve the excitation energies remarkably. The choice of the exchange-correlation functional effects the excitation energies differently in the different energy regions. For low excitations, the small–r behavior of the exchange-correlation functional plays an important role. For high excitations, the large–r behavior of the exchange-correlation functional is crucial. The LSDxc/TDLSDxc functional gives quite good low excitation energies. To develop one functional that can provide accurate excitation energies for both low and high excitations will require further investigation.

Geometry is a crucial ingredient in the calculation of excitation spectra. Different quality of geometry may lead to different spectra.

The excitation energy calculations of small lithium clusters are very sensitive to orbital basis set, but less sensitive to auxiliary basis set. Lithium cluster excitation energies are in general overestimated by the time-dependent DFT. This is in contrast with those of open-shell molecules at the right–hand side of the periodic table (e.g. CN, CO^+, and N_2^+) for which the time-dependent DFT underestimated excitation energies in most cases.

The present calculations found that the main features of these excitation spectra of the small lithium clusters are the spectroscopic pattern with only two or three strong peaks located around 1.8 eV, 2.3 eV, and 2.8 eV regions. The present calculated excitation spectra also show that the open–shell clusters (the trimer and the pentamer) have many more bands than do the closed–shell clusters (the dimer, the tetramer, and the hexamer).

Table XXXVI. Ionization threshold ($-\varepsilon_{HOMO}$) of Li clusters from the dimer up to hexamer calculated with the Sadlej basis and by the LSDxc and the LB94xc functionals.

Clusters	$-\varepsilon^{\alpha}_{HOMO}$ (eV)	
	LSDxc (AE)	LB94xc (AE)
Li_2	3.76	6.13
Li_3	2.58	4.78
Li_4	2.87	5.12
Li_5	2.80	4.95
$Li_6(D_{3h})$	3.18	5.45
$Li_6(C_{2v}, CIgeom)$	2.85	5.11
$Li_6(C_{2v}, DFTgeom)$	3.00	5.28

Table XXXVII. Ground state configurations and the ground state symmetry of lithium clusters calculated by the present DFT SCF calculations with LSDxc functional.

Clusters (symmetry)	Lowest electron configuration	Ground state symmetry
$Li_2(D_{\infty h})$	$(1\sigma_g^+)^2(1\sigma_u^+)^2(2\sigma_g^+)^2$	$1^1\Sigma_g^+$
$Li_3(C_{2v})$	$(1a_1)^2(2a_1)^2(1b_2)^2(3a_1)^2(2b_2)^1$	1^2B_2
$Li_4(D_{2h})$	$(1a_g)^2(1b_{2u})^2(1b_{3u})^2(2a_g)^2(3a_g)^2(2b_{3u})^2$	1^1A_g
$Li_5(C_{2v})$	$(1b_2)^2(1a_1)^2(2a_1)^2(2b_2)^2(3a_1)^2(4a_1)^2(3b_2)^2(5a_1)^1$	1^2A_1
$Li_6(D_{3h} \rightarrow C_{2v})$	$(1a_1)^2(1b_2)^2(2a_1)^2(3a_1)^2(2b_2)^2(4a_1)^2(5a_1)^2(6a_1)^2(3b_2)^2$	1^1A_1
$Li_6(C_{2v})(CIgeom)$	$(1b_2)^2(2b_2)^2(1a_1)^2(3b_2)^2(2a_1)^2(1b_1)^2(3a_1)^2(4b_2)^2(4a_1)^2$	1^1A_1
$Li_6(C_{2v})(DFTgeom)$	$(1a_1)^2(1b_2)^2(2a_1)^2(2b_2)^2(3a_1)^2(1b_1)^2(4a_1)^2(3b_2)^2(5a_1)^2$	1^1A_1

Table XXXVIII. Li_2 vertical excitation energies (eV) calculated with the LSDxc/TDLSDxc and the LB94xc/TDLSDxc functional using the Sadlej basis compared with available experimental results and conventional *ab initio* calculations.

	Vertical excitation energies (eV).					
State	LSDxc/ TDLSDxc	LB94xc/ TDLSDxc	EXPT[a]	CCSD[b]	AEVCI[a]	CIS[c]
$1^1\Sigma_g^+$	0.000	0.000	0.000	0.000	0.000	0.000
$1^3\Pi_u$		0.384	1.398	1.375	1.400	0.888
$1^3\Sigma_u^+$	1.465	1.313		1.023	1.236	0.480
$1^1\Pi_u$	2.387	2.526	2.574	2.557	2.538	2.627
$1^1\Sigma_u^+$	2.638	2.608	1.846	1.750	1.843	2.093
$1^3\Sigma_g^+$	2.819	2.498		2.032	2.108	1.407
$2^1\Sigma_g^+$	3.525	3.456		2.530		2.878
$2^3\Sigma_g^+$	3.846	4.052			3.480	
$1^3\Pi_g$	3.848	4.105				2.741
$3^1\Sigma_g^+$	3.849	4.230	3.489		3.487	
$2^3\Pi_u$	3.871	4.353				
$1^1\Pi_g$	3.896	4.294		2.726	2.977	3.291
$2^1\Pi_u$	3.910	4.447	3.871[d]			
$2^3\Sigma_u^+$	3.944	4.545				
$2^1\Sigma_u^+$	3.968	4.574			3.822	
$3^3\Sigma_g^+$	4.188	4.696			3.940	
$4^1\Sigma_g^+$	4.296	4.832	4.203		4.205	

[a] Converted from Ref. [474].

[b] Coupled cluster calculations taken from Ref. [476].

[c] Calculated from Ref. [475].

[d] Converted from Ref. [379].

Table XXXIX. Li_3 vertical excitation energies (eV) calculated with the LSDxc/TDLSDxc and the LB94xc/TDLSDxc functional using the Sadlej basis compared with traditional *ab initio* results.

	Vertical excitation energies (eV).					
State	LSDxc/ TDLSDxc	LB94xc/ TDLSDxc	EXPT	SCF[a]	MRD-CI[a]	Full-CI[a]
1^2B_2	0.000	0.000		0.000	0.000	0.000
1^2A_1	0.401	0.074		0.286	0.317	0.216
1^2B_1	0.784	0.568		0.679	0.787	0.711
2^2A_1	1.146	1.053			1.206	1.136
2^2B_2	1.186	0.931			1.430	1.346
3^2B_2	1.487	1.244			2.615	2.407
3^2A_1	1.537	1.286			1.612	1.498
1^2A_2	1.618	1.459		2.472	1.975	1.937
2^2A_2	1.989	1.960				
4^2A_1	2.125	2.026	1.8 (A)[b,c]			
4^2B_2	2.128	2.085				
2^2B_1	2.352	2.359			2.320	2.245
5^2B_2	2.390	2.324	2.1[c]			
6^2B_2	2.515	2.563				
5^2A_1	2.531	2.334				
6^2A_1	2.643	2.679				
7^2A_1	2.689	2.898				
3^2B_1	2.744	3.188				
3^2A_2	2.816	2.879	2.7 (C)[c,d]			

[a] Results taken from Ref. [466].

[b] Result taken from Ref. [58].

[c] Estimated from spectra graph in Ref .[10].

[d] Number was cited in Ref. [10].

Table XL. Li_4 optically allowed vertical excitation energies (eV) calculated with the LSDxc/TDLSDxc and the LB94xc/TDLSDxc functional using the Sadlej basis and compared with traditional *ab initio* results and available experiment.

	Vertical excitation energies (eV).						
State	LSDxc/ TDLSDxc	LB94xc/ TDLSDxc	EXPT[a]	MCLR[b]	CI[c]	RPA[c]	CIS[c]
1^1B_{1u}	2.134	2.103	2.356(C)	2.56	2.36	2.77	2.84
2^1B_{1u}	2.907	3.005	2.928(E)	3.12	3.01	3.26	3.42
3^1B_{1u}	4.104	4.062				5.30	5.31
4^1B_{1u}	4.295	4.311				5.99	6.09
5^1B_{1u}		4.887				6.77	6.79
1^1B_{2u}	1.656	1.516		1.94	1.81	2.49	2.55
2^1B_{2u}	2.621	2.664	2.651(D)	2.69	2.65	2.86	3.09
3^1B_{2u}	3.254	3.753				4.38	4.44
4^1B_{2u}	3.391	3.969				5.17	5.22
5^1B_{2u}	3.443	4.377				5.48	5.56
1^1B_{3u}	1.661	1.627	1.801(A)	1.82	1.78	1.80	1.85
2^1B_{3u}	2.074	1.874	2.084(B)	2.29	2.09	2.32	2.33
3^1B_{3u}	2.992	3.061				3.55	3.55
4^1B_{3u}	3.069	3.231				4.18	4.20
5^1B_{3u}	3.166	3.533				4.22	4.29

[a] Experimental results taken from Ref. [449, 69].

[b] Results taken from Ref. [11].

[c] Results taken from Ref. [69].

Table XLI. Li_5 vertical excitation energies (eV) calculated with the LSDxc/TDLSDxc and the LB94xc/TDLSDxc functionals using the Sadlej basis.

	Vertical excitation energies (eV).				
State	LSDxc/ TDLSDxc	LB94xc/ TDLSDxc	State	LSDxc/ TDLSDxc	LB94xc/ TDLSDxc
1^2A_1	0.000	0.000	3^2A_2	1.690	1.520
2^2A_1	0.682	0.529	2^2B_1	1.701	1.536
1^2B_2	0.843	0.571	7^2A_1	1.781	1.694
1^2B_1	0.869	0.646	6^2B_2	1.787	1.806
2^2B_2	0.878	0.706	8^2A_1	1.898	1.805
1^2A_2	1.182	1.006	9^2A_1	2.039	1.999
3^2A_1	1.183	0.992	7^2B_2	2.090	2.015
3^2B_2	1.189	0.958	3^2B_1	2.095	1.946
4^2B_2	1.340	1.355	4^2B_1	2.191	2.069
4^2A_1	1.372	1.257	8^2B_2	2.224	2.107
5^2A_1	1.492	1.411	5^2B_1	2.236	2.137
2^2A_2	1.553	1.386	9^2B_2	2.287	2.142
5^2B_2	1.619	1.608	10^2A_1	2.289	2.292
6^2A_1	1.668	1.470	10^2B_2	2.387	2.217

Table XLII. Li_6 ($D_{3h} \rightarrow C_{2v}$) optically allowed vertical excitation energies (eV) calculated with the LSDxc/TDLSDxc and the LB94xc/TDLSDxc functionals using the Sadlej basis compared with traditional *ab initio* calculations.

	Vertical excitation energies (eV).			
State	LSDxc/ TDLSDxc	LB94xc/ TDLSDxc	EXPT[a]	CI[b]
2^1A_1	1.273	1.228		1.58
3^1A_1	1.372	1.332		1.68
4^1A_1	1.939	1.999	1.82	2.18
5^1A_1	2.062	2.097		2.31
6^1A_1	2.095	2.149		2.35
7^1A_1	2.235	2.196		2.43
8^1A_1	2.499	2.450		2.59
9^1A_1	2.860	2.945		2.76
10^1A_1	2.896	2.978	2.58	2.89
11^1A_1	3.084	3.172		3.03
1^1B_1	1.455	1.331		1.84
2^1B_1	2.236	2.135		2.49
3^1B_1	2.278	2.233		2.74
4^1B_1	3.064	3.106		2.79
5^1B_1	3.165	3.164		3.15
1^1B_2	1.258	1.215		1.52
2^1B_2	1.581	1.490		1.87
3^1B_2	1.941	1.998	1.82	2.13
4^1B_2	1.957	2.069		2.24
5^1B_2	2.069	2.146		2.34
6^1B_2	2.236	2.206		2.44
7^1B_2	2.490	2.441		2.52
8^1B_2	2.894	2.975	2.58	2.81
9^1B_2	3.083	3.172		3.01
10^1B_2	3.241	3.273		3.06

[a] Results taken from Ref. [69].

[b] Estimated from spectra in Ref. [12].

Table XLIII. Li_6 (C_{2v}) optically allowed vertical excitation energies (eV) calculated with the LSDxc/TDLSDxc and the LB94xc/TDLSDxc functionals using the Sadlej basis and compared with traditional *ab initio* calculations.

	Vertical excitation energies (eV).						
State	LSDxc(DFT)/ TDLSDxc	LB94xc(DFT)/ TDLSDxc	LSDxc(CI)/ TDLSDxc	LB94xc(CI)/ TDLSDxc	CI[a]	RPA[a]	CIS[a]
2^1A_1	1.394	1.305	1.113	1.049	1.42	1.51	1.54
3^1A_1	1.652	1.604	1.551	1.468	1.70	1.82	1.87
4^1A_1	2.132	1.815	1.953	1.645	1.84	2.36	2.42
5^1A_1	2.185	2.057	2.038	1.941	2.11	2.49	2.55
6^1A_1	2.358	2.265	2.274	2.202	2.20	2.60	2.72
7^1A_1	2.433	2.469	2.347	2.377	2.37	2.96	3.10
8^1A_1	2.958	2.950	2.379	2.735	2.51	3.53	3.60
9^1A_1	3.013	3.120	2.775	2.939	2.59	3.63	3.66
10^1A_1	3.067	3.297	2.854	3.135	2.81	4.18	4.20
11^1A_1	3.140	3.409	2.912	3.284	2.88	4.20	4.23
1^1B_1	0.801	0.460	0.647	0.335	0.81	0.91	0.97
2^1B_1	1.821	1.685	1.796	1.684	1.80	2.22	2.23
3^1B_1	1.948	1.781	1.944	1.767	2.10	2.90	3.06
4^1B_1	2.978	3.060	2.841	2.597	2.24	3.56	3.57[b]
5^1B_1	3.004	3.094	2.918	2.823	2.43	3.57	3.58
6^1B_1	3.102	3.224	3.045	2.967	2.62	3.76	3.77
7^1B_1	3.340	3.354	3.096	3.183	2.76	3.81	3.84
8^1B_1	3.387	3.641	3.223	3.330	2.93	4.47	4.52
1^1B_2			1.348	1.206	1.65	1.70	1.73
2^1B_2	1.403	1.311	1.640	1.600	1.73	1.77	1.81
3^1B_2	1.652	1.605	1.799	1.792	1.79	2.30	2.34
4^1B_2	2.079	1.827	2.128	1.977	2.10	2.42	2.53
5^1B_2	2.112	1.992	2.302	2.130	2.40	2.63	2.65
6^1B_2	2.194	2.108	2.444	2.367	2.47	2.69	2.79
7^1B_2	2.436	2.471	2.581	2.565	2.62	3.42	3.44
8^1B_2	3.014	2.801	2.950	2.869	2.74	3.83	3.87
9^1B_2	3.051	3.201	3.016	3.384	2.81	4.21	4.22

[a] Results taken from Ref. [69].

[b] There is an error for 4^1B_1 excitation energy being 3.75 eV in original Ref. [69], it should be 3.57 eV.

Table XLIV. Comparison of Li_3 vertical excitation energies (eV) calculated with different auxiliary basis sets using the LSDxc/TDLSDxc functional.

	Vertical excitation energies (eV).				
State	A(4,3;4,3)	A(4,4;4,4)	A(5,3;5,3)	A(5,4;5,4)	A(5,5;5,5)
1^2B_2	0.000	0.000	0.000	0.000	0.000
1^2A_1	0.401	0.403	0.404	0.402	0.408
1^2B_1	0.784	0.787	0.789	0.787	0.789
2^2A_1	1.146	1.144	1.144	1.144	1.145
2^2B_2	1.186	1.190	1.190	1.190	1.192
3^2B_2	1.487	1.491	1.491	1.1491	1.496
3^2A_1	1.537	1.536	1.538	1.536	1.535
1^2A_2	1.618	1.623	1.625	1.623	1.623
2^2A_2	1.989	1.978	1.983	1.978	1.979
4^2A_1	2.125	2.123	2.123	2.123	2.123
4^2B_2	2.128	2.126	2.125	2.126	2.125
2^2B_1	2.352	2.336	2.339	2.336	2.334
5^2B_2	2.390	2.389	2.389	2.389	2.392
6^2B_2	2.515	2.489	2.501	2.489	2.488
5^2A_1	2.531	2.530	2.532	2.530	2.530
6^2A_1	2.643	2.617	2.637	2.617	2.615
7^2A_1	2.689	2.667	2.677	2.667	2.666
3^2B_1	2.744	2.710	2.737	2.710	2.708
3^2A_2	2.816	2.789	2.816	2.789	2.788

Table XLV. Comparison of Li_3 vertical excitation energies (eV) calculated with different orbital basis sets using the LSDxc/TDLSDxc functional.

	Vertical excitation energies (eV).				
State	Huzinaga	BKK	DZVP	Sadlej	Sadlej (FD)
1^2B_2	0.000	0.000	0.000	0.000	0.000
1^2A_1	0.444	0.399	0.433	0.401	0.401
1^2B_1	3.727	0.795	1.169	0.784	0.784
2^2A_1	1.840	1.159	1.412	1.146	1.141
2^2B_2	1.541	1.220	1.392	1.186	1.184
3^2B_2	2.315	1.529	1.768	1.487	1.485
3^2A_1	2.123	1.557	1.816	1.537	1.536
1^2A_2	4.781	2.106	2.057	1.618	1.621
2^2A_2	5.071	3.087	2.649	1.989	1.991
4^2A_1	4.215	2.208	2.577	2.125	2.122
4^2B_2	2.967	2.207	2.475	2.128	2.125
2^2B_1	5.687	1.703	3.299	2.352	2.361
5^2B_2	3.333	2.441	2.693	2.390	2.385
6^2B_2	4.241	2.608	3.392	2.515	2.510
5^2A_1	4.336	2.582	3.013	2.531	2.525
6^2A_1	4.527	2.698	3.719	2.643	2.607
7^2A_1	4.781	2.738	4.033	2.689	2.641
3^2B_1	6.413	2.584	4.056	2.744	2.735
3^2A_2	6.142	3.753	3.738	2.816	2.806

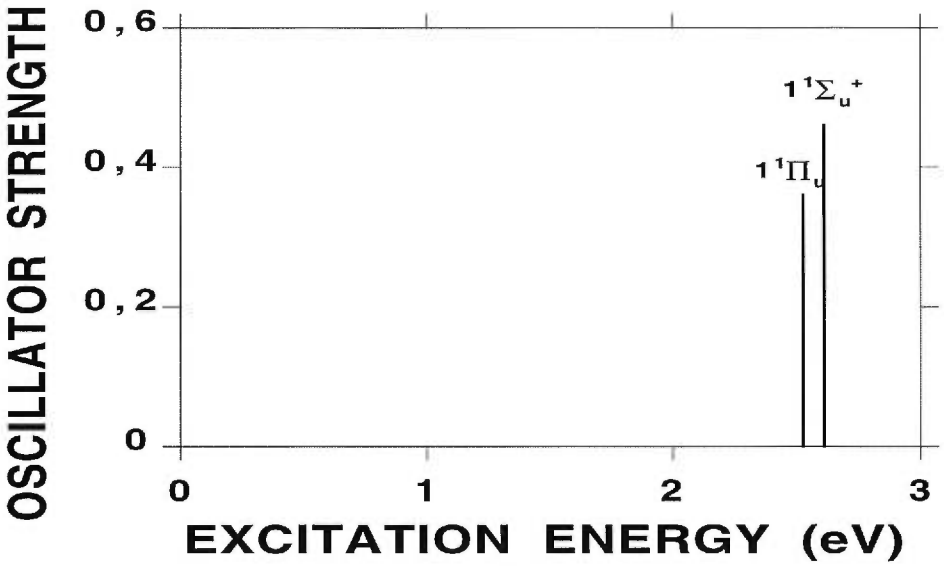

Figure 31. Excitation spectrum of the lithium dimer carried out with the LS-Dxc/TDLSDxc functional and the Sadlej basis.

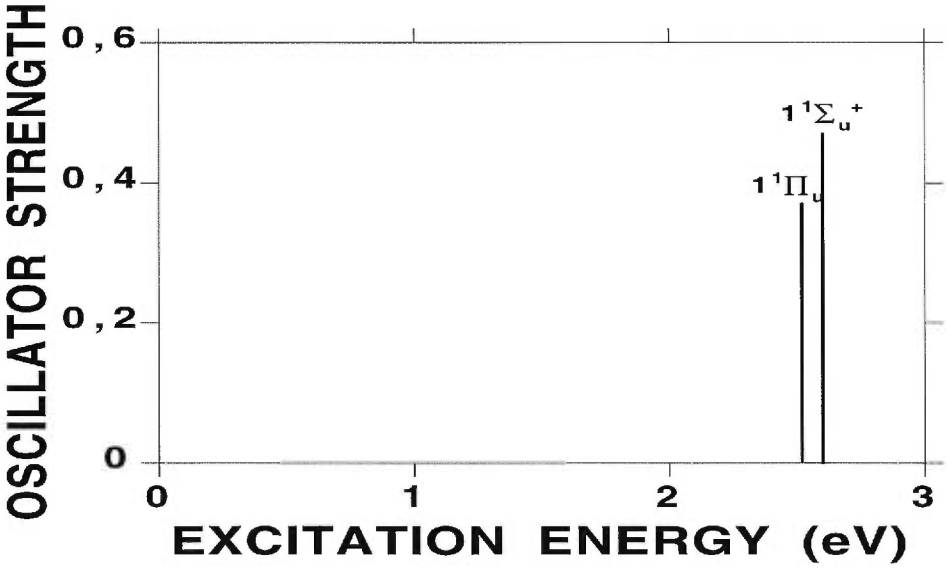

Figure 32. Excitation spectrum of the lithium dimer carried out with the LB94xc/TDLSDxc functional and the Sadlej basis.

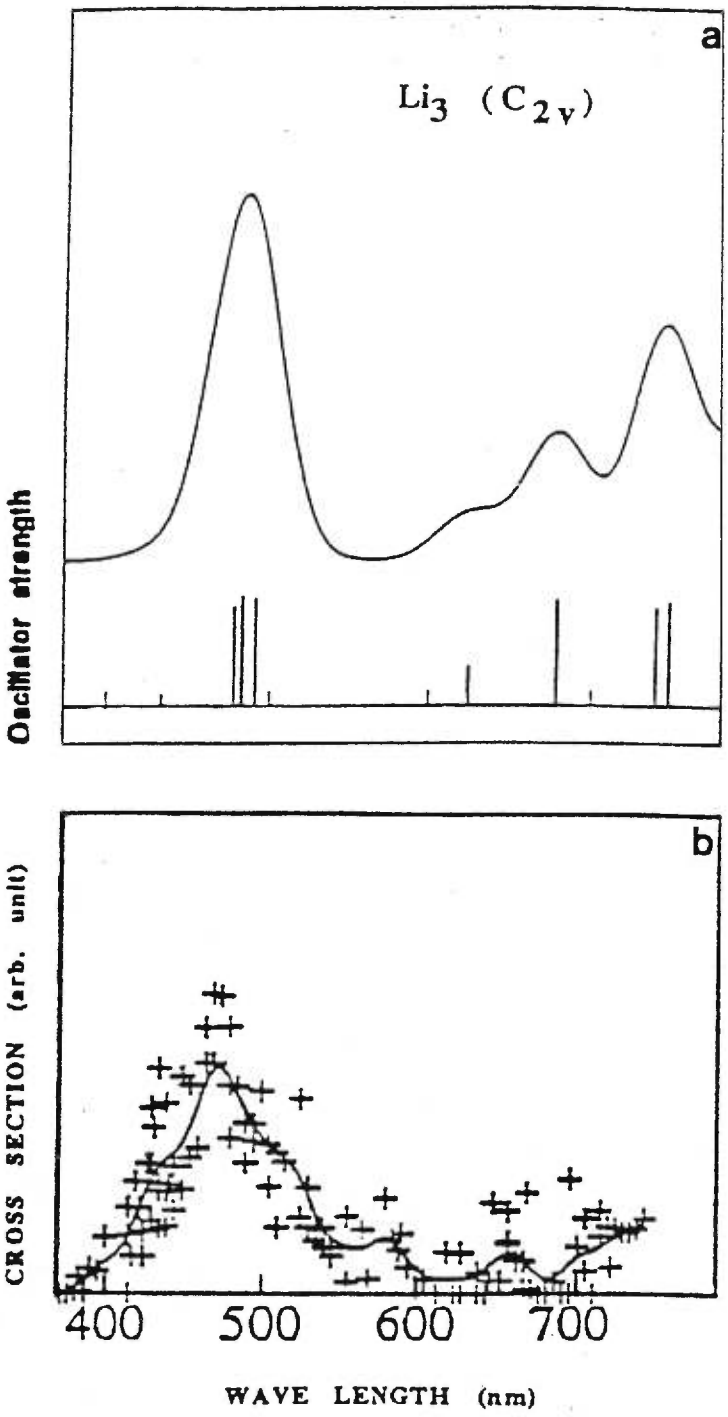

Figure 33. Comparison between spectra of the lithium trimer calculated by DFT "multiplets" approach (a) and experiment (b), taken from Ref. [10].

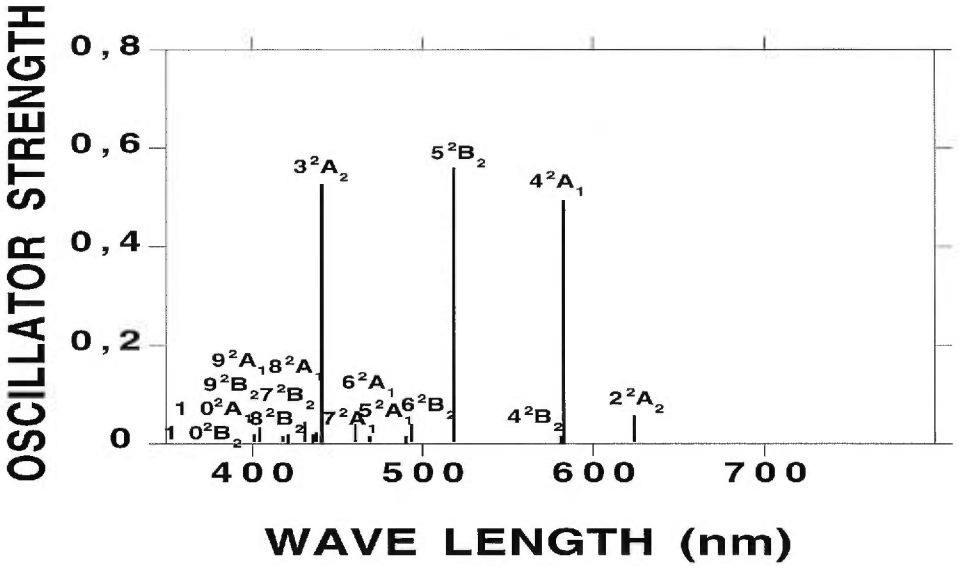

Figure 34. Excitation spectrum of the lithium trimer carried out with the LS-Dxc/TDLSDxc functional and the Sadlej basis.

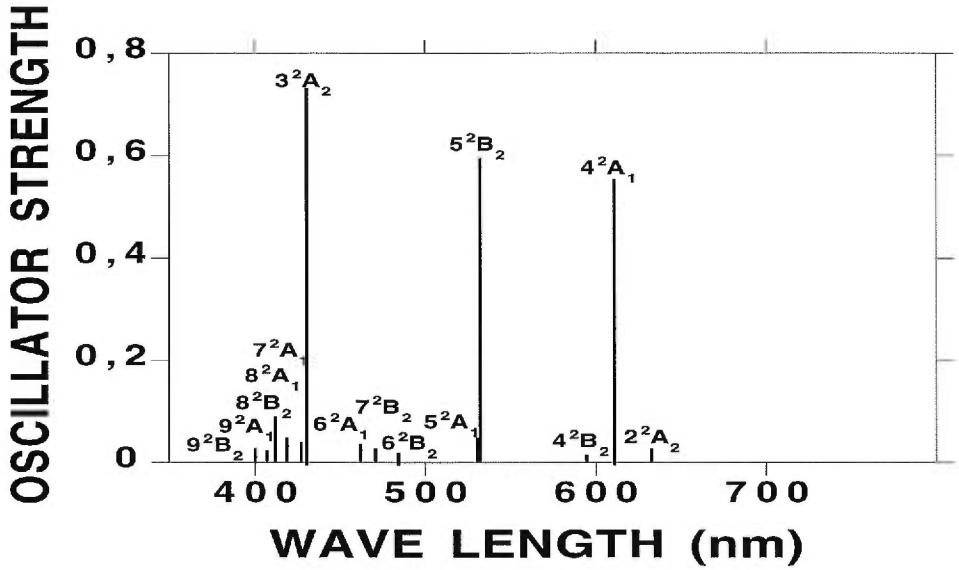

Figure 35. Excitation spectrum of the lithium trimer carried out with the LB94xc/TDLSDxc functional and the Sadlej basis.

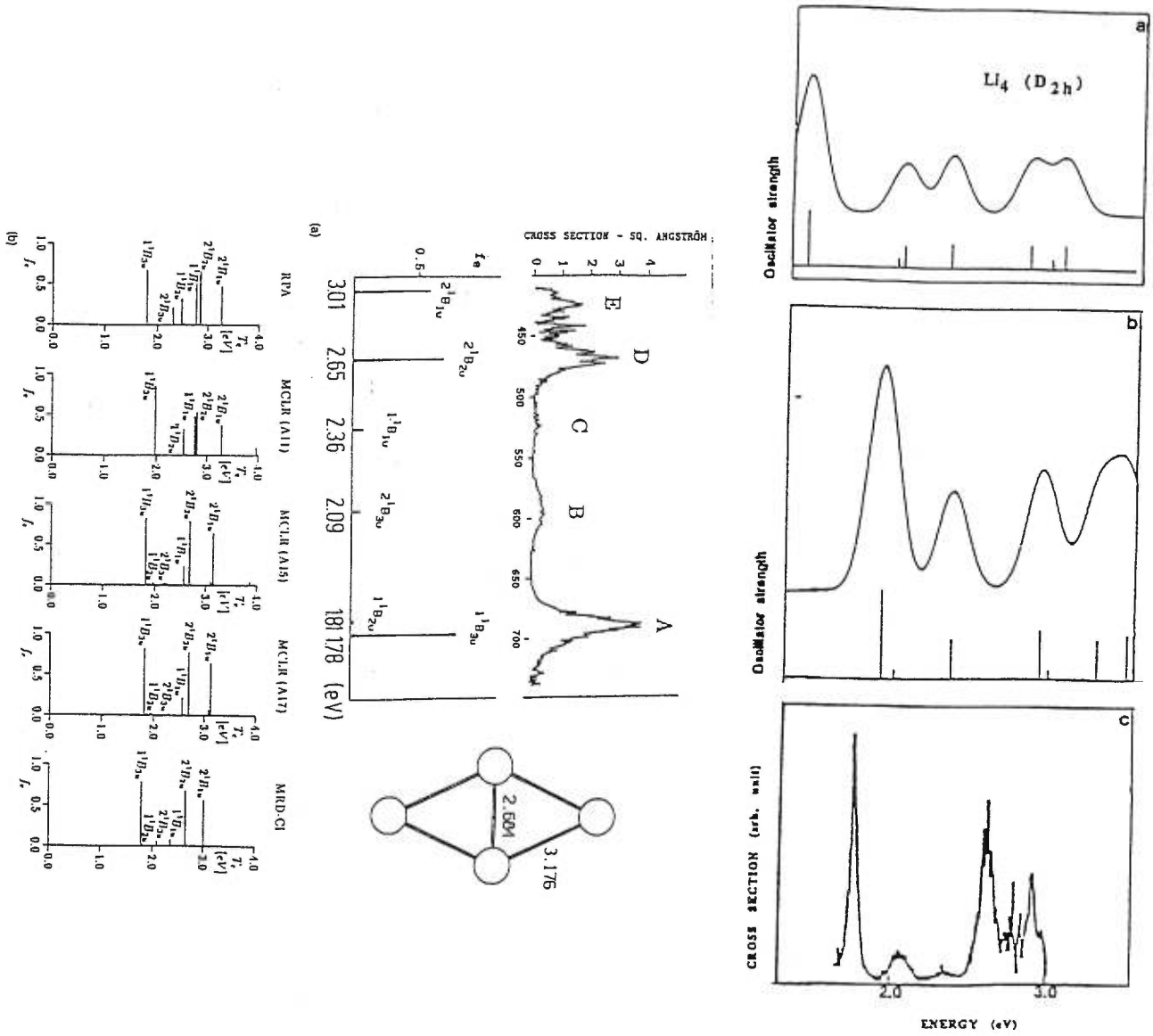

Figure 36. Left: (a) Comparison between the optically allowed transitions and oscillator strengths predicted by CI calculations and high resolution experimental spectrum of Li_4. (b) Comparison of optically allowed transitions (eV) and oscillator strengths for Li4, obtained with the RPA, the MCLR, and the MRD-CI treatment. Taken from Ref. [11]. Right: Comparison between spectrum of the tetramer calculated with the DFT "multiplets" approach (a), the DFT Fritsche approach (b), and the experimental spectrum (c). Taken from Ref. [10].

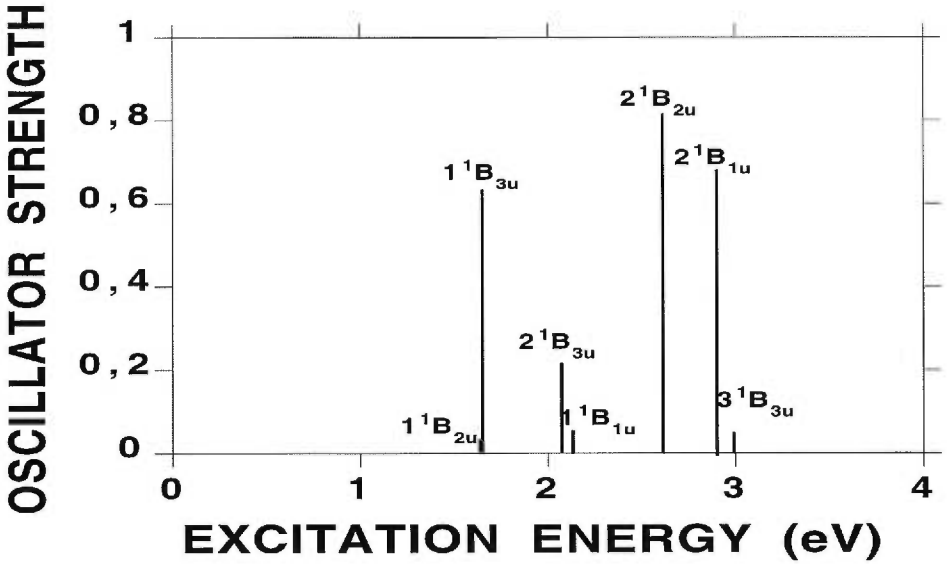

Figure 37. Excitation spectrum of the lithium tetramer performed with the LS-Dxc/TDLSDxc functional and the Sadlej basis.

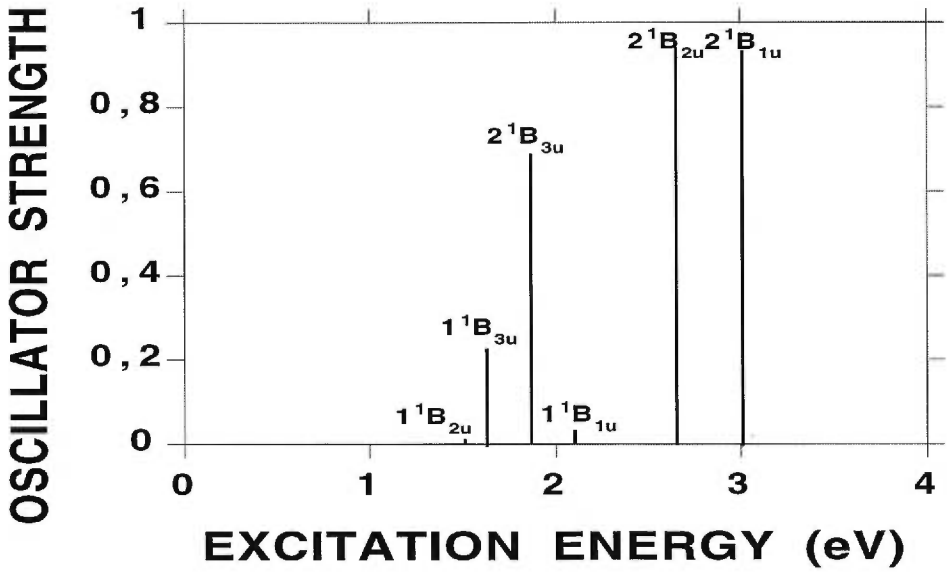

Figure 38. Excitation spectrum of the lithium tetramer performed with the LB94xc/TDLSDxc functional and the Sadlej basis.

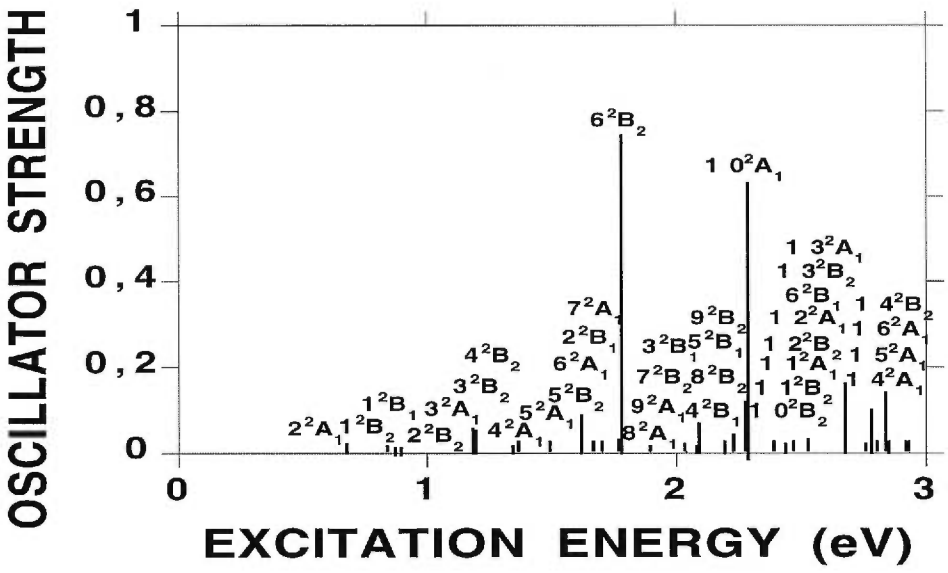

Figure 39. Excitation spectrum of the lithium pentamer calculated with the LSDxc/TDLSDxc functional and the Sadlej basis.

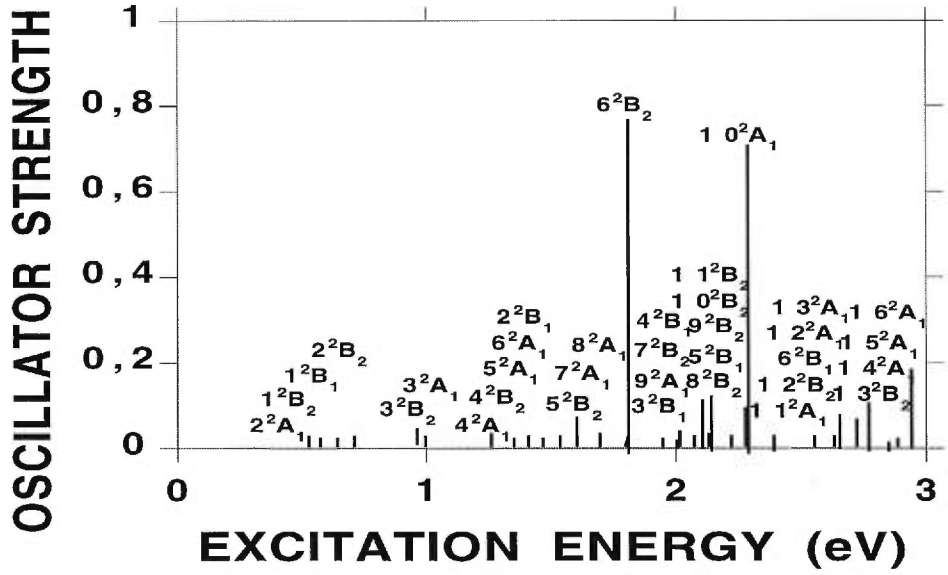

Figure 40. Excitation spectrum of the lithium pentamer calculated with the LB94xc/TDLSDxc functional and the Sadlej basis.

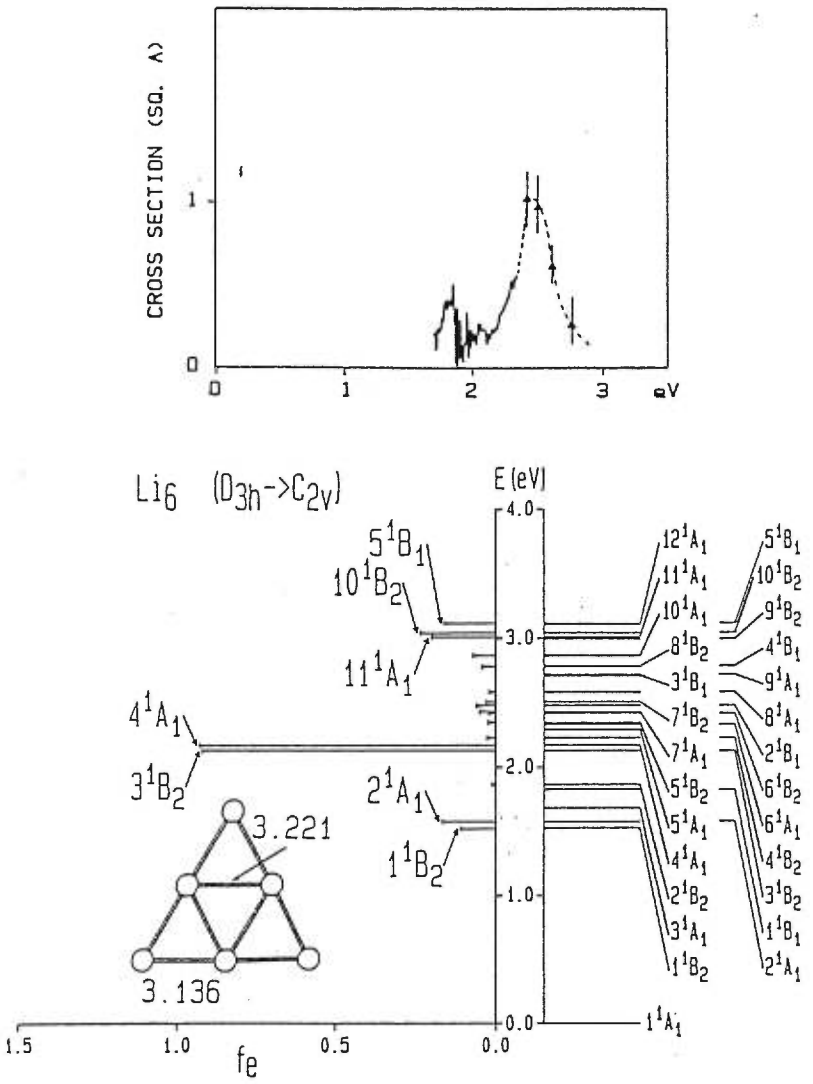

Figure 41. Comparison between the experimental spectrum (upper) and the CI calculated transitions (lower) for the planar D_{3h} geometry of the lithium hexamer. Taken from Ref [12].

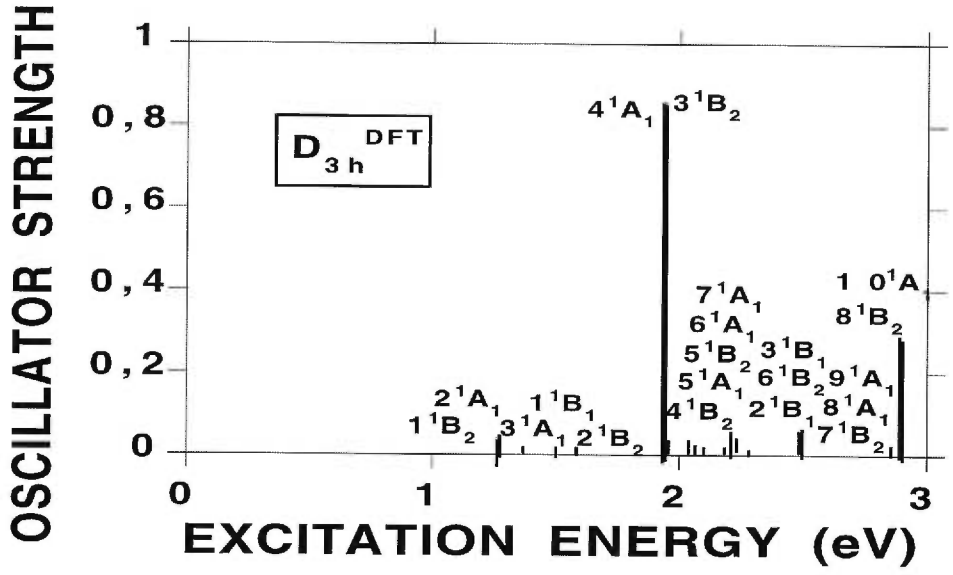

Figure 42. Excitation spectrum of the lithium hexamer ($D_{3h} \longrightarrow C_{2v}$) carried out with the LSDxc/TDLSDxc functional and the Sadlej basis.

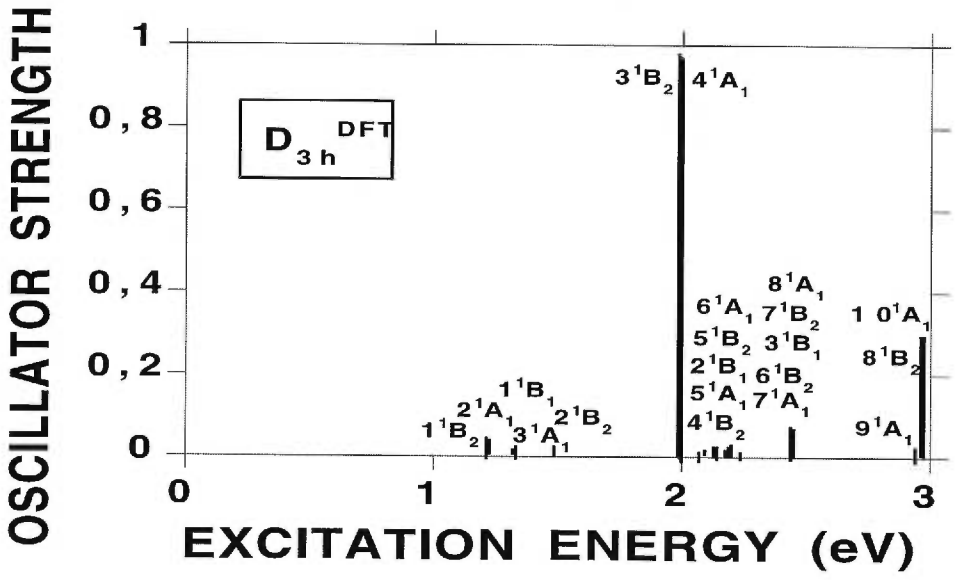

Figure 43. Excitation spectrum of the lithium hexamer ($D_{3h} \longrightarrow C_{2v}$) carried out with the LB94xc/TDLSDxc functional and the Sadlej basis.

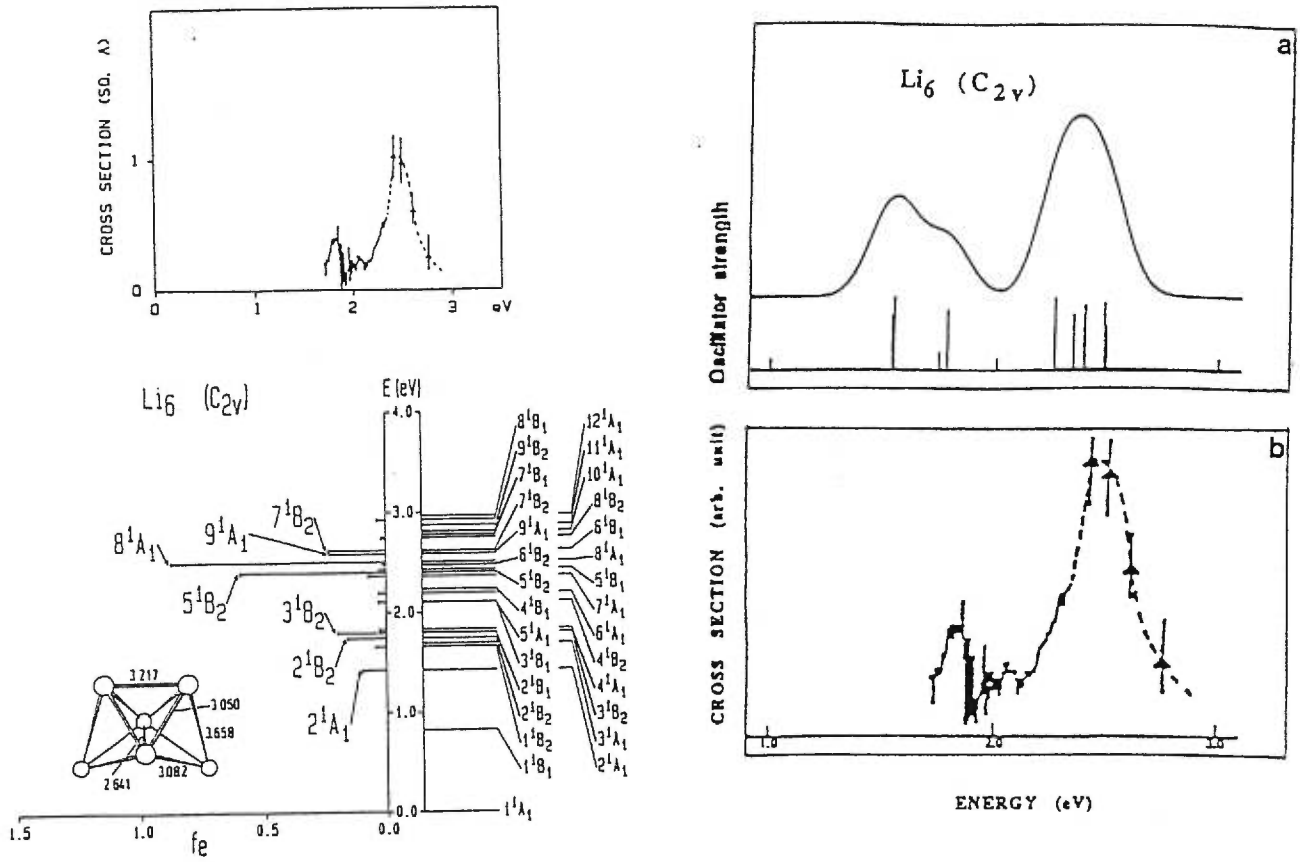

Figure 44. Left: Comparison between the experimental spectrum (upper) and the CI calculated transitions (lower) for the C_{2v} geometry of the lithium hexamer. Taken from Ref [12]. Right: Comparison between DFT computed spectrum of the lithium hexamer with the C_{2v} geometry by the "multiplets" approach (a) and the experimental spectrum (b). Taken from Ref [10].

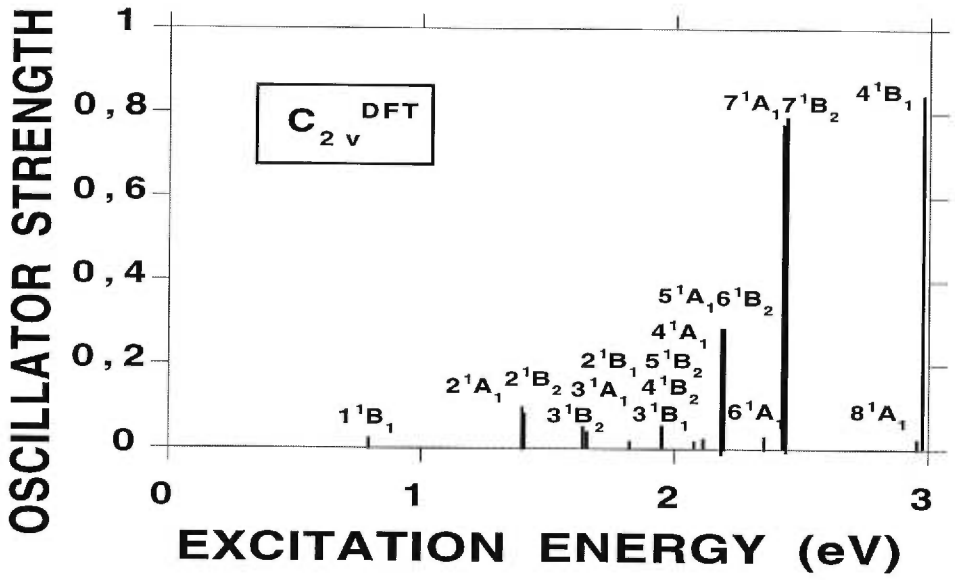

Figure 45. Excitation spectrum of the lithium hexamer, with the DFT C_{2v} geometry, carried out with the LSDxc/TDLSDxc functional and the Sadlej basis.

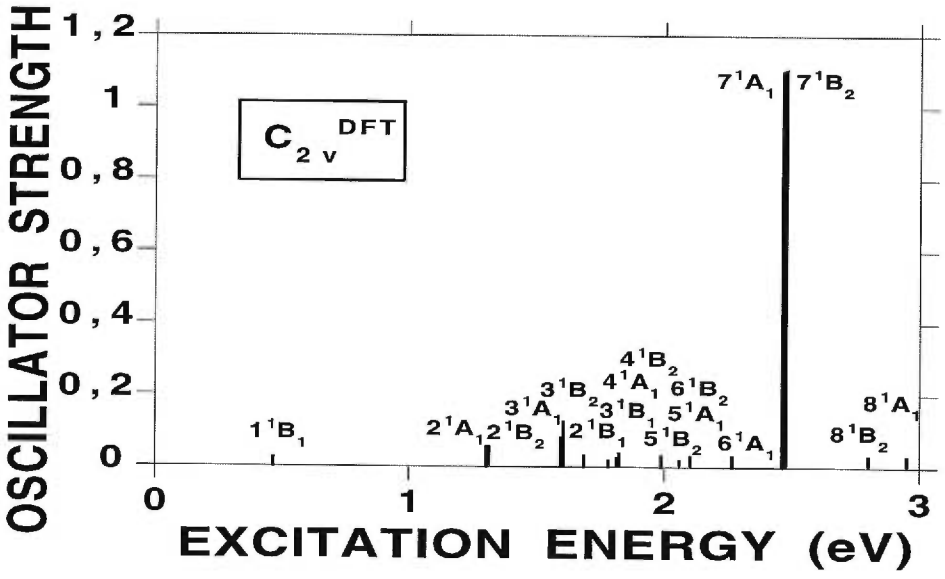

Figure 46. Excitation spectrum of the lithium hexamer, with the DFT C_{2v} geometry, carried out with the LB94xc/TDLSDxc functional and the Sadlej basis.

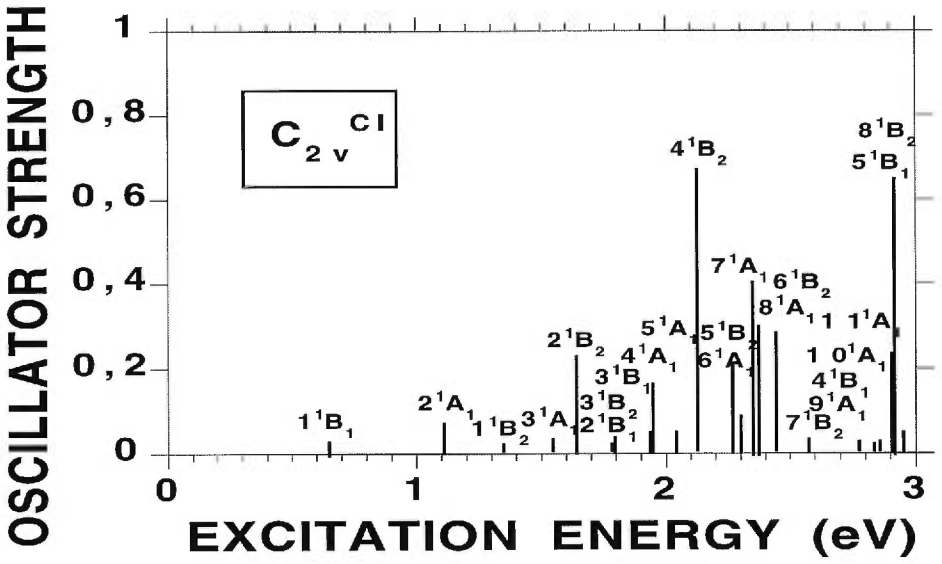

Figure 47. Excitation spectrum of the lithium hexamer, with the CI C_{2v} geometry, carried out with the LSDxc/TDLSDxc functional and the Sadlej basis.

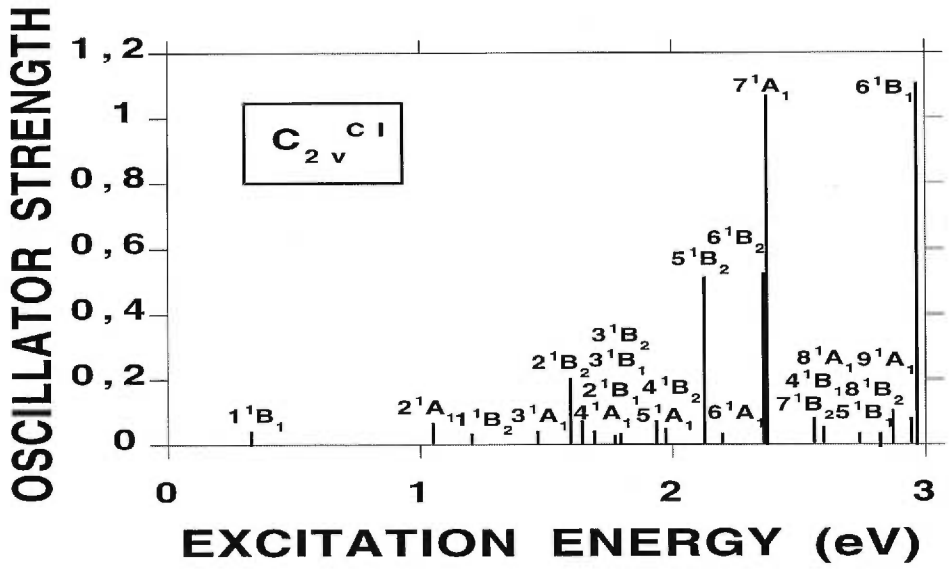

Figure 48. Excitation spectrum of the lithium hexamer, with the CI C_{2v} geometry, carried out with the LB94xc/TDLSDxc functional and the Sadlej basis.

CHAPTER 7

TIME–DEPENDENT DENSITY–FUNCTIONAL THEORY INTERPRETATION OF THE ABSORPTION SPECTRA OF SMALL SODIUM CLUSTERS WITH ALL-ELECTRON AND MODEL CORE POTENTIAL

7.1 INTRODUCTION

Theoretical study of excitation spectra of alkali metal clusters (sodium clusters are another example here, except the lithium clusters discussed in the previous chapter), which have been well measured for some time, plays an important role in understanding and interpreting characteristic features in the absorption spectra. It also provides useful information for determining equilibrium structure of the clusters by comparing with corresponding experimental spectra.

Geometric structure plays a crucial role in determining electronic properties of the cluster materials. Unfortunately, direct experimental information about cluster geometries is very limited and sodium clusters are no exception in this regard. Hence, most geometries have to be obtained by theoretical geometry optimizations. But sometimes different methods may provide different optimized equilibrium geometries. Sodium clusters are one of the examples. DFT and CI methods yield different geometric structures for the sodium hexamer, although the geometries of the dimer through to the pentamer are similar (with the same

symmetry). Bonačič-Koutecký and co-workers with the CI method [3, 15] predicted that the hexamer has a planar D_{3h} structure as the most stable geometry which is built from four triangles. The isomer, very close in energy (higher in energy by 0.04 eV), is a pentagonal pyramid C_{5v} structure in which there is one atom on top of the center of the pentagonal plane. The CI method yielded some negative frequencies for the pentagonal pyramid structure and the pentagonal pyramid geometry is not a local minimum on the Hartree–Fock energy surface [15]. In contrast, the DFT with pseudopotentials [344] or with molecular dynamics (Car-Parrinello method) [477] yielded the pentagonal pyramid C_{5v} structure as the most stable geometry. The planar D_{3h} isomer has higher energy by 0.04 eV (or 0.01 eV/atom in Ref. [477]). This pentagonal pyramid structure was also noticed as being more compact than the planar structure [477]. Recently, all-electron DFT calculations [327, 122] also predicted that the pentagonal pyramid C_{5v} structure is the most stable structure and that the planar D_{3h} isomer is about 0.05 eV higher in energy [327]. However, all-electron DFT [327] predicted that both geometries of the pentagonal pyramid C_{5v} structure and the planar D_{3h} structure are minima on the DFT energy surface, both geometries yielded all positive vibrational frequencies. This is different from the CI prediction. Moreover, the DFT with pseudopotentials [341] predicted that the sodium trimer has two equilibrium geometries, namely the obtuse and the acute structures, the obtuse geometry with 0.02 eV in energy lower than that of the acute structure. But the recent all-electron DFT calculations [327, 122] yielded only the obtuse minimum structure and found the acute geometry to be a saddle point with one negative vibrational frequency. This obtuse structure predicted by the all-electron DFT [327, 122] is the same as that predicted by the CI method [368, 3] and the CI method [368] also predicted that the acute structure is a saddle point. However, it is interesting to see the difference in the absorption spectra of these geometries and which structure is supported to be an equilibrium geometry by the absorption spectra.

The *ab initio* CI method has successfully provided numerous predictions and interpretations of photoabsorption spectra of alkali metal clusters. Excitation energies and oscillator strengths of sodium dimer [478, 13], trimer [368, 479, 14, 480], tetramer [14, 481, 77, 482, 480], pentamer [15, 480], hexamer [15, 480], heptamer [15, 480], and octamer [77, 14, 482, 480] were calculated by CI methods and reported in the literature. The calculated spectroscopic pattern of the tetramer with rhombic structure is in good agreement with the recorded spectra [67, 23, 483]. The CI predicted spectrum of the pentamer supports the planar trapezoidal structure, since the planar trapezoidal structure yielded the locations of the strong bands coincide with the intense broad feature of the recorded spectrum. At the same time, the pentamer trigonal bipyramid geometry was excluded due to the disagreement between the calculated absorption spectrum and the experiment. In the hexamer case, a comparison of the two absorption spectra of the planar D_{3h} structure and of the three-dimensional pentagonal pyramid C_{5v} geometry with the experiment shows that the two absorption spectra with the planar D_{3h} structure and with the pentagonal pyramid C_{5v} geometry are very similar, and both agreed with the experiment. However, the degeneracy of the two strong bands in the spectrum with the pentagonal pyramid structure is not as good as that in the spectrum with the planar D_{3h} structure. Nevertheless, it is difficult to rule out the contributions of the pentagonal pyramid C_{5v} geometry to the recorded spectrum. This near degeneracy in energy of the planar D_{3h} and the C_{5v} geometries may also be the reason why the DFT and the CI predicted different equilibrium geometries for the hexamer. In this regard, it is very desirable to see what spectrum the DFT predicts for the hexamer with the two competitive geometries.

DFT is well established for the study of ground state properties of molecules or clusters due to the good quality of the results for structural and energetic properties and its advantages (correlation effects, simplicity, and computational efficiency). Study of excited state properties provides a challenge for the tradi-

tional DFT. However, several recent works [138, 29, 30, 31, 388, 33, 22, 32, 35] and the present work (see chapter 3, chapter 5, and chapter 6 of this thesis) provide a new tool – time-dependent DFT for the study of excited state properties, such as excitation energies and oscillator strengths. Nevertheless, there are very few time-dependent DFT studies of absorption spectra of sodium clusters. Ekardt [75] employed the time-dependent local density approximation (TDLDAxc) with the spherical jellium model to discuss size–dependent photoabsorption of small closed–shell sodium particles. Madjet, Guet, and Johnson [484] used the TDLDAxc jellium model to calculate absorption spectra of Na_8, Na_{18}, Na_{20}, Na_{34}, Na_{40} and some even larger closed–shell clusters. Pacheco and Martins [450] used TDLDAxc and pseudopotentials to predict photoabsorption spectra of Na_8 and Na_{20}. Vasiliev, Öğüt, and Chelikowsky [485] recently applied TDLDAxc to the photoabsorption spectra of the sodium dimer and tetramer also with a pseudopotential. However, time-dependent DFT all-electron excitation spectral calculations of the sodium clusters taking into account the molecular nature of the clusters have not been found in the literature, especially for open–shell sodium clusters. The present work provides the first all-electron time-dependent DFT calculations of photoabsorption spectra of the sodium clusters for both cases of closed-shell (the dimer, the tetramer and the hexamer) and open-shell (the trimer and the pentamer) clusters.

In addition to the all-electron calculations, the present work also provides a model core potential (MCP) study of excitation spectra of the sodium clusters from the dimer up to the hexamer. In the MCP, core electron interactions are replaced by a core potential and only valence electrons are treated explicitly. Hence the MCP provides an efficient computational tool for the study of larger clusters. The quality of the MCP in the applications to ground state properties of the sodium clusters, such as geometric structures, vibrational frequencies, binding energies, ionization potentials, and static polarizabilities, was assessed against the all-electron DFT calculations with the local density approximation (LDAxc), and

two gradient-corrected functionals (GCFs), B88x + P86c and PW86x +P86c (see Chapter 4 of this thesis). Here, the present calculations assess the quality of the MCP in the applications to excited state properties, such as excitation energies, oscillator strengths, by comparison of absorption spectra of the sodium clusters calculated by all-electron and by the MCP using the local spin density (LSDxc) approximation and the van Leeuwen and Baerends' [212] exchange-correlation functional.

7.2 COMPUTATIONAL DETAILS

Absorption spectra of small sodium clusters from the dimer through the hexamer (ground state symmetry and configuration of sodium clusters shown in Table XLVI and XLVII (please note that Tables and Figs. are given at the end of the chapter) for all-electron and MCP calculations) were predicted by the time-dependent DFT program, *deMon–DynaRho* version 2pX [208]. Version 2pX permits one to calculate excited state properties for open–shell systems; this differs from the previous version 1 in Ref. [29] or version 2 in Ref. [387] which only treat closed–shell systems.

The program, *deMon–DynaRho*, divides calculations into an SCF step and a post–SCF step. This permits one to use different exchange–correlation functionals in the calculations at the SCF step and at the time-dependent DFT step. The present calculations employed the local spin density approximation (LSDxc) and the van Leeuwen and Baerends [212] exchange-correlation functional proposed in 1994 (LB94xc),respectively, in the SCF calculations and used the time–dependent local spin density approximation (TDLSDxc) in the time-dependent DFT calculations. These functionals used in the SCF step and the functional utilized in the post–SCF step are referred to as LSDxc/TDLSDxc and LB94xc/TDLSDxc functionals, respectively. The grid used in the present calculations is the EXTRA–FINE grid and NonRandom option which is referred to as (XF,NR), However,

the FINE and the EXTRA–FINE grids associated with the Random option [the FINE and the Random grid option is labelled as (F,R) and the EXTRA-FINE and the Random grid option is referred to as (XF,R)] were also tested in the excitation energy calculations of the sodium trimer. These grids resulted in symmetry breaking in the symmetry assignments for the transitions. Nevertheless, these transitions calculated with the the FINE and the EXTRA–FINE grids combined with the Random option were assigned based on the largest transition coefficient which is on the order of one magnitude larger than the other transition coefficients. The convergence criteria in the SCF calculations are 10^{-8} hartree in the total energy and 10^{-7} a.u. in the charge density fitting coefficients. However, the MCP calculations with the LB94xc functional and with the bases MCP, MCP1, and MCP2 for the dimer and the trimer are difficult to converge in the SCF step. The total energy could be only converged to 10^{-3} hartree, whereas the charge density fitting coefficients could be converged to 10^{-2} a.u.. However, the dimer calculation could finally be converged with the larger basis MCP+, but this larger basis MCP+ was no help for the convergence in the trimer calculation.

Gaussian–type orbital basis sets are used in both the all-electron and the MCP calculations. Several orbital basis sets were examined in the all-electron calculations. The STO-3G basis (a Slater–type orbital replaced by three primitive Gaussian functions), (333/33) and the DZVP basis (double zeta valence plus polarization), (6321/411*/1+), seem to be too small in excitation energy calculations. A medium–sized basis, (6311111/61111/22), developed by Sadlej and Urban [334], (referred to as BASIS1) seems to be flexible enough to describe excitations, at least for the low excitation energies. However, some larger basis sets were also tested, for example, based on the BASIS1, all s functions, or all p functions, or all d functions, are decontracted, respectively, to make larger bases, namely, BASIS2, (11111111111111/61111/22), BASIS3, (6311111/1111111111/22), and BASIS4, (6311111/61111/1111). The largest basis set used in the sodium trimer excitation energy calculations is a full decontraction of the BASIS1 which is referred

to as BASIS5, (11111111111111/1111111111/1111). These decontracted larger basis sets yield no significant improvement in the excitation energies compared to the results calculated by the BASIS1. Hence, the medium–sized BASIS1 is chosen in the present calculations. The auxiliary basis, (5,4;5,4), in the all-electron calculations, was taken from the *deMon-KS* basis set library. The MCP orbital bases used in the present calculations are the simplest basis, (311/2), referred to as MCP. The p function in the (311/2) basis replaced by the two outermost p functions in the all-electron DZVP basis produces basis MCP1, (311/11). This MCP1 basis seems to be reasonable for the description of ground state properties (see Chapter 4 of this thesis for details), but it seems not to be flexible enough to describe excited state properties, here. In the previous work (see Chapter 6 of this thesis), it found that diffuse functions and polarization functions are very important in the calculation of excitation energies, therefore, the basis MCP1 was supplemented with the field-induced polarization function which was used in the all-electron polarizability calculations (see Chapter 4 of this thesis and Ref. [122]). This augmented basis, MCP2, did improve excitation energies remarkably and it seems to yield reasonable results in comparison with the all-electron calculations and experiments for the trimer. But it did not show convergence compared with the results carried out by the MCP and the MCP1 bases. On the other hand, this basis, MCP2, yields somehow large errors in the excitation energy calculations of the tetramer. Hence, an additional polarization function (d function), with the component of $\alpha = 0.09$, taken from Ref. [368], was added to the basis MCP2. This supplemented basis, referred to as MCP+, did yield better excitation energies for both the trimer and the tetramer, and the convergence of the basis sets used in the excitation energy calculations was observed. Hence, the basis MCP+ is the choice for the present calculations. The auxiliary basis set used in the MCP calculations is (5,1;5,1), and the model core potential is (5:6,4), which were given in Chapter 4 of this thesis.

All the geometries used in the present all-electron calculations were opti-

mized with *deMon–KS* at the all-electron level in the previous work [327, 122]. Except for the trimer calculations, the geometries optimized at both all-electron level and at the MCP level were used in order to examine the geometrical distortion effects on the excitation energies. The geometries used in the MCP calculations were the MCP geometries optimized at the MCP level with the MCP1 basis (see Chapter 4 of this thesis for details), except in the MCP calculations for the hexamer, the all-electron D_{3h} geometry was used in the MCP calculations, in order to test the performance of the MCP at fixed geometry. These MCP excitation energy calculations with the MCP optimized geometries are simply referred to as MCP and the MCP calculations with the all-electron optimized geometries are labelled as MCPAE. These all-electron calculations with the all-electron optimized geometries are referred to as AEAE and the all-electron calculations with the MCP optimized geometries are labelled as AEMCP. The orientation of the geometries in the present calculations follows the rules in Ref. [473]. Specifically, the dimer lies on the z-axis. The trimer, the pentamer, and the hexamer with the D_{3h} symmetry lie in the yz–plane, since the hexamer, with D_{3h} symmetry, was assigned under the C_{2v} subgroup. The tetramer and the hexamer with C_{5v} symmetry lie in the xy–plane. The hexamer, with C_{5v} symmetry, was assigned under the C_S subgroup in order to compare with the CI calculations.

7.3 RESULTS AND DISCUSSION

Absorption spectra of small sodium clusters (from the dimer up to the hexamer) are predicted by the time-dependent DFT with the LSDxc/TDLSDxc functional and the LB94xc/TDLSDxc functional at the all-electron level and are shown in Figs. 49, 50, 56, 57, 64, 65, 71, 72, 78, and 85 (please note that Figs. and Tables are given at the end of the chapter). In order to assess the quality of the model core potential (MCP) calculations in the absorption spectra of the sodium clusters and applying it to predict the excitation spec-

tra of larger clusters in the future, the present work calculates the absorption spectra of small sodium clusters using the MCP with the small basis (MCP basis) and with the larger basis sets (MCP+). The MCP predicted absorption spectra with the small basis are given in Figs. 51, 60, 66, 67, 73, 74, 81, and 82. The MCP calculations with the larger basis (MCP+) yields the excitation spectra shown in Figs. 52, 53, 61, 68, 69, 75, 76, 83, 84, 79, and 80. The absorption spectra are useful for determining the equilibrium geometry. The sensitivity of the absorption spectra to geometrical distortion is studied in the present work. The effect of small geometric distortions is tested using the all-electron optimized geometry and the MCP optimized geometry to calculate the absorption spectra at the all-electron level for the trimer. The absorption spectra calculated at the all-electron level with the MCP optimized geometry are given in Figs. 58 and 59, and with the all-electron optimized geometry are shown in Figs. 56 and 57. The large geometrical distortion effects on the absorption spectra are studied by calculating the absorption spectra of the obtuse and the acute structures for the trimer, as well as the planar D_{3h} geometry and the pentagonal pyramid C_{5v} structure for the hexamer. This is also useful for determining equilibrium geometries which are uncertain or contradictary with those from theoretical geometry optimizations, such as the obtuse and the acute structures for the trimer, the planar D_{3h} geometry and the pentagonal pyramid C_{5v} structure for the hexamer. The absorption spectra with the obtuse and the acute structures are predicted using the LSDxc/TDLSDxc functional at the all-electron level and are shown in Figs. 56, 62. The absorption spectra of the hexamer with the planar and the pentagonal pyramid structures are performed using both the LSDxc/TDLSDxc functional and the LB94xc/TDLSDxc functional at the MCP level with the larger MCP basis (MCP+) and are given in Figs. 83, 83, 79, and 80. The present predicted absorption spectra are compared with available experimental results from Refs. [23, 67, 483, 16, 71] and traditional *ab initio* CI calculations [14, 481, 482, 15, 480, 13]. Hence, the equilibrium geometry of the

trimer and the hexamer are discussed in the present work.

To ensure the quality of the present calculations, several basis sets were examined for the trimer at the all-electron level and the MCP level. (these MCP bases were also tested for the tetramer). These examinations show that diffuse basis functions and polarization functions are indispensable in calculations of excitation energies. Table LII shows that the STO-3G basis is really too small for calculating excitation energies, it leads to errors of about 5 eV or more in comparison with the excitation energies calculated by the fully decontracted basis from the medium–size BASIS1 – BASIS5. The DZVP basis improves the excitation energies remarkably and it yields errors in excitation energies less than 1 eV compared with those carried out by the BASIS5, except for the 6^2A_1 state which has an error of 1.1 eV and the 4^2A_2 state which has an error of 1.3 eV. This is certainly due to the diffuse functions (the outermost s and p functions) and polarization functions (d function) in the DZVP basis. The large errors indicate that more diffuse and polarization functions are needed in the orbital basis. The larger basis should reduce the errors in the excitation energies. The BASIS1, which has three s functions, two p functions, and one d function more compared to the DZVP basis, yields satisfactory excitation energies. The deviations of the excitation energies between the BASIS1 and the BASIS5 bases are no larger than 0.01 eV. The partially decontracted basis sets (the BASIS2, the BASIS3, and the BASIS4) from the BASIS1 do not yield any significant improvements in comparison with the results calculated by the BASIS1. Hence the medium – size BASIS1 is the choice in the calculations of absorption spectra of the sodium clusters in the present work.

Diffuse basis functions and polarization functions play the same roles in the MCP excitation energy calculations as in the all-electron cases. The basis MCP and the MCP1 differ by the p functions, the MCP has one p function which is contracted from two primitive Gaussian functions, the MCP1 has two

p functions replacing the one p function in the MCP basis. The two p functions in the MCP1 are taken from the outermost two p functions in the all-electron DZVP basis, but they are not as diffuse as that in the MCP basis. Hence, the MCP1 yields larger errors in excitation energies. This is in contrast to the ground state property calculations, where the basis MCP1 seems to be better, especially in the geometric structure predictions, than those of the MCP basis (see Chapter 4 of this thesis for details). Table LIII and LIV show that the MCP basis yields the largest deviations in excitation energies of 0.5 eV for the 6^2B_2 state in the trimer, and 1.7 eV for the 5^1B_{3u} state in the tetramer compared with the largest basis MCP+ calculations. But the MCP1 yields even larger errors than those of the MCP basis, the 3^2A_2 state in the trimer has an error of 0.8 eV, while the 4^1B_{3u} state in the tetramer has a deviation of 2 eV and 1.9 eV for the 5^1B_{3u} state. However, using one additional diffuse function to supplement the MCP1 basis, namely the MCP2 basis, helps to eliminate the deviations, it reduces the error to 0.01 eV for the 3^2A_2 state in the trimer and to 0.2 eV and 0.5 eV for the 4^1B_{3u} and the 5^1B_{3u} states in the tetramer, respectively. Nevertheless, the final basis set used in the present MCP calculations is the larger basis, MCP+, which has one more polarization function (d function) than in the MCP2 basis.

The grid effects on excitation energies are small between FINE and EXTRA-FINE grids or between Random and NonRandom grids. Table L shows that in the exchange only case, the biggest difference between the excitation energies of the trimer calculated by the FINE and the EXTRA-FINE grids is 0.003 eV for the 1^2A_2 state, while the deviation between the Random and the NonRandom grids seems to be larger than that between the EXTRA-FINE and the FINE grids, the largest deviation is 0.02 eV for the 2^2B_2 state. In the exchange–correlation case, the deviations are larger than that for the exchange only case. The biggest difference between the FINE and the EXTRA-FINE grids is 0.006 eV for the 2^2A_1 state, the largest deviation between the Random and the NonRandom option is 0.068 eV for the lowest excited state (1^2A_1). However, the FINE and the EXTRA-

FINE with the Random grid option have symmetry breaking in the assignments of the excitations in the trimer calculations.

Excitation energies are not sensitive to small geometric distortions. However, large geometric differences may not only lead to big deviations in excitation energies, but also change the ground state symmetry. For example, in the trimer case, the MCP and the all-electron optimized geometries (obtuse geometry) have small differences in the bond lengths and bond angles. The difference in bond length of the short side of the triangle between the MCP and the all-electron optimized geometries is 0.23 bohr, and in bond angle between the two short sides of the triangle is 1.2 degrees (see Chapter 4 of this thesis for details). The all-electron optimized obtuse and acute geometries [327] differ quite significantly in the bond length of the isosceles sides of the triangle (0.5 bohr) and in the bond angle between the two isosceles sides of the triangle (23 degrees). Table LI shows that the all-electron calculated excitation energies with the all-electron optimized geometry and with the MCP optimized geometry differ by 0.06 eV or less for the given fifteen excited states of sodium trimer. However, excitation energies carried out with obtuse and acute geometries show large deviations (0.8 eV for the 2^2A_2 state), and the ground state symmetry of the two geometries is also different. The obtuse geometry has $^2B_2$ symmetry and the acute geometry has $^2A_1$ symmetry.

Electron Coulomb, exchange, and correlation interactions have different contributions to excitation energies. Table XLIX shows that electronic Coulomb interactions provide the largest contribution to the excitation energies and its role is to push electronic states towards each other dramatically, hence it reduces the excitation energies remarkably from the Core level calculations. The Coulomb interactions can change excitation energies as much as 27 eV (e.g. 26.6 eV for the 4^2A_2 state and 27.3 eV for the 5^2A_2 states) in the given twenty states of the sodium trimer. Fortunately all theoretical methods treat the Coulomb interactions in the same way. Therefore different methods yield excitation energies

only due to the treatments of electron exchange and correlation interactions. The contributions of the electron exchange is much smaller than that of the Coulomb interactions, but it is larger than the contributions of the electron correlation. Both contributions of the electron exchange and correlation are to separate the electronic states, hence the electron exchange and correlation interactions increase the excitation energies from the Coulomb calculations. The electron exchange effects on excitation energies can be as large as 1.8 eV (e.g. 1.8 eV for the 2^2B_1 state and 1.6 eV for the 3^2B_1 state). The electron correlation contributions may change excitation energies by 0.6 eV (e.g. 0.6 eV for the 1^2A_2 state and 0.5 eV for the 5^2A_2 state). This indicates that different theoretical methods which treat electron exchange and correlation differently may yield excitation energies differing by a maximum of 2.4 eV at least in the sodium trimer case and for low excitation energies.

The electron-interaction effects on the excitation energies at the MCP level are different from that at the all-electron level. The contributions of the Coulomb interactions are much smaller than those of the all-electron case. This indicates that the Coulomb interactions of core electrons are important and have large contributions. The electron exchange and correlation contributions to the excitation energies are slightly smaller than those in the all-electron case. This indicates that the exchange and the correlation of valence electrons are the most important contributions to excitation energies. Moreover, the directions of the excitation energy changes are also different between the MCP and the all-electron calculations. In the MCP case, the electron exchange and correlation contributions effects on excitation energies seem to be random (with positive or negative changes). But the Coulomb interactions still reduce excitation energies. This different behavior of the MCP results from the all-electron case is assumed to be due to the model core potential, since the interactions of the core electrons were already built into the core potential. Even though the calculations are carried out with the MCP at the Core/IPA level, core-electron Coulomb interactions, electron exchange and

correlation interactions are already included in the calculations.

Excitation energies of the small sodium clusters calculated with the LSDxc/TDLSDxc functional are in fairly good agreement with experimental results. The LSDxc/TDLSDxc functional slightly overestimates the excitation energies of the small sodium clusters. The differences between the calculated excitation energies and the available experimental ones are less than 0.2 eV, except for the $1^1\Sigma_u^+$ state having an error of 0.28 eV in the dimer; for the 3^2A_2 state with a difference of 0.29 eV in the trimer; and for the 3^1B_{3u} state having a deviation of 0.21 eV in the tetramer. These deviations between the calculated excitation energies and the measurements can be understood, since the experiments yield adiabatic excitation energies which include excited state relaxations, but not the present vertical excitations. On the other hand, *ab initio* CI calculations [368] with the GTO basis, (521111/4111/1), yielded the largest errors in the excitation energies being 0.3 eV for the trimer. In particular, 0.31 eV for the 2^2A_2 state and 0.2 eV for both the 4^2B_2 and the 3^2A_1 states. However, CI calculations [14] with the larger basis, (5211111/4211/1), reduced the errors to no larger than 0.1 eV in the trimer excitations. This seems to suggest that the diffuse s basis functions are important in the excitation energy calculations. The high quality *ab initio* CI calculations also agree well with the present time-dependent DFT calculations of the excitation energies. In the dimer case, the deviations between the present LSDxc/TDLSDxc calculations and the full CI excitation energies [13] are no larger than 0.2 eV. This difference is smaller than that between the CI calculations [13] and the MBPT (many body perturbation theory) results [486] which has a largest deviation of 0.5 eV (e.g. 0.51 eV for the $1^1\Pi_g$ state). However, the largest deviation between the present calculations and the MRD-CI [14] occurred in the tetramer, where a 0.7 eV (for the 3^1B_{2u} state) difference is observed. But the RPA (random phase approximation) [11] yields even larger deviations (1.1 eV for the 3^1B_{2u} state) in comparison with the MRD-CI [14] results. However, it is not obvious in the present calculations that the excitation energies of small sodium clusters collapse

when the excitation energies are larger than the ionization threshold, $-\varepsilon_{HOMO}^{LSDxc}$, in comparison with available experiments or CI calculations, which was observed clearly in Ref. [387] and in free radical calculations (see Chapter 5 of this thesis).

Excitation energies of the sodium clusters carried out with the LB94xc/TDLSDxc functional are higher than those calculated with the LSDxc/TDLSDxc functional for the closed–shell small sodium clusters (the dimer, the tetramer, and the hexamer). For the open–shell small sodium clusters (the trimer and the pentamer), the first few excitation energies calculated with the LB94xc/TDLSDxc functional are lower than those from the LSDxc/TDLSDxc calculations. When the excitation energies are above $-\varepsilon_{HOMO}^{LSDxc}$, the LB94xc/TDLSDxc excitation energies become even larger compared to the excitation energies calculated with the LSDxc/TDLSDxc functional for both the closed–shell and the open–shell sodium clusters studied here. This is different from the situation for the small lithium clusters (see Chapter 6 of this thesis) and for the free radicals (see Chapter 5 of this thesis) for which the LB94xc/TDLSDxc functional gave lower excitation energies than those of the LSDxc/TDLSDxc functional. When the excitation energies are larger than (or close to) the ionization threshold of the LSDxc, $-\varepsilon_{HOMO}^{LSDxc}$, the ordering starts to change, the LB94xc/TDLSDxc excitation energies begin to be higher than the LSDxc/TDLSDxc excitation energies. This different observation, between the LSDxc/TDLSDxc and the LB94xc/TDLSDxc functional calculations for the small sodium clusters, for the small lithium clusters, and for the free radicals, may be due to the extremely flat potential energy surface of the small sodium clusters [368, 327, 122].

The LSDxc/TDLSDxc MCP excitation energies, no matter with the MCP optimized geometries (calculations for the dimer up to the pentamer and the hexamer with the the pentagonal pyramid C_{5v} structure) or with the all-electron optimized geometries (calculations for the hexamer with the planar D_{3h} geometry), are slightly larger than those calculated with the all-electron approach. The

differences in excitation energies between the MCP and the all-electron calculations are less than 0.1 eV from the dimer up to the hexamer [except for the 5^1A_1 (0.20 eV), the 7^1A_1 (0.25 eV), and the 8^1A_1 (0.21 eV) states for the hexamer with planar geometry]. However, when the excitation energies are larger than the ionization threshold of the LSDxc, $-\varepsilon_{HOMO}^{LSDxc}$, (the MCP and the all-electron calculations produce very similar ionization potentials and both are too low compared with the experiment, see Table LVIII), the all-electron excitation energies fall off much faster than do the MCP excitation energies. Hence, the differences between the MCP excitation energies and the all-electron results are suddenly increased. This increase can be as large as 3 eV (e.g. 3.4 eV for the $4^1\Sigma_u^+$ state and 3.1 eV for the $4^3\Sigma_u^+$ state in the dimer case). This different degree of excitation energy falling off between the MCP and all-electron results may be due to the small basis set used in the MCP calculations. In principle, above the ionization threshold, $-\varepsilon_{HOMO}^{LSDxc}$, the continuum is reached, with an infinitely large basis set, the excitation energies should fall off to the ionization threshold, since a finite basis set is used in the practice, and a small basis is certainly not flexible enough to describe the continuum, the degree of excitation energies falling off depend on the quality of the basis set used. In the all-electron calculations, the basis set used is much richer than that used in the MCP calulations, hence, the all-electron excitation energies fall off faster than those of the MCP calculations. On the other hand, higher excitations should be more sensitive to diffuse basis functions than the low excitations. Table LIII shows that diffuse basis functions in the MCP calculations did make higher excitation energies fall off remarkably (see the differences between the results calculated with the basis MCP1 and with the basis MCP2). However, this falling off for the higher excitations is not obvious with additional polarization function in the MCP2 basis (namely, the basis MCP+). This may be due to the polarization function in the MCP+ basis being not as diffuse as the outermost diffuse p function in the basis MCP2.

It is expected, because the MCP was made by fitting the all-electron LSDxc

functional calculations, that the deviations between the excitation energies calculated by the MCP and by the all-electron approach with the LSDxc/TDLSDxc functional are smaller than those between the MCP and the all-electron results with the LB94/TDLSDxc functional for the low excitations. The deviations of the excitation energies between the MCP and the all-electron calculations with the LB94xc/TDLSDxc functional are as large as 0.5 eV (e.g. 0.56 eV for the $1^3\Pi_g$ state in the dimer, 0.36 eV for the 3^1B_{3u} state in the tetramer, and 0.34 eV for the 11^2B_2 state in the pentamer). As it occurred in the LSDxc/TDLSDxc functional calculations, when the excitation energies are larger than the ionization threshold of the LB94xc functional, $-\varepsilon_{HOMO}^{LB94xc}$, the MCP excitation energies have a sudden rise and lead to a large difference between the MCP and the all-electron calculations. The largest deviation observed is 2.1 eV for both the $4^1\Sigma_g^+$ state and the $4^1\Sigma_u^+$ state in the dimer. Since the LB94xc functional produces too high ionization potentials for the sodium clusters and, in contrast, the LSDxc functional yields too low ionization thresholds (see Table LVIII), the absolute average error between the LSDxc/TDLSDxc MCP and the all-electron excitation energies (1.32 eV for the dimer, 0.42 eV for the tetramer, and 0.07 eV for the pentamer) may be larger than those between the LB94xc/TDLSDxc MCP and the all-electron calculations (1.08 eV for the dimer, 0.12 eV for the tetramer, and 0.09 eV for the pentamer) depending on how many high excitations are included.

It is worth mentioning that, as it should be, there are some pairs of degenerate states in the hexamer calculations (in both cases, $C_{5v} \longrightarrow C_S$ and $D_{3h} \longrightarrow C_{2v}$) which do appear in the LSDxc/TDLSDxc all-electron and the MCP (with the MCP+ basis) excitations. But the degeneracy is slightly broken in the LB94xc/TDLSDxc MCP calculations with both the MCP basis and the MCP+ basis, as well as in the LSDxc/TDLSDxc MCP calculations with the MCP basis. *Ab initio* CI [15] calculations also broke the degeneracy remarkably. Bonačič-Koutecký and co-workers [15] believe that the degeneracy breaking in the CI calculations is partly due to slight geometrical deviation from the C_{5v} group

and partly to the larger truncation of the CI expansions in the C_S point group. However, this shows the quality of the calculations.

It is noticed that the MCP calculations with the LB94xc/TDLSDxc functional have some convergence problems in the SCF step for small sodium clusters. The dimer and the trimer MCP calculations with the LB94xc/TDLSDxc functional and with both the MCP basis and the MCP+ basis (except for the dimer calculation with the MCP+ basis) could not be converged to the criteria for both the total energy (10^{-8}) and the change in density fitting coefficients (10^{-7}). it was only converged to 10^{-3} for the total energy and to 10^{-2} for the density fitting coefficients.

ECP (effective core potential) CI calculations [479, 11] of excitation energies yield quite large differences from all-electron CI calculations [368, 14]. The biggest deviation between the ECP CI excitation energies and the all-electron CI results is about 0.7 eV for the 5^2A_1 and the 6^2A_1 states in the trimer. This deviation is larger than that between the present MCP calculations and the all-electron calculated excitation energies in the trimer case which has the biggest difference being 0.5 eV for the 6^2A_1 and the 4^2A_2 states. However, deviation between the ECP CI and the all-electron CI calculations for the tetramer (0.2 eV for the 3^1B_{2u} state) is smaller than that between the present MCP calculations and the all-electron time-dependent DFT results which yields the largest deviation of 1.1 eV for the 3^1B_{1u} state for the tetramer.

The absorption spectra of the small sodium clusters predicted by the present LSDxc/TDLSDxc calculations agreed very nicely with the experimental results. The predicted energy interval of the intense bands is similar to the measured results. The numbers of predicted strong bands are the same as those recorded. The predicted positions of the bands are close to those of the measurements.

The absorption spectrum of the dimer has a simple spectroscopic pattern,

only two strong bands are predicted by the present calculations with the LS-Dxc/TDLSDxc functional, located at 2.1 eV and 2.7 eV and assigned to the $1^1\Sigma_u^+$ and the $1^1\Pi_u$ states, respectively (see Fig 49). The oscillator strength of the $1^1\Sigma_u^+$ state (0.6172) is larger than that of the $1^1\Pi_u$ state (0.5309). This is similar to that predicted by the *ab initio* CI method [13]. The oscillator strengths of the $1^1\Sigma_u^+$ and the $1^1\Pi_u$ states carried out by the CI method are 0.8813 and 0.6621, respectively. The difference in the positions of the two bands between the present calculations and the CI results is 0.18 eV and 0.09 eV for the $1^1\Sigma_u^+$ and the $1^1\Pi_u$ states, respectively (see Fig. 54 and 49).

The trimer absorption spectrum is calculated with the two previous LS-Dxc all-electron optimized geometries, namely, the obtuse and the acute structures. These predicted spectra are helpful in confirming previous optimized geometries [327, 341] by comparing with recorded results. The spectroscopic pattern predicted with the LSDxc/TDLSDxc functional and with the obtuse geometry is in fairly good agreement with the experiment. Fig. 56 shows that the predicted intense bands are in the energy interval of 1.8 eV – 3.1 eV which is similar to the recorded spectrum with the strong bands in the energy range of 1.67 eV – 3.00 eV. There are six strong peaks observed by the present work and the positions of the six peaks differ from corresponding measured bands [23] by no more than 0.2 eV. The present predicted bands of the A group located at 1.83 eV and 1.95 eV and assigned to 3^2A_1 and 1^2A_2 states agree well with the recorded bands located at 1.67 eV and 1.84 eV and labelled as A$'$ and A, respectively. The predicted three intense peaks around 2.19 eV, 2.41 eV, and 2.52 eV and assigned to 4^2A_1, 4^2B_2, and 6^2B_2 states are responsible for the measured B group bands which are located at 2.03 eV, 2.22 eV, and 2.40 eV and labelled as B, B$'$, and B$''$, respectively. The rest of the predicted strong peaks located at 2.88 eV and 3.09 eV and assigned to 3^2A_2 and 4^2A_2 correspond to the measured C band and D band which is around 2.59 eV and 3.00 eV, respectively. The spectroscopic pattern predicted with the LSDxc/TDLSDxc functional and with the acute structure is different

from that with the obtuse geometry and also different from the experiment. The acute structure yields a spectrum with four intense bands at 2.11 eV, 2.41 eV, 2.47 eV, and 3.05 eV and assigned to the 4^2A_1, 4^2B_2, 5^2B_2, and 6^2B_1 states, respectively. There are two other peaks with small oscillator strengths, but not negligible, located at 1.39 eV and 2.83 eV and assigned to the 2^2A_1 and 5^2B_1 states, respectively. This spectroscopic pattern is different from that predicted with the obtuse structure or the experiment (see Figs. 56 and 62). Moreover, the acute geometry yielded strong bands within the energy range of 2.1 eV – 3.1 eV. This is too narrow compared to the spectrum predicted with the obtuse structure or the recorded spectrum. The above difference between the spectrum predicted with the acute structure and the experiment can exclude the contribution of the acute geometry in the recorded spectrum. On the other hand, it confirms that the obtuse structure is the equilibrium geometry and contributes to the recorded spectrum.

It is expected that small geometric distortions will not change the absorption spectrum remarkably. Figs. 58 and 57 show that the spectroscopic pattern predicted with the previous MCP optimized obtuse structure (the MCP geometry is slightly different from that optimized by the all-electron approach, see Chapter 4 of this thesis) is quite similar to the absorption spectrum predicted with the all-electron optimized geometry, but different in details. For example, the absorption spectrum predicted with the MCP optimized geometry has one more strong peak, in comparison with the spectrum predicted with the all-electron optimized geometry, located at 2.46 eV with an oscillator strength of 0.2168 and assigned to 5^2B_2 state. Moreover, the oscillator strengths calculated with the MCP optimized structure and with the all-electron optimized geometry are different. The oscillator strengths of the 6^2B_2 state (0.2729) is smaller than that with the all-electron optimized geometry which is 0.5047. In contrast, the oscillator strength of the 3^2A_2 state (0.5003) is larger than that predicted with the all-electron structure (0.4315). However, the positions of the intense bands predicted with the MCP

geometry and the all-electron structure are very close, the difference is no larger than 0.05 eV.

The *ab initio* CI method [14] predicted a nice absorption spectrum for the trimer compared with experiment and it has a similar spectroscopic pattern as the present predicted spectrum. The CI method predicted the band locations and oscillator strengths of the A group, the B group, and the C group bands which agree very well with the recorded peaks. However, the oscillator strength of the D band predicted with the CI method seems to be too small in comparison with the measured band (see Fig. 55).

The absorption spectrum of the tetramer is predicted with the rhombic geometry. Fig. 64 shows that the rich spectroscopic pattern (two strong peaks, three medium bands, and some small peaks) predicted by the LSDxc/TDLSDxc functional is in the energy interval of 1.8 eV – 3.3 eV. This is very similar to that in the recorded spectrum which is in the energy region of 1.6 – 3.3 eV. The present predicted two intense peaks are located at 1.84 eV and 2.67 eV and assigned to 1^1B_{3u} and 2^1B_{2u} states, respectively, which agree well with the two measured strong bands [67, 23] located at 1.80 eV and 2.51 eV and labelled as B and E bands, respectively. The predicted three medium peaks are located at 2.98 eV, 3.13 eV, and 3.31 eV and assigned to 2^1B_{1u}, 3^1B_{2u}, and 3^1B_{1u} states, respectively, which are fairly close to the three experimental medium bands [67, 23] located at 2.78 eV, 2.85 eV, and 3.33 eV and labelled as F, F$'$, and H, respectively. A few predicted small peaks located at 1.81 eV, 2.12 eV, 2.27 eV, 2.84 eV, and 3.08 eV and assigned to 1^1B_{2u}, 2^1B_{3u}, 1^1B_{1u}, 3^1B_{3u}, and 5^1B_{3u} states, respectively, correspond to the recorded bands [67, 23] located at 1.63 eV (A band), 1.98 eV (C band), 2.18 eV (D band), 2.63 eV (E$'$ band), and 3.15 eV (G band), respectively. The predicted 4^1B_{3u} peak located at 2.93 eV should correspond to the small recorded band [14, 67, 23] around 3.0 eV which was unlabelled.

The spectroscopic pattern of the tetramer predicted by the conventional CI

method [14] seems not to be that close to the recorded spectrum. The CI method predicted the absorption spectrum with three strong peaks and a few small peaks, but there are no obvious medium peaks to correspond to the recorded spectrum, although the positions of the predicted bands agree very well with the recorded bands (see Fig. 63). The ECP CI results [11] are very similar to the all-electron CI calculations, except that the F band (2^1B_{1u} state) predicted by the ECP CI method is smaller than that predicted by the all-electron CI approach. MCLR calculations [11] shifted the positions of the predicted bands to slightly higher energies and the spectroscopic pattern predicted by the MCLR method is very similar to the CI results. However, the RPA performance [11] showed a completely different spectrum from that predicted by the CI and the MCLR methods. The big difference is that the RPA calculations yielded oscillator strengths different from the CI and the MCLR results.

The absorption spectra of the sodium pentamer measured by Knight and co–workers [16] and by Wang *et al.* [71] seem to be different. Knight and co–workers [16] measured the absorption spectrum with two strong bands located around 2.1 eV and 2.6 eV. In contrast, Wang *et al.* [71] recorded spectrum with one strong and very wide band which cover the energy range of 1.8 eV – 2.5 eV, but in the energy interval of 2.25 eV – 2.7 eV, the measurement provides a lower limit cross section which is at worst within several percent of the actual value. This may be the reason why the second intense band did not appear in the spectrum recorded by Wang *et al.* [71]. The present LSDxc/TDLSDxc predicted spectrum of the pentamer has a number of small peaks with negligible intensities in the energy interval of 0 eV – 2.0 eV and 2.4 eV – 3.0 eV. The bands with considerable oscillator strengths are located within the energy range of 2.0 eV – 2.4 eV. The two intense peaks located at 2.0 eV and 2.4 eV and assigned to 6^2B_2 and 10^2A_1 states, respectively, agree fairly well with the spectrum measured by Knight and co–workers [16]. This also covers quite well the energy interval of the strong and broad band recorded by Wang *et al.* [71]. Lorentzian simulation [15]

based on the MRD-CI results also predicted two strong peaks for the pentamer and the positions of the two simulated bands are similar to the present results.

In contrast, the traditional CI method [15] predicted that the absorption spectrum of the pentamer has three intense peaks and assigned to 4^2B_2, 5^2B_2, and 9^2A_1 states, respectively. Moreover, the CI approach yielded three medium size bands and assigned to 6^2B_2, 8^2A_1, and 8^2B_2 states, respectively. All these peaks are within the energy interval of the recorded broad band by Wang *et al.* [71], but the 8^2B_2 state oscillator strength is too large (see Fig. 70).

The absorption spectra of the hexamer are carried out with the two competitive geometries, the planar D_{3h} geometry and the pentagonal pyramid C_{5v} structure. Figs. 78, 79, 80, 81, 82, and 85, show that the two structures have competitive contributions in the recorded absorption spectrum. The present predicted spectra with the two structures are very similar. The pentagonal pyramid C_{5v} structure (in order to compare with the CI results which were analysed under C_S subgroup [15, the present analysis and symmetry assignments are also under C_S subgroup, $C_{5v} \longrightarrow C_S$) yields one degenerate strong peak located at 2.28 eV and assigned to $7^1A'$ and $6^1A''$ states. This strong peak agrees well with the recorded intense band [71] located at 2.1 eV and labelled as II. The present predicted one degenerate medium peak, located at 2.85 eV and assigned to $12^1A'$ and $11^1A''$ states, is in good agreement with the measured band [71] located at 2.83 eV and labelled as IV. The transition to the $4^1A'$ and $3^1A''$ states around 1.67 eV has a small oscillator strength and agrees nicely with the recorded band located at 1.78 eV and labelled as I. The present predicted small peaks located at 2.61 eV and assigned to $10^1A'$ and $9^1A''$ states are responsible for the measured band III located at 2.44 eV. The absorption spectrum predicted with the planar D_{3h} structure (analysis and symmetry assignments are under C_{2v} subgroup, $D_{3h} \longrightarrow C_{2v}$ for comparing with the CI results which were assigned ubder C_{2v} subgroup [15]) has a very similar spectroscopic pattern to that with the pen-

tagonal pyramid geometry. Fig. 78 shows that the planar structure yields two strong peaks, which should be degenerate in the D_{3h} point group, located at 2.146 eV (with oscillator strength of 1.316) and 2.153 eV (with oscillator strength of 1.312) and assigned to 3^1B_2 and 4^1A_1 states, respectively. However, the degeneracy of the two intense bands with the planar structure is not as good as that with the pentagonal pyramid geometry, it is slightly broken (the two strong bands lie within 0.007 eV). Nevertheless, the two intense peaks coincide well with the recorded band II. Moreover, the degeneracy of the two intense bands with the LB94xc/TDLSDxc functional is broken in both cases with the planar structure (the two peaks lies within 0.014 eV) and with the pentagonal pyramid geometry (the two bands separated by 0.001 eV).

It is noticed that the pentagonal pyramid C_{5v} geometry and the planar D_{3h} structure yield very similar spectroscopic patterns and both agree well with the experimental results. The absorption spectra of the hexamer predicted with the two geometries with comparison to the recorded spectrum support the DFT geometry optimizations. Since the two competitive geometries, obtained with the DFT geometry optimization, differ in energy only by 0.05 eV and both geometries are minima on the DFT energy surface (both geometries with all positive frequencies), it is difficult to rule out completely either of the two structures from the equilibrium geometry. Hence, both geometries probably have similar contributions to the recorded spectrum. However, this similarity of the spectrum predicted with the pentagonal pyramid structure and with the planar geometry was also found by Bonačić–Koutecký and co-workers with the CI calculations [15]. The two structures in the CI calculations also yielded two intense bands, but the degeneracy of the two bands is broken in both spectra predicted with the planar structure and with the pentagonal pyramid geometry. The two peaks are separated by around 0.01 eV in the planar structure spectrum and by about 0.16 eV in the pentagonal pyramid geometry spectrum (see Fig. 77). This degeneracy breaking is much larger than that in the present calculations in which the pentagonal

pyramid geometry yields exact degenerate intense bands and the planar structure slightly breaks the degeneracy. Moreover, the pentagonal pyramid structure was not predicted as a minimum on the Hartree–Fock energy surface [15]. In contrast, MCLR [11] and RPA [11] methods did obtain the degeneracy for the predicted strong peaks (with D_{3h} planar structure). However, the MCLR and the RPA approaches yielded one additional medium peak or intense peak for the RPA (3^1B_1) and lead to the spectroscopic pattern to be different from the recorded spectrum.

The LB94xc/TDLSDxc functional yields similar spectroscopic patterns for the sodium clusters as those predicted by the LSDxc/TDLSDxc functional in most cases, but they differ in details. The LB94xc/TDLSDxc functional produces fewer bands in the same energy interval as in the LSDxc/TDLSDxc functional calculations and the positions of the peaks are slightly shifted to higher energy. The oscillator strengths calculated by the LB94xc/TDLSDxc functional are larger than those carried out by the LSDxc/TDLSDxc functional. Sometimes, the heights of the peaks (pattern of the spectra) change order in comparison with those predicted by the LSDxc/TDLSDxc functional. For example, the tetramer spectrum predicted by the LB94xc/TDLSDxc functional has a similar spectroscopic pattern as that predicted by the LSDxc/TDLSDxc functional. Three strong peaks are observed and located at 2.02 eV, 2.98 eV, and 3.45 eV and assigned to 1^1B_{3u}, 2^1B_{2u}, and 2^1B_{1u} states, respectively. These bands are shifted to higher energy in comparison with those calculated by the LSDxc/TDLSDxc functional [at 1.84 eV (1^1B_{3u}), 2.67 eV (2^1B_{2u}), and 2.99 eV (2^1B_{1u})]. The oscillator strengths of these three intense bands calculated with the LB94xc/TDLSDxc functional [1.990 ($^1B_{3u}$), 1.1525 (2^1B_{2u}), 0.9228 (2^1B_{1u})] are larger than those calculated with the LSDxc/TDLSDxc functional [1.008 (1^1B_{3u}), 0.8551 ((2^1B_{2u}), 0.3959 (2^1B_{1u})]. Since the positions of the bands predicted by the LB94xc/TDLSDxc functional are shifted to higher energy, in the same energy interval as in the LSDxc/TDLSDxc functional calculations, of course, fewer peaks are observed in the spectrum predicted by the LB94xc/TDLSDxc functional.

Moreover, some medium bands observed with the LSDxc/TDLSDxc functional do not appear in the spectrum predicted by the LB94xc/TDLSDxc functional (see Figs. 65 and 64). But the same symmetry assignments are obtained in the spectrum of the tetramer predicted by the LB94xc/TDLSDxc functional and by the LSDxc/TDLSDxc functional. However, the LB94xc/TDLSDxc functional may yield a quite different spectroscopic pattern from that predicted by the LSDxc/TDLSDxc functional. For example, in the spectrum of the trimer, in Figs. 56, 57, 58, and 59, there are four strong peaks [at 1.83 eV (3^2A_1), 2.19 (4^2A_1), 2.52 eV (6^2B_2), and 2.88 eV (3^2A_2)] and two medium bands [at 2.41 eV (4^2B_2) and 3.09 eV (4^2A_2)] predicted by the LSDxc/TDLSDxc functional. But the LB94xc/TDLSDxc functional yields only three intense peaks [at 2.11 eV (3^2A_1), 2.68 eV (4^2B_2), and 3.31 eV (3^2A_2)] and one medium peak [at 2.35 eV (4^2A_1)]. This difference is not caused by the limited energy interval, it is due to the fact that the oscillator strengths calculated by the two functionals are different. The LSDxc/TDLSDxc functional yields the 4^2B_2 state as a medium band with an oscillator strength of 0.1634, whereas the LB94/TDLSDxc functional produces the 4^2B_2 state as a strong peak with an oscillator strength of 0.7742. The LSDxc/TDLSDxc functional gives the 6^2B_2 state with large oscillator strength (0.5047), whereas the LB94xc/TDLSDxc functional yields the 6^2B_2 state with small oscillator strength (0.0153). This is the source of the different for predicted spectroscopic pattern between the LSDxc/TDLSDxc and the LB94xc/TDLSDxc functionals and leads to different assignments.

These differences between the performances of the LSDxc/TDLSDxc and the LB94xc/TDLSDxc functionals may be partly due to the different short–r behavior and large–r behavior of the two functionals, and partly due to using geometries optimized for one functional (LSDxc), which may not be exactly the minima on the energy surface of the other functional (LB94xc). For example, the calculations of the hexamer ($C_{5v} \rightarrow C_s$ or $D_{3h} \rightarrow C_{2v}$) with the LSDxc/TDLSDxc functional yield much better degenerency than those with the LB94xc/TDLSDxc

functional, since the geometry (D_{3h} or C_{5v}) was optimized with LSDxc functional, it may not be exact minimum on the energy surface of the LB94xc functional. On the other hand, charge density with LSDxc functional is more distributed around the nuclei, it is more like a spherical, hence, the grid can discrbe it better. But the charge density with LB94xc functional has a long tail, the grid may not well discribe it. This may also be the reason which causes the degenerency breaking with the LB94xc/TDLSDxc functional.

MCP calculations reasonably reproduce the dominant features of the absorption spectra predicted by the all-electron calculations. It is interesting to note that the differences between the MCP and the all-electron predicted spectra are similar to those between the LSDxc/TDLSDxc and the LB94xc/TDLSDxc functionals. The MCP predicted spectroscopic pattern moves the bands to higher energy and with larger oscillator strengths or changes the oscillator strengths remarkably from those calculated by the all electron approach, especially with the small basis set (MCP basis). But the MCP calculations with the larger basis (MCP+) normally yield similar results to the all-electron calculations. For example, in the predicted spectrum of the trimer, the MCP calculations with the small basis (MCP) predicted a different spectroscopic pattern from that predicted by the all-electron calculations, even though it gives the same dominant bands as the all-electron approach (comparing Fig. 56 and 60). The locations of the peaks predicted by the MCP with the small basis MCP are shifted to higher energy and the oscillator strengths of the intense bands are different from those calculated by the all-electron approach. The A$'$ band (3^2A_1 state) predicted by the MCP is located at 2.10 eV, which is about 0.27 eV higher than that in the all-electron prediction. Its oscillator strength performed by the MCP (0.8402) is almost double to that of the all-electron calculation (0.4490). The MCP predicted B band (4^2A_1 state) located at 2.52 eV is about 0.3 eV higher than that in the all-electron calculations. Its height predicted by the MCP (0.1661) is about twice smaller than the all-electron prediction (0.3424). The MCP yields the C band (3^2A_2 state)

at 3.44 eV which may be compared with the value of all-electron at 2.88 eV. The MCP oscillator strength of this peak (1.1908) is almost the triple of that calculated by the all-electron approach (0.4315). It is expected that the larger basis should correct these deviations between the MCP (with the small basis) and all-electron calculations or at least eliminates the differences partly. This is indeed the case, the MCP calculations with larger basis (MCP+) do improve the results remarkably and lead to similar spectroscopic pattern to that predicted by the all-electron calculations. The MCP with the larger basis (MCP+) predicted states 3^2A_1 (MCP: 1.95 eV; AE: 1.83 eV), 1^2A_2 (MCP: 2.03 eV; AE: 1.95 eV), 4^2A_1 (MCP: 2.28 eV; AE: 2.19 eV), 4^2B_2 (MCP: 2.45 eV; AE: 2.41 eV), 5^2B_2 (MCP: 2.55 eV; AE: 2.52 eV), 3^2A_2 (MCP: 3.04 eV; AE: 2.88 eV), and 8^2B_2 (MCP: 3.20 eV; AE: 3.09 eV) (see Fig. 61) are much closer to the all-electron calculations and are responsible for the recorded A$'$, A, B, B$'$, B$''$, C, and D bands, respectively. The oscillator strengths calculated by the MCP with the larger basis (MCP+) are improved remarkably (0.6724 for the A$'$ band, 0.2779 for the B band, and 0.8306 for the C band). However, the small MCP basis is unstable, sometimes it may lead to different assignments from the all-electron calculations. For example, in the spectrum of the pentamer predicted by the MCP (with the small basis), the first of the two strong peaks is assigned to the 4^2B_2 state which is different from the all-electron symmetry assignment (6^2B_2). It is obvious that the different assignments between the MCP and the all-electron approach are due to the inadequate MCP basis set used. The larger MCP basis (MCP+) yields the same assignment as in the all-electron LSDxc/TDLSDxc case. However, the MCP calculations (with the MCP+ basis) with the LB94xc/TDLSDxc functional yields an unexpected absorption spectrum for the pentamer, which has only one intense peak with an assignment of the 9^2A_1 and three medium peaks assigned to 4^2B_2, 5^2B_2, and 9^2A_1 states, respectively.

7.4 CONCLUSION

Absorption spectra of small sodium clusters (from the dimer through to the hexamer) have been predicted and interpreted by time-dependent DFT using the LSDxc/TDLSDxc functional and the LB94xc/TDLSDxc functional at the all-electron level and the MCP level. The absorption spectra predicted by the present work agree fairly well with the recorded spectra and are competitive with the high quality *ab initio* CI predictions.

It is not obvious in the present work that the excitation energies of the small sodium clusters collapse when they are larger than the ionization threshold of the LSDxc functional, even though the negative of the HOMO (highest occupied molecular orbital) energies, $-\varepsilon_{HOMO}^{LSDxc}$, of the sodium clusters calculated by the LSDxc functional are still too low in comparison with the experimental ionization potentials. But excitation energy collapses were observed for the compounds (closed–shell) at the right–hand side of the periodic table in Ref. [387] and for the free radical (open–shell) calculations at the Chapter 5 of this thesis. This indicates that the LSDxc (or LSDxc/TDLSDxc) functional behaves differently in the applications to the compounds at the right–hand side of the periodic table and those at the left-hand side of the periodic table, regardless of whether the compounds are closed–shell molecules or open–shell radicals. However, the MCP excitation energies become much larger than the corresponding all-electron results when the excitation energies are larger than the ionization threshold corresponding to the functional used, $-\varepsilon_{HOMO}^{LSDxc}$ or $-\varepsilon_{HOMO}^{LB94xc}$. This different degree of falling off between the MCP excitation energies and the all-electron results is probably due to the orbital basis set used in the MCP calculations which is inadequate for the high excitations.

The present time-dependent DFT calculations overestimate the excitation energies of the small sodium clusters in comparison with the experimental results.

This is similar to the calculations of the small lithium clusters, but it is different from the calculations for the free radicals and other small molecules (closed–shell) at the right–hand side of the periodical table in Ref. [387] which underestimated excitation energies. In contrast, the polarizabilities of the small sodium clusters calculated by DFT are underestimated in Refs. [327, 122], whereas the polarizabilities of small molecules at the right–hand side of the periodic table are overestimated by the DFT in Ref. [119]. This observation agrees with the theoretical relationship between excitation energy and polarizability (see Chapter 2 of this thesis).

The LB94xc/TDLSDxc functional produces too high excitation energies for the small sodium clusters in both cases of the low and the high transitions, this leads to larger errors from the available experiments and the high quality *ab initio* CI results in comparison with the calculations by the LSDxc/TDLSDxc functional. This is in contrast to the LB94xc/TDLSDxc functional calculations for the free radicals and the small lithium clusters which yielded too low excitation energies for the low transitions.

The present work found that electron Coulomb, exchange, and correlation interactions have different contributions to the excitation energies. The Coulomb interactions seem to have the largest contributions to excitation energies for the molecules or clusters studied here and their role is to push electronic states towards to each other. In contrast, the electron exchange and correlation interactions push electronic states apart, hence the two interactions increase the excitation energies from the Coulomb calculations. However, the exchange interactions contribute to the excitation energies more than do the correlation interactions, the differences on the excitation energies between the two interactions are about one order of magnitude.

The present calculations show that the excitation energies are insensitive to small geometrical distortions, but the oscillator strengths are more sensitive.

Large geometrical distortions not only lead to large changes in the excitation energies and oscillator strengths, but also yield different ground state symmetry.

The equilibrium geometry of the sodium hexamer is very competitive between the planar structure and the pentagonal pyramid structure from the geometry optimizations. The present predicted absorption spectra of the hexamer with the two structures show that both structures are also very competitive in the contributions to the recorded spectrum. Neither of the two geometries can be excluded completely from the recorded spectrum. This supports the DFT optimized geometries in the previous work [327, 122]. However, the equilibrium geometry of the sodium hexamer (the planer D_{3h} or pentagonal pyramid C_{5v}) is different from the equilibrium geometry of the lithium hexamer which has a three-dimensional C_{2v} structure.

The MCP assessed here reasonably reproduces the spectroscopic pattern of the small sodium clusters as predicted by the all-electron calculations. However, small orbital basis which is flexible enough to describe ground state properties is not flexible enough to describe excited state properties. A larger basis set is needed for the excitation energy calculations. Especially, diffuse functions and polarization functions are essential.

Table XLVI. Ground state configurations and ground state symmetry of sodium clusters calculated by the present DFT SCF calculations at all-electron level with LSDxc functional.

Clusters (symmetry)	Ground state electron configuration	Ground state symmetry
$Na_2(D_{\infty h})$	$(1\sigma_g^+)^2(1\sigma_u^+)^2(2\sigma_g^+)^2(2\sigma_u^+)^2(3\sigma_g^+)^2$	
	$(1\pi_u)^4(1\pi_g)^4(3\sigma_u^+)^2(4\sigma_g^+)^2$	$1^1\Sigma_g^+$
$Na_3(C_{2v})$	$(1a_1)^2(1b_2)^2(2a_1)^2(3a_1)^2(2b_2)^2(4a_1)^2$	
	$(1b_1)^2(5a_1)^2(3b_2)^2(6a_1)^2(2b_1)^2(1a_2)^2$	
	$(4b_2)^2(7a_1)^2(5b_2)^2(8a_1)^2(6b_2)^1$	1^2B_2
$Na_4(D_{2h})$	$(1b_{2u})^2(1a_g)^2(1b_{3u})^2(2a_g)^2(3a_g)^2(2b_{2u})^2$	
	$(2b_{3u})^2(4a_g)^2(5a_g)^2(1b_{1u})^2(1b_{3g})^2(3b_{2u})^2$	
	$(3b_{3u})^2(1b_{1g})^2(4b_{2u})^2(2b_{1g})^2(1b_{2g})^2(2b_{1u})^2$	
	$(6a_g)^2(4b_{3u})^2(7a_g)^2(5b_{3u})^2$	1^1A_g
$Na_5(C_{2v})$	$(1a_1)^2(1b_2)^2(2b_2)^2(2a_1)^2(3a_1)^2(4a_1)^2$	
	$(3b_2)^2(4b_2)^2(5a_1)^2(6a_1)^2(1b_1)^2(1a_2)^2$	
	$(5b_2)^2(2b_1)^2(7a_1)^2(2a_2)^2(8a_1)^2(6b_2)^2$	
	$(9a_1)^2(7b_2)^2(10a_1)^2(8b_2)^2(3b_1)^2(11a_1)^2$	
	$(9b_2)^2(12a_1)^2(10b_2)^2(13a_1)^1$	1^2A_1
$Na_6(D_{3h} \rightarrow C_{2v})$	$(1a_1)^2(1b_2)^2(2a_1)^2(3a_1)^2(2b_2)^2(4a_1)^2$	
	$(5a_1)^2(3b_2)^2(6a_1)^2(7a_1)^2(4b_2)^2(8a_1)^2$	
	$(5b_2)^2(9a_1)^2(1b_1)^2(1a_2)^2(6b_2)^2(10a_1)^2$	
	$(7b_2)^2(2b_1)^2(11a_1)^2(12a_1)^2(3b_1)^2(4b_1)^2$	
	$(2a_2)^2(13a_1)^2(8b_2)^2(9b_2)^2(14a_1)^2$	
	$(10b_2)^2(15a_1)^2(11b_2)^2(16a_1)^2$	1^1A_1
$Na_6(C_{5v} \rightarrow C_s)$	$(1a')^2(1a'')^2(2a'')^2(3a'')^2(2a')^2(3a')^2$	
	$(4a')^2(4a'')^2(5a'')^2(5a')^2(6a')^2(7a')^2$	
	$(8a')^2(6a'')^2(9a')^2(10a')^2(11a')^2(7a'')^2$	
	$(8a'')^2(12a')^2(9a'')^2(13a')^2(14a')^2$	
	$(15a')^2(10a'')^2(11a'')^2(16a')^2(12a'')^2$	
	$(17a')^2(13a'')^2(18a')^2(14a'')^2(19a')^2$	$1^1A'$

Table XLVII. Ground state configurations and ground state symmetry of sodium clusters calculated by the present DFT SCF calculations at MCP level with LS-Dxc functional.

Clusters (symmetry)	Ground state electron configuration	Ground state symmetry
$Na_2(D_{\infty h})$	$(1\sigma_g^+)^2$	$1^1\Sigma_g^+$
$Na_3(C_{2v})$	$(1a_1)^2(1b_2)^1$	1^2B_2
$Na_4(D_{2h})$	$(1a_g)^2(1b_{3u})^2$	1^1A_g
$Na_5(C_{2v})$	$(1a_1)^2(1b_2)^2(2a_1)^1$	1^2A_1
$Na_6(D_{3h} \rightarrow C_{2v})$	$(1a_1)^2(1b_2)^2(2a_1)^2$	1^1A_1
$Na_6(C_{5v} \rightarrow C_s)$	$(1a')^2(2a')^2(1a'')^2$	$1^1A'$

Table XLVIII. Sodium dimer vertical excitation energies (eV) calculated with the all-electron and the MCP and with different functionals in comparison with experiment and other theoretical results.

	Vertical excitation energies (eV)								
State	LSDxc TDLSDxc (AE)	LB94xc TDLSDxc (AE)	LSDxc TDLSDxc (MCP+)	LB94xc TDLSDxc (MCP+)	LSDxc TDLSDxc (MCP)	EXPT[a]	F-CI[b] (AE)	CI[c]	MBPT[d] (AE)
$1^1\Sigma_g^+$	0.000	0.000	0.000	0.000	0.000	0.000	0.000	0.000	0.000
$1^3\Sigma_u^+$	0.966	0.703	0.929	1.120	1.007		1.046	0.707	0.619
$1^3\Pi_u$	1.822	2.216	1.851	2.704	1.978	1.692	1.669	1.711	1.568
$1^1\Sigma_u^+$	2.103	2.298	2.140	2.611	2.191	1.820	1.928	1.823	1.627
$1^3\Sigma_g^+$	2.363	2.720	2.476	3.210	2.738		2.414	2.286	2.134
$1^1\Pi_u$	2.666	3.124	2.785	3.622	3.144	2.519	2.576	2.517	2.572
$2^1\Sigma_g^+$	2.905	3.472	3.052	3.783	3.622		2.717	2.442	
$1^3\Pi_g$	3.062	3.464	3.180	4.021	3.544				
$1^1\Pi_g$	3.116	3.658	3.309	4.089	3.843		2.961	2.728	2.450
$2^3\Sigma_g^+$	3.268	3.997	4.178	5.089	5.527			3.221	
$3^1\Sigma_g^+$	3.275	4.086	4.602	5.480	6.015			3.209	
$2^3\Sigma_u^+$	3.325	4.326	4.004	4.606	5.442			3.397	
$2^1\Sigma_u^+$	3.367	4.487	4.153	4.923	5.639			3.509	
$2^3\Pi_u$	3.452	4.665	5.281	5.839				3.583	
$3^3\Sigma_g^+$	3.547	5.042	5.588	6.730				3.749	
$2^1\Pi_u$	3.574	4.880	5.990	6.553				3.583	
$4^1\Sigma_g^+$	3.647	5.251	6.079	7.313				3.558	
$2^3\Pi_g$	3.715	5.299	6.464	6.799				3.608	
$2^1\Pi_g$	3.753	5.381	6.699	6.950				3.831	
$3^3\Sigma_u^+$	3.940	5.032	5.797	6.685	6.719			3.571	
$3^1\Sigma_u^+$	4.010	4.919	5.718	6.652	7.094			3.918	
$4^1\Sigma_u^+$	4.098	5.872	7.545	8.015				4.129	
$4^3\Sigma_u^+$	4.206	5.805	7.348	7.766				4.029	

[a] Experimental results were cited in Ref. [487].

[b] Full CI calculations taken from Ref. [13].

[c] Results are taken from Ref. [478].

[d] Results are taken from Ref. [486].

Table XLIX. Sodium trimer vertical excitation energies (eV) calculated with different levels of electronic interactions at the all-electron (AE) level with (XF,NR) grid.

State	Core/IPA	Hartree/RPA	LSDx/TDLSDx	LSDxc/TDLSDxc
		Vertical excitation energies (eV)		
1^2A_1	0.058	0.093	0.677	0.618
2^2A_1	1.655	0.327	1.235	1.317
3^2A_1	3.852	0.430	1.691	1.803
4^2A_1	12.265	0.515	2.045	2.151
5^2A_1	13.687	0.713	2.247	2.626
1^2A_2	3.705	0.483	1.382	1.944
2^2A_2	14.698	1.157	1.923	2.160
3^2A_2	15.143	1.239	2.530	2.850
4^2A_2	26.982	1.397	2.719	3.080
5^2A_2	28.677	1.412	2.920	3.436
1^2B_1	2.877	0.235	1.167	1.232
2^2B_1	14.716	0.438	2.255	2.456
3^2B_1	15.970	0.809	2.382	2.794
4^2B_1	16.412	1.412	2.751	3.104
5^2B_1	26.963	1.419	2.797	3.186
2^2B_2	1.421	0.485	0.864	1.355
3^2B_2	12.323	0.506	1.579	1.664
4^2B_2	13.790	0.635	1.994	2.358
5^2B_2	13.920	1.012	2.129	2.456
6^2B_2	14.392	1.152	2.351	2.471

Table L. Sodium trimer vertical excitation energies (eV) calculated with different levels of electronic interactions at the MCP level with different qualities of grids.

State	Core/IPA	Hartree/RPA	LSDx/TDLSDx	LSDxc/TDLSDxc
Vertical excitation energies (eV) with (XF,NR) grid				
1^2A_1	0.812	0.319	0.839	0.684
2^2A_1	2.719	1.408	1.370	1.404
1^2A_2	3.503	2.421	1.659	2.162
2^2A_2	4.227	3.673	2.450	2.512
1^2B_1	1.508	1.202	1.420	1.349
2^2B_1	3.955	2.896	3.356	3.186
2^2B_2	2.893	1.811	1.021	1.504
3^2B_2	3.531	2.760	1.968	1.939
Vertical excitation energies (eV) with (XF,R) grid				
1^2A_1	0.812	0.319	0.839	0.616
2^2A_1	2.719	1.408	1.369	1.069
1^2A_2	3.503	2.421	1.658	2.146
2^2A_2	4.227	3.676	2.450	2.512
1^2B_1	1.508	1.202	1.420	1.350
2^2B_1	3.955	2.896	3.356	3.180
2^2B_2	2.893	1.811	1.020	1.485
3^2B_2	3.531	2.760	1.968	1.938
Vertical excitation energies (eV) with (F,R) grid				
1^2A_1	0.812	0.319	0.841	0.615
2^2A_1	2.719	1.408	1.367	1.063
1^2A_2	3.503	2.421	1.655	2.143
2^2A_2	4.227	3.676	2.448	2.512
1^2B_1	1.508	1.202	1.418	1.348
2^2B_1	3.955	2.896	3.354	3.181
2^2B_2	2.893	1.811	1.021	1.487
3^2B_2	3.531	2.760	1.970	1.939

Table LI. Comparison of excitation energies (eV) of the sodium trimer calculated by the all-electron and the MCP with available experiment and other theoretical calculations.

	Vertical excitation energies (eV)								
State	LSDxc/ TDLSDxc (AEAE)	LB94xc/ TDLSDxc (AEAE)	LSDxc/ TDLSDxc (AEMCP)	LB94xc/ TDLSDxc (AEMCP)	LSDxc/ TDLSDxc (MCP+)	EXPT[a]	MRDCI[b] (AE)	CI[c] (AE)	CI[d] (ECP
$1\ ^2B_2$	0.000	0.000	0.000	0.000	0.000	0.000	0.00	0.00	0.000
$1\ ^2A_1$	0.631	0.433	0.618	0.396	0.675		0.52	0.6	0.018
$2\ ^2A_1$	1.339	1.327	1.317	1.293	1.334		1.07	1.3	1.025
$2\ ^2B_2$	1.419	1.239	1.355	1.136	1.412		1.33	1.5	1.194
$3\ ^2B_2$	1.698	1.875	1.664	1.846	1.756		2.14	2.4	1.983
$3\ ^2A_1$	1.826	2.105	1.803	2.096	1.945	1.67	1.61	1.8	1.261
$1\ ^2A_2$	1.953	2.309	1.944	2.302	2.026	1.84	1.77	2.0	1.753
$2\ ^2A_2$	2.172	2.478	2.159	2.467	2.288		2.61	2.9	2.567
$4\ ^2A_1$	2.189	2.352	2.151	2.318	2.275	2.03	1.97	2.2	1.849
$4\ ^2B_2$	2.409	2.676	2.358	2.612	2.448	2.22	2.36	2.6	2.126
$5\ ^2B_2$	2.487	2.778	2.456	2.729	2.554		2.50	2.9	2.327
$6\ ^2B_2$	2.516	2.914	2.471	2.895	2.726	2.40	2.85		
$5\ ^2A_1$	2.629	3.007	2.626	2.926	2.824		2.52	2.7	1.992
$6\ ^2A_1$	2.707	3.191	2.677	3.199	3.194		2.72	3.0	2.330
$3\ ^2A_2$	2.878	3.307	2.850	3.263	3.036	2.59	2.90	3.1	
$4\ ^2A_2$	3.090	3.925	3.080	3.822	3.676	3.00	3.09		

[a] Experimental results are taken from Ref. [23]. The assignments are based on all-electron calculations with all-electron geometry (AEAE).

[b] Results are taken from Ref. [14].

[c] Results are taken from Ref. [368].

[d] Results are taken from Ref. [479].

Table LII. Sodium trimer vertical excitation energies (eV) calculated with different functionals and various basis sets at the all-electron level.

	Vertical excitation energies (eV)						
State	STO3G	DZVP	BASIS1	BASIS2	BASIS3	BASIS4	BASIS5
	Calculations with LSDxc/TDLSDxc						
1^2B_2	0.000	0.000	0.000	0.000	0.000	0.000	0.000
1^2A_1	1.178	0.633	0.618	0.620	0.619	0.618	0.620
2^2A_1	2.938	1.425	1.317	1.321	1.320	1.316	1.320
2^2B_2	1.848	1.374	1.355	1.355	1.358	1.350	1.354
3^2B_2	4.233	1.911	1.664	1.669	1.669	1.667	1.673
3^2A_1	6.263	2.038	1.803	1.807	1.807	1.804	1.810
1^2A_2	7.767	2.298	1.944	1.952	1.950	1.940	1.948
4^2A_1	6.770	2.624	2.151	2.156	2.155	2.150	2.154
2^2A_2	7.941	2.706	2.159	2.167	2.165	2.158	2.165
4^2B_2	6.546	2.544	2.358	2.363	2.364	2.356	2.363
5^2B_2	6.724	2.680	2.456	2.461	2.462	2.454	2.461
6^2B_2	7.857	3.192	2.471	2.476	2.475	2.472	2.477
5^2A_1	7.602	2.995	2.626	2.636	2.630	2.631	2.636
6^2A_1	8.436	3.750	2.677	2.684	2.683	2.679	2.686
3^2A_2	9.113	3.710	2.850	2.857	2.855	2.847	2.852
4^2A_2	9.615	4.357	3.080	3.088	3.083	3.081	3.085
	Calculations with LB94xc/TDLSDxc						
1^2B_2	0.000	0.000	0.000	0.000	0.000	0.000	0.000
1^2A_1	0.617	0.401	0.396	0.367	0.394	0.383	0.379
2^2A_1	2.631	1.380	1.293	1.271	1.293	1.295	1.293
2^2B_2	1.449	1.161	1.136	1.100	1.137	1.135	1.134
3^2B_2	3.978	2.047	1.846	1.838	1.847	1.859	1.861
3^2A_1	5.988	2.395	2.096	2.094	2.099	2.100	2.107
1^2A_2	7.412	1.787	2.302	2.261	2.307	2.312	2.320
4^2A_1	6.649	2.718	2.318	2.311	2.323	2.321	2.327
2^2A_2	7.714	2.582	2.467	2.451	2.473	2.470	2.479
4^2B_2	6.322	2.879	2.612	2.592	2.615	2.614	2.617
5^2B_2	6.553	3.034	2.729	2.729	2.734	2.757	2.765
6^2B_2	7.578	3.386	2.895	2.890	2.907	2.913	2.922
5^2A_1	7.377	3.221	2.926	2.919	2.931	2.953	2.958
6^2A_1	8.314	3.867	3.199	3.155	3.210	3.158	3.162
3^2A_2	8.778	2.929	3.263	3.247	3.267	3.263	3.268
4^2A_2	9.294	3.920	3.822	3.883	3.826	3.860	3.874

Table LIII. MCP vertical excitation energies (eV) of sodium trimer calculated with various MCP basis sets using the LSDxc/TDLSDxc functional.

	MCP vertical excitation energies (eV)			
State	MCP	MCP1	MCP2	MCP+
$1\ ^2B_2$	0.000	0.000	0.000	0.000
$1\ ^2A_1$	0.684	0.684	0.667	0.675
$1\ ^2B_1$	1.349	1.684	1.219	1.299
$2\ ^2A_1$	1.404	1.457	1.335	1.334
$2\ ^2B_2$	1.504	1.499	1.459	1.412
$3\ ^2B_2$	1.939	2.046	1.760	1.756
$3\ ^2A_1$	2.101	2.179	1.948	1.945
$1\ ^2A_2$	2.162	2.446	2.004	2.026
$2\ ^2A_2$	2.512	2.882	2.255	2.288
$4\ ^2A_1$	2.519	2.766	2.266	2.275
$4\ ^2B_2$	2.637	2.699	2.479	2.448
$5\ ^2B_2$	2.747	2.833	2.584	2.554
$5\ ^2A_1$	3.065	3.229	2.848	2.824
$2\ ^2B_1$	3.186	3.660	2.670	2.691
$6\ ^2B_2$	3.231	3.520	2.730	2.726
$3\ ^2A_2$	3.437	3.884	3.043	3.036
$7\ ^2B_2$	3.444	3.665	3.141	3.118
$6\ ^2A_1$	3.625	3.943	3.216	3.194
$3\ ^2B_1$	3.681	4.050	3.351	3.357
$8\ ^2B_2$	3.748	4.149	3.189	3.196
$4\ ^2B_1$	3.999	4.423	3.544	3.558
$9\ ^2B_2$	4.028	4.301	3.343	3.324
$4\ ^2A_2$	4.185	4.650	3.678	3.676
$5\ ^2A_2$	4.445	4.906	3.874	3.880

Table LIV. Sodium tetramer vertical excitation energies (eV) calculated by the all-electron (AE) with the Sadlej basis and by the MCP with various basis sets using the LSDxc/TDLSDxc and the LB94xc/TDLSDxc functionals.

	AE vertical excitation energies (eV)						
State	LSDxc/ TDLSDxc	LB94xc/ TDLSDxc	EXPT[a]	MRD-CI[b] (AE)	MRD-CI[c] (ECP)	MCLR[c] (ECP)	RPA[c] (ECP)
1^1A_g	0.000	0.000	0.000	0.000	0.000	0.000	0.000
1^1B_{2u}	1.816	1.966	1.63	1.51	1.57	1.68	2.29
1^1B_{3u}	1.842	2.025	1.80	1.71	1.77	1.81	1.76
2^1B_{3u}	2.123	2.229	1.98	1.87	1.96	2.07	2.12
1^1B_{1u}	2.267	2.623	2.18	2.07	2.20	2.31	2.51
2^1B_{2u}	2.670	2.981	2.51	2.45	2.57	2.68	2.76
3^1B_{3u}	2.836	3.384	2.63	3.03		3.02	2.91
4^1B_{3u}	2.933	3.721					
2^1B_{1u}	2.989	3.450	2.78	2.76	2.90	3.03	3.29
5^1B_{3u}	3.088	4.119	3.15				
3^1B_{2u}	3.135	4.089	2.85	2.46	2.63	2.77	3.52
3^1B_{1u}	3.307		3.33	3.00		3.55	4.00
	MCP vertical excitation energies (eV)						
State	LSDxc/ TDLSDxc (MCP+)	LSDxc/ TDLSDxc (MCP2)	LSDxc/ TDLSDxc (MCP1)	LSDxc/ TDLSDxc (MCP)	LB94xc/ TDLSDxc (MCP)	LB94xc/ TDLSDxc (MCP+)	EXPT[a]
1^1A_g	0.000	0.000	0.000	0.000	0.000	0.000	0.000
1^1B_{2u}	1.806	1.826	2.045	1.960	1.997	1.957	1.63
1^1B_{3u}	1.918	1.909	1.986	1.990	2.084	2.067	1.80
2^1B_{3u}	2.181	2.223	2.585	2.445	2.439	2.337	1.98
1^1B_{1u}	2.333	2.301	2.979	2.591	2.879	2.627	2.18
2^1B_{2u}	2.751	2.756	3.343	3.120	3.125	2.880	2.51
3^1B_{3u}	3.483	3.492	4.109	4.010	4.014	3.746	2.63
4^1B_{3u}	3.598	3.775	5.574	5.103	5.178	3.958	2.78
2^1B_{1u}	3.201	3.249	4.144	3.699	3.897	3.388	2.85
5^1B_{3u}	4.023	4.558	5.932	5.738	5.749	4.299	
3^1B_{2u}	3.865	3.900	4.974	4.666	4.613	4.034	3.15
3^1B_{1u}	4.451	4.443	5.415	5.076	5.180	4.490	3.33

[a] Experimental Results are taken from Ref. [23].

[b] Results are taken from Ref. [14]. [c] Results are taken from Ref. [11].

Table LV. Sodium pentamer vertical excitation energies (eV) calculated with the all-electron and the MCP and with different functionals in comparison with other theoretical results.

	Vertical excitation energies (eV)						
State	LSDxc/ TDLSDxc (AE)	LB94xc/ TDLSDxc (AE)	LSDxc/ TDLSDxc (MCP+)	LB94xc/ TDLSDxc (MCP+)	LSDxc/ TDLSDxc (MCP)	LB94xc/ TDLSDxc (MCP)	CI[a] (ECP)
1^2A_1	0.000	0.000	0.000	0.000	0.000	0.000	0.000
1^2B_2	0.760	0.495	0.729	0.704	0.740	0.757	0.72
2^2A_1	0.896	0.751	0.898	0.768	0.910	0.836	0.90
2^2B_2	1.061	0.937	1.033	1.006	1.087	1.054	1.20
1^2B_1	1.154	1.312	1.269	1.304	1.277	1.299	1.20
3^2B_2	1.167	1.064	1.137	1.086	1.162	1.168	1.32
3^2A_1	1.310	1.137	1.247	1.221	1.313	1.192	1.20
4^2A_1	1.523	1.392	1.525	1.478	1.615	1.447	1.72
5^2A_1	1.650	1.725	1.616	1.610	1.690	1.637	1.87
4^2B_2	1.914	2.146	1.942	1.966	2.067	1.864	1.92
5^2B_2	1.926	2.160	1.989	2.159	2.146	2.169	1.97
6^2A_1	1.958	1.949	1.928	1.904	2.058	1.984	1.94
6^2B_2	2.011	2.186	2.029	2.253	2.177	2.257	2.13
2^2B_1	2.022	2.291	2.051	2.183	2.191	2.352	2.06
7^2A_1	2.168	2.282	2.202	2.200	2.364	2.290	2.21
8^2A_1	2.230	2.516	2.238	2.521	2.440	2.530	2.33
3^2B_1	2.247	2.492	2.337	2.356	2.559	2.593	2.28
7^2B_2	2.282	2.325	2.286	2.359	2.433	2.338	2.32
8^2B_2	2.377	2.518	2.341	2.432	2.501	2.477	2.35
9^2A_1	2.392	2.539	2.394	2.542	2.541	2.577	2.41
4^2B_1	2.402	2.661	2.462	2.655	2.636	2.717	2.55
10^2A_1	2.411	2.631	2.475	2.644	2.663	2.687	2.65
9^2B_2	2.450	2.619	2.434	2.701	2.644	2.496	2.52
5^2B_1	2.460	2.754	2.40	2.767	2.693	2.897	2.58
10^2B_2	2.564	2.756	2.585	2.855	2.798	2.652	2.68
11^2B_2	2.650	2.799	2.660	3.142	2.862	2.944	2.73
11^2A_1	2.712	2.995	2.735	2.782	2.972	2.807	2.81
12^2A_1	2.764	3.156	2.894	2.954	3.181	2.976	2.91
13^2A_1	2.800	3.248	2.989	3.076	3.278	3.224	2.93
6^2B_1	2.802	3.153	3.058	2.900	3.627	3.652	2.84
7^2B_1	3.081	3.530	3.309	3.427	3.822	3.905	2.90
8^2B_1	3.100	3.741	3.544	3.531	3.961	4.016	3.02

[a] Results are taken from Ref. [15].

Table LVI. Sodium hexamer ($C_{5V} \rightarrow C_S$) singlet vertical excitation energies (eV) calculated with the all-electron and the MCP and with different functionals in comparison with other theoretical results.

	Vertical excitation energies (eV)					
State	LSDxc/ TDLSDxc (AE)	LSDxc/ TDLSDxc (MCP+)	LB94xc/ TDLSDxc (MCP+)	LSDxc/ TDLSDxc (MCP)	LB94xc/ TDLSDxc (MCP)	CI[a] (ECP)
$1^1A'$	0.000	0.000	0.000	0.000	0.000	0.000
$2^1A'$	1.232	1.236	1.253	1.269	1.216	1.45
$1^1A''$	1.232	1.236	1.251	1.269	1.216	1.37
$2^1A''$	1.489	1.469	1.484	1.501	1.441	1.52
$3^1A'$	1.489	1.469	1.484	1.501	1.441	1.50
$4^1A'$	1.666	1.712	1.908	1.800	1.911	1.81
$3^1A''$	1.666	1.712	1.906	1.800	1.911	1.82
$4^1A''$	2.168	2.229	2.339	2.404	2.381	2.08
$5^1A'$	2.192	2.246	2.340	2.410	2.366	1.96
$5^1A''$	2.192	2.246	2.408	2.430	2.483	2.09
$6^1A'$	2.245	2.268	2.352	2.430	2.381	2.10
$7^1A'$	2.278	2.327	2.414	2.436	2.515	2.12
$6^1A''$	2.278	2.327	2.415	2.436	2.515	2.21
$8^1A'$	2.563	2.584	2.556	2.709	2.558	2.17
$7^1A''$	2.563	2.584	2.555	2.709	2.558	2.29
$8^1A''$	2.591	2.647	2.715	2.923	2.802	2.43
$9^1A'$	2.591	2.647	2.715	2.923	2.802	2.51
$10^1A'$	2.608	2.730	2.754	3.048	3.028	2.53
$9^1A''$	2.608	2.730	2.754	3.057	3.009	2.50
$10^1A''$	2.614	2.759	2.793	3.069	3.028	2.59
$11^1A'$	2.702	2.820	2.825	3.069	3.052	2.57
$12^1A'$	2.851	2.977	2.877	3.361	3.245	2.60
$11^1A''$	2.851	2.977	2.824	3.361	3.245	2.65
$13^1A'$	3.043	3.115	3.122	3.389	3.251	2.78
$14^1A'$	3.061	3.219	3.264	3.750	3.712	2.85

[a] CI results are estimated from Ref. [15].

Table LVII. Sodium hexamer ($D_{3h} \rightarrow C_{2v}$) singlet vertical excitation energies (eV) calculated with the all-electron and the MCP and with different functionals in comparison with other theoretical results.

	Vertical excitation energies (eV)					
State	LSDxc/ TDLSDxc (AE)	LSDxc/ TDLSDxc (MCP+AE)	LB94xc/ TDLSDxc (MCP+AE)	CI[a] (ECP)	MCLR[b] (ECP)	RPA[b] (ECP)
1^1A_1	0.000	0.000	0.000	0.00	0.00	0.00
2^1A_1	1.326	1.384	1.384	1.59	1.63	1.80
1^1B_2	1.437	1.500	1.516	1.50	1.63	1.69
3^1A_1	1.561	1.608	1.707	1.66	1.82	2.12
2^1B_2	1.613	1.670	1.691	1.75	1.75	1.80
1^1B_1	1.618	1.689	1.708	1.85	2.04	1.92
3^1B_2	2.146	2.238	2.380	2.13	2.02	2.24
4^1A_1	2.153	2.250	2.394	2.17	2.05	2.24
4^1B_2	2.501	2.503	2.755	2.25	2.13	2.85
2^1B_1	2.431	2.531	2.622	2.53	2.78	2.83
5^1A_1	2.359	2.558	2.638	2.22	2.13	2.84
6^1A_1	2.413	2.591	2.777	2.25	2.42	2.87
5^1B_2	2.530	2.612	2.875	2.36	2.49	2.99
3^1B_1	2.495	2.617	2.660	2.58	2.81	2.85
6^1B_2	2.741	2.666	3.040	2.41	2.71	3.15
7^1A_1	2.458	2.711	3.020	2.56	2.50	3.15
8^1A_1	2.588	2.801	3.098	2.58	2.72	3.22
7^1B_2	3.019	2.880	3.179	2.57	2.76	3.22
8^1B_2	3.169	3.206	3.453	2.78	2.79	3.38
9^1A_1	3.015	3.210	3.444	2.89	2.79	3.38
10^1A_1	3.019	3.246	3.466	2.97	2.93	3.48
4^1B_1	3.095	3.427	3.524	2.98	3.26	3.36
5^1B_1	3.179	3.444	3.584	3.09	3.33	3.63
6^1B_1	3.327	3.644	3.660	3.23	3.49	3.75
7^1B_1	3.413	3.718	3.742	3.35	3.66	3.84
11^1A_1	3.107	3.724	3.870	3.04	3.17	3.59
9^1B_2	3.272	3.756	3.953	2.99	3.16	3.48
10^1B_2	3.294	3.770	3.966	3.00	3.21	3.51
12^1A_1	3.175	3.804	4.012	3.10		
8^1B_1	3.504	3.805	3.875	3.41	3.70	4.07
11^1B_2	3.310	3.844	4.056	3.22		
12^1B_2	3.396	3.888	4.076	3.33		

[a] CI results are estimated from Ref. [15].

[b] Results are taken from Ref. [11].

Table LVIII. Comparison of experimental ionization potential and $-\varepsilon_{HOMO}$ of sodium clusters from the dimer up to the hexamer calculated by the all-electron and the MCP with the LSDxc and the LB94xc functionals.

	$-\varepsilon^{\alpha}_{HOMO}$ (eV)						
Clusters	LSDxc (MCP)	LSDxc (MCP+)	LSDxc (AE)	LB94xc (AE)	LB94xc (MCP+)	LB94xc (MCP)	EXPT[a] (I.P.)
Na_2	3.28	3.21	3.21	5.88	5.97		4.87
Na_3	2.65	2.60	2.60	5.09			3.97
Na_4	2.82	2.74	2.75	5.27	5.01	4.97	4.27
Na_5	2.84	2.77	2.77	5.21	4.79	4.59	4.05
$Na_6(C_{5v})$	3.18	3.08	3.08		5.18	5.01	4.12
$Na_6(D_{3h})$		3.13	3.11		5.55		4.12

[a] Experimental ionization potentials are taken from Ref. [6].

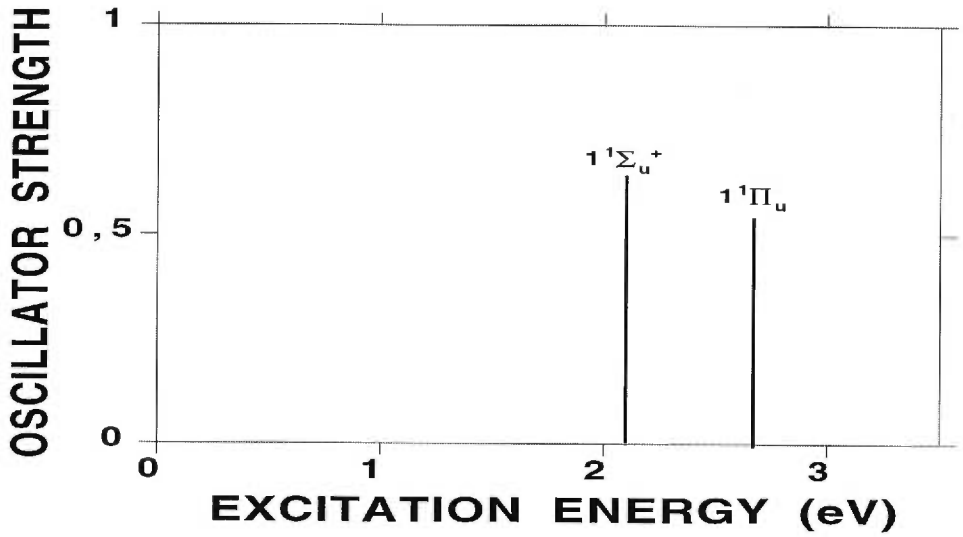

Figure 49. Absorption spectrum of the sodium dimer carried out at the all-electron level with the all-electron optimized geometry using the LS-Dxc/TDLSDxc functional and the BASIS1.

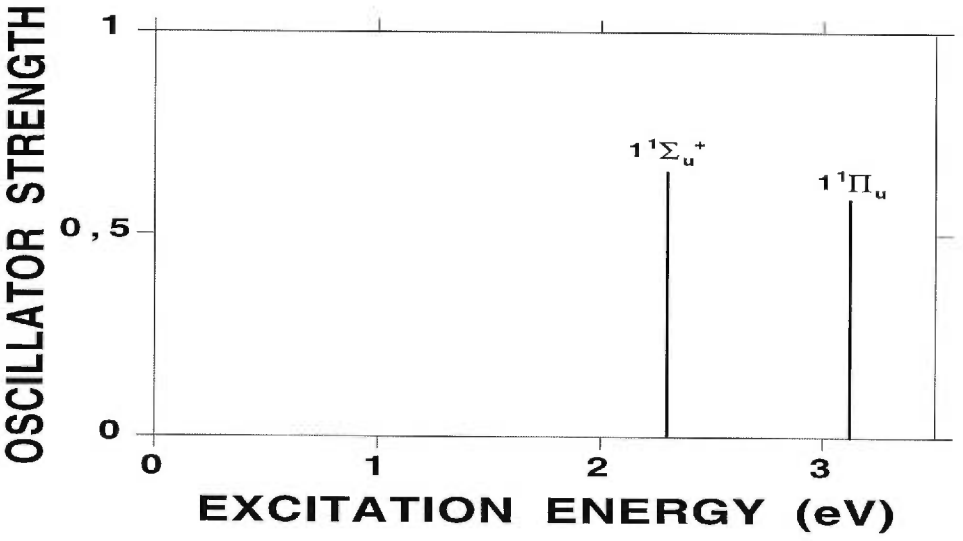

Figure 50. Absorption spectrum of the sodium dimer carried out at the all-electron level with the all-electron optimized geometry using the LB94xc/TDLSDxc functional and the BASIS1.

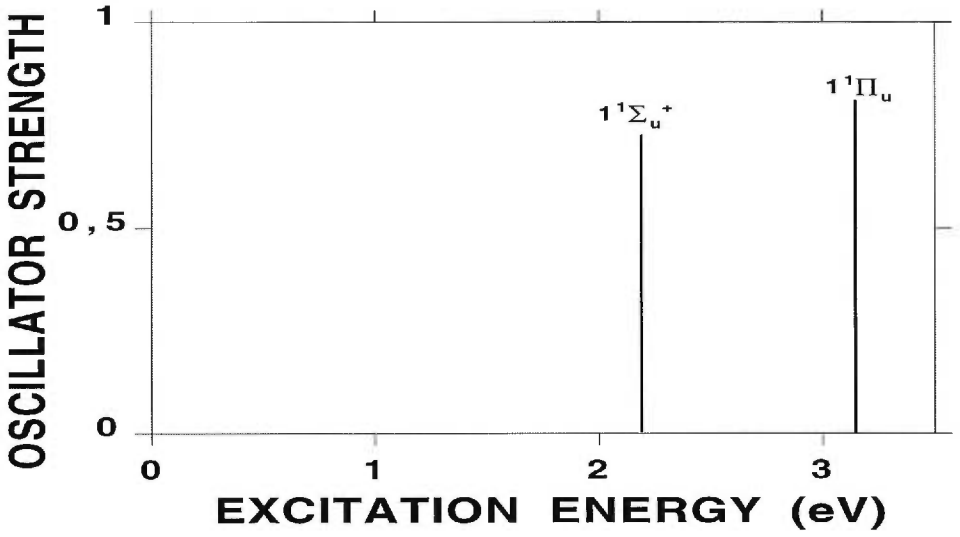

Figure 51. Absorption spectrum of the sodium dimer carried out at the MCP level with the MCP optimized geometry using the LSDxc/TDLSDxc functional and the MCP basis.

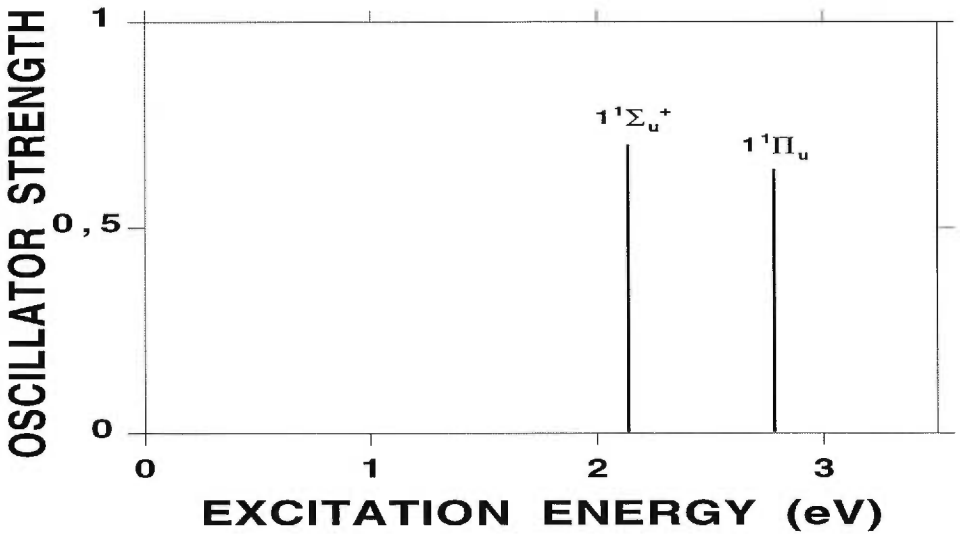

Figure 52. Absorption spectrum of the sodium dimer carried out at the MCP level with the MCP optimized geometry using the LSDxc/TDLSDxc functional and the MCP+ basis.

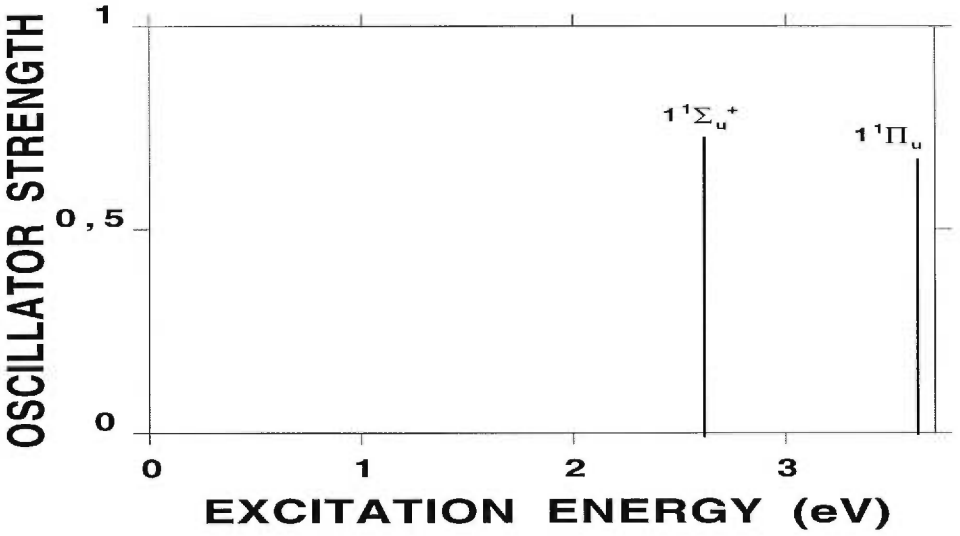

Figure 53. Absorption spectrum of the sodium dimer carried out at the MCP level with the MCP optimized geometry using the LB94xc/TDLSDxc functional and the MCP+ basis.

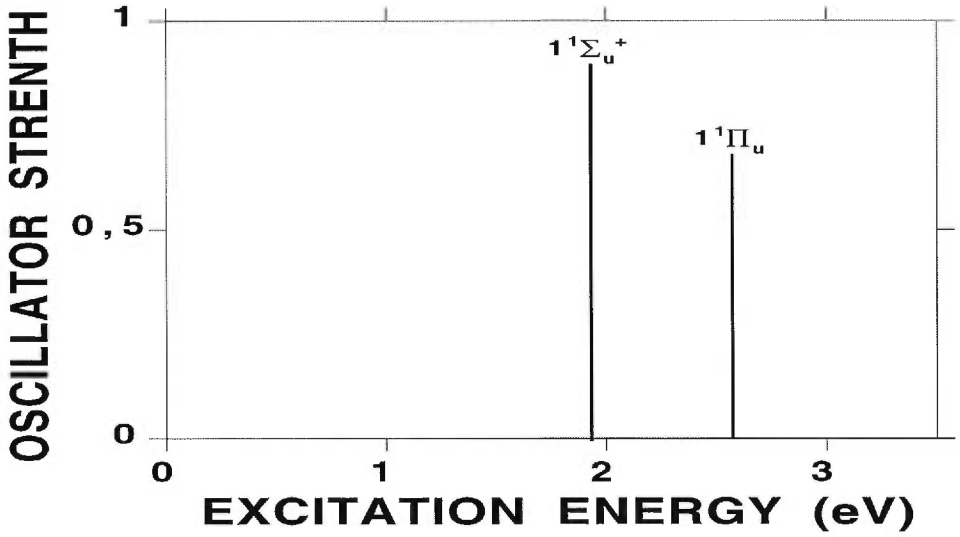

Figure 54. Absorption spectrum of the sodium dimer carried out with the CI method. Taken from Ref. [13].

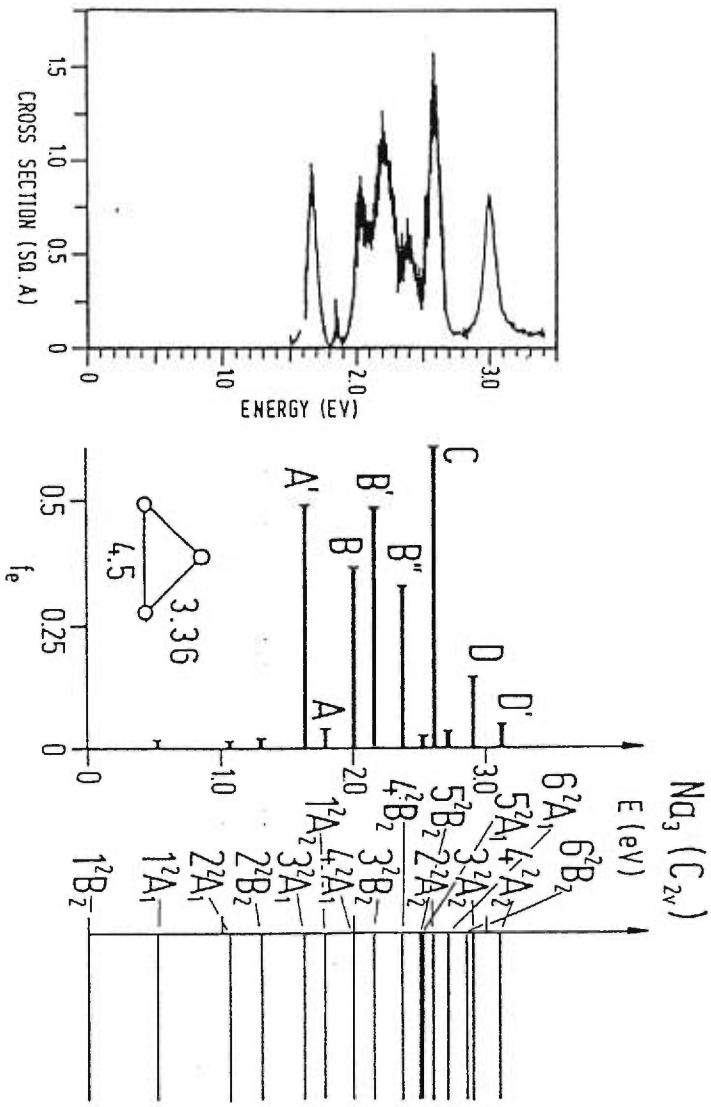

Figure 55. Comparison of absorption spectrum of the sodium trimer between the CI prediction and the experiment. The results are taken from Ref. [14].

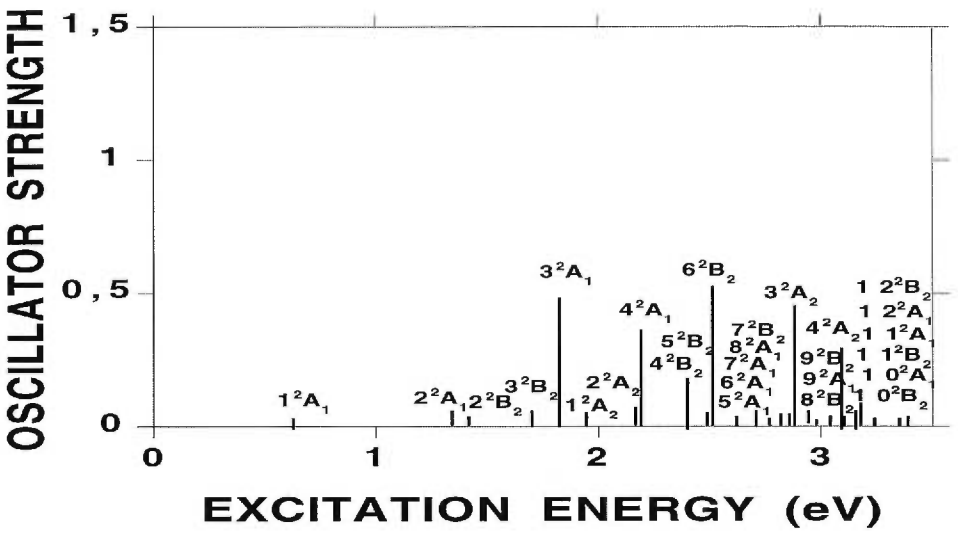

Figure 56. Absorption spectrum of the sodium trimer carried out at the all-electron level with the all-electron optimized obtuse geometry using the LS-Dxc/TDLSDxc functional and the BASIS1.

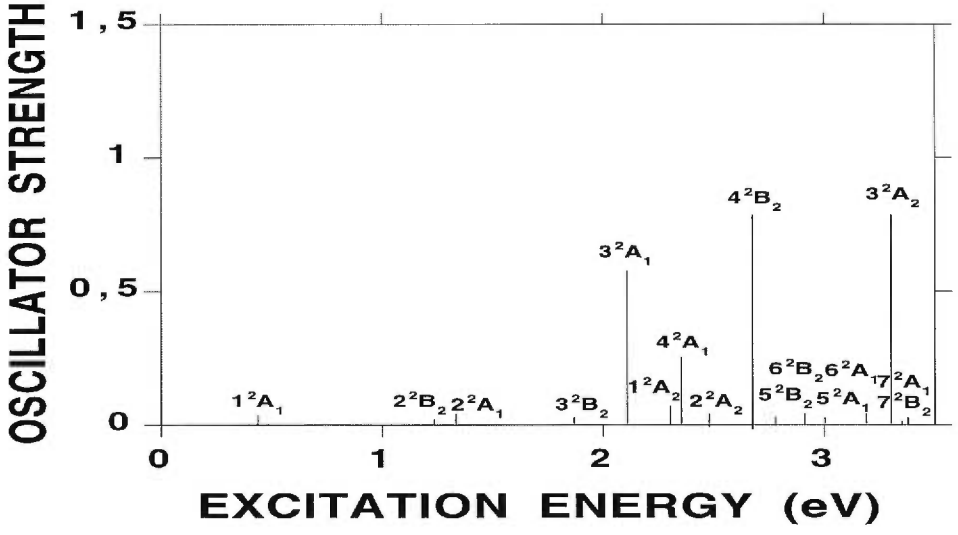

Figure 57. Absorption spectrum of the sodium trimer carried out at the all-electron level with the all-electron optimized obtuse geometry using the LB94xc/TDLSDxc functional and the BASIS1.

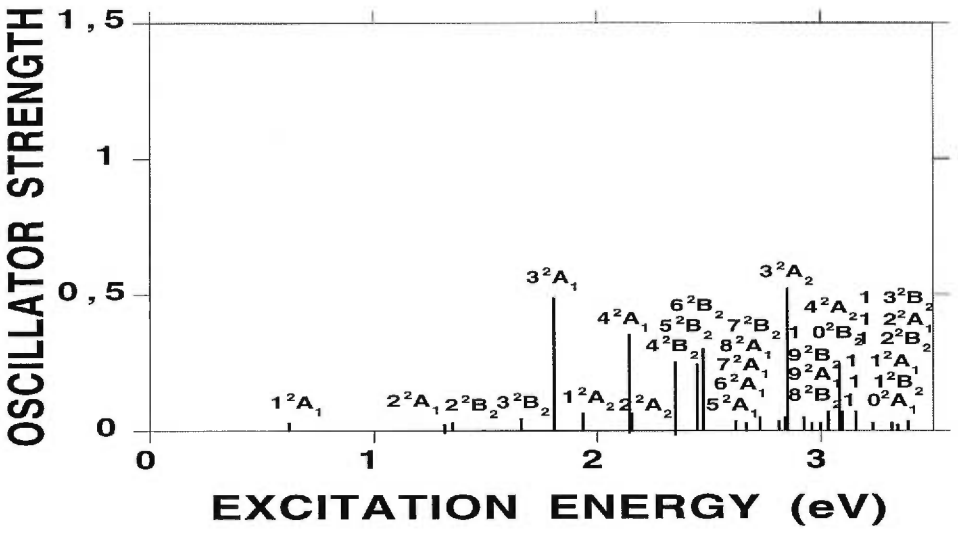

Figure 58. Absorption spectrum of the sodium trimer carried out at the all-electron level with the MCP optimized obtuse geometry using the LS-Dxc/TDLSDxc functional and the BASIS1.

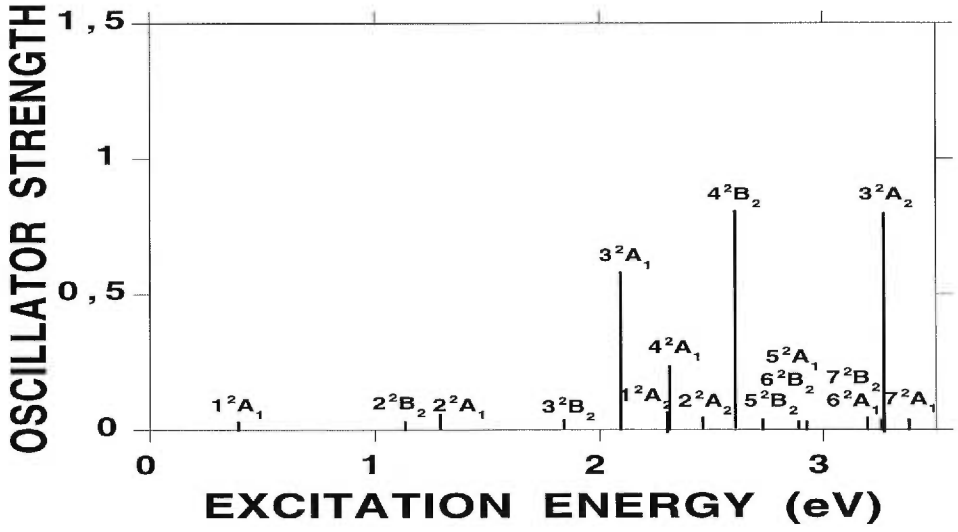

Figure 59. Absorption spectrum of the sodium trimer carried out at the all-electron level with the MCP optimized obtuse geometry using the LB94xc/TDLSDxc functional and the BASIS1.

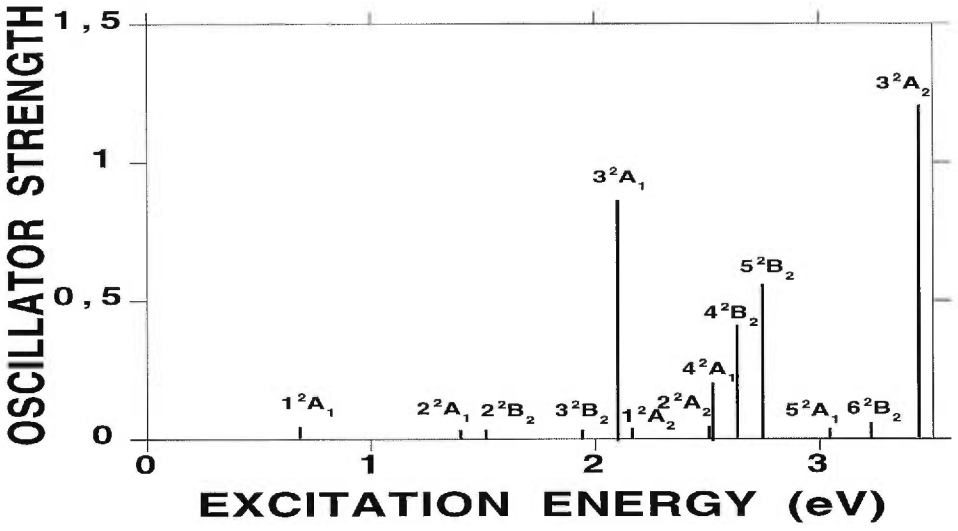

Figure 60. Absorption spectrum of the sodium trimer carried out at the MCP level with the MCP optimized obtuse geometry using the LSDxc/TDLSDxc functional and the MCP basis.

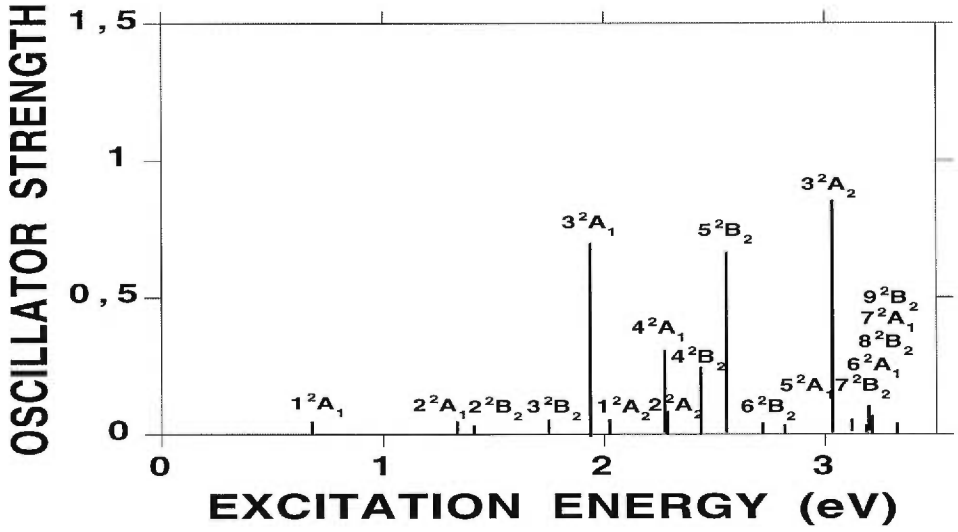

Figure 61. Absorption spectrum of the sodium trimer carried out at the MCP level with the MCP optimized obtuse geometry using the LSDxc/TDLSDxc functional and the MCP+ basis.

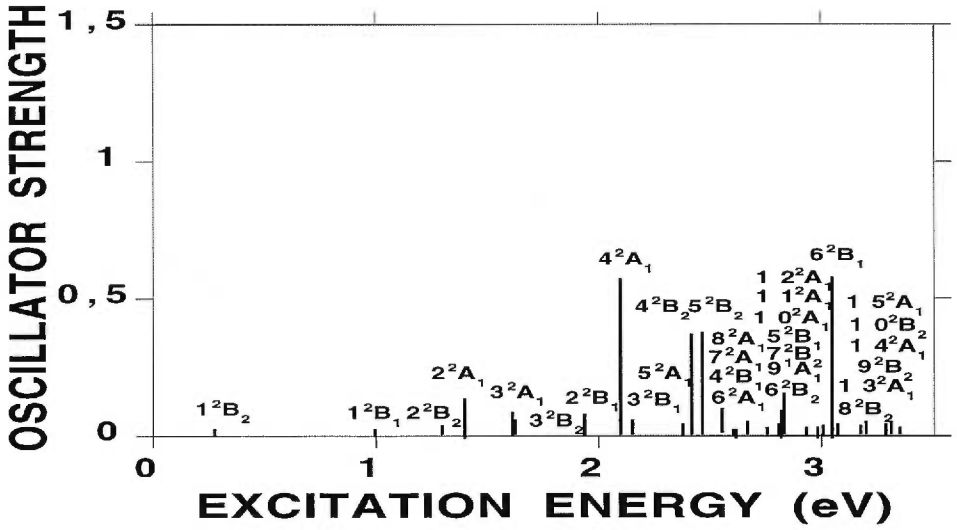

Figure 62. Absorption spectrum of the sodium trimer carried out at the all-electron level with the all-electron optimized acute geometry using the LS-Dxc/TDLSDxc functional and the BASIS1.

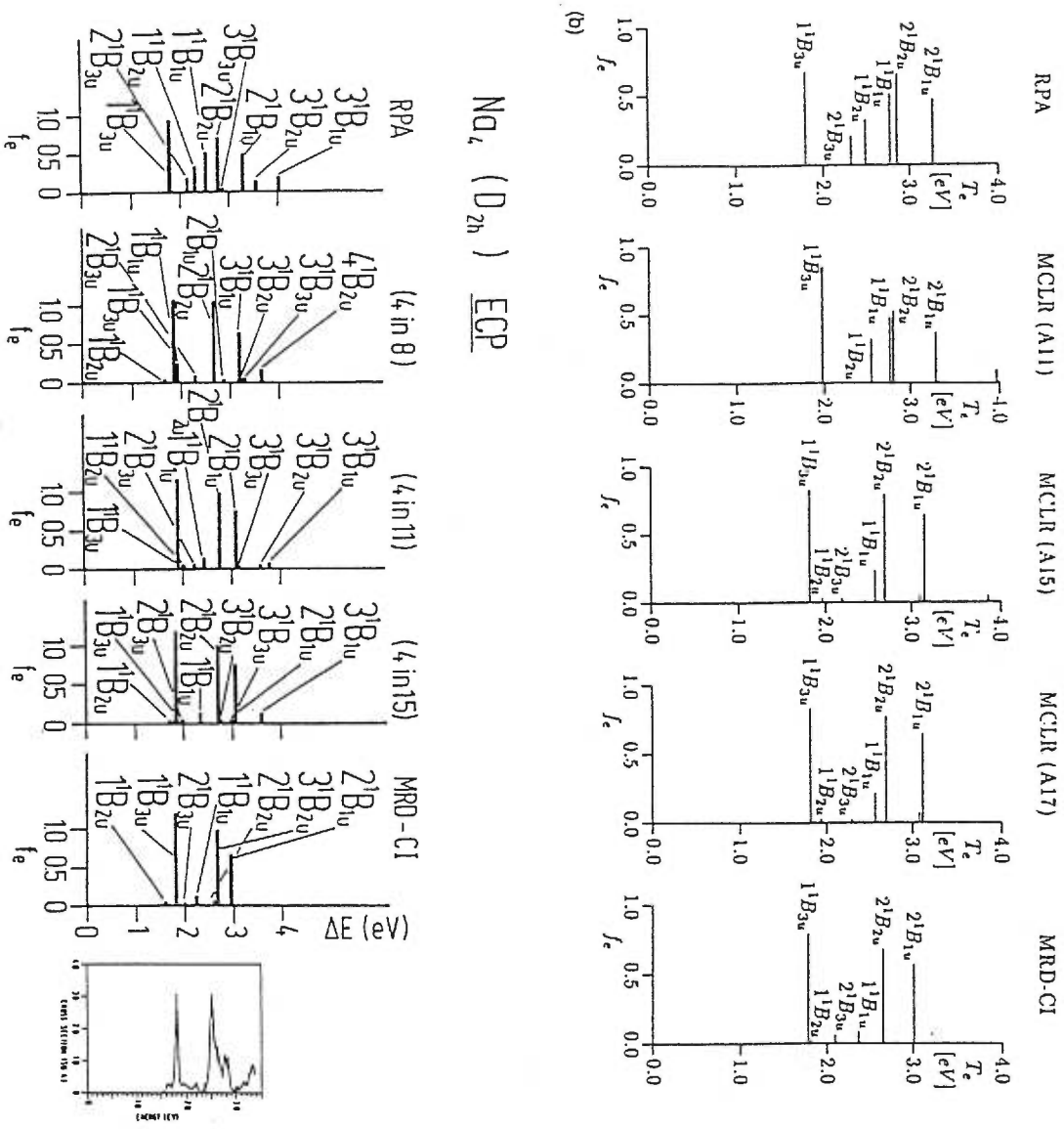

Figure 63. Comparison of absorption spectrum of the sodium tetramer between the recorded and the predicted all-electron MRD-CI, all-electron MCLR, and all-electron RPA results, taken from Ref. [14, 11] (right side graphs). And between predicted by ECP MRD-CI, ECP MCLR, and ECP RPA results, taken from Ref. [11] (left side graphs).

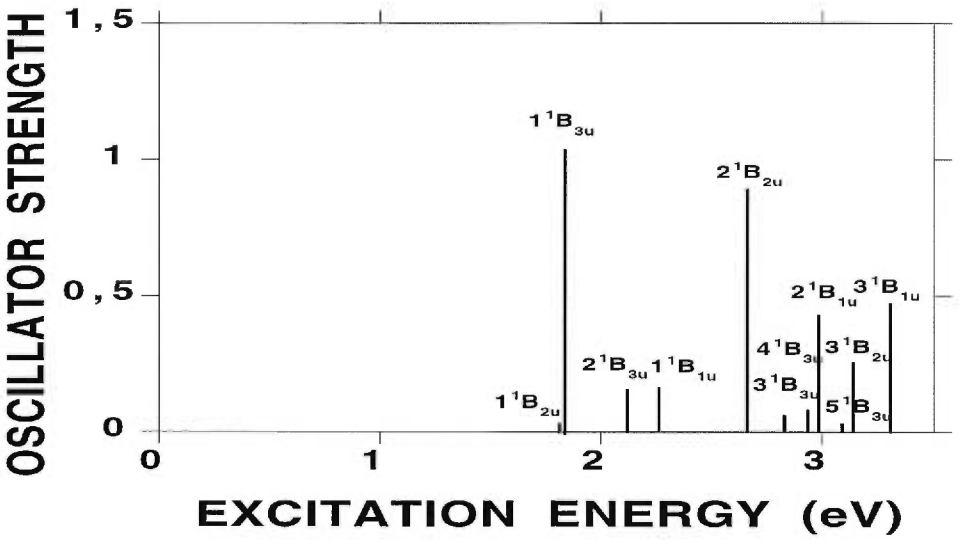

Figure 64. Absorption spectrum of the sodium tetramer performed at the all-electron level with the all-electron optimized geometry using the LS-Dxc/TDLSDxc functional and the BASIS1.

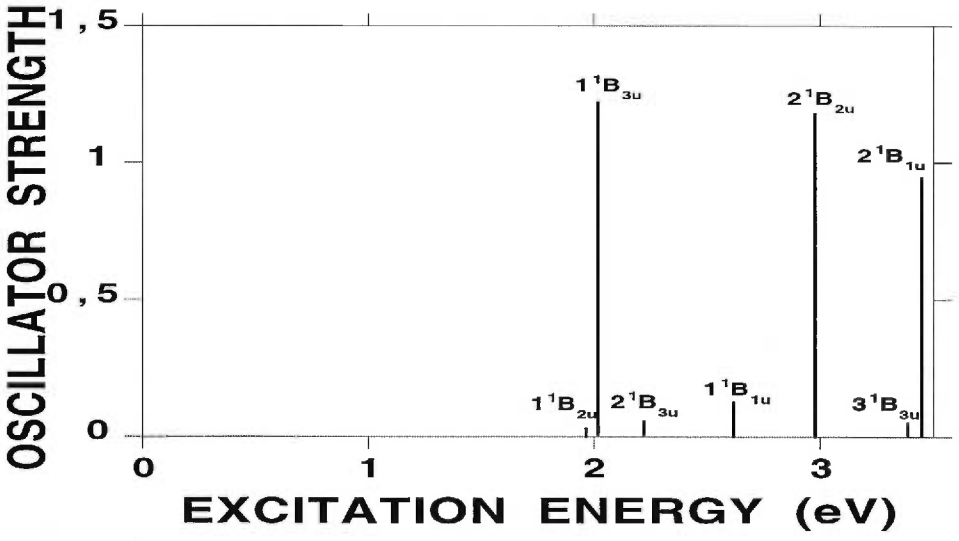

Figure 65. Absorption spectrum of the sodium tetramer performed at the all-electron level with the all-electron optimized geometry using the LB94xc/TDLSDxc functional and the BASIS1.

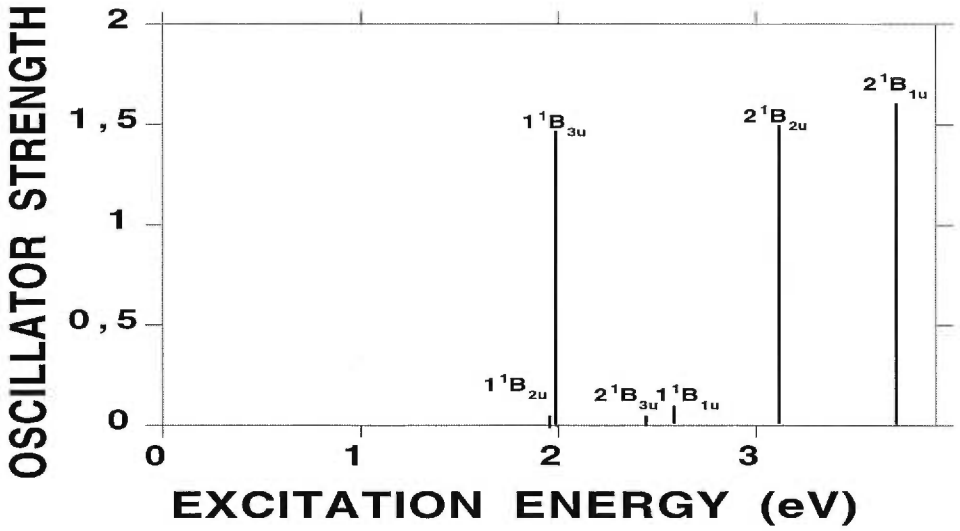

Figure 66. Absorption spectrum of the sodium tetramer performed at the MCP level with the MCP optimized geometry using the LSDxc/TDLSDxc functional and the MCP basis.

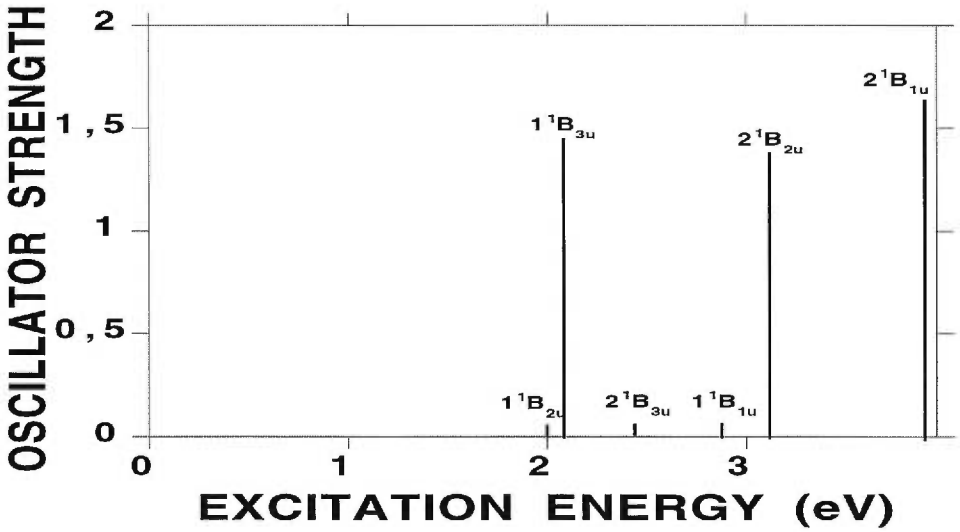

Figure 67. Absorption spectrum of the sodium tetramer performed at the MCP level with the MCP optimized geometry using the LB94xc/TDLSDxc functional and the MCP basis.

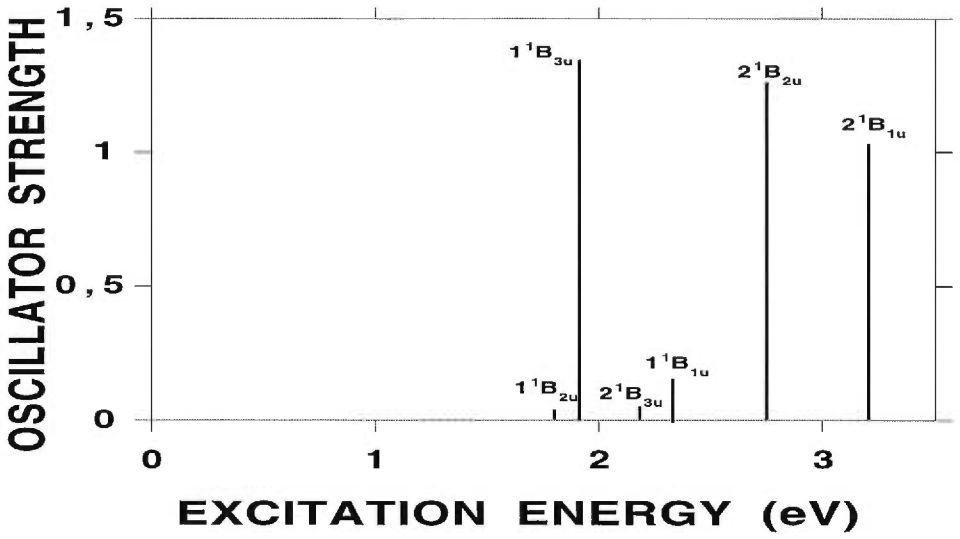

Figure 68. Absorption spectrum of the sodium tetramer performed at the MCP level with the MCP optimized geometry using the LSDxc/TDLSDxc functional and the MCP+ basis.

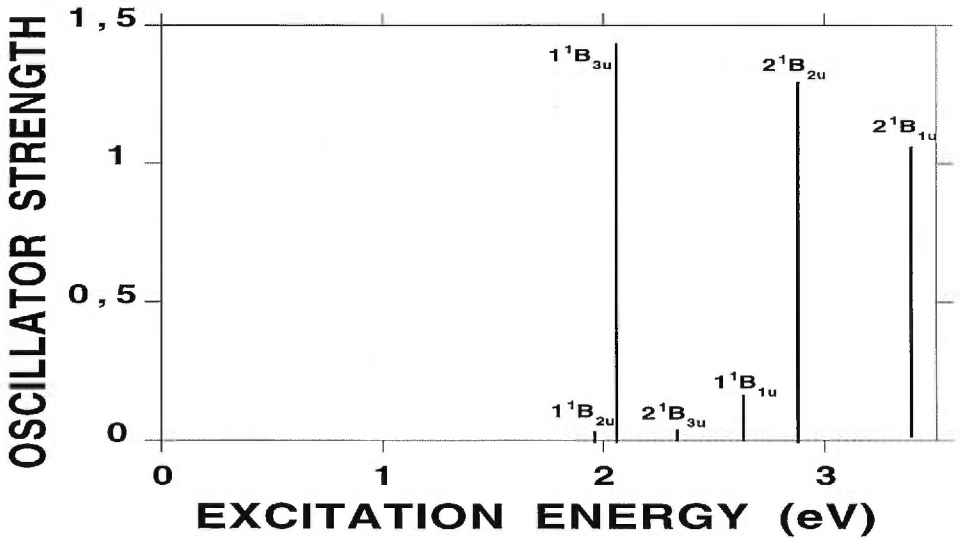

Figure 69. Absorption spectrum of the sodium tetramer performed at the MCP level with the MCP optimized geometry using the LB94xc/TDLSDxc functional and the MCP+ basis.

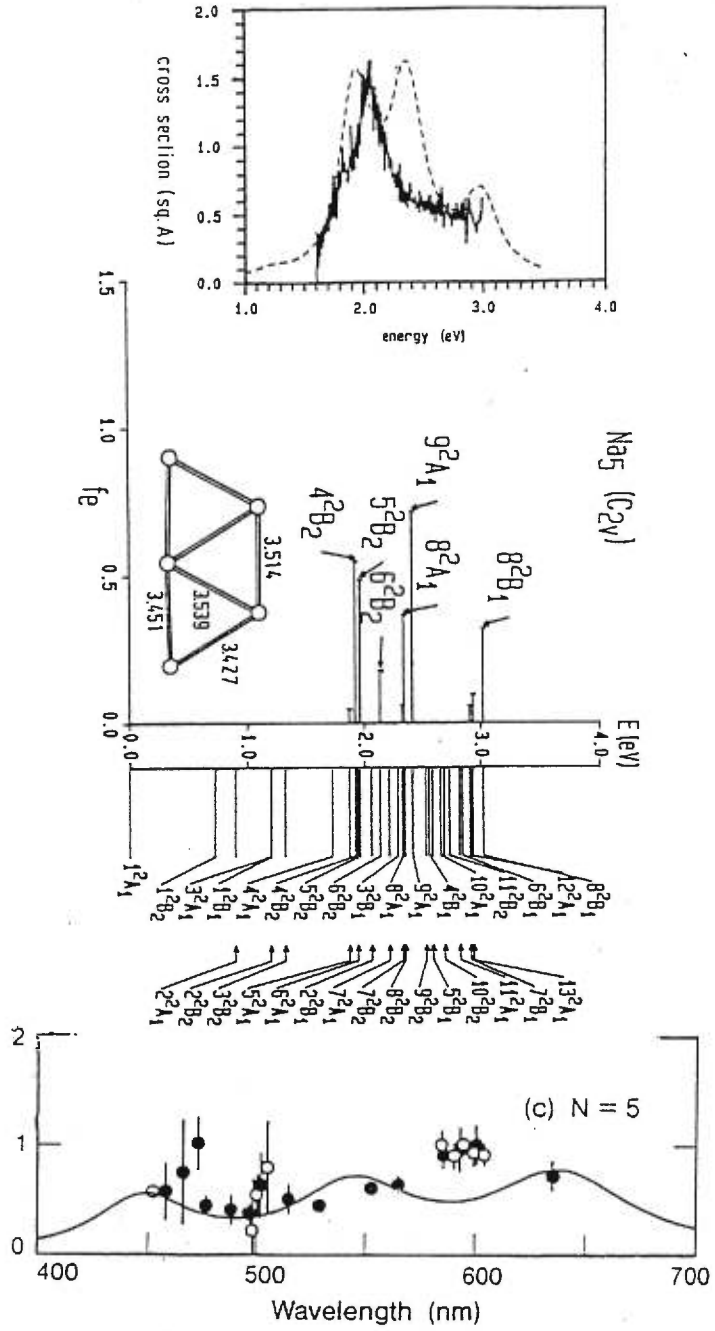

Figure 70. Comparison of absorption spectrum of the sodium pentamer between the recorded and predicted ECP CI results, taken from Ref. [15] (top two graphs) and other recorded spectrum taken from Ref.[16] (bottom graph) in which the circles are experimental results and the solid line is calculated with the ellipsoidal shell model.

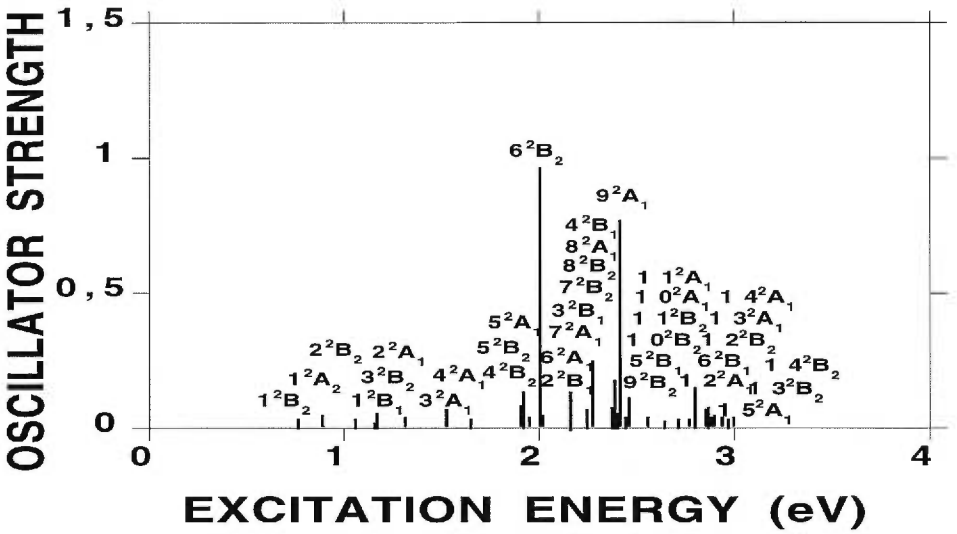

Figure 71. Absorption spectrum of the sodium pentamer calculated at the all-electron level with the all-electron optimized geometry using the LS-Dxc/TDLSDxc functional and the BASIS1.

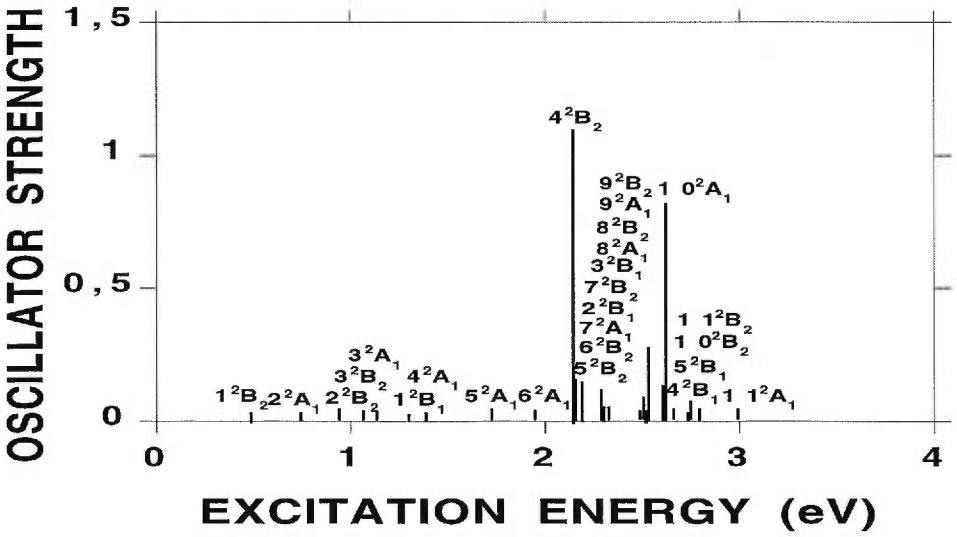

Figure 72. Absorption spectrum of the sodium pentamer calculated at the all-electron level with the all-electron optimized geometry using the LB94xc/TDLSDxc functional and the BASIS1.

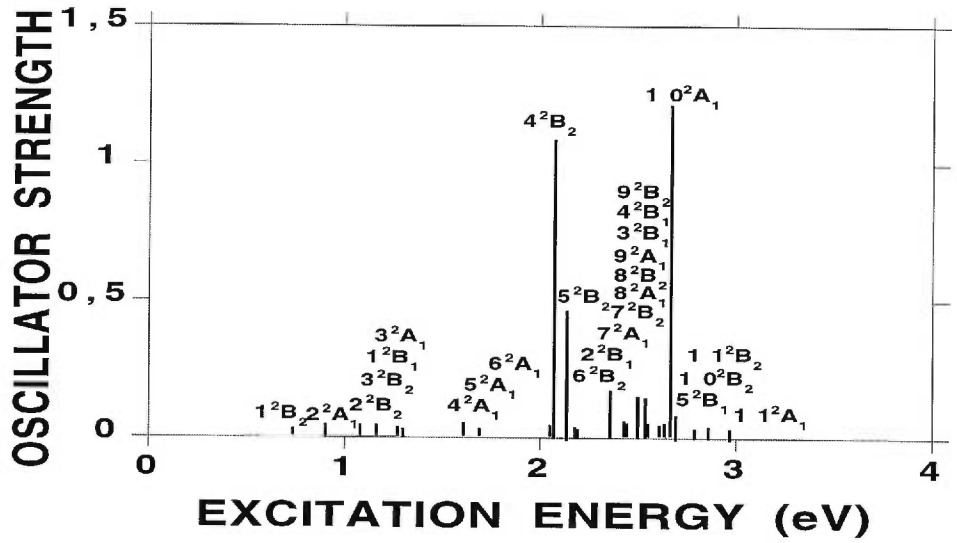

Figure 73. Absorption spectrum of the sodium pentamer calculated at the MCP level with the MCP optimized geometry using the LSDxc/TDLSDxc functional and the MCP basis.

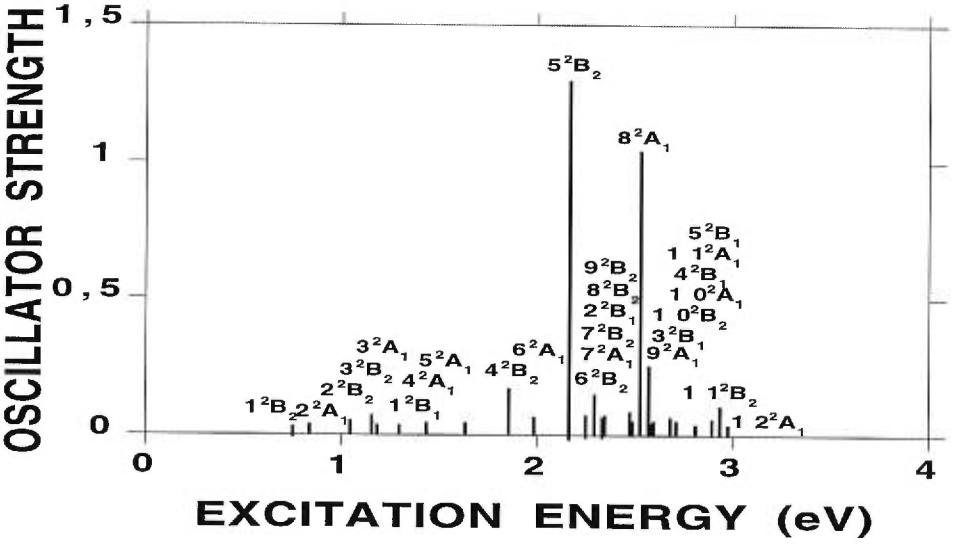

Figure 74. Absorption spectrum of the sodium pentamer calculated at the MCP level with the MCP optimized geometry using the LB94xc/TDLSDxc functional and the MCP basis.

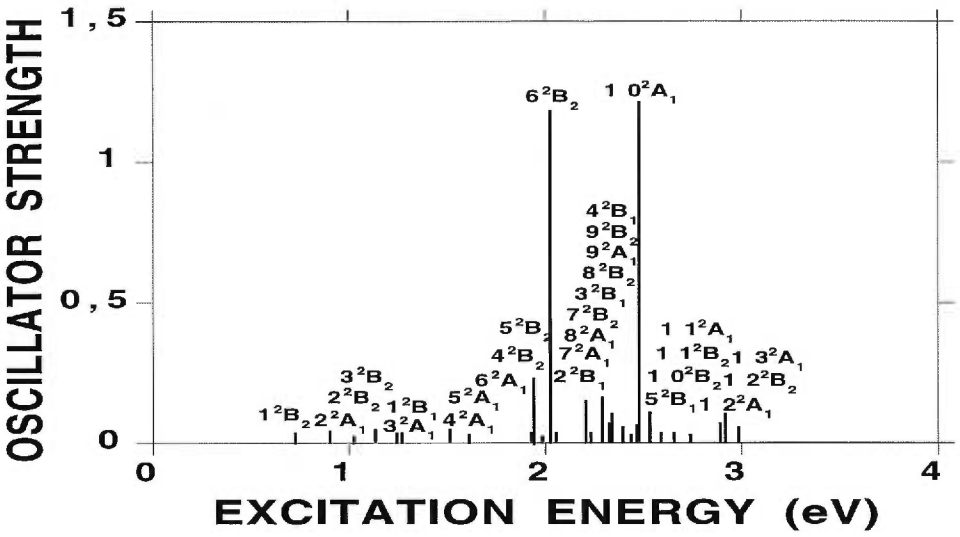

Figure 75. Absorption spectrum of the sodium pentamer calculated at the MCP level with the MCP optimized geometry using the LSDxc/TDLSDxc functional and the MCP+ basis.

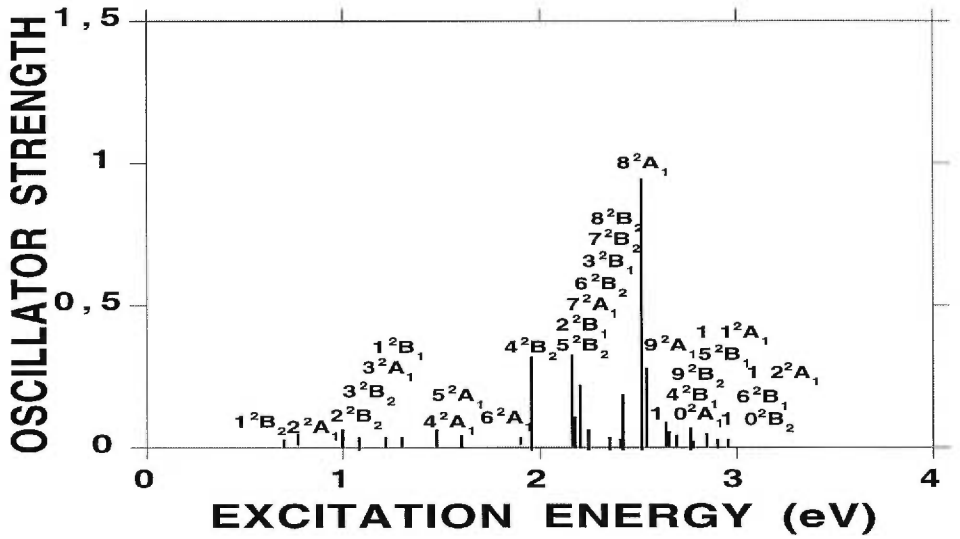

Figure 76. Absorption spectrum of the sodium pentamer calculated at the MCP level with the MCP optimized geometry using the LB94xc/TDLSDxc functional and the MCP+ basis.

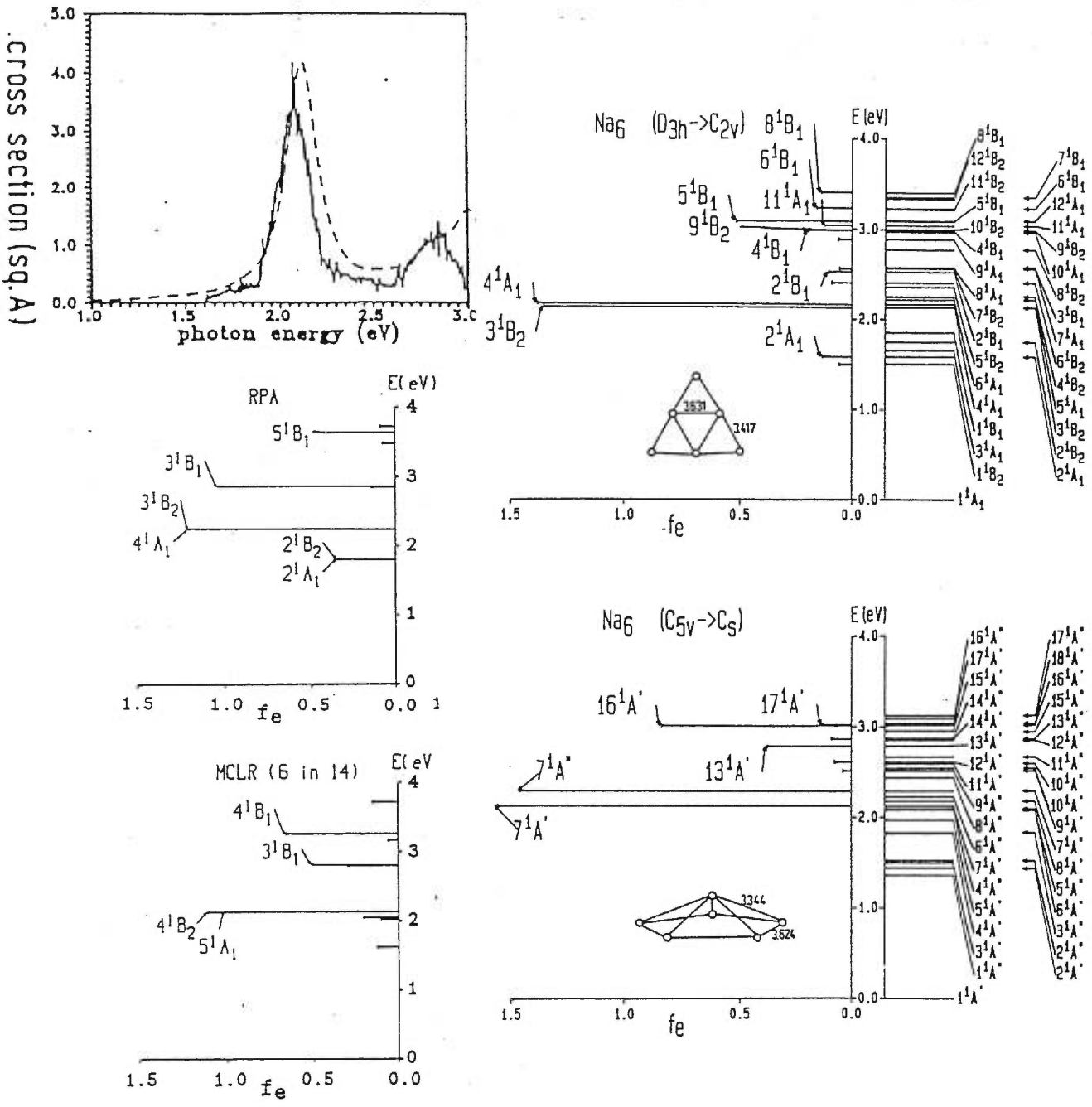

Figure 77. Comparison of the photodepletion spectrum and the ECP CI predicted spectrum for the two structures of the sodium hexamer, taken from Ref. [15] (right side graphs) and predicted by the ECP MCLR and the ECP RPA, taken from Ref. [11] (left side graphs).

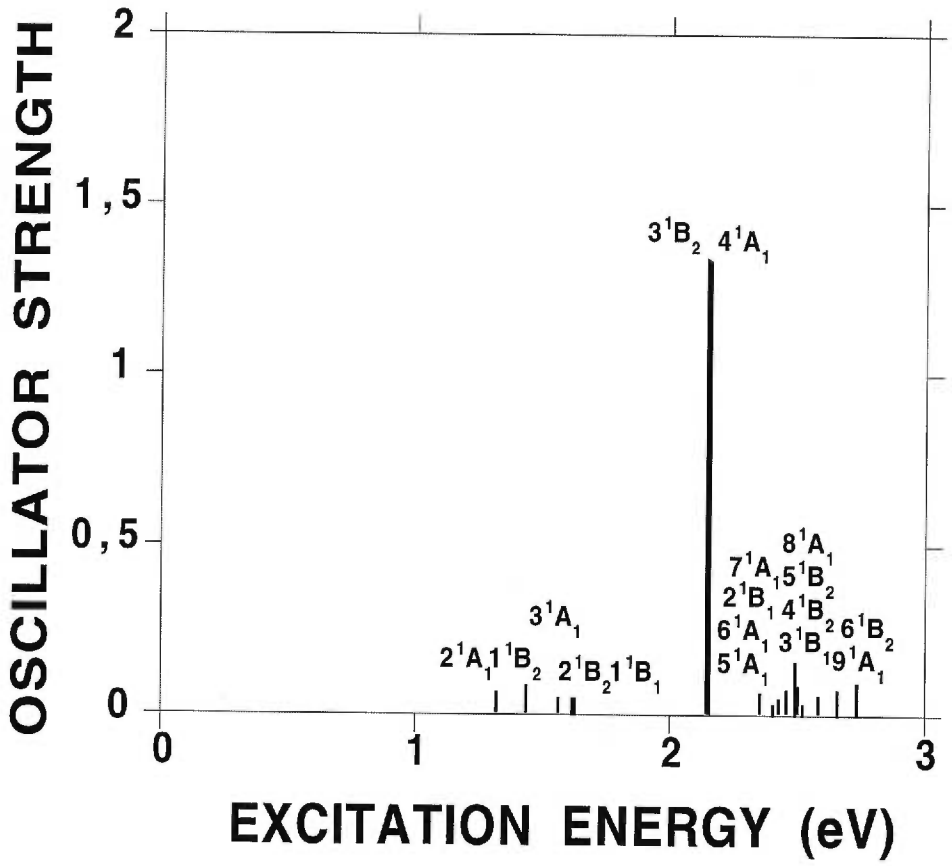

Figure 78. Absorption spectrum of the sodium hexamer ($D_{3h} \longrightarrow C_{2v}$) carried out at the all-electron level with the all-electron optimized geometry using the LSDxc/TDLSDxc functional and the BASIS1 basis.

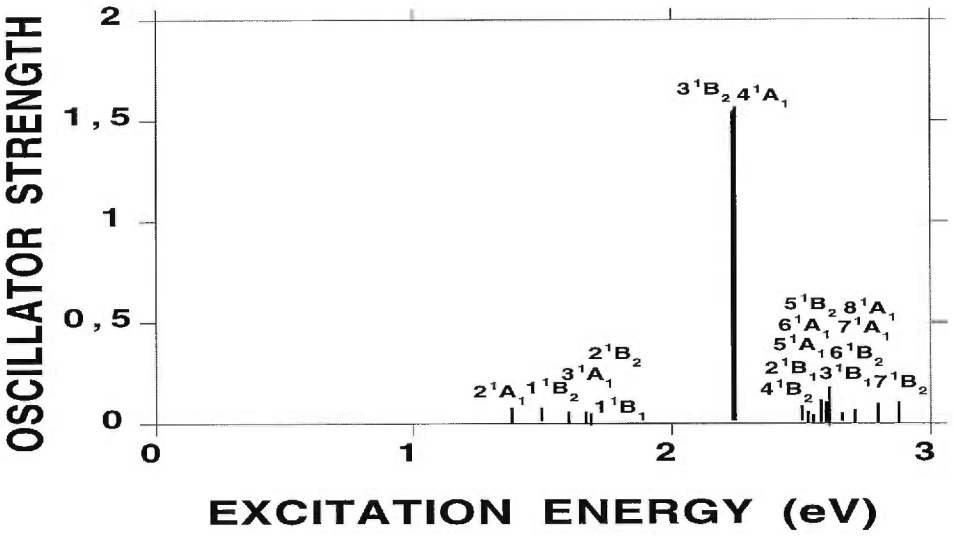

Figure 79. Absorption spectrum of the sodium hexamer ($D_{3h} \longrightarrow C_{2v}$) carried out at the MCP level with the all-electron optimized geometry using the LS-Dxc/TDLSDxc functional and the MCP+ basis.

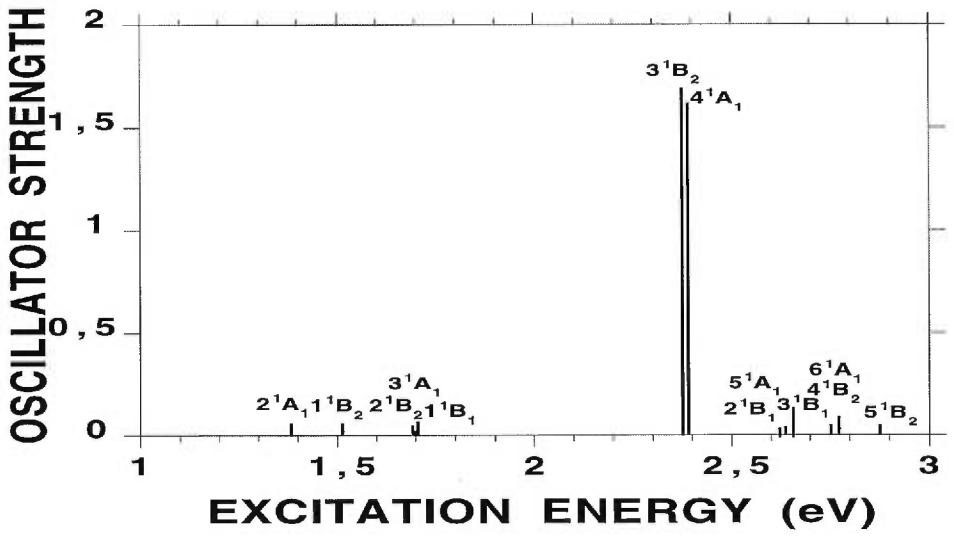

Figure 80. Absorption spectrum of the sodium hexamer ($D_{3h} \longrightarrow C_{2v}$) carried out at the MCP level with the all-electron optimized geometry using the LB94xc/TDLSDxc functional and the MCP+ basis.

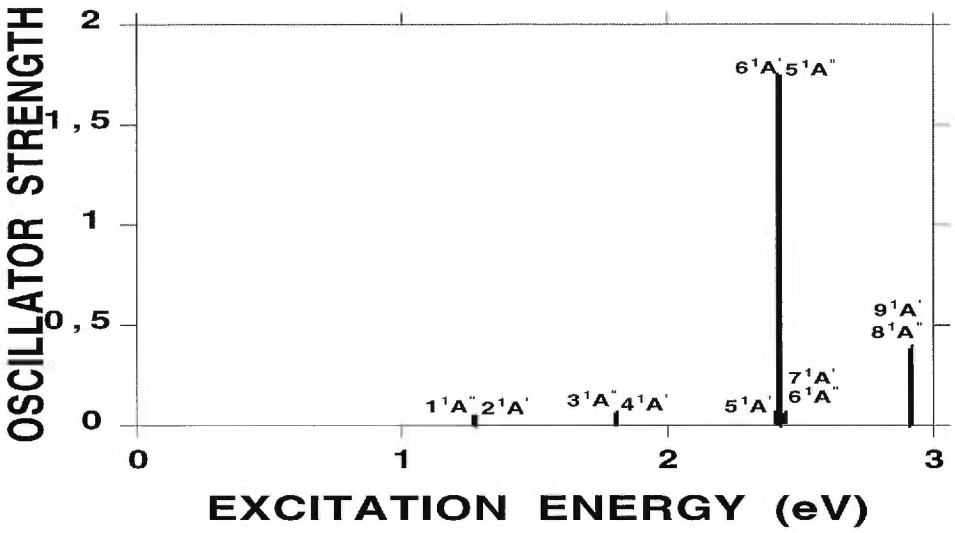

Figure 81. Absorption spectrum of the sodium hexamer ($C_{5v} \longrightarrow C_S$) carried out at the MCP level with the MCP optimized geometry using the LSDxc/TDLSDxc functional and the MCP basis.

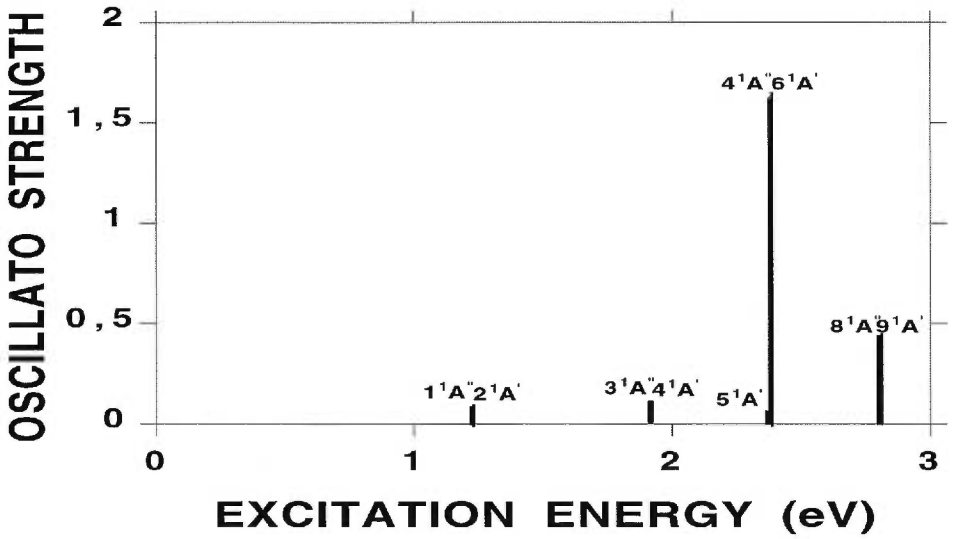

Figure 82. Absorption spectrum of the sodium hexamer ($C_{5v} \longrightarrow C_S$) carried out at the MCP level with the MCP optimized geometry using the LB94xc/TDLSDxc functional and the MCP basis.

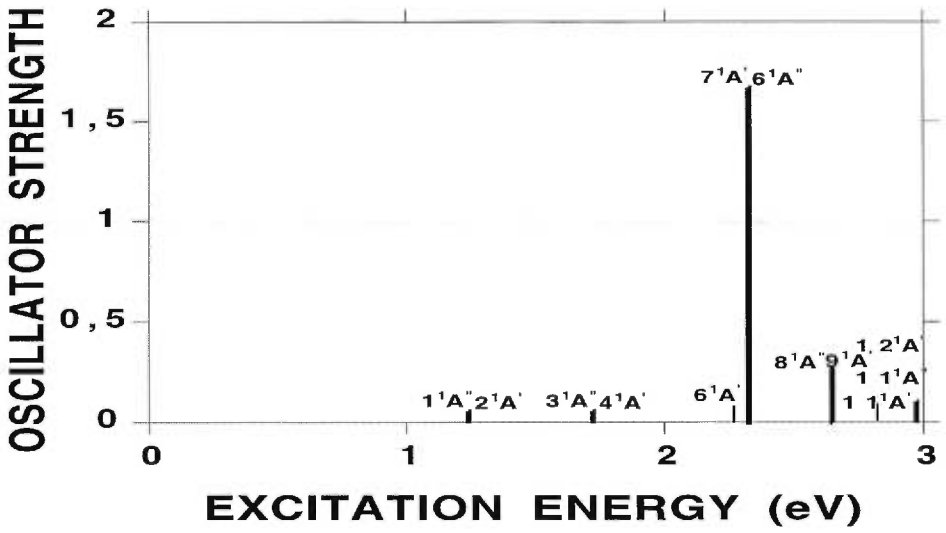

Figure 83. Absorption spectrum of the sodium hexamer ($C_{5v} \longrightarrow C_S$) carried out at the MCP level with the MCP optimized geometry using the LSDxc/TDLSDxc functional and the MCP+ basis.

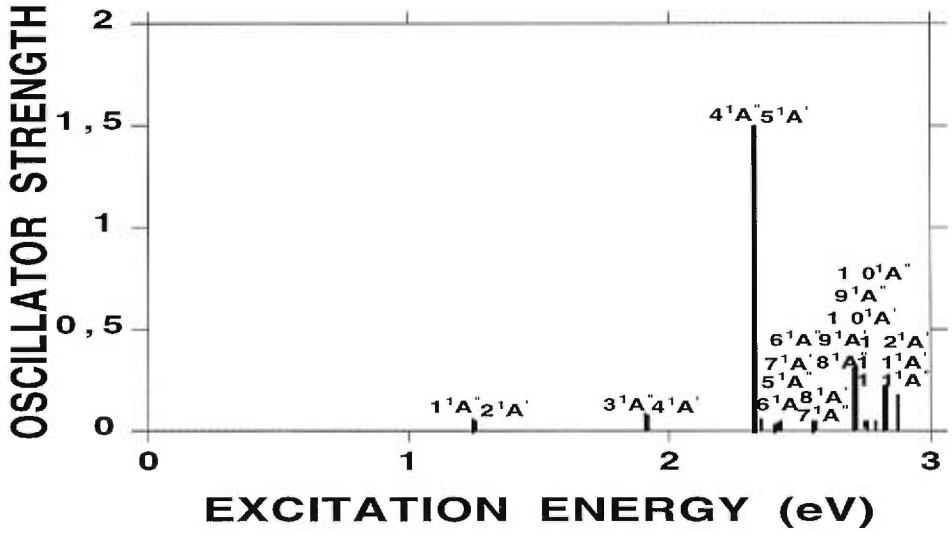

Figure 84. Absorption spectrum of the sodium hexamer ($C_{5v} \longrightarrow C_S$) carried out at the MCP level with the MCP optimized geometry using the LB94xc/TDLSDxc functional and the MCP+ basis.

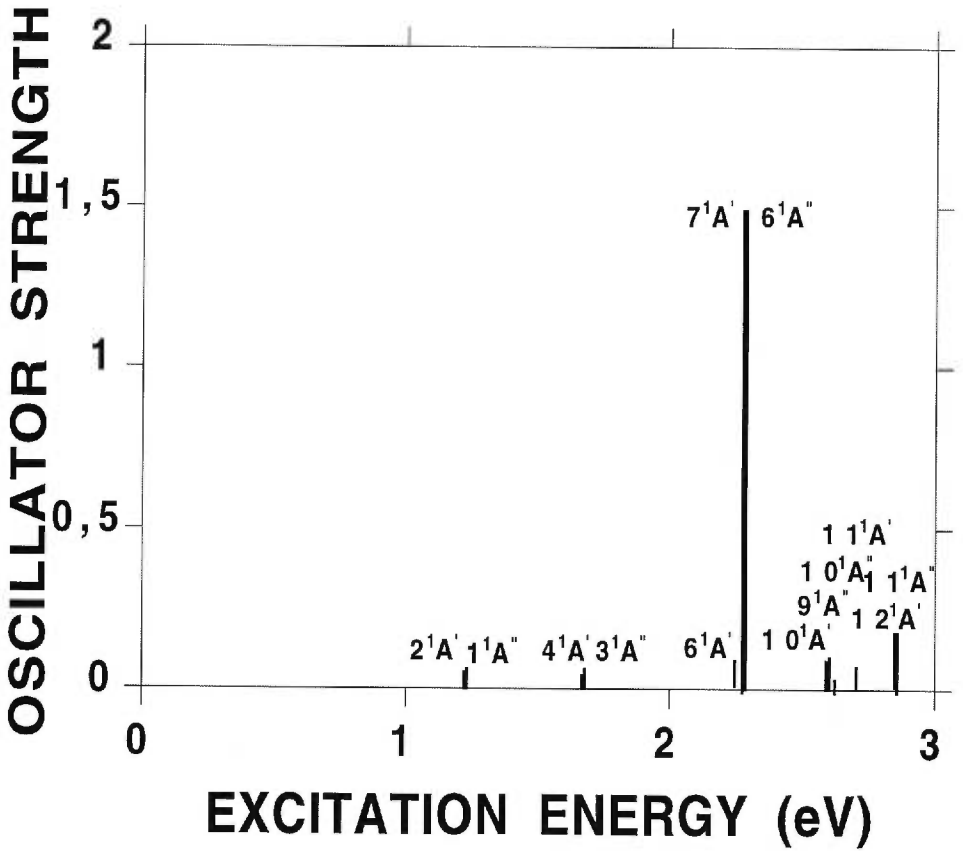

Figure 85. Absorption spectrum of the sodium hexamer ($C_{5v} \longrightarrow C_S$) carried out at the all-electron level with the all-electron optimized geometry using the LSDxc/TDLSDxc functional and the BASIS1.

CHAPTER 8

CONCLUSION AND PERSPECTIVE

The objective of the present work is to provide a new computational tool for the study of excited state properties (excitation energies, oscillator strengths, dynamic polarizabilities, etc.) of open–shell systems (molecules or clusters). To do so, time-dependent DFT for open–shell systems has been coded by the present work in version 2pX of the program *deMon-DynaRho*. As a case study, six small well studied open-shell molecules, three neutral molecules (BeH, BeF, CN) and three positive ions (CO^+, N_2^+, CH_2O^+), are chosen to evaluate the quality of the time-dependent DFT for calculating excitation energies and for predicting absorption spectra of open-shell systems (molecules or clusters). This new modification and implementation of the time-dependent DFT is also applied to predict and interpret the absorption spectra of alkali metal clusters (lithium clusters and sodium clusters) from the dimer though to the hexamer. With the exception of the lowest two excitation energies (without oscillator strengths) of a few open–shell molecules which recently appeared in the literature [1], the present all-electron calculations of absorption spectra of the six open–shell molecules and alkali metal clusters (the lithium and the sodium clusters) are the first time-dependent DFT study reported in the literature. These all-electron calculated excitation energies and absorption spectra nicely coincide with measured results and are competitive with high quality *ab initio* CI methods. The time-dependent DFT results are much improved over those calculated by traditional DFT "multiplets" and Fritsche approaches [10], especially for the oscillator strengths. The present work found that the time-dependent DFT is able to provide fairly good treatments for

excited state properties of open–shell systems. These all-electron calculations of excitation energies and absorption spectra are also useful as benchmarks to assess the quality of the MCP in the applications to excited state properties.

The exchange-correlation functional plays a significant role in the calculation of excitation energies. Both the short–r behavior and asymptotic behavior of the functional are crucial. Low excitations mainly depend on the short–r behavior of the functional; in contrast, the large–r behavior of the functional may be important for high excitations. A better functional can be chosen depending on whether one is calculating low or high excitations. The LSDxc/TDLSDxc functional seems to be the choice for low excitations, while the LB94xc/TDLSDxc functional is better for high excitations of the free radicals. Surprisingly the deviations of excitation energies between the two functionals can be as much as 1.5 eV or more for the open–shell molecules and sodium clusters. The deviations for the lithium clusters are normally less than 1.0 eV. The LB94xc/TDLSDxc functional, in the open-shell molecule calculations, yields smaller excitation energies than those of the LSDxc/TDLSDxc functional. This ordering is inverted when the excitation energies are larger than the LSDxc ionization threshold, $-\varepsilon_{HOMO}^{LSDxc}$, the LB94xc/TDLSDxc functional starts to give larger excitation energies than those calculated with the LSDxc/TDLSDxc functional and the LB94xc/TDLSDxc excitation energies are in better agreement with the experimental results. This LSDxc/TDLSDxc excitation energy collapse above $-\varepsilon_{HOMO}^{LSDxc}$ is due to the well-known incorrect asymptotic behavior of the LSDxc functional which leads to too low ionization threshold compared with the true ionization potential. However, the ordering inversion is not observed in the sodium clusters calculations for which the LB94xc/TDLSDxc functional yields larger excitation energies than those calculated by the LSDxc/TDLSDxc functional for both low and high excitations and give larger errors. Moreover, excitation energies of sodium clusters are overestimated by about 0.15 eV with the LSDxc/TDLSDxc functional. In contrast, those of free radicals are underestimated by about 1.0 eV. This is opposite

to the previous DFT polarizability calculations for which the polarizabilities of sodium clusters [122] were underestimated and those of the small molecules [119] at the right–hand side of the periodic table were overestimated. This observation agrees with the theoretical relationship between excitation energy and polarizability (see Chapter 2 of this thesis for details), and also indicates that the LSDxc (or LSDxc/TDLSDxc) functional behaves differently in the applications to the compounds at the right–hand side of the periodic table and those at the left-hand side of the periodic table.

Electron Coulomb, exchange, and correlation interactions have different effects on excitation energies. The Coulomb interactions have the largest effects on excitation energies, their contributions are to push electronic states towards each other significantly, hence it dramatically reduces the excitation energies (27 eV) from the Core/IPA level calculations. The effects of the electron exchange are much smaller than those of the Coulomb interactions, but larger than the electron correlation. The contributions of both the electron exchange and the correlation are to make electronic states further apart, hence the two interactions increase the excitation energies. 1.8 eV change in excitation energies from the electron exchange interactions and 0.6 eV change in excitation energies from the correlation effects are observed for the sodium trimer.

The present work, using the sodium trimer and hexamer as case studies, discussed the use of absorption spectra to help determine equilibrium geometries and the sensitivity of excitation energies and oscillator strengths to small and large geometric distortions. Excitation energies are found to be insensitive to small geometrical distortions, but oscillator strengths are not. The sodium trimer geometry optimized by the all-electron and the MCP approaches differ by 0.23 bohr in bond length of the short side of the triangle and by 1.2 degrees in the bond angle between the isosceles sides of the triangle, leading to a difference in excitation energies of 0.06 eV. Large geometrical distortions may lead to large

deviations in the excitation energies and oscillator strengths and yield different ground state symmetry depending on whether the two geometries are minima. The sodium trimer is an example for which the obtuse geometry is the minimum and the acute structure is a saddle point. The absorption spectra are different between predictions with the obtuse and with the acute structures and excitation energies can vary by 0.8 eV in the calculations with the obtuse geometry and with the acute structure. The $^2B_2$ and $^2A_1$ symmetries for the ground state are observed, respectively, for the obtuse and the acute geometries. Due to the difference of the spectrum predicted with the acute structure from the recorded spectroscopic pattern, the acute geometry can be excluded. The obtuse structure is the equilibrium geometry for sodium trimer and is responsible for the recorded spectrum. The sodium hexamer is a case for which both the planar geometry and the pentagonal pyramid structures are minima. As in the geometry optimizations, the two structures are very competitive in the contributions to the recorded spectrum. The two structures yield very similar absorption spectra, neither of the two geometries can be excluded completely as the contributions to the recorded spectrum. However, the equilibrium geometry of the sodium hexamer (the planer D_{3h} or pentagonal pyramid C_{5v}) is different from the lithium hexamer which has a three-dimensional C_{2v} equilibrium geometry.

The present calculations found that the main features of these absorption spectra of the small lithium and the sodium clusters are the spectroscopic pattern with only two or three strong peaks (sodium trimer and tetramer with additional two or three medium bands) located around the 1.8 eV, 2.3 eV, and 2.8 eV regions. The present predicted absorption spectra also show that the open–shell clusters (the trimer and the pentamer) have many more bands than do the closed–shell clusters (the dimer, the tetramer, and the hexamer). The intense bands of free radicals are located at higher energies.

The MCP calculations reasonably reproduce the all-electron results. The

differences in excitation energies between the MCP and the all-electron calculations are less than 0.1 eV for the sodium dimer up to the hexamer. However, when the excitation energies are larger than the ionization threshold, $-\varepsilon_{HOMO}^{LSDxc}$ or $-\varepsilon_{HOMO}^{LB94xc}$, regardless of the exchange–correlation functional used, the MCP excitation energies have a sudden rise. Hence, the deviations between the MCP and the all-electron results become larger, by as much as 3 eV. This may be due to the inadequate basis set used in the MCP calculations, since above the ionization threshold, the continuum is reached and a small basis is not flexible enough to describe it. Therefore, for high excitation calculations more diffuse functions and (or) polarization functions are needed in the MCP basis.

In the future, there are some interesting subjects which can be pursued following the present work. First, it is interesting to implement restricted open-shell time-dependent DFT in the program *deMon-DynaRho* for calculating excited state properties. A similar approach has been applied in the CIS method, restricted open–shell CIS (ROCIS) did give some improvement over unrestricted CIS (UCIS) in the calculation of excitation energies for some free radicals [336]. Whether restricted open–shell time-dependent DFT can improve the excitation energies from the unrestricted time-dependent DFT will require further investigation. Moreover, UCIS [336] yields excited states which are highly spin contaminated, although the ground state has little spin contamination. In this regard, to investigate spin contamination in the unrestricted time-dependent DFT would also be interesting (details see Chapter 3 of this thesis).

Further investigation of the exchange–correlation functional is another interesting subject. The LSDxc/TDLSDxc functional is a better choice for low excitations, but it leads to excitation energies that collapse for the free radicals and some small molecules [387] when the excitation energies lie above $-\varepsilon_{HOMO}^{LSDxc}$, due to the incorrect asymptotic behavior of the LSDxc functional. The LB94xc functional with the correct asymptotic behavior improves the high excitation en-

ergies, but it gives too small excitation energies for low excitations. To find one suitable functional which can yield better excitation energies for both low and high excitations definitely needs more work, although some work has been done attempting to find a better functional for both low and high excitations. Casida and Salahub [488] proposed an asymptotic correction approach which combines the LSDxc (for low excitations) and the LB94xc (for high excitations) functionals to avoid excitation energy collapse for high excitations. This approach may be a better choice for small molecules (at the right-hand side of the periodic table), but it may not be suitable for sodium clusters due to the LB94xc/TDLSDxc functional yielding too high excitation energies.

The final subject is to further apply the time-dependent DFT to predict and interpret the absorption spectra for larger alkali metal clusters (with the MCP) and transition metal clusters (e.g. nickel and niobium metal clusters) which lag far behind the measurements; experimental absorption spectra of the larger alkali metal clusters [16] and transition metal clusters [489, 490, 491] have been available for a few years. Transition metal clusters are notoriously challenging for traditional *ab initio* methods, due to the strong correlation effects and combined with the size of the systems. DFT has been successfully established for treating ground state properties, even for transition metal clusters. Salahub and co-workers [492, 493] investigated ground state properties for small nickel, cobalt, and iron clusters, the results obtained with the DFT are quite encouraging, especially with the generalized gradient approximation (the functional of Perdew and Wang (1986) for exchange and Perdew (1986) for correlation). The excited state properties of transition metal clusters may be an area where time-dependent DFT could make an important contribution.

REFERENCES

[1] S. Hirata and M. Head-Gordon. *Chem. Phys. Lett.* **302**, 375 (1999).

[2] J.G. Aguilar, A. Mananes, M.J. Lopez, M.P. Iniguez, and J.A. Alonso. *Intern. J. Quan. Chem.* **56**, 589 (1995).

[3] V. Bonačič-Koutecký, P. Fantucci, and J. Koutecký. *Phys. Rev. B* **37**, 4369 (1988).

[4] P. Fantucci, S. Polezzo, V. Bonačič-Koutecký, and J. Koutecký. *J. Chem. Phys.* **92**, 6645 (1990).

[5] A.K. Ray. *Solid State Communications* **71**, 311 (1989).

[6] A. Herrmann, E. Schumacher, and L. Wöste. *J. Chem. Phys.* **68**, 2327 (1978).

[7] I. Moullet, J.L. Martins, F. Reuse, and J. Buttet. *Phys. Rev. Lett.* **65**, 476 (1990).

[8] I. Moullet, J.L. Martins, F. Reuse, and J. Buttet. *Phys. Rev. B* **19**, 31 (1990).

[9] P.J. Bruna, M.R.J. Hachey, and F. Grein. *Mol. Phys.* **94**, 917 (1998).

[10] G. Gardet, F. Rogemond, and H. Chermette. *Theor. Chim. Acta* **91**, 249 (1995).

[11] C. Fuchs, V. Bonačić-Koutecký, and J. Koutecký. *J. Chem. Phys.* **98**, 3121 (1993).

[12] Ph. Dugourd, J. Blanc, V. Bonačić-Koutecký, M. Broyer, J. Chevaleyre, J. Koutecký, J. Pittner, J.P. Wolf, and L. Wöste. *Phys. Rev. Lett.* **67**, 2638 (1991).

[13] M. Groβ and F. Spiegelmann. *J. Chem. Phys.* **108**, 4148 (1998).

[14] V. Bonačić-Koutecký, P. Fantucci, and J. Koutecký. *J. Chem. Phys.* **93**, 3802 (1990).

[15] V. Bonačić-Koutecký, J. Pittner, C. Scheuch, M.F. Gues, and J. Koutecký. *J. Chem. Phys.* **96**, 7938 (1992).

[16] K. Selby, V. Kresin, J. Masui, M. Vollmer, W.A. de Heer, A. Scheidemann, and W.D. Knight. *Phys. Rev. B* **43**, 4565 (1991).

[17] E.S. Nielsen, P. Jørgensen, and J. Oddershede. *J. Chem. Phys.* **73**, 6238 (1980).

[18] S. Pal, M. Rittby, R.J. Barlett, D. Sinha, and D. Mukherjee. *J. Chem. Phys.* **88**, 4357 (1988).

[19] P. Ertl and J. Leška. *J. Mol. Struct.(Theochem)* **165**, 1 (1988).

[20] M. Petersilka and E.K.U. Gross. *Int. J. Quantum Chem. Symp.* **30**, 181 (1996).

[21] M. Petersilka, U.J. Gossmann, and E.K.U. Gross. *Phys. Rev. Lett.* **76**, 1212 (1996).

[22] R. Bauernschmitt, M. Häser, O. Treutler, and R. Ahlrichs. *Chem. Phys. Lett.* **264**, 573 (1997).

[23] C.R.C. Wang, S. Pollack, D. Cameron, and M. Kappes. *J. Chem. Phys.* **93**, 3787 (1990).

[24] C. Ellert, M. Schmidt, C. Schmitt, Thomas Reiners, and H. Haberland. *Phys. Rev. Lett.* **75**, 1731 (1995).

[25] R. Siegel. *Phys. Today* **46**, 64 (1993).

[26] R.G. Parr and W. Yang. *Density-Functional theory of Atoms and Molecules.* Oxford University Press, New York, (1989).

[27] R.M. Dreizler and E.K.U. Gross. *Density functional theory, An approach to the quantum many-body problem.* Springer, Berlin Heidelberg, New York, (1990).

[28] Á. Nagy. *Phys. Reports* **298**, 1 (1998).

[29] M.E. Casida, C. Jamorski, F. Bohr, J. Guan, and D.R. S alahub. *in Theoretical and Computational Modeling of NLO and Electronic Materials.* Proceedings of ACS Symposium, Washington, D.C, (1994). ACS Press: Washington, D.C., 1996. Ed. by S.P. Karna and A.T. Yeates.

[30] M.E. Casida. *in Recent Developments and Applications of Modern Density Functional Theory.* Elsevier, Amsterdam, (1996). p. 391. Ed. by J.M. Seminario.

[31] S.J.A. van Gisbergen, J.G. Snijders, and E.J. Baerends. *J. Chem. Phys.* **103**, 9347 (1995).

[32] S.M. Collwell, N.C. Handy, and A.M. Lee. *Phys. Rev. A* **53**, 1316 (1996).

[33] R. Bauernschmitt and R. Ahlrichs. *Chem. Phys. Lett.* **256**, 454 (1996).

[34] N.C. Handy and D.J. Tozer. *J. Comp. Chem.* **20**, 106 (1999).

[35] D.J. Tozer and N.C. Handy. *J. Chem. Phys.* **109**, 10180 (1998).

[36] K. Yabana and G.F. Bertsch. *J. Chem. Phys.* (1998). submitted.

[37] R.E. Stratmann, G.E. Scuseria, and M.J. Frisch. *J. Chem. Phys.* **109**, 8218 (1998).

[38] M. Kappes, M. Schär, P. Radi, and E. Schumacher. *J. Chem. Phys.* **84**, 1863 (1986).

[39] M. Kappes, M Schär, U. Röthlisberger, C. Yeretzian, and E. Schumacher. *Chem. Phys. Lett.* **143**, 251 (1988).

[40] M. Kappes, R. Kunz, and E. Schumacher. *Chem. Phys. Lett.* **91**, 413 (1982).

[41] W. Knight, K. Clemenger, W. de Heer, W. Saunders, M. Chou, and M. Cohen. *Phys. Rev. Lett.* **52**, 2141 (1984).

[42] M. Kappes, P. Radi, M. Schär, C. Yeretzian, and E. Schumacher. *Z. Phys. D* **3**, 115 (1986).

[43] W. de Heer, W. Knight, M. Chou, and M. Cohen. *Solid State Phys.* **40**, 93 (1987).

[44] E. Schumacher. *Chimia* **42**, 357 (1988).

[45] A. Kaldor, D. Cox, and M. Zakin. *Adv. Chem. Phys.* **70**, 211 (1988).

[46] W. Knight, K. Clemenger, W. de Heer, and W. Saunders. *Phys. Rev. B* **31**, 2539 (1985).

[47] J. Gole, G. Green, S. Pace, and D. Preuss. *J. Chem. Phys.* **76**, 2247 (1982).

[48] W. Crumley, J. Hayden, and J. Gole. *J. Chem. Phys.* **84**, 5250 (1986).

[49] E. Rohlfing and J. Valentini. *J. Chem. Phys. Lett.* **126**, 113 (1986).

[50] J. Woodward, S. Cobb, and J. Gole. *J. Phys. Chem.* **92**, 1404 (1988).

[51] A. Herrmann, S. Leutwyler, E. Schumacher, and L. Wöste. *Helv. Chem. Acta* **61**, 453 (1978).

[52] M. Morse, J. Hopkins, P.R.R. Langridge-Smith, and R. Smalley. *J. Chem. Phys.* **79**, 5316 (1983).

[53] M. Broyer, G. Delacretaz, P. Labastie, J.P. Wolf, and L. Wöste. *Phys. Rev. Lett.* **57**, 1851 (1986).

[54] G. Delacretaz, E. Grant, R. Whetten, L. Wöste, and J. Zwanziger. *Phys. Rev. Lett.* **56**, 2598 (1986).

[55] M. Broyer, G. Delacretaz, G.Q. Ni, J.P. Wolf, and L. Wöste. *Chem. Phys. Lett.* **145**, 232 (1988).

[56] P. Cheng and M. Duncan. *Chem. Phys. Lett.* **152**, 341 (1988).

[57] M. Broyer, G. Delacretaz, G.Q. Ni, J.P. Wolf, and L. Wöste. *J. Chem. Phys.* **90**, 4620 (1989).

[58] J. P. Wolf, G. Delacretaz, and L. Wöste. *Phys. Rev. Lett.* **63**, 1946 (1989).

[59] D.G. Leopold and K. Lineberger. *J. Chem. Phys.* **85**, 51 (1986).

[60] D. Leopold, J. Ho, and W. Lineberger. *J. Chem. Phys.* **86**, 1715 (1987).

[61] O. Cheshnovsky, P. Brucat, S. Yang, C. Petiette, M . Craycraft, and R. Smalley. *in Physics and Chemistry of Small Clusters.* Plenum, New York, (1988). Proceedings of the NATO Advanced Research Workshop, Richmond, 1986. Ed. by P. Jena, B. Rao and S. Khanna.

[62] R.E. Smalley. *in Cluster Spectroscopy.* Elsevier, Amsterdam, (1988). Ed. by E.R. Bernstein.

[63] J. Ho, K.M. Ervin, and W.C. Lineberger. *J. Chem. Phys.* **93**, 6987 (1990).

[64] W.A. de Heer, K. Selby, V. Kresin, J. Masui, M. Vollmer, A. Chatelain, and W.D. Knight. *Phys. Rev. Lett.* **59**, 1805 (1987).

[65] K. Selby, M. Vollmer, J. Masui, V. Kresin, W.A. de Heer, and W.D. Knight. *Phys. Rev. B* **40**, 5417 (1989).

[66] M. Jarrold and K. Creengan. *Chem. Phys. Lett.* **166**, 116 (1990).

[67] C. Wang, S. Pollack, and M.M. Kappes. *Chem. Phys. Lett.* **166**, 26 (1990).

[68] M. Broyer, J. Chevaleyre, Ph. Dugourd, J.P. Wolf, and L. Wöste. *Phys. Rev. A* **42**, 6954 (1990).

[69] J. Blanc, V. Bonaŏić-Koutecký, M. Broyer, J. Chevaleyre, Ph. Dugourd, J. Koutecký, C. Scheuch, J.P. Wolf, and L. Wöste. *J. Chem. Phys.* **96**, 1793 (1992).

[70] K. Selby, M. Vollmer, J. Masui, V. Kresin, W.A. de Heer, and W.D. Knight. *Z. Physik D* **12**, 477 (1989).

[71] C.R.C. Wang, S. Pollack, T.A. Dahlseid, G.M. Koretsky, and M.M. Kappes. *J. Chem. Phys.* **96**, 7931 (1992).

[72] S. Pollack, C.R.C. Wang, and M.M. Kappes. *J. Chem. Phys.* **94**, 2496 (1991).

[73] G. Mie. *Ann. Physik* **25**, 377 (1908).

[74] W. Ekardt. *Phys. Rev. Lett.* **52**, 1925 (1984).

[75] W. Ekardt. *Phys. Rev. B* **31**, 6360 (1985).

[76] C. Yannouleas, R. Broglia, M. Brack, and P. Bortignon. *Phys. Rev. Lett.* **63**, 255 (1989).

[77] V. Bonačić-Koutecký, M. Kappes, G. Fantucci, and J. Koutecký. *Chem. Phys. Lett.* **170**, 26 (1990).

[78] V. Bonačić-Koutecký, P. Fantucci, and J. Koutecký. *Chem. Phys. Lett.* **146**, 518 (1988).

[79] V. Bonačić-Koutecký, P. Fantucci, and J. Koutecký. *J. Chem. Phys.* **91**, 3794 (1989).

[80] K.C. Kulander, K.R. Sandhya Devi, and S.E. Koonin. *Phys. Rev. A* **25**, 2968 (1982).

[81] W. Stich, H.-J. Lüdde, and R.M. Dreizler. *Phys. Lett. A* **99**, 41 (1983).

[82] K.R. Sandhya Devi and J.D. Garcia. *Phys. Rev. A* **30**, 600 (1984).

[83] W. Stich, H.-J. Lüdde, and R.M. Dreizler. *J. Phys. B* **18**, 1195 (1985).

[84] S. L. Guberman. *J. Chem. Phys.* **78**, 1404 (1983).

[85] D. Tiszauer and K.C. Kulander. *Phys. Rev. A* **29**, 2909 (1984).

[86] P. Bruna and S. Peyerimhoff. *Adv. Chem. Phys.* **67**, 1 (1987).

[87] S. Pal, M. Rittby, and R.J. Bartlett. *J. Chem. Phys.* **88**, 4357 (1988).

[88] O. Christiansen, H. Koch, P. Jørgensen, and J. Olsen. *Chem. Phys. Lett.* **256**, 185 (1996).

[89] C.W. Bauschlicher Jr, S.R. Langhoff, and H.J. Partridge. *Chem. Phys.* **91**, 2412 (1989).

[90] V. Bonačić-Koutecký, P. Fantucci, and J. Koutecký. *Chem. Rev.* **91**, 1035 (1991).

[91] P. Bonche and P. Quentin. *Time-Dependent Hartree Fock Method.* Editions de Physique, Paris, (1979).

[92] J.W. Negele. *Rev. Mod. Phys.* **54**, 913 (1982).

[93] J.D. Bene, R. Ditchfield, and J.A. Pople. *J. Chem. Phys.* **55**, 2236 (1971).

[94] J.B. Foresman, M. Head-Gordon, J.A. Pople, and M.J. Frisch. *J. Phys. Chem.* **96**, 135 (1992).

[95] M. Head-Gordon, R.J. Rico, J.A. Pople, and T.J. Lee. *Chem. Phys. Lett.* **219**, 21 (1994).

[96] C. Ochsenfeld, J. Gauss, and R. Ahlrichs. *J. Chem. Phys.* **103**, 7401 (1995).

[97] P.A.M. Dirac. *Proc. Cambridge Phil. Soc.* **26**, 376 (1930).

[98] D.J. Rowe. *Nucl. Phys. A* **107**, 99 (1968).

[99] J. Linderberg and Y. Öhrn. *Propagators in Quantum Chemistry.* London Academic, (1973).

[100] P. Jørgensen. *Annual Rev. of Phys. Chem.* **26**, 359 (1975).

[101] D.J. Rowe. *Nuclear Collective Motion, Models, and Thoery.* Methuen and Co. Ltd., London, (1970).

[102] J. Berkowitz. *Photoabsorption, Photoionnization, and Photoelectron Spectroscopy.* Academic Press, New York, (1979).

[103] Jr. C.W. McCurdy, T.N. Rescigno, D.L. Yeager, and V. McK oy. *in Modern Theoretical Chemistry*, volume 3. Plenum Press, New York, (1977). Ed. by H.F. Schaefer III.

[104] D.J. Thouless. *Nucl. Phys.* **22**, 78 (1961).

[105] H.J. Silverstone and O. Sinanoglu. *J. Chem. Phys.* **44**, 1899 (1966).

[106] C. Hollister and O. Sinanoglu. *J. Am. Chem. Soc.* **88**, 13 (1966).

[107] O. Sinanoglu. *Proc. Nat. Acad. Sci. USA* **47**, 1217 (1961).

[108] S. Weinbaum. *J. Chem. Phys.* **1**, 593 (1933).

[109] H.M. James and A.S. Coolidge. *J. Chem. Phys.* **1**, 825 (1933).

[110] I. Shavitt. *in Modern Theoretical Chemistry*, volume 3. Plenum Press, New York, (1977). Ed. by H.F. Schaefer III.

[111] M. Perić, B. Engels, and S.D. Peyerimhoff. *in Quantum mechanical structure calculations with chemical accuracy.* Kluwer Academic Publishers, Dordrecht, The Netherlands, (1995). Ed. by S.R. Langhoff.

[112] B.O. Roos, M. Fülscher, P. Malmqvist, M. Merchán, and L. Serrano-Andrés. *in Quantum mechanical structure calculations with chemical accuracy.* Kluwer Academic Publishers, Dordrecht, The Netherlands, (1995). Ed. by S.R. Langhoff.

[113] P. Hohenberg and W. Kohn. *Phys. Rev. B* **136**, 864 (1964).

[114] W. Kohn and L.J. Sham. *Phys. Rev. A* **140**, 1133 (1965).

[115] D.R. Salahub. *Adv. Chem. Phys.* **69**, 447 (1987).

[116] A.K. Rajagopal. *Adv. Chem. Phys.* **41**, 59 (1980).

[117] R.O. Jones and O. Gunnarson. *Rev. Mod. Phys.* **61**, 689 (1989).

[118] N.H. March. *Electron Density Theory of Atoms and Molecules.* Academic Press, New York, (1992).

[119] J. Guan, P. Duffy, J. Carter, D.P. Chong, K. Casida, M.E. Casida, and M. Wrinn. *J. Chem. Phys.* **98**, 4753 (1993).

[120] D.R. Salahub, M. Castro, and E.I. Proynov. *in Relativistic and Electron Correlation Effects in Molecules and Solids.* Plenum Press, New York, (1994). Ed. by G.L. Malli.

[121] E.K.U. Gross and R.M. Dreizler. *Density-Functional Theory.* Plenum Press, New York, (1995).

[122] J. Guan, M.E. Casida, M. Köster, and D.R. Salahub. *Phys. Rev. B* **52**, 2184 (1995).

[123] J.P. Lu and W. Yang. *Phys. Rev. B* **49**, 11421 (1994).

[124] Q. Zhao and W. Yang. *J. Chem. Phys.* **102**, 9598 (1995).

[125] G. Tobias and E.K.U. Gross. *Chem. Phys. Lett.* **240**, 141 (1995).

[126] G. Tobias and E.K.U. Gross. *Chem. Phys. Lett.* **241**, 635(E) (1995).

[127] R.P. Messmer and D.R. Salahub. *J. Chem. Phys.* **65**, 779 (1976).

[128] T. Ziegler, A. Rauk, and E.J. Baerends. *Theor. Chim. Acta.* **43**, 261 (1977).

[129] U. von Barth. *Phys. Rev. A* **20**, 1693 (1979).

[130] C. Daul, H.U. Güdel, and J. Weber. *J. Chem. Phys.* **85**, 4023 (1993).

[131] C. Daul. *Int. J. Quant. Chem.* **52**, 867 (1994).

[132] F. Rogemond, H. Chermette, and D.R. Salahub. *Chem. Phys. Lett.* **219**, 228 (1994).

[133] R.M. Dickson and T. Ziegler. *Int. J. Quantum Chem.* **58**, 681 (1996).

[134] F. Gilardon, J. Weber, K. Bellafrouh, C. Daul, and H.U. Güdel. *J. Chem. Phys.* **104**, 7624 (1996).

[135] J.C. Slater. *Adv. Qutanm Chem.* **6**, 1 (1972).

[136] J.C. Slater. *The Self-Consistent Field for Molecules and Solids.* McGraw-Hill, New York, (1974).

[137] O. Gunnarson and B.I. Lundquist. *Phys. Rev. B* **13**, 4274 (1976).

[138] E.K.U. Gross and W. Kohn. *Adv. Quant. Chem.* **21**, 255 (1990).

[139] E.K.U. Gross, J.F. Dobson, and M. Petersilka. *Topics in Current Chemistry*, volume 181. Springer-Verlas, Berlin, Heidelberg, (1996).

[140] A.K. Theophilou. *J. Phys. C* **12**, 5419 (1978).

[141] E.K.U. Gross, L.N. Oliveira, and W. Kohn. *Phys. Rev. A* **37**, 2805 (1988).

[142] E.K.U. Gross, L.N. Oliveira, and W. Kohn. *Phys. Rev. A* **37**, 2809 (1988).

[143] L.N. Oliveira, E.K.U. Gross, and W. Kohn. *Phys. Rev. A* **37**, 2821 (1988).

[144] R. Gáspár. *Acta Phys. Hung.* **35**, 213 (1974).

[145] Á. Nagy. *Phys. Rev. A* **42**, 4388 (1990).

[146] Á. Nagy. *J. Phys. B* **24**, 4691 (1991).

[147] Á. Nagy. *J. Phys. B* **29**, 389 (1996).

[148] A.K. Theophilou. *J. Phys. C* **12**, 5419 (1979).

[149] N. Hadjisavvas and A. K. Theophilou. *Phys. Rev. A* **32**, 720 (1985).

[150] W. Kohn. *Phys. Rev. A* **34**, 737 (1986).

[151] Á. Nagy and I. Andrejkovics. *J. Phys. B* **27**, 233 (1994).

[152] I. Andrejkovics and Nagy Á. *Acta. Phys. et Chim. Debr.* **29**, 7 (1994).

[153] S. Chakravarty, M.B. Fogel, and W. Kohn. *Phys. Rev. Lett.* **43**, 775 (1979).

[154] L.J. Bartolotti. *Phys. Rev. A* **24**, 1661 (1981).

[155] B.M. Deb and S.K. Ghosh. *J. Chem. Phys.* **77**, 342 (1982).

[156] E. Runge and E.K.U. Gross. *Phys. Rev. Lett.* **52**, 997 (1984).

[157] K.L. Liu and S.H. Vosko. *Can. J. Phys.* **67**, 1015 (1989).

[158] F. Bloch. *Z. Physik* **81**, 363 (1933).

[159] V. Peuckert. *J. Phys. C* **11**, 4945 (1978).

[160] A. Zangwill and P. Soven. *Phys. Rev. A* **21**, 1561 (1980).

[161] S.K. Ghosh and B.M. Deb. *Chem. Phys.* **71**, 295 (1982).

[162] S.K. Ghosh and B.M. Deb. *Theoret. Chim. Acta.* **62**, 209 (1983).

[163] S.K. Ghosh and B.M. Deb. *J. Mol. Struct.* **103**, 163 (1983).

[164] L.J. Bartolotti. *Phys. Rev. A* **26**, 2243 (1982).

[165] L.J. Bartolotti. *J. Chem. Phys.* **80**, 5687 (1984).

[166] L.J. Bartolotti. *Phys. Rev. A* **36**, 4492 (1987).

[167] E.K.U. Gross and R.M. Dreizler. *in Density Functional Methods in Physics.* NATO ASI Series. Plenum Press, New York, (1985). Ed. by R.M. Dreizler and João da Providencia.

[168] E.K.U. Gross, C.A. Ullrich, and U.J. Gossman. *in Density-Functional Theory.* NATO ASI series. Plenum, (1994). Ed. by E.K.U. Gross and R.M. Dreizler.

[169] K. Burke and E.K.U. Gross. *in Density Functional: Theory and Applications.* Springer, Berlin, (1997). Ed. by D. Joubert.

[170] A. Zangwill and P. Soven. *Phys. Rev. Lett.* **45**, 204 (1980).

[171] M.J. Stott and E. Zaremba. *Phys. Rev. A* **21**, 12 (1980).

[172] Z.H. Levine and P. Soven. *Phys. Rev. B* **24**, 4121 (1981).

[173] Z.H. Levine and P. Soven. *Phys. Rev. A* **29**, 625 (1984).

[174] P. Gies and R.R. Gerhardts. *Phys. Rev. B* **31**, 6843 (1985).

[175] P. Gies and R.R. Gerhardts. *Phys. Rev. B* **36**, 4422 (1987).

[176] Z.H. Levine and D.C. Allan. *Phys. Rev. Lett.* **63**, 1719 (1989).

[177] G.D. Mahan and K.R. Subbaswamy. *Local Density Theory of Polarizabilities.* Plenum, New York, (1990).

[178] Z.H. Levine. *Phys. Rev. B* **42**, 3567 (1990).

[179] Z.H. Levine and D.C. Allan. *Phys. Rev. Lett.* **66**, 41 (1991).

[180] H. Zhong, Z.H. Levine, and J.W. Wilkins. *Phys. Rev. A* **43**, 4629 (1991).

[181] H. Zhong, Z.H. Levine, D.C. Allan, and J.W. Wilkins. *Phys. Rev. Lett.* **69**, 379 (1992).

[182] Z.H. Levine and P. Soven. *Phys. Rev. Lett.* **50**, 2074 (1983).

[183] C. Jamorski, M.E. Casida, and D.R. Salahub. *J Chem. Phys.* **104**, 5134 (1996).

[184] S.J.A. van Gisbergen, J.G. Snijders, and E.J. Baerends. *Phys. Rev. Lett.* **78**, 3097 (1997).

[185] J. Theilhaber. *Phys. Rev. B* **46**, 12990 (1992).

[186] A. Rubio, L.C. Balbás, and J.A. Alonso. *Phys. Rev. B* **46**, 4891 (1992).

[187] A. Liebsch. *Phys. Rev. B* **36**, 7378 (1987).

[188] J.F. Dobson and G.H. Harris. *J. Phys. C* **21**, L792 (1988).

[189] P. Gies and R.R. Gerhardts. *Phys. Rev. B* **37**, 10020 (1988).

[190] H. Bross, O. Belhachemi, B. Mekk, and A. Seoud. *J. Phys. B* **2**, 3919 (1990).

[191] N.E. Maddocks, R.W. Godby, and R.J. Needs. *Phys. Rev. B* **49**, 8502 (1990).

[192] N.E. Maddocks, R.W. Godby, and R.J. Needs. *Europhys. Lett.* **27**, 681 (1994).

[193] M. Petersilka. Diplomarbeit. Universitä Würzburg, (1993).

[194] D.E. Beck. *Phys. Rev. B* **30**, 6935 (1984).

[195] M.J. Puska, R.M. Nieminen, and M. Manninen. *Phys. Rev. B* **31**, 3486 (1985).

[196] M. Manninen, R.M. Nieminen, and M.J. Puska. *Phys. Rev. B* **33**, 4289 (1986).

[197] P. Stampfli and K.H. Bennemann. *Phys. Rev. A* **39**, 1007 (1989).

[198] G. Bertsch. *Comput. Phys. Commun.* **60**, 247 (1990).

[199] A. Rubio, L.C. Balbás, and J.A. Alonso. *Phys. Rev. B* **45**, 13657 (1992).

[200] L.C. Balbás, A. Rubio, and M.B. Torres. *Comput. Mat. Sci.* **2**, 509 (1994).

[201] S.J.A. van Gisbergen, J.G. Snijders, and E.J. Baerends. *J. Chem. Phys.* **109**, 10644 (1998).

[202] S.J.A. van Gisbergen, J.G. Snijders, and E.J. Baerends. *J. Chem. Phys.* **109**, 10657 (1998).

[203] A. Zangwill. *J. Chem. Phys.* **78**, 5926 (1983).

[204] G. Senatore and K.R. Subbaswamy. *Phys. Rev. A* **35**, 2440 (1987).

[205] A.D. Becke. *J. Chem. Phys.* **98**, 5648 (1993).

[206] F.P. Billingsley and J.E. Bloor. *J. Chem. Phys.* **55**, 5178 (1971).

[207] M.E. Casida. *in Recent Advances in Density-Functional Methods*, volume 1. World Scientific, Singapore, (1995). Ed. by D.P. Chong.

[208] J. Guan, M.E. Casida, C. Jamorski, and D.R. Salahub. *deMon–DynaRho, version 2pX.* University of Montreal, (1998). This new version 2pX is a modified version based on original version 2p0 which can only treat closed–shell systems. The new version 2pX can treat both closed-shell and open–shell systems.

[209] A.D. Becke. *Phys. Rev. A* **38**, 3098 (1988).

[210] J.P. Perdew. *Phys. Rev. B* **33**, 8822 (1986).

[211] J.P. Perdew and Y. Wang. *Phys. Rev. B* **33**, 8800 (1986).

[212] R. van Leeuwen and E.J. Baerends. *Phys. Rev. A* **49**, 2421 (1994).

[213] D. Halliday and R. Resnick. *Physics II.* John Wiley & Sons Inc., (1966). Page 985.

[214] C. Sandorfy. *Electronic Spectra and Quantum Chemistry.* Prentice-Hall, Inc., New Jersey, (1964). Page 140 to Page 181.

[215] J.I. Steinfeld. *An Introduction to Modern Molecular Spectroscopy.* The MIT Press, London, England, 2nd edition, (1985). Page 87 to Page 92.

[216] T. Ziegler. *Chem. Rev.* **91**, 651 (1991).

[217] E.K.U. Gross and S. Kurth. *in Relativistic and Electron Correlation Effects in Molecules and Solids.* New York, (1994). Ed. by G.L. Malli.

[218] J.M. Seminario and P. Politzer, editors. *Modern Density Functional Theory, A Tool for Chemistry.* Amsterdam, The Netherlands, (1995).

[219] I.N. Levine. *Quantum Chemistry.* Prentice-Hall, New Jersey, 4th edition, (1991).

[220] E.B. Wilson. (1965). unpublished results.

[221] J.C. Stoddart and N.H. March. *Ann. Phys. NY* **64**, 174 (1970).

[222] L. Hedin and B.I. Lundqvist. *J. Phys. C* **4**, 2064 (1971).

[223] U. von Barth and L. Hedin. *J. Phys. C* **5**, 1629 (1972).

[224] J.F. Janak, V.L. Moruzzi, and A.R. Williams. *Phys. Rev. B* **12**, 1257 (1975).

[225] A.H. MacDonald and S.H. Vosko. *J. Phys. C* **12**, 2977 (1979).

[226] J.P. Perdew and A. Zunger. *Phys. Rev. B* **23**, 5048 (1981).

[227] M.V. Ramana and A.K. Rajagopal. *Adv. Chem.Phys.* **54**, 231 (1983).

[228] E.I. Proynov, A. Vela, and D.R. Salahub. *Chem. Phys. Lett.* **230**, 419 (1994).

[229] E.I. Proynov and D.R. Salahub. *Int. J. Quantum Chem.* **49**, 67 (1994).

[230] E. Engel and S.H. Vosko. *Phys. Rev. B* **50**, 10498 (1994).

[231] A.G. Koures and F.E. Harris. *Int. J. Quantum Chem.* **59**, 3 (1996).

[232] S.H. Vosko, L. Wilk, and M. Nusair. *Can. J. Phys.* **58**, 1200 (1980).

[233] R.G. Parr and W. Yang. *Annu. Rev. Phys. Chem.* **46**, 701 (1995).

[234] F. Herman, I.B. Ortenburger, and J.P. van Dyke. *Int. J. Quantum Chem. S* **3**, 827 (1970).

[235] D.C. Langreth and M. J. Mehl. *Phys. Rev. B* **28**, 1809 (1983).

[236] J.P. Perdew. *Phys. Rev. Lett.* **55**, 1665 (1985).

[237] J.P. Perdew. *Phys. Rev. B* **34**, 7406 (1986).

[238] A.D. Becke. *J. Chem. Phys.* (1986).

[239] A.E. Depristo and J.D. Kress. *J. Chem. Phys.* **86**, 1425 (1987).

[240] C. Lee, W. Yang, and R.G. Parr. *Phys. Rev. B* **37**, 785 (1988).

[241] J.A. Alonso and L.A. Girifalco. *Solid State Commun.* **24**, 135 (1977).

[242] O. Gunnarsson and R.O. Jones. *Phys. Scr.* **21**, 394 (1980).

[243] A.D. Becke. *in The Challenge of d and f Electrons Theory and Computation.* American Chemical Society, Washington D.C., (1989). Ed. by D.R. Salahub and M.C. Zerner.

[244] D.M. Ceperley and B.J. Alder. *Phys. Rev. Lett.* **45**, 566 (1980).

[245] J.C. Slater. *Phys. Rev.* **81**, 381 (1951).

[246] R. Gáspár. *Acta. Phys. Hung.* **3**, 263 (1954).

[247] P. Mlynarski and D.R. Salahub. *J. Chem. Phys.* **95**, 6050 (1991).

[248] R. Fournier and D.R. Salahub. *Surf. Sci.* **245**, 263 (1991).

[249] deMon user guide. Biosym Technologies, San Diego, (1992). version 1.0 beta.

[250] F. Sim, A. St-Amant, I. Papai, and D.R. Salahub. *J. Amer. Chem. Soc.* submitted.

[251] R. Gáspár and Á. Nagy. *Acta. Phys. Chem. Debr.* **26**, 7 (1989).

[252] P. Gombás. *Pseudopotentials.* Springer, Berlin, (1967).

[253] G.C. Lee and E. Clementi. *J. Chem. Phys.* **60**, 1275 (1974).

[254] L.C. Wilson and M. Levy. *Phys. Rev. B* **41**, 12930 (1990).

[255] C. Lee and R.G. Parr. *Phys. Rev. A* **42**, 193 (1990).

[256] P. Süle and Á. Nagy. *Acta Phys. Chem. Debr.* **29**, 1 (1994).

[257] D.G. Langreth and J.P. Perdew. *Phys. Rev. B* **21**, 5469 (1980).

[258] C.D. Hu and D.G. Langreth. *Physica Scripta* **32**, 391 (1985).

[259] S.H. Vosko and L.D. Macdonald. *in Condensed Matter Theories*, volume 2. Plenum, New York, (1987). Ed. by P. Vashishta, R.K. Kalia, and R.F. Bishop.

[260] J.P. Perdew, J.A. Chevary, S.H. Vosko, K.A. Jackson, M.R. Pederson, D.J. Singh, and C. Fiolhais. *Phys. Rev. B* **46**, 6671 (1992).

[261] H. Stoll, E. Golka, and H. Preuss. *Thoer. Chim. Acta.* **49**, 143 (1978).

[262] D.C. Langreth and M.J. Mehl. *Phys. Rev. B* **29**, 2310 (1983).

[263] C.D. Hu and D.C. Langreth. *Phys. Rev. B* **33**, 943 (1986).

[264] R. Colle and D. Salvetti. *Theor. Chim. Acta* **37**, 329 (1975).

[265] R. Colle, F. Moscardo, P. Riani, and O. Salvetti. *Theor. Chim. Acta* **44**, 1 (1977).

[266] R. Colle, R. Montagnani, P. Riani, and O. Salvetti. *Theor. Chim. Acta* **49**, 37 (1978).

[267] R. Colle and D. Salvetti. *Thoer. Chim. Acta* **53**, 55 (1979).

[268] R. Colle and D. Salvetti. *J. Chem. Phys.* **79**, 1404 (1983).

[269] J.K. Labanowski and J. Andzelm, editors. *Density-Functional Methods in Chemistry.* Springer Verlag, New York, (1991).

[270] B.G. Johnson, P.M.W. Gill, and J.A. Pople. *J. Chem. Phys.* **98**, 5612 (1993).

[271] N.C. Handy, C.W. Murray, and R.D. Amos. *J. Phys. Chem.* **97**, 4392 (1993).

[272] M.J. Frisch and co workers. Gaussian 92. Gaussian Inc., Pittsburgh, Pennsylvania, (1992).

[273] P.J. Stephens, F.J. Devlin, C.F. Chabalowski, and M.J. Frisch. *J. Phys. Chem.* **98**, 11623 (1994).

[274] A.D. Becke. *J. Chem. Phys.* **98**, 1372 (1993).

[275] P.M.W. Gill, B.G. Johnson, J.A. Pople, and M.J. Frisch. *Int. J. Quantum Chem. Symp.* **26**, 319 (1992).

[276] J.P. Perdew. *in Electronic Structure of Solids.* Academic Press, Berlin, (1991). Ed. by P. Ziesche and H. Eschrig.

[277] J.P. Perdew and Y. Wang. *Phys. Rev. B* **45**, 13244 (1992).

[278] A. St-Amant and D.R. Salahub. *Chem. Phys. Lett.* **169**, 387 (1990).

[279] D.R. Salahub, R. Fournier, P. Mlymarski, I. Papai, A. St-Amant, , and J. Ushio. *in Density-Functional Methods in Chemistry.* Springer, Berlin, (1991). Ed. by J.K. Labanowski and J.W. Andzelm.

[280] A. St-Amant. *deMon, un programme de chimie quantique sur ordinateur et une étude théoritique de l'adsorption de l'hydrogène sur les monomères et dimères de Ni, Rh et Pd.* PhD thesis, Université de Montréal, (1992).

[281] B. Delly. *J. Chem. Phys.* **92**, 508 (1990).

[282] A.D. Becke and R.M. Dickson. *J. Chem. Phys.* **89**, 2993 (1988).

[283] A.D. Becke. *Int. J. Quantum Chem. Symp.* **23**, 1280 (1989).

[284] A.D. Becke and R.M. Dickson. *J. Chem. Phys.* **92**, 3610 (1990).

[285] R. Car and M. Parrinello. *Phys. Rev. Lett.* **55**, 2471 (1985).

[286] M.P. Teter, M.C. Payne, and D.C. Allan. *Phys. Rev. B* **40**, 12255 (1989).

[287] J.C. Slater. *Phys. Rev.* **36**, 57 (1930).

[288] G.S. Painter and D.E. Ellis. *Phys. Rev. B* **1**, 4747 (1970).

[289] D.E. Ellis and G.S. Painter. *Phys. Rev. B* **2**, 2887 (1970).

[290] E.J. Baerends, D.E. Ellis, and P. Ros. *Chem. Phys.* **2**, 41 (1973).

[291] S.F. Boys. *Proc. R. Soc. (London) A* **200**, 542 (1950).

[292] S. Huzinaga. *J. Chem. Phys.* **42**, 1293 (1965).

[293] W.J. Hehre, R.F. Stewart, and J.A. Pople. *J. Chem. Phys.* **51**, 2657 (1969).

[294] J.A. Pople. *in Modern Theoretical Chemistry*, volume 4. Plenum Press, New York, (1977). Ed. by H.F. Schaefer III.

[295] N. Godbout, D.R. Salahub, J. Andzelm, and E. Wimmer. *Can. J. Chem.* **70**, 560 (1992).

[296] J. Andzelm. *in Density-Functional Methods in Chemistry.* Springer, Verlag, New York, (1991). Ed. by J.K. Labanowski and J.W. Andzelm.

[297] J. Andzelm and W. Wimmer. *J. Chem. Phys.* **96**, 1280 (1992).

[298] P.M.W. Gill, B.G. Johnson, and J. Pople. *Chem. Phys. Lett.* **209**, 506 (1993).

[299] C.W. Murray, N.C. Handy, and G.J. Laming. *Mol. Phys.* **78**, 997 (1993).

[300] R. Ahlrichs, M. B r, M. H ser, H. Horn, and C. K lmel. *Chem. Phys. Lett.* **162**, 165 (1989).

[301] C.V. Wuellen. *Chem. Phys. Lett.* **219**, 8 (1994).

[302] R. Ahlrichs and M.V. Arnim. *in Methods and Techniques in Computational Chemistry.* METECC-95, (1995). Ed. by E. Clementi and G. Corongiu.

[303] J. Andzelm, E. Wimmer, and D.R. Salahub. *in The Challenge of d and f Electrons Theory and Computation.* American Chemical Society, Washington, D.C., (1989). Ed. by D.R. Salahub and M.C. Zerner.

[304] S. Huzinaga, J. Andzelm, M. Klobukowski, E. Radzio-Andzelm, E. Sakai, and H. Tatewaki. *Gaussian Basis Sets for Molecular Calculations.* Elsevier, Amsterdam, (1984).

[305] H. Sambe and R.H. Felton. *J. Chem. Phys.* **62**, 1122 (1975).

[306] B.I. Dunlap, J.W.D. Connolly, and J.R. Sabin. *J. Chem. Phys.* **71**, 3396 (1979).

[307] B.I. Dunlap, J.W.D. Connolly, and J.R. Sabin. *J. Chem. Phys.* **71**, 4993 (1979).

[308] Y.C. Zheng and J. Almlöf. *Chem. Phys. Lett.* **214**, 397 (1993).

[309] P.M.W. Gill, B.G. Johnson, and C.A. Gonzalez. Q-chem. Q-CHEM Inc, (1993).

[310] S.F. Boys and P. Rajagopal. *Adv. Quantum Chem.* **2**, 1 (1965).

[311] A.D. Becke. *J. Chem. Phys.* **88**, 2547 (1988).

[312] J.M. Pérez-Jorda, A.D. Becke, and E. San-Fabián. *J. Chem. Phys.* **100**, 6520 (1994).

[313] P.M. Boerrigter, G. Te. Velde, and E.J. Baerends. *Int. J. Quantum Chem.* **33**, 87 (1988).

[314] F.W. Averill and G.S. Painter. *Phys. Rev. B* **39**, 8115 (1989).

[315] M.R. Pederson and K.A. Jackson. *Phys. Rev. B* **41**, 7453 (1990).

[316] G.Te. Velde and E.J. Baerends. *J. Comput. Phys.* **99**, 84 (1992).

[317] M. Abramowitz and I.A. Stegun, editors. *Handbook of Mathematical Functions.* Dover, New York, (1970).

[318] W.H. Press, B.P. Flannery, S.A. Teukolski, and W.T. Vetterling. *Numerical Recipes.* Cambridge University Press, New York, (1989).

[319] S.L. Sobollev. *Sibirsk. Mat. Zh.* **3**, 769 (1962).

[320] A.D. McLaren. *Math. Comput.* **17**, 361 (1963).

[321] A.H. Stroud. *Approximate Calculation of Multiple Integrals.* Prentice Hall, Englewood Cliffs, (1971).

[322] V.I. Lebedev. *Zh. Vychisl. Mat. Fiz.* **15**, 48 (1975).

[323] V.I. Lebedev. *Zh. Vychisl. Mat. Fiz.* **16**, 293 (1976).

[324] V.I. Lebedev. *Sibirsk. Mat. Zh.* **18**, 132 (1977).

[325] V.I. Lebedev. *in Proc. Conf. Novosibirsk (1978).* Nauka Sibirsk. Otdel., Novosibirsk, (1980). Ed. by S.L. Sobolev.

[326] S.I. Konyaev. *Mat. Zametki* **25**, 629 (1979).

[327] J. Guan. Density-functional study of sodium cluster polarizabilities. Master's thesis, Université de Montréal, (1995).

[328] S.J.A. van Gisbergen, J.G. Snijder, and E.J. Baerends. *Comput. Phys. Commun.* **118**, 119 (1999).

[329] R. Singh and B.M. Deb. *Phys. Reports* **311**, 50 (1999).

[330] J. Frenkel. *Wave Mechnics: Advanced General Theory.* Oxford University Press, (1934).

[331] R. van Leewen. *Phys. Rev. Lett.* **80**, 1280 (1998).

[332] A.L. Fetter and J.D. Walecka. *Quantum Theory of Many–Particle Systems.* McGraw-Hill Book Company, (1971).

[333] F. Sim, D.R. Salahub, and S. Chin. *Int. J. Quant. Chem.* **43**, 463 (1992).

[334] A. Sadlej and M. Urban. *J. Mol. Struc.(Theochem)* **234**, 147 (1991).

[335] J.A. Pople, P.M.W. Gill, and N.C. Handy. *Int. J. Quant. Chem.* **56**, 303 (1995).

[336] D. Maurice and M. Head-Gordon. *Int. J. Quant. Chem. Symp.* **29**, 361 (1995).

[337] D.R. Salahub and N. Russo, editors. *Metal-Ligand Interactions: From Atoms, to Clusters, to Surfaces.* Kluwer Academic Publishers, Dordrechet, The Netherlands, (1992).

[338] Bruce. C. Gates, editor. *Metal Clusters in Catalysis.* Amsterdam, New York: New York, NY, U.S.A., (1986).

[339] G. Süss-Fink and G. Meister. *Adv. Org. Chem.* **35**, 41 (1993).

[340] F. Spiegelmann and D. Pavolini. *J. Chem. Phys.* **89**, 4954 (1988).

[341] J. Flad, H. Stoll, and H. Preuss. *J. Chem. Phys.* **71**, 3042 (1979).

[342] J. Flad, G. Igel, M. Dolg, H. Stoll, and H. Preuss. *Chem. Phys.* **75**, 331 (1983).

[343] J.L. Martins, J. Buttet, and R. Car. *Phys. Rev. Lett.* **53**, 655 (1984).

[344] J.L. Martins, J. Buttet, and R. Car. *Phys. Rev. B* **31**, 1804 (1985).

[345] U. Röthlisberger and W. Andreoni. *J. Chem. Phys.* **94**, 8129 (1991).

[346] Walt A. de Heer. *Rev. Modern Phys.* **65**, 611 (1993).

[347] Keith Clemenger. *Phys. Rev. B* **32**, 1359 (1985).

[348] Y. Wang, T.F. George, D.M. Lindsay, and A.C. Beri. *J. Chem. Phys.* **86**, 3493 (1987).

[349] F. Spiegelmann and R. Poteau. *Phys. Chem. Finite Systems: From Clusters to Crystal* **I**, 465 (1992).

[350] J.L. Martins, R. Car, and J. Buttet. *J. Chem. Phys.* **78**, 5646 (1983).

[351] H.-O. Beckmann, J. Koutecký, and V. Bonačić-Koutecký. *J. Chem. Phys.* **73**, 5182 (1980).

[352] L. Szasz. *Pseudopotential Theory of Atoms and Molecules.* John Wiley, New York, (1985).

[353] W.R. Wadt and P.J. Hay. *J. Chem. Phys.* **82**, 284 (1985).

[354] P.J. Hay and W.R. Wadt. *J. Chem. Phys.* **82**, 270 (1985).

[355] V. Bonifacic and S. Huzinaga. *J. Chem. Phys.* **83**, 4573 (1974).

[356] S. Katsuki and H. Takata. *Int. J. Quantum Chem.* **18**, 25 (1980).

[357] S. Katsuki and M. Inokuchi. *J. Phys. Soc. Jpn.* **51**, 3652 (1982).

[358] J. Andzelm, E. Radzio, and D.R. Salahub. *J. Chem. Phys.* **83**, 4573 (1985).

[359] S. Huzinaga, L. Seijo, Z. Barandiaran, and M. Klobukowski. *J. Chem. Phys.* **86**, 2132 (1987).

[360] M. Klobukowski. *Chem. Phys. Lett.* **172**, 361 (1990).

[361] M. Klobukowski. *Chem. Phys. Lett.* **183**, 417 (1991).

[362] I. Moullet. PhD thesis, Ecole Polytechnique Féderale de Lausanne, (1989).

[363] I. Moullet, J.L. Martins, F. Reuse, and J. Buttet. *Z. Phys. D: At., Mol. Clusters* **12**, 353 (1989).

[364] G. Höjer and J. Chung. *Int. J. Quan. Chem.* **14**, 623 (1978).

[365] Y. Sakai and S. Huzinaga. *J. Chem. Phys.* **76**, 2537 (1982).

[366] J. Andzelm, N. Russo, and D.R. Salahub. *J. Chem. Phys.* **87**, 6562 (1987).

[367] J.W. Andzelm, M.E. Casida, A. Koester, E. Proynov, A. St-Amant, D.R. Salahub, H. Duarte, N. Godbout, J. Guan, C. Jamorski, M. Leboeuf, V. Malkin, O. Malkina, F. Sim, and A. Vela. deMon-KS. University of Montreal, (1995). version 1.2.

[368] R.L. Martin and E.R. Davidson. *Mol. Phys.* **35**, 1713 (1978).

[369] G.B. Bachelet, D.R. Hamann, and M. Schlüter. *Phys. Rev. B* **26**, 4199 (1982).

[370] J.N. Bardsley. *Case Stud. At. Phys.* **4**, 299 (1974).

[371] G. Pacchioni and J. Koutecký. *J. Chem. Phys.* **81**, 3588 (1984).

[372] U. Röthlisberger, W. Andreoni, and P. Giannozzi. *J. Chem. Phys.* **96**, 1248 (1992).

[373] W.J. Stephens, M.M. Hessel, P.J. Bertoncini, and A.C. Wahl. *J. Chem. Phys.* **66**, 1477 (1977).

[374] Z. Liu, L.E. Carter, and E.A. Carter. *J. Phys. Chem.* **99**, 4355 (1995).

[375] C. Kittel. *Introduction to Solid State Physics.* Wiley, New York, (1976).

[376] K.I. Peterson, P.D. Dao, R.W. Farley, and Jr. A.W. Castleman. *J. Chem. Phys.* **80**, 1780 (1978).

[377] K.K. Verma, J.T. Bahns, A.R. Rejei-Rizi, W.C. Stwalley, and W.T. Zemke. *J. Chem. Phys.* **78**, 3599 (1983).

[378] H.-A. Eckel, J.-M. Gress, J. Biele, and W. Demtröder. *J. Chem. Phys.* **98**, 135 (1992).

[379] K.P. Huber and G. Herzberg. *Constants of Diatomic Molecules.* Van Nostrand Reinhold, New York, (1979).

[380] M. Broyer, G. Delacretaz, P. Labastie, J.P. Wolf, and L. Wöste. *J. Phys. Chem.* **91**, 2626 (1987).

[381] K. Hilpert and Ber. Bunsenges. *Phys. Chem.* **88**, 260 (1984).

[382] R.W. Molof, H.L. Schwartz, T.M. Miller, and B. Bederson. *Phys. Rev. A* **10**, 1131 (1974).

[383] R.C. Weast, editor. *CRC Handbook of Chem. and Phys.* CRC Press, Cleveland, Ohio, 57th edition, (1976).

[384] K. Nuroh, M.J. Stott, and E. Zaremba. *Phys. Rev. Lett.* **49**, 862 (1982).

[385] G.D. Mahan. *J. Chem. Phys.* **76**, 493 (1982).

[386] S. Baroni, P. Giannozzi, and A. Testa. *Phys. Rev. Lett.* **58**, 1861 (1987).

[387] M.E. Casida, C. Jamorski, K.C. Casida, and D.R. Salahub. *J. Chem. Phys.* **108**, 4439 (1998).

[388] S.J.A. van Gisbergen, J.G. Snijders, and E. J. Baerends. *Chem. Phys. Lett.* **259**, 599 (1996).

[389] S.J.A. van Gisbegen, V.P. Osinga, O.V. Gritsenko, R. van Leeuwen, J.G. Snijders, and E.J. Baerends. *J. Chem. Phys.* **105**, 3142 (1996).

[390] V.P. Osinga, S.J.A. van Gisbegen, J.G. Snijders, and E.J. Baerends. *J. Chem. Phys.* **106**, 5091 (1996).

[391] T.A. Miller, R.S. Freund, and R. W. Field. *J. Chem. Phys.* **65**, 3790 (1976).

[392] D.C. Cartwright and P.J. Hay. *Astrophys. J.* **257**, 383 (1982).

[393] A.C.H. Chan and E.R. Davidson. *J. Chem. Phys.* **49**, 727 (1968).

[394] P.S. Bagus, C.M. Mosera, P. Goethals, and G. Verhaegen. *J. Chem. Phys.* **58**, 1886 (1972).

[395] D.L. Cooper. *J. Chem. Phys.* **80**, 1961 (1984).

[396] I.D. Petsalakis, G. Theodorakopoulos, and C.A. Nicolaides. *J. Chem. Phys.* **97**, 7623 (1992).

[397] H.E. Popkie and W.H. Henneker. *J. Chem. Phys.* **55**, 616 (1971).

[398] D.L. Cooper, S.J. Prosser, and W.G. Richards. *J. Phys. B* **14**, L487 (1981).

[399] P.J. Kuntz and A.C. Roach. *J. Chem. Phys.* **74**, 3420 (1981).

[400] A.C. Roach and P.J. Kuntz. *Mol. Phys.* **45**, 853 (1982).

[401] R. Montagnani, P. Riani, and O. Salvetti. *Theor. Chim. Acta* **60**, 399 (1982).

[402] C.M. Marian. *Chem. Phys.* **100**, 13 (1985).

[403] S.R. Langhoff, C.W. Bauschlicher, and H. Partridge. *J. Chem. Phys.* **84**, 1687 (1986).

[404] S.R. Langhoff, C.W. Bauschlicher, H. Partridge, and A. Ahlrichs. *J. Chem. phys.* **84**, 5025 (1986).

[405] F.B.C. Machado and F.R. Ornellas. *Mol. Phys.* **67**, 1129 (1989).

[406] F.R. Ornellas, F.B.C. Machado, and O. Roberto-Neto. *Mol. Phys.* **77**, 1169 (1992).

[407] N. Washida, D. Kley, K.H. Becker, and W. Groth. *J. Chem. Phys.* **63**, 4230 (1975).

[408] J.A. Coxon, D.A. Ramsay, and D.W. Setser. *Can. J. Phys.* **53**, 1587 (1975).

[409] G. Das, T. Janis, and A.C. Wahl. *J. Chem. Phys.* **61**, 1274 (1974).

[410] A.D. McLean, B. Liu, and G.S. Chandler. *J. Chem. Phys.* **97**, 8459 (1992).

[411] H.F. Schaefer III and T.G. Heil. *J. Chem. Phys.* **54**, 2573 (1971).

[412] H. Lavendy, G. Gandara, and J.M. Robbe. *J. Mol. Spectry.* **106**, 395 (1984).

[413] G. Peris, F. Rajadell, X. Li, J. Planelles, and J. Paldus. *Mol. Phys.* **94**, 235 (1998).

[414] T.G. Heil and H.F. Schaefer III. *Astrophys. J.* **163**, 425 (1971).

[415] H. Ito, Y. Ozaki, T. Nagata, T. Kondow, K. Kuchitsu, K. Takatsuka, H. Nakamura, and Y. Osamura. *Chem. Phys.* **98**, 81 (1985).

[416] P.J. Bruna, H. Dohmann, and S.D. Peyerimhoff. *Can. J. Phys.* **62**, 1508 (1984).

[417] M.R. Gorbal and M.I. Savadatti. *Chem. Rev.* **82**, 527 (1982).

[418] A. Carrington and P.J. Sarre. *Mol. Phys.* **33**, 1495 (1977).

[419] N. Honjou and F. Sasaki. *Mol. Phys.* **37**, 1593 (1979).

[420] P. Rosmus and H.J. Werner. *Mol. Phys.* **47**, 661 (1982).

[421] N. Honjou and D.R. Yarkony. *J. Phys. Chem.* **89**, 44 (1985).

[422] C.M. Marian, M. Larsson, B.J. Olsson, and P. Sigray. *Chem. Phys.* **130**, 361 (1989).

[423] K.K. Baeck, M. S. Lee, and Y.S. Lee. *Chem. Phys. Lett.* **198**, 273 (1992).

[424] H. Lavendy, J.M. Robbe, and J.P. Flamment. *Chem. Phys. Lett.* **205**, 456 (1993).

[425] P. Baltzer, M. Lundqvist, B. Wannberg, L. Karlsson, M. Larsson, M.A. Hayes, J.B. West, M.R.F. Siggel, A.C. Parr, and J.L. Dehmer. *J. Phys. B* **27**, 4915 (1994).

[426] N. Honjou and E. Miyoshi. *Chem. Phys.* **212**, 363 (1996).

[427] M. Carlsson-Göthe, B. Wannberg, F. Falk, L. Karlsson, S. Svensson, and P. Baltzer. *Phys. Rev. A* **44**, R17 (1991).

[428] D.C. Cartwright and T.H. Dunning Jr. *J. Phys. B* **8**, L100 (1975).

[429] E.W. Thulstrup and A. Andersen. *J. Phys. B* **8**, 965 (1975).

[430] P. Senn and F.A. Grimm. *J. Mol. Struc.(Theochem)* **150**, 215 (1987).

[431] N. Honjou and E. Miyoshi. *J. Mol. Struc.(Theochem)* **451**, 41 (1998).

[432] N. Kosugi, H. Kuroda, and S. Iwata. *Chem. Phys.* **39**, 337 (1979).

[433] P.W. Langhoff, S.R. Langhoff, T.N. Rescigno, J. Schirmer, L.S. Cederbaum, W. Domcke, and W. Von Niessen. *Chem. Phys.* **58**, 71 (1981).

[434] H. Agren, R. Arneberg, J. Müller, and R. Manne. *Chem. Phys.* **83**, 53 (1984).

[435] J.A. Nichols, D.L. Yeager, and P. Jørgensen. *J. Chem. Phys.* **80**, 293 (1984).

[436] M. Head-Gordon, D. Maurice, and M. Oumi. *Chem. Phys. Lett.* **246**, 114 (1995).

[437] D. Maurice and M. Head-Gordon. *J. Phys. Chem.* **100**, 6131 (1996).

[438] M. Head-Gordon, A.M. Graña, D. Maurice, and C.A. White. *J. Phys. Chem.* **99**, 14261 (1995).

[439] A.J. Sadlej. *Theor. Chim. Acta* **79**, 123 (1991).

[440] G. Herzberg. *Spectra of diatomic molecules.* D. Van Nostrand, New York, (1950).

[441] S. Svensson, M. Carlsson-Göthe, L. Karlsson, A. Nilsson, N. Martensson, and U. Gelius. *Phys. Scr.* **44**, 184 (1991).

[442] H. Agren, R. Arneberg, J. Müller, and R. Manne. *Chem. Phys.* **83**, 53 (1984).

[443] H. Nakatsuji. *Chem. Phys. Lett.* **177**, 331 (1991).

[444] A. J. Sadlej. *Coll. Czech. Chem. Comm.* **53**, 1995 (1988).

[445] R. Colin and D.D. Greef. *Can. J. Phys.* **53**, 2142 (1975).

[446] P. Baltzer, M. Larsson, L. Karlsson, B. Wannberg, and M. Carlsson-Göthe. *Phys. Rev.* **46**, 5545 (1992).

[447] J. Schirmer and O. Walter. *Chem. Phys.* **78**, 201 (1983).

[448] A.O. Bawagan, C.E. Brion, E.R. Davidson, C. Boyle, and R.F. Frey. *Chem. Phys.* **128**, 439 (1988).

[449] M. Broyer, J. Chevaleyre, and Ph. Dugourd. *Phys. Rev. Lett. A* **42**, 6954 (1990).

[450] J.M. Pacheco and J.L. Martins. *J. Chem. Phys.* **106**, 6039 (1997).

[451] A. Rubio, J.A. Alonso, X. Blase, L.C. Balbás, and S.G. Louie. *Phys. Rev. Lett.* **77**, 247 (1996).

[452] F.W. Loomis and R.E. Nussbaum. *Phys. Rev.* **38**, 1447 (1931).

[453] J.E. Vance and J.R. Huffman. *Phys. Rev.* **47**, 215 (1935).

[454] A. Herrmann, M. Hoffmann, S. Leutwyler, E. Schumacher, and L. Wöste. *Chem. Phys. Lett.* **62**, 216 (1979).

[455] C. Bréchignac, Ph. Cahuzac, F. Carlier, and J. Leygnier. *Chem. Phys. Lett.* **164**, 433 (1989).

[456] J. Blanc, M. Broyer, J. Chevaleyre, Ph. Dugourd, H. Kühling, P. Labastie, M. Ulbricht, J.P. Wolf, and L. Wöste. *Z. Physik D* **19**, 7 (1991).

[457] J.H. Bartlett and W.H. Furry. *Phys. Rev.* **38**, 1615 (1931).

[458] W.H. Furry. *Phys. Rev.* **39**, 1015 (1932).

[459] W.H. Furry. *Phys. Rev.* **43**, 361 (1933).

[460] A.L. Companion, D.J. Steible, and A.J. Starshak. *Chem. Phys.* **49**, 3637 (1968).

[461] R.N. Yardley and G.G. Balint-Kurti. *Chem. Phys.* **16**, 287 (1976).

[462] D.W. Davies and G. DelConde. *Chem. Phys.* **12**, 45 (1976).

[463] P.S. Bagus, G. DelConde, and D.W. Davies. *Faraday Discuss. Chem. Soc.* **62**, 321 (1977).

[464] W.H. Gerber and E. Schumacher. *J. Chem. Phys.* **69**, 1692 (1978).

[465] G. Gardet, F. Rogemond, and H. Chermette. *J. Chem. Phys.* **105**, 9933 (1996).

[466] H.-O. Beckmann. *Chem. Phys. Lett.* **93**, 240 (1982).

[467] J. Koutecký, I. Boustani, and V. Bonačić-Koutecký. *Int. J. Quantum Chem.* **38**, 149 (1990).

[468] V. Bonačić-Koutecký, C. Fuchs, J. Pittner, and J. Koutecký. *Ber. Bunsenges. Phys. Chem.* **96**, 1262 (1992).

[469] J. Jellinek, V. Bonačić-Koutecký, P. Fantucci, and M. Wiechert. *J. Chem. Phys.* **101**, 10092 (1994).

[470] V. Bonačić-Koutecký, J. Jellinek, M. Wiechert, and P. Fantucci. *J. Chem. Phys.* **107**, 6321 (1997).

[471] D. Reichardt, V. Bonačić-Koutecký, P. Fantucci, and J. Jellinek. *Chem. Phys. Lett.* **279**, 129 (1997).

[472] I. Boustani, W. Pewestorf, P. Fantucci, V. Bonačić-Koutecký, and J. Koutecký. *Phys. Rev. B* **35**, 9437 (1987).

[473] Joint Commission for Spectroscopy of the International Astronomical Union (JCSIAU), the International Union of Pure, and Applied Physics (IUPAP). *J. Chem. Phys.* **23**, 1997 (1955).

[474] I. Schmidt-Mink, W. Müller, and W. Meyer. *Chem. Phys.* **92**, 263 (1985).

[475] P. Fernandez-Sera, V. Botella, Y.G. Smeyers, A. Galano, and G. Delgado-Barrio. *Intern. J. Quant. Chem.* **54**, 305 (1995).

[476] U. Kaldor. *Chem. Phys.* **140**, 1 (1990).

[477] U. Röthlisberger. *J. Chem. Phys.* **94**, 8129 (1991).

[478] A. Henriet and F. Masnou-Seeuws. *J. Phys. B* **20**, 671 (1987).

[479] F. Cocchini, T.H. Upton, and W. Andreoni. *J. Chem. Phys.* **88**, 6068 (1988).

[480] V. Bonačić-Koutecký, P. Fantucci, C. Fuchs, J. Koutecký, and J. Pittner. *Z. Phys. D* **26**, 17 (1993).

[481] V. Bonačić-Koutecký, P. Fantucci, and J. Koutecký. *Chem. Phys. Lett.* **166**, 32 (1990).

[482] V. Bonačić-Koutecký, P. Fantucci, J. Gaus, and J. Koutecký. *Z. Phys. D* **19**, 37 (1991).

[483] C.R.C. Wang, S. Pollack, J. Hunter, G. Alameddin, T. Hoover, D. Cameron, S. Liu, and M.M. Kappes. *Z. Phys. D* **19**, 13 (1991).

[484] M. Madjet, C. Guet, and W.R. Johnson. *Phys. Rev. A* **51**, 1327 (1995).

[485] I. Vasiliev, S. Öğüt, and J. Chelikowsky. *Phys. Rev. Lett.* **82**, 1919 (1999).

[486] D.W. Davies and G.J.R. Jones. *Chem. Phys. Lett.* **81**, 279 (1981).

[487] U. Kaldor. *Israel J. Chem.* **31**, 345 (1991).

[488] M.E. Casida and D.R. Salahub. (1999). submitted.

[489] B.A. Collings, K. Athanassenas, D.M. Rayner, and P.A. Hackett. *Z. Physik D* **26**, 36 (1993).

[490] M.B. Knickelbein. *J. Chem. Phys.* **99**, 2377 (1993).

[491] M.B. Knickelbein and W.J.C. Menezes. *Phys. Rev. Lett.* **69**, 1046 (1993).

[492] M. Castro, C. Jamorski, and D.R. Salahub. *Chem. Phys. Lett.* **271**, 133 (1997).

[493] G.A. Cisneros, M. Castro, and D.R. Salahub. *Int. J. Quant. Chem.* (1999). submitted.